The Late Cenozoic Climatic and Tectonic Evolution of the Mount Everest Region, Central Himalaya

by

Mary Hannah Schultz

A Dissertation Presented in Partial Fulfillment
of the Requirements for the Degree
Doctor of Philosophy

Approved June 2017 by the
Graduate Supervisory Committee:

Kip V. Hodges, Chair
Kelin X. Whipple
Steven Semken
Arjun M. Heimsath
Christy Till

ARIZONA STATE UNIVERSITY

August 2017

ABSTRACT

The collision of India and Eurasia constructed the Himalayan Mountains. Questions remain regarding how subsequent exhumation by climatic and tectonic processes shaped the landscape throughout the Late Cenozoic to create the complex architecture observed today. The Mount Everest region underwent tectonic denudation by extension and bestrides one of the world's most significant rain shadows. Also, glacial and fluvial processes eroded the Everest massif over shorter timescales. In this work, I review new bedrock and detrital thermochronological and geochronological data and both one- and two-dimensional thermal-mechanical modeling that provides insights on the age range and rates of tectonic and erosional processes in this region.

A strand of the South Tibetan detachment system (STDS), a series of prominent normal-sense structures that dip to the north and strike along the Himalayan spine, is exposed in the Rongbuk valley near Everest. Using thermochronometric techniques, thermal-kinematic modeling, and published (U-Th)/Pb geochronology, I show exhumation rates were high (~3-4 mm/a) from at least 20 to 13 Ma because of slip on the STDS. Subsequently, exhumation rates dropped drastically to ≤ 0.5 mm/a and remain low today. However, thermochronometric datasets and thermal-kinematic modeling results from Nepal south of Everest reveal a sharp transition in cooling ages and exhumation rates across a major knickpoint in the river profile, corresponding to the modern-day Himalayan rainfall transition. To the north of this transition, exhumation histories are similar to those in Tibet. Conversely, < 3 km south of the transition, exhumation rates were relatively low until the Pliocene, when they increased to ~4 mm/a before slowing at ~3 Ma. Such contrasting exhumation histories over a short distance suggest that bedrock

exhumation rates correlate with modern precipitation patterns in deep time, however, there are competing interpretations regarding this correlation.

My work also provides insights regarding how processes of glacial erosion act in a glacio-fluvial valley north of Everest. Integrated laser ablation U/Pb and (U-Th)/He dating of detrital zircon from fluvial and moraine sediments reveal sourcing from distinctive areas of the catchment. In general, the glacial advances eroded material from lower elevations, while the glacial outwash system carries material from higher elevations.

DEDICATION

This dissertation is dedicated to all of the families affected by the April 2015 Gorkha earthquake in Nepal.

ACKNOWLEDGMENTS

This dissertation would not have been possible without the help and support of my family and friends from both ASU and around the world. The past four and a half years have been an adventure in every sense of the word.

Thank you to Kip Hodges for accepting me as a student and for all your support. The learning curve was a steep one, but I was able to succeed with your patience and encouragement. Thank you for all you have taught me and for being such a steadfast supporter of women in science. Thanks also to the rest of my committee: Kelin Whipple, Steven Semken, Arjun Heimsath, and Christy Till for your wonderful guidance and mentorship. I must give a special thanks to Kelin for the many helpful and insightful discussions about my data, geothermal gradients, and knickpoints. A special thank you also must be given to Steven Semken. Your enthusiastic support for ASU and its students is astounding and your work will forever inspire me.

I would also like to give a big thank you to Matthijs van Soest, Jo-Anne Wartho, and Chris McDonald for their wonderful mentorship in the laboratories. All of you patiently helped me with analyses and participated in many informative discussions about my results. Thank you to Michelle Aigner for teaching me how to use the lab equipment, being my dissolution buddy, and for many wonderful discussions about science, music, and life.

Many thanks go to Todd Ehlers for teaching me about thermo-kinematic modeling and being so helpful and supportive half a world away and to Byron Adams, Adam Forte, and Cameron Mercer for their advice regarding *Matlab* codes and numerical methods.

Fieldwork in the Himalaya requires a lot of careful organization and planning. Many thanks go to Ding Lin (Chinese Academy of Geosciences), Ross Waldrip (University of Arizona), Paul Kapp (University of Arizona), and our guides and drivers for their excellent logistical assistance in Tibet. Thanks to Nathaniel Borneman for helping me get through my short bout of altitude sickness. Many thanks also to Bhim Chand and Bir Tamang of Earth's Paradise Trekking and Expeditions for organizing our fantastic fieldwork trek in Nepal.

A tremendous thanks to the National Science Foundation for funding my research in the form of Tectonics division grants EAR1007929 and EAR1346360 to my advisor, Kip Hodges.

Many thanks to Alexandra Horne, my seven sister. Thank you for being such an amazing field assistant in Nepal and partaking in rebooked flights and visas, 500 rummy, boiled potatoes, tingly fingers and toes, Mars chocolate pie, yaks, hummocky moraines, and all that came with the Himalaya.

I could not thank my current and past fellow research group members and colleagues enough: Alex, Alka, Alyssa, Anna, Byron, Cameron, Chris, Frances, Kelsey, Nate, Pye, Wendy, and all the folks in 603, you are all the reason why completing this dissertation was possible. Thank you thank you thank for all your encouragement and support through this process.

Finally, thank you to my incredible mother, Kathy, my father TC, Elizabeth, and Cee. You believed in me and have supported me every step of the way. I also owe so much to my fur-babies, Emm, Josie, and Leonard for the many cozy cuddles.

TABLE OF CONTENTS

Page

CHAPTER Page

CHAPTER Page

LIST OF TABLES

LIST OF FIGURES

Figure Page

CHAPTER 1

INTRODUCTION

1. Motivation

The Himalayan Mountains were built by intense uplift following the collision of two continents, India and Eurasia. Climatic and tectonic forces have acted in concert, particularly over the last 20 million years, to develop the complex architecture of one of the world's younger ranges. Although much recent work has been done to study the modern-day interactions of these processes, understanding how Himalayan climate and tectonics have shaped landscape over longer timescales throughout the Late Cenozoic remains ambiguous. The Mount Everest region that straddles the border of eastern Nepal and south-central Tibet in the central Himalaya provides a unique opportunity to study a variety of these processes in detail. For example, the central Himalaya exhibit one of the most profound rain shadows in the world and questions remain regarding how long this rainfall pattern has existed and whether or not it is correlated with the modern-day precipitation pattern. Moreover, south-central Tibet underwent tectonic denudation by normal faulting, the magnitude and significance of which has generated considerable scientific discussion over the past few decades. On shorter timescales, glaciers have eroded the highest elevations, carving out well-defined peaks, depositing moraines, and eventually establishing modern-day glacio-fluvial systems. How these processes have acted in space in time to erode glacial catchments of the High Himalaya has not been quantified. In the following chapters, I review new bedrock and detrital thermochonological and geochronological data and both one- and two-dimensional

thermal-mechanical modeling that provides insights on the age range and rates of tectonic and erosional processes in the Everest region, as well as whether or not the modern precipitation pattern associated with the Himalayan rain shadow may have extended back in time and influenced erosion patterns over several million years.

The structurally highest feature of the Himalayan orogenic wedge is a north-dipping, low-angle extensional fault system called the South Tibetan detachment system (STDS) that is exposed at the crest of the range and can be traced across the majority of the range (e.g., Hodges, 2000). The significance of the STDS in the Miocene tectonic evolution of the Himalaya remains hotly debated. Some workers argue that the STDS accommodated tens to hundreds of kilometers of displacement and acted as the top boundary of a southward extruding channel containing the metamorphic core of the Himalaya, aided with the extreme precipitation from the Indian summer monsoon (ISM) on the southern flank of the range (Nelson et al., 1996; Beaumont et al., 2001; Hodges et al., 2001; Grujic et al., 2002). Others insist that the STDS was a former thrust system that reactivated as a normal fault and displaced no more than a few kilometers (Yin, 2013; Webb et al., 2007; Webb, 2013). The Mount Everest region in south-central Tibet offers a unique opportunity to study the slip history of this structure due to the spectacular exposure of the STDS footwall rocks. By the combination of thermochronological dating of footwall rocks and 1- and preliminary 2-D thermal-kinematic modeling, we determined that the minimum total displacement on the STDS in the Everest region from *ca.* 20 to 13 Ma was *ca.* 61 to 289 km, suggesting that the STDS was a defining structure in the tectonic evolution of the Miocene Himalaya.

Our thermal-kinematic results from the southern Tibetan plateau indicate the majority of rapid exhumation took place during slip on the STDS during the Miocene and any exhumation subsequent to *ca.* 13 Ma was low (≤0.5 mm/a) due to background erosion on the plateau. In contrast, the steep southern flank of the range exposes some of the highest modern-day erosion rates. Observations concerning present-day erosion in the Himalaya are generally consistent with data from the NASA/JAXA (Japan Aerospace Agency)'s joint Tropical Rainfall Measurement Mission (TRMM) that reveal a stark rain shadow existing across the ranges of the central Himalaya, with the rapidly eroding regions on the southern flank of the range receiving up to four meters of rainfall per year, while the southern Tibetan plateau with very low background erosion sees less than half a meter of rainfall annually. How far back in time the Himalayan rain shadow existed, however, remains uncertain. Previous studies have shown that exhumation rates north and south of the rainfall transition are uniform, with no change in rates across the precipitation gradient (Burbank et al., 2003; Blythe et al., 2007; McDermott, 2012). These studies, however, were all conducted along major Transhimalayan rivers with sources on the Tibetan plateau and that display extreme knickpoints in the river profile as they cross the range crest, their grand valleys possibly enabling large monsoon storms to track farther to the north (Barros et al., 2006). A transect across Mount Everest avoids this potential issue and indeed, we observed a sharp change in exhumation rates not at the top of the range crest, as proposed by Carrapa et al. (2016), but well to the south of the range crest, at the location of the major rainfall transition itself. To the north of this transition, cooling ages and exhumation histories were similar to our results from Chapter 2, with relatively high exhumation rates from at least *ca.* 20 to 13 Ma and very low

exhumation rates thereafter. In contrast, exhumation histories to the south of the rainfall change are relatively low throughout the Miocene until *ca.* 5 to 4 Ma, when they abruptly increase before relaxing slightly at *ca.* 3 Ma. The acute transition we observe in our cooling ages and modeled exhumation histories at the location of the rainfall transition suggests that the rainfall pattern has retained stability since at least the Pliocene and that bedrock exhumation has mimicked this pattern over millennial timescales.

In addition to tectonic denudation and precipitation, erosion due to glaciers has been crucial in shaping the spectacular topography of the Himalaya. Numerous studies have described and dated Himalayan glacial moraine deposits (Benn et al., 2002; Finkel et al., 2003; Gayer et al., 2006; Barnard et al., 2006; Owen et al., 2009); however, the spatial and temporal variations in Himalayan glacial erosion over long timescales have not yet been quantified unlike the glacial-fluvial systems of other orogens (Stock et al., 2006; Tranel et al., 2011; Ehlers et al., 2015; Enkelmann and Ehlers, 2015). We use geologic mapping of the Rongbuk glacial catchment in the Everest region, as well as the recently developed laser ablation U/Pb and (U-Th)/He double dating (LADD) technique on detrital zircons, to provide insight to how the erosive mechanisms of glaciers differ from those of the modern fluvial system. The results suggest that sediment from the modern fluvial system is sourced from much higher elevations than the glacial moraine material, implying that glacial and fluvial erosive processes act on distinctively different parts of a catchment.

2. Outline of Chapters 2-5

In Chapter 2, we constrain the Miocene slip history of the South Tibetan detachment system in the Rongbuk valley of south-central Tibet in the Everest region through a combination of low-temperature thermochronometric datasets consisting of muscovite $^{40}Ar/^{39}Ar$ step heating, zircon (U-Th)/He (ZrnHe), and apatite (U-Th)/He (ApHe) and 1-D thermal and thermal-kinematic modeling. The thermochronologic cooling ages show no variation down the dip-direction of the fault and 1-D thermal modeling results suggest rapid cooling of the detachment's footwall occurred between *ca.* 15.5 and 11 Ma. We interpret the sharp decrease in modeled exhumation rates (*ca.* 3 mm/a to ≤0.5 mm/a) from *ca.*15.4 to 13 Ma to indicate brittle displacement following ductile slip. We estimate that between *ca.* 61 to 289 km of total displacement occurred on the STDS during the Miocene in this area, suggesting that the STDS played a significant role in Himalayan tectonic evolution.

In Chapter 3, we use new thermochronometric datasets from the Dzakar Chu and Ra Chu (two valleys to the north of the Rongbuk valley), our published data from Chapter 2 (Schultz et al., 2017), and the more sophisticated 2-D thermal-kinematic modeling software package *Pecube* (Braun, 2003; Braun et al., 2012) to expand our understanding slip history of the STDS and to determine the appropriateness of the simpler 1-D modeling methodology we employed in Chapter 2. The amount of total displacement on the STDS from 2-D thermal-kinematic modeling is *ca.* 167 to 338 km, which agrees with the estimates from Chapter 2. We suggest that for rapidly exhuming orogenic environments, 1-D thermal-kinematic modeling methods are adequate.

Chapter 4 explores the longevity of the Himalayan rain shadow using data of the NASA/Japan Aerospace Agency's Tropical Rainfall Measurement Mission (TRMM), our thermochronologic and 1-D thermal-kinematic modeling results from Chapter 2, and additional 1-D thermal-kinematic modeling of new muscovite and biotite $^{40}Ar/^{39}Ar$ and zircon and apatite (U-Th)/He datasets from the Khumbu region in eastern Nepal south of the range crest. Thermochronologic data and 1-D model results reveal a sharp transition in both cooling ages and exhumation rate histories across a major knickpoint in the Dudh Kosi river profile, well to the south of the range crest. This transition, occurring over the distance of only a few kilometers, also corresponds with the modern-day rainfall transition, suggesting that the Himalayan rain shadow has held its present pattern since at least the Pliocene.

In Chapter 5, we examine and compare various glacial erosional processes acting on the Rongbuk valley using our bedrock zircon (U-Th)/He results from Chapter 2 as well as new detrital zircon (U-Th)/He and U/Pb datasets from sediment of a Holocene moraine and material from the modern-day fluvial outwash system. Detrital zircon (U-Th)/He and U/Pb results indicate that glacial moraine and outwash processes contrast in both space and time in a catchment, with the glacial moraine eroding material from lower elevations and the modern outwash system source region being much higher in elevation.

Chapter 6 provides a synthesis of the previous chapters and discusses valuable future work.

3. References

Barnard, P.L., Owen, L.A., Finkel, R.C., (2006). Quaternary fans and terraces in the Khumbu Himal south of Mount Everest: their characteristics, age and formation.

Journal of Geological Society of London, 163, 383-399.

Barros, A. P., Chiao, S., Lang, T.J., Burbank, D., and Putkonen, J. (2006). In *Tectonics, Climate, and Landscape Evolution* Vol. Geological Society of America Special Paper *398* (eds S.D. Willett, N. Hovius, M.T. Brandon, & D.M. Fisher), 17-38 (Geological Society of America).

Beaumont, C., Jamieson, R. A., Nguyen, M.H., and Lee, B. (2001). Himalayan tectonics explained by extrusion of a low-viscosity crustal channel coupled to focused surface denudation. *Nature, 414*, 738-742.

Benn, D.I., and Owen, L.A. (2002). Himalayan glacial sedimentary environments: a framework for reconstructing and dating former glacial extents in high mountain regions. *Quaternary International, 97/98,* 3-26.

Blythe, A. E., Burbank, D. W., Carter, A., Schmidt, K., and Putkonen J. (2007). Plio-Quaternary exhumation history of the central Nepalese Himalaya: 1. Apatite and zircon fission track and apatite U-Th /He analyses. *Tectonics, 26*, doi:Tc300210.1029/2006tc001990.

Braun, J. (2003). Pecube: A new finite-element code to solve the 3D heat transport equation including the effects of a time-varying, finite amplitude surface topography. *Computers & Geosciences*, *29*(6), 787-794.

Braun, J., van der Beek, P., Valla, P., Robert, X., Herman, F., Glotzbach, C., Pedersen, V., Perry, C., Simon-Labric, T., and Prigent, C. (2012). Quantifying rates of landscape evolution and tectonic processes by thermochronology and numerical modeling of crustal heat transport using PECUBE. *Tectonophysics*, *524–525*, 1-28.

Burbank, D. W., Blythe, A. E., Putkonen, J., Pratt-Sitaula, B., Gabet, E., Oskin, M., Barros, A., and Ojha, T.P. (2003). Decoupling of erosion and precipitation in the Himalayas, *Nature, 426*, 652-655, doi:10.1038/nature02187.

Carrapa, B., Robert, X., DeCelles, P.G., Orme, D.A., Thomson, S.N., and Schoenbohm, L.M. (2016). Asymmetric exhumation of the Mount Everest region: Implications for the tectono-topographic evolution of the Himalaya. *Geology*, doi: 10.1130/G37756.1.

Cattin, R., and Avouac, J.P., (2000). Modeling mountain building and the seismic cycle in the Himalaya of Nepal. *Journal of Geophysical Research: Solid Earth*. doi: 10.1029/2000JB90032.

Ehlers, T.A., Szameitat, A., Enkelmann, E., Yanites, B.J., and Woodsworth, G.J. (2015). Identifying spatial variations in glacial erosion with detrital thermochronology, Coast Mountains British Columbia. *Journal of Geophysical Research: Earth Surface*, doi: 10.1002/2014JF003432.

Enkelmann, E. and Ehlers, T.A. (2015). Evaluation of detrital thermochronology for quantification of glacial catchment denudation and sediment mixing. *Chemical Geology*, *411,* 299-309.

Finkel, R.C., Owen, L.A., Barnard, P.L., Caffee, M.W., (2003). Beryllium-10 dating of Mount Everest moraines indicates a strong monsoonal influence and glacial synchroneity throughout the Himalaya. *Geology, 31,* 561-564.

Gayer, E., Lavé, J., Pik, R., and France-Lanord, C. (2006). Monsoonal forcing of Holocene glacier fluctuations in Ganesh Himal (Central Nepal) constrained by cosmogenic ^{3}He exposure of garnets. *Earth and Planetary Science Letters*, *252*(3-4), 275-288.

Grujic, D., Hollister, L., and Parrish, R. R. (2002). Himalayan metamorphic sequence as an orogenic channel: insight from Bhutan. *Earth Planetary Science Letters*, *198*, 177–191.

Herman, F., Copeland, P., Avouac, J-P., Bollinger, L., Mahéo, G., Le Fort, P., Rai, S., Foster, D., Pêcher, A., Stüwe, K., and Henry, P. (2010). Exhumation, crustal deformation, and thermal structure of the Nepal Himalaya derived from the inversion of thermochronological and thermobarometric data and modeling of the topography. *Journal of Geophysical Research – Solid Earth, 115*, doi:B0640710.1029/2008jb006126.

Hodges, K. V. (2000). Tectonics of the Himalaya and southern Tibet from two perspectives. *Geological Society of America Bulletin*, *112*, 324-350.

Hodges, K. V., Hurtado, J.M., and Whipple, K.X. (2001). Southward extrusion of Tibetan crust and its effect on Himalayan tectonics. *Tectonics, 20*, 799-809.

Lavé, J. and Avouac, J.P. (2001). Fluvial incision and tectonic uplift across the Himalayas of central Nepal. *Journal of Geophysical Research, 106,* 26561-26591.

McDermott, J. A. (2012). Plio-Pleistocene North-South and East-West Extension at the Southern Margin of the Tibetan Plateau. Ph.D. thesis, Arizona State University.

McDermott, J.A., Whipple, K.X., Hodges, K.V., and van Soest, M.C. (2013). Evidence for Plio-Pleistocene north-south extension at the southern margin of the Tibetan Plateau, Nyalam region. *Tectonics, 32*, 317-333, doi:10.1002/tect.20018.

McDermott, J.A., Hodges, K.V., Whipple, K.X., van Soest, M.C., and Hurtado, J.M. (2015). Evidence for Pleistocene Low-Angle Normal Faulting in the Annapurna-Dhaulagiri Region, Nepal. *Journal of Geology*, *123*(2), 133 – 151.

Nelson, K.D., Zhao, W., Brown, L.D., Kuo, J., Che, J., Xianwen, L., Klemperer, S., Makovsky, Y., Meissner, R., Mechie, J., Kind, R., Wenzel, F., Ni, J., Nabelek, J., Chen, L., Handong, T., Wenbo, W., Jones, A.G., Booker, J., Unsworth, N., Kidd,

W.S.F., Hauk, M., Alsdorf, D., Ross, A., Cogan, M., Wu, C., Sandvol, E.A., and Edwards, M. (1996). Partially molten middle crust beneath southern Tibet: Synthesis of Project INDEPTH Results. *Science*, *274*, 1684-1688.

Owen, L.A., Robinson, R., Benn, D.I., Finkel, R.C., Davis, N.K., Yi, C., Putkonen, J., Li, D., and Murray, A.S. (2009). Quaternary glaciation of Mount Everest. *Quaternary Science Reviews*, *28,* 1412-1433.

Stock, G.M., Ehlers, T.A. and Farley, K.A. (2006). Where does sediment come from? Quantifying catchment erosion with detrital apatite (U-Th)/He thermochronology. *Geology*, *34*, 725-728.

Tranel, L.M., Spotila, J.A., Kowalewski, M.J., and Waller, C.M. (2011). Spatial variation of erosion in a small, glaciated basin in the Teton Range, Wyoming, based on detrital apatite (U-Th)/He thermochronology. *Basin Research*, *23*, 571-590.

Wang, A., Garver, J.I., Wang, G., Smith, J.A., and Zhang, K. (2010). Episodic exhumation of the Greater Himalayan Sequence since the Miocene constrained by fission track thermochronology in Nyalam central Himalaya. *Tectonophysics*, *495*, 315-323.

Webb, A. A. G. (2013). Preliminary balanced palinspastic reconstruction of Cenozoic deformation across the Himachal Himalaya (northwestern India). *Geosphere*, *9*(3), 572-587.

Webb, A. A. G., Yin, A., Harrison, T.M., Celerier, J. and Burgess, W.P. (2007). The leading edge of the Greater Himalayan Crystalline complex revealed in the NW Indian Himalaya: Implications for the evolution of the Himalayan orogen. *Geology*, *35*(10), 955-958.

Yin, A. (2006). Cenozoic tectonic evolution of the Himalayan orogen as constrained by along-strike variation of structural geometry, exhumation history, and foreland sedimentation. *Earth Science Reviews*, *76*, 1-131.

CHAPTER 2

THERMOCHRONOLOGIC CONSTRAINTS ON THE SLIP HISTORY OF THE SOUTH TIBETAN DETACHMENT SYSTEM IN THE EVEREST REGION, SOUTHERN TIBET

1. Abstract

North-dipping, low-angle normal faults of the South Tibetan detachment system (STDS) are tectonically important features of the Himalayan-Tibetan orogenic system. The STDS is best exposed in the N-S-trending Rongbuk Valley in southern Tibet, where the primary strand of the system – the Qomolangma detachment – can be traced down dip from the summit of Everest for a distance of over 30 km. The metamorphic discontinuity across this detachment implies a large net displacement, with previous studies suggesting >200 km of slip. Here we refine those estimates through thermal-kinematic modeling of new (U-Th)/He and $^{40}Ar/^{39}Ar$ data from deformed footwall leucogranites. While previous studies focused on the early ductile history of deformation along the detachment, our data provide new insights regarding the brittle-ductile to brittle slip history. Thermal modeling results generated with the program *QTQt* indicate rapid, monotonic cooling from muscovite $^{40}Ar/^{39}Ar$ closure (*ca.* 15.4 – 14.4 Ma at *ca.* 490˚C) to zircon (U-Th)/He closure (*ca.* 14.3 – 11.0 Ma at ca. 200˚C), followed by slower cooling to apatite (U-Th)/He closure at *ca.* 9 – 8 Ma (at ca. 70˚C). Although previous work has suggested that ductile slip on the detachment lasted only until *ca.* 15.6 Ma, thermal-kinematic modeling of our new data suggests that rapid (*ca.* 3-4 km/Ma) tectonic exhumation by brittle-ductile to brittle fault slip continued to at least *ca.* 13.0 Ma. Much lower modeled

exhumation rates (≤0.5 km/Ma) after *ca.*13 Ma are interpreted to reflect erosional denudation rather than tectonic exhumation. Projection of fault-related exhumation rates backward through time suggests total slip of *ca.* 61 to 289 km on the Qomolangma detachment, with slightly more than a third of that slip occurring under brittle-ductile to brittle conditions.

2. Introduction

Regional-scale, low-angle normal fault ('detachment') systems are common features of extensional tectonic regimes such as the Basin and Range province of the North American Cordillera, but similar features are also found in convergent settings and their significance has proved to be controversial. One of the most impressive confirmed structures of this type is the South Tibetan detachment system (STDS), which crops out near the crest of the Himalaya in Bhutan, India, and Nepal over a distance of well over 1000 km along strike (Burchfiel et al., 1992; Hodges, 2000). Some researchers have argued that normal-sense displacement along the STDS has been one of the defining structural events of Himalayan evolution, enabling the southward extrusion of a thick, mid-crustal channel, over distances of well over 100 km, during the Miocene (Nelson et al., 1996; Beaumont et al., 2001; Hodges et al., 2001; Grujic et al., 2002). Others have instead argued that this structure is comparatively minor and was initiated simply as the upper bounding thrust fault of a tectonic wedge that subsequently accommodated at most a few tens of kilometers of normal-sense offset (Yin, 2006; Webb et al., 2007; Webb, 2013).

One way to objectively evaluate these competing hypotheses is to establish robust constraints on the total normal-sense offset across the STDS. Here we report the results of a study designed to contribute to this effort through medium- and low-temperature thermochronometry and thermal-kinematic modeling of the results. Specifically, we present new $^{40}Ar/^{39}Ar$ muscovite (MsAr), (U-Th)/He zircon (ZrnHe), and (U-Th)/He apatite (ApHe) data for samples collected in the Rongbuk Valley, 28.063159°N 86.865197°E to 28.273212°N 86.805560°E, north of the Everest massif, in southern

Tibet (Figure 2.1). In this region, the principal strand of the STDS is called the Qomolangma detachment (Burchfiel et al., 1992). Exposures of Qomolangma detachment footwall metamorphic and igneous rocks in this valley are among the best and most continuous examples discovered thus far in the orogen. As a consequence, there have been many detailed studies of the structural, metamorphic, and igneous processes that took place in these rocks during an early (ductile) phase of Qomolangma detachment displacement in the early to middle Miocene (Hodges et al., 1992; 1998; Murphy and Harrison, 1999; Law et al., 2004, 2011; Jessup et al., 2006, 2008; Cottle et al., 2015a; Corthouts et al., 2016). The goal of this study has been to build upon these efforts by examining the younger exhumation history of the detachment footwall during the waning stages of fault slip.

3. The South Tibetan Detachment System in Rongbuk Valley

The structural architecture of the Himalaya is a south-facing orogenic wedge that developed subsequent to the initial collision between Greater India and Eurasia at ~50-55 Ma (Najman et al., 2010; van Hinsbergen et al., 2012). Its basic geology and structural development were reviewed by Hodges (2000), to which interested readers might turn for additional information. In the context of the wedge, the shallowly north-dipping STDS is an anomalous, topographically high structural feature, typically cropping out near the crest of the Himalaya and marking the top of the metamorphic core of the range. The core – referred to here as the Greater Himalayan sequence (GHS) – includes high-grade metasedimentary and metaigneous gneisses with lowermost Paleozoic-Neoproterozoic protolith ages and Indian provenance (Parrish and Hodges, 1996). In some places,

particularly at high structural levels, the intensity of Oligocene-Miocene amphibolite-granulite facies metamorphism was such that anatectic melting occurred (Le Fort, 1987), and mobilization of this melt led to the intrusion of leucogranitic bodies of a variety of sizes (Searle et al., 2010). In contrast, the STDS hanging wall comprises Cambrian and younger, unmetamorphosed or weakly metamorphosed strata deposited along the thinned northern continental margin of India prior to collision (Gaetani and Garzanti, 1991; Myrow et al., 2009).

Hanging wall and footwall rocks of the STDS are spectacularly exposed in the Rongbuk Valley of southern Tibet, which extends north from the foot of Mount Everest for about 35 km before opening to the more subdued topography of the Dzakar Chu drainage (Figure 2.1). Exposures of the STDS, while present on both the eastern and western sides of the valley, are more obvious on the east (Burchfiel et al., 1992). As part of the first reconnaissance work on the STDS in the Rongbuk Valley in the mid-1980's, Burchfiel and colleagues identified the principle strand of the detachment system as a low-angle (< 15˚ NE) brittle fault that they named the Qomolangma detachment. In the northern part of the valley, where it dips into the valley floor and is most accessible, the Qomolangma detachment is marked by a zone of fault breccia and gouge several meters thick and juxtaposes weakly metamorphosed to unmetamorphosed hanging wall rocks on mylonitized amphibolite facies metamorphic rocks and leucogranitic dikes and sills. Noting that descriptions of rocks making up the summit pyramid of Everest by Yin and Kuo, (1978) suggested a similarity with rocks above the detachment in the northern Rongbuk Valley, Burchfiel et al. (1992) postulated that the fault projected to the south from the floor of the Rongbuk Valley, up dip, to the summit pyramid, a distance of

roughly 34 km. Subsequent work confirmed that the Qomolangma detachment is indeed exposed on the north face of Everest at an elevation of ~ 8520 m (Sakai et al., 2005). In the Rongbuk Valley exposures, the immediate hanging wall rocks are fossiliferous, silty to relatively pure limestones of the Lower-Middle Ordovician Mt. Qomolangma Formation (Myrow et al., 2009), and similar lithologies dominate rock exposures on the summit pyramid of Everest (Searle et al., 2003; Sakai et al., 2005; Jessup et al., 2006; Corthouts et al., 2016). Brecciated hanging wall rocks above the detachment are cut by minor, high-angle, NNE-dipping normal faults that are truncated down dip by the detachment, while footwall rocks in the brittlely deformed zone contain numerous shear bands separating asymmetric boudins of footwall rocks (Burchfiel et al., 1992; Carosi et al., 1998). The asymmetry of these features indicates hanging wall-to-the-NNE brittle displacement on the Qomolangma detachment.

Although hanging wall rocks display similar characteristics all along the roughly displacement-parallel cross section of the Qomolangma detachment between Everest and the northern end of Rongbuk Valley, the same is not true of the footwall. On Everest, the immediate footwall of the Qomolangma detachment comprises marbles, as well as calcareous metapsammites and metapelites, of the 'Yellow Band', a distinctive unit frequently described in the mountaineering literature (Figure 2.1). The rocks of the Yellow Band and underlying schists, metapsammites, and metaquartzites of the North Col Formation – sometimes less formally referred to as the Everest Series – are part of a coherent Cambrian stratigraphic sequence recognized along most of the length of the Himalaya (Myrow et al., 2009). The Mt. Qomolangma Formation and North Col Formation locally represent the structurally and stratigraphically lowest components of

the succession often referred to throughout the Himalaya as the Tibetan sedimentary sequence (e.g., Hodges, 2000). On Everest, the North Col Formation units overlay Precambrian high-grade metasedimentary units (pelitic, psammitic, and carbonaceous) that have been intruded by a complicated network of predominantly Miocene leucogranitic dikes, sills, and plutons (Yin and Kuo, 1978; Burchfiel et al., 1992; Carosi et al., 1998, 1999; Searle, 1999; Searle et al., 2003). Here as elsewhere in the Himalaya, these rocks are typically assigned to the Greater Himalayan tectonostratigraphic sequence (e.g., Hodges, 2000). In this contribution, we follow the convention of Burchfiel et al. (1992) in referring to these rocks as exposed in the Rongbuk Valley collectively as an 'injection complex' (Figure 2.1).

Several authors (e.g., Lombardo et al., 1993; Pognante and Benna, 1993; Carosi et al., 1998, 1999; Searle, 1999) have interpreted the sharp, N-dipping contact at the base of the North Col Formation as a second, structurally deeper extensional shear zone. In the interpretation of Searle (1999), this inferred structure – which he referred to as the Lhotse detachment – is the basal strand of the South Tibetan detachment system in the Everest area, and the Qomolangma detachment is a hanging wall splay from it. However, the contact at the base of the North Col Formation has not been studied in detail on the Everest massif and has not been confirmed to have ductile or brittle fabrics along it that would support its interpretation as a detachment. Observations on the north side of Everest have shown that this contact – whatever its structural significance – dips northward more shallowly than the Qomolangma detachment, such that the Qomolangma detachment cuts out the North Col Formation rocks entirely near the northern end of the Rongbuk Valley and places Mt. Qomolangma Formation carbonates directly on to the

injection complex as mapped by Burchfiel et al. (1992), Carosi et al. (1998), and Jessup et al. (2008). Although we follow Searle (1999) and Jessup et al. (2008) in showing exposures of the Lhotse detachment in the upper Rongbuk Valley on Figure 2.1 for the sake of consistency with earlier published maps, direct evidence for the existence of the Lhotse detachment has not been found in the Rongbuk Valley.

Wherever the structural geology of the North Col Formation or injection complex beneath the brittle Qomolangma detachment has been studied in the valley, both units display conspicuous mylonitic fabrics up to at least 1000 m-thick (Carosi et al., 1998); these fabrics are universally interpreted as having developed as a consequence of STDS extensional displacement (Figure 2.3). They include well-developed mineral and stretching lineations and S-C fabrics indicative of a significant component of top-to-the-NNE simple shear deformation (Burchfiel et al., 1992), although subsequent, more detailed studies have shown that these rocks were deformed through general shear during tectonic denudation related to slip on the STDS (Law et al., 2004; Jessup et al., 2006). Law et al. (2011) presented the results of a detailed study of microstructures and quartz c-axis fabrics in which they inferred a substantial, extension-related telescoping of isotherms in the footwall based on quartz fabric opening angles.

Of particular significance for interpreting the thermochronologic data presented below, Law et al. (2011) estimated a deformation temperature of 625 ± 50 ˚C for one mylonitized sample collected ~ 420 m beneath the detachment near the mouth of Hermit's Gorge (Figure 2.1). This is the same locality where a sillimanite-grade pelitic schist sample was collected that has yielded the only published quantitative pressure and temperature estimates for Qomolangma detachment footwall rocks in the Rongbuk

Valley (Hodges et al., 1992) based on major element partitioning thermobarometry: *ca*. 630˚C and 460 MPa. Collectively, these data suggest that the mylonitic fabrics found beneath the Qomolangma detachment near Hermit's Gorge developed at paleodepths of roughly 17 km (Hodges et al., 1992).

The initiation age and duration of slip on the Qomolangma detachment in the Everest region are actively debated. Most estimates are based on (U-Th)/Pb dates obtained for accessory minerals in the leucogranites of the injection complex, which exhibit field relationships suggesting that their intrusions into the detachment footwall occurred before, during, and after the development of mylonitic fabrics (Copeland et al., 1988; Hodges et al., 1992; 1998; Murphy and Harrison, 1999; Cottle et al., 2007; 2015b). Unfortunately, obtaining easily interpretable ages for these leucogranites based on their accessory mineral (U-Th)/Pb systematics has proven extremely difficult. These leucogranites are products of local anatexis of the Greater Himalayan sequence, and many contain accessory minerals, inherited from their proximal sources that are only a few million years older. Published dates range from *ca.* 20 Ma to *ca.* 15 Ma, with the most dominant population ranging from 16.8 ± 0.8 to 16.4 ± 0.1 Ma (Hodges et al., 1998; Murphy and Harrison, 1999; Cottle et al., 2015b). (Note that throughout this contribution, we cite geochronologic and thermochronologic uncertainties at 2σ.) A second important population of leucogranites, some of which contain mylonitic fabrics and some of which are undeformed and cut the mylonitic fabrics at high angles, yields dates from 15.6 ± 0.1 to 15.3 ± 0.1 Ma, which Cottle et al. (2015b) interpreted as indicating that cessation of ductile deformational activity on the STDS in the Rongbuk Valley occurred before 15.6 Ma. However, none of these young granites obviously crosscut the brittle Qomolangma

detachment, leaving open the possibility of significant brittle displacement on the detachment after intrusion of the youngest of this population of granites.

4. Exploring the Late-Stage Slip History of the Qomolangma Detachment

The juxtaposition of unmetamorphosed and weakly metamorphosed hanging wall rocks and amphibolite facies footwall rocks across the Qomolangma detachment suggests that the total displacement across the structure is much greater than the minimum of ~ 34 km required by the total hanging wall-footwall overlap observed in cross section (Burchfiel et al., 1992). The stratigraphic level of the Mt. Qomolangma Formation exposed in the immediate hanging wall of the detachment is essentially the same on Everest and at the northernmost outcrops of the detachment in the Rongbuk Valley. Similarly, although the detachment does cut out the North Col Formation down dip, prograde metamorphic pressures and temperatures of the detachment footwall constrained by thermobarometry are similar on Everest and at the mouth of Hermit's Gorge, roughly 18 km to the north (Figure 2.1; Hodges et al., 1992; Jessup et al., 2008). Such observations demonstrate that the detachment occupies approximately the same structural level in both the hanging wall and footwall wherever it is exposed. Coupled with the present-day low ($\leq 15^{\circ}$) dip of the detachment, this means that the structure has not been appreciably rotated since its development (Figure 2.2). Thus, the net displacement on the structure can be estimated from trigonometry from its current dip and its tectonostratigraphic throw, the latter of which is calculated using the amount of vertical exhumation of the footwall during detachment slip.

One example of such an estimate was obtained by Searle et al. (2003), who calculated total slip amounts between 90 and 216 km (depending on different assumptions for the regional dip on the detachment: 10˚and 5˚, respectively) based on thermobarometrically constrained metamorphic depths of the footwall rocks. Subsequently, Law et al. (2011) estimated slip of between 25 and 170 km using particle path models based on the apparent telescoping of synkinematic isotherms during ductile deformation. As noted by Law et al. (2011), the latter set of estimates largely refer to the portion of offset accommodated by ductile deformation, whereas the higher values estimated by Searle et al. (2003) refer to the total offset and include both ductile and brittle deformation. An important goal of our low-temperature thermochronometric work has been to determine to what extent the differences between these estimates might be explained by transitional ductile-brittle and brittle faulting along the Qomolangma detachment.

4.1. Research Strategy

One of the most effective ways to explore the thermal history of an orogenic environment is the application of isotopic thermochronometers to a single sample or a single structural horizon. Many lithologies from the Qomolangma footwall are amenable to such studies, particularly the leucogranites, which contain a wide variety of major and accessory minerals. For this study, we collected eight deformed and undeformed leucogranite samples along a transect east of, and just above, the valley floor, over a distance of ~ 8.7 km roughly parallel to the dip direction of the Qomolangma detachment (Figure 2.2). The southernmost sample (R01), collected near the mouth of Hermit's

Gorge (Figures 1.2 and 2.2), is from an outcrop roughly 800 m beneath the projection of the Qomolangma detachment, whereas the northernmost sample (R08) is from roughly 300 m beneath the fault. Our strategy was to determine dates for the MsAr, ZrnHe, and ApHe thermochronometric systems, which have nominal closure temperatures (assuming a cooling rate of 10˚C/Ma) of *ca.* 490˚C (Harrison et al., 2009), *ca.* 170˚C (Reiners et al., 2004), and *ca.* 70˚C (Farley, 2000) respectively. We then used this information to constrain the cooling and exhumation history of the detachment footwall. We were particularly interested in whether or not we would find down-dip variations in the dating results because such variations have been found in thermochronologic datasets from detachment footwalls in other tectonic settings (e.g., John and Foster, 1993; Stockli et al., 2001; Brady, 2002; Brichau, 2004; Stockli, 2005; Evans et al., 2015). For our highest-temperature thermochronometer, we chose MsAr because the nominal closure temperature range for this chronometer overlaps with the low end of the 680-480˚C range of deformation temperatures estimated for the Rongbuk mylonites by Law et al. (2011) based on quartz fabric opening angles. Collectively, the Law et al. (2011) dataset implies that our MsAr closure dates might roughly reflect the timing of the waning stages of ductile deformation. Lower-temperature ZrnHe and ApHe thermochronometers were anticipated to provide constraints on the thermal and kinematic evolution of these rocks subsequent to the cessation of ductile deformation. Unfortunately, when the mineral separates for all samples were examined, most were found to contain only very small (60 μm) apatites with abundant inclusions, which were thus not suitable for ApHe dating due to concerns regarding the large alpha ejection corrections needed for such small grain sizes (Farley et al., 1996) and the effects of inclusions on the (U-Th)/He systematics

(Vermeesch et al., 2007). As a consequence, we dated muscovite and zircon from all eight samples, but apatite from only two samples, R01 and R02. $^{40}Ar/^{39}Ar$ and (U-Th)/He analyses were performed at the Group 18 Laboratories at Arizona State University using procedures outlined in Appendix A.

5. Thermochronology Results and Age Interpretations

Muscovite $^{40}Ar/^{39}Ar$ laser step-heating age spectra data for the Rongbuk samples can be found in Figures 2.4 and A1 and Table A1. All samples exhibited uncomplicated behavior and yielded statistically defined plateau dates ranging from 15.420 ± 0.050 Ma (R04) to 14.400 ± 0.060 (R05) Ma. There is no obvious correlation between the MsAr cooling age of a sample and the latitude at which it was collected or its structural distance below the detachment (Table 2.1).

As noted in the Supplementary Materials (Tables A2 and A3), several of our samples yielded (U-Th)/He zircon and apatite age datasets that are 'over-dispersed', meaning that their dispersion is greater than would be expected from analytical imprecision alone. For example, only two samples (R04 and R08) yielded inverse-variance weighted mean ZrnHe dates that are not overdispersed (Table 2.1 and Table A2). The remainder of the samples yielded over-dispersed (U-Th)/He results as defined by the mean squared weighted deviation (MSWD) of each dataset (Wendt and Carl, 1991). For those datasets, we tried to identify obvious outliers using the Hampel identifier method with a threshold value of four (Pearson, 2011), but unfortunately, no outliers were identified. As a consequence, we conservatively report uncertainties for the ZrnHe inverse-variance weighted mean dates of the six over-dispersed datasets using

twice the standard deviation of the population of ZrnHe dates for the sample (Table 2.1 and A2). The complete set of ZrnHe mean dates range from 14.32 ± 0.28 Ma (sample R04) to 11.0 ± 1.1 Ma for sample R06. We noted no correlation between individual ZrnHe dates and effective uranium (eU) values (Guenthner et al., 2013), calculated from the U and Th concentrations for the dated grains as eU = 0.235[Th] + [U], where the brackets indicate mass concentrations. Inasmuch as such values are sometimes used as a proxy for radiation damage (Guenthner et al., 2013), we see no evidence that radiation damage played a major role in the dispersion of observed ZrnHe dates. As was the case for the MsAr dates from the same samples, the ZrnHe dates show no clear pattern geographically or with structural depth (Table 2.1).

Apatite (U-Th)/He dates for samples R01 and R02 are summarized in Table 2.1 and presented in detail in Table A3. For sample R01, one ApHe date (4.09 ± 0.26 Ma) was identified as an outlier by the Hampel identifier method and remaining six dates ranged from 10.99 ± 0.34 Ma to 7.38 ± 0.42 Ma. Even after removal of the 4.09 Ma outlier date, the remaining R01 sample dates were still over-dispersed, with an inverse-variance weighted mean date of 9.3 ± 2.8 Ma, with the 2σ uncertainty again reported as twice the standard deviation of the population distribution. Only three datable apatite crystals were found in sample R02, and one of them – with an apparent age of 11.96 ± 0.62 Ma – was identified as an outlier using the Hampel identifier method. The other two yielded a mean ApHe date of 7.76 ± 0.52 Ma, younger than, but statistically indistinguishable from, the mean ApHe date for sample R01. If the apparent outlier is not excluded, the inverse-variance weighted mean date for all three R02 apatites would be

9.5 ± 5.0 Ma. For both R01 and R02, the ApHe dates are predictably younger than the ZrnHe dates.

We interpret the MsAr, ZrnHe, and ApHe dates (Table 2.1) as indicative of the ages of cooling of the samples through nominal closure conditions for the applied thermochronometers. Our new MsAr data indicate that the temperature of the Qomolangma detachment footwall did not cool below amphibolite facies temperatures until after at least 15.420 ± 0.050 Ma, consistent with the interpretation of Cottle et al. (2015b), based on U/Pb monazite ages of different generations of leucogranites, that ductile activity on the Qomolangma detachment, recorded by its high-temperature footwall mylonites, was largely over by *ca.* 15.6 Ma. There are two previously published $^{40}Ar/^{39}Ar$ mica dates for a sample collected in 1986 from the approximate location of our sample R05, which yielded a MsAr plateau date of 16.56 ± 0.23 Ma and a biotite plateau date of 16.51 ± 0.30 Ma (Hodges et al., 1998). The inconsistency of these previous results with our new data – as well as the Cottle et al. (2015b) inference regarding the cooling history – is interpreted as a reflection of the much higher analytical precision of the new MsAr data, and the fact that the Hodges et al. (1998) data were obtained for large, multigrain aliquots rather than single mica crystals.

6. Reconstructions of the Thermal and Exhumation History of the Qomolangma Detachment Footwall

We present here the results of two different, but complimentary, approaches to modeling the thermal and thermal-kinematic history of the Qomolangma detachment

footwall during its exhumation, and we use the results to infer the late-stage slip history of the structure.

6.1. Temperature-Time Trajectories from QTQt Modeling

Many recent attempts to model time-temperature histories of rocks from thermochronologic data have taken advantage of one of two, freely available software packages: *HeFTy* (Ketcham, 2005) and *QTQt* (Gallagher, 2012). Here we apply the *QTQt* software because of its capacity to simulate the three mineral-isotopic systems measured in the Rongbuk Valley samples.

Employing a Bayesian transdimensional Markov chain Monte Carlo (MCMC) inversion scheme, *QTQt* constrains a set of best-fit temperature-time paths given a posterior probability distribution (Gallagher, 2012). Essential input parameters for models using this program are diffusion parameters for the mineral-isotopic systems, diffusion domain sizes, diffusion geometry, apparent ages, and uncertainties in these apparent ages.

We assumed diffusion parameters for MsAr as determined by Harrison et al. (2009) for MsAr and corrected to a pressure of 500 MPa, which is within uncertainty of the thermobarometrically estimated pressure for amphibolite facies metamorphism in the Rongbuk Valley as determined by Hodges et al. (1992). We employed the diffusion parameters of Reiners et al. (2004) for ZrnHe and Farley (2000) for ApHe. We made no attempt to adjust these helium diffusion parameters to account for radiation damage as suggested by Shuster et al. (2006), Flowers et al. (2009), and Guenthner et al. (2013) for two reasons. First, as noted above, there is no clear correlation between eU and apparent

age for our sample set. Second, these samples experienced amphibolite facies metamorphism in the Miocene, only a few million years prior to ZrnHe and ApHe closure. That metamorphism was of sufficiently high grade to have effectively annealed any pre-Miocene radiation damage, such that we would expect any radiation damage accumulated between metamorphism and ZrnHe and ApHe closure to be negligible. We assumed a spherical geometry for He and Ar diffusion, consistent with the experimental interpretations of Farley (2000), Harrison et al. (2009), and Reiners et al. (2004) of their experimental results. We then calculated equivalent spherical radii from grain sizes using the equations of Reiners and Brandon (2006). Our sieved muscovite grains had a mean equivalent spherical radius of 375 μm; for zircon and apatite, we used the average of the spherical radii for all the crystals in each sample (Tables A2 and A3) for *QTQt* modeling purposes.

QTQt also requires the input of certain characteristics of the inversion search protocol (usually determined by trial-and-error, as outlined by Gallagher, 2012), and it permits the specification of certain temperature-time constraints to narrow the search space. For our models, we specified that the modeled cooling trajectories pass through: 1) the 17-15 Ma time window at temperatures between 750 and 550˚C; and 2) the 0.38-0.28 Ma time window at temperatures between 10 and 0˚C. The first specification reflects the presumption that these samples had temperatures near that of the muscovite- or biotite-dehydration melting reactions at *ca.* 500 MPa (Le Breton and Thompson, 1988; Patiño-Douce and Harris, 1998) in the age range of most leucogranites in the injection complex. The second reflects the requirement that these samples had to be at the surface by at least the time of deposition of the oldest known glacial deposits in the valley (Owen et al.,

2009). All models represent 20,000 iterations: 10,000 used to stabilize or 'burn-in' the inversion process, and the second 10,000 used for the inversion itself; see Gallagher, (2012). Exploratory runs using larger numbers did not appreciably change model outcomes.

The resulting models for samples R01 and R02 (which include ApHe constraints) are presented in Figure 2.5, along with the models for R05 and R08 to illustrate results for samples for which ApHe are unavailable; the figures for all other samples may be found Appendix Figure A2. In the figures, we illustrate the expected model from *QTQt* (the weighted mean of all best-fitting thermal histories) as well as the 95% credible confidence intervals for that model.

Overall, this modeling exercise suggests that the thermochronologic data for the Rongbuk Valley imply a simple, monotonic cooling history, with a progressive decrease in cooling rate since ductile deformation on the Qomolangma detachment. Specifically, they indicate rapid cooling from ambient temperatures of *ca.* 500˚C at *ca.* 15.4 to 14.4 Ma to *ca.* 170˚C by no later than *ca.* 12 Ma. Although the model output for sample R01 suggests that it cooled less rapidly compared to the other samples, we note that the uncertainties of the ZrnHe dates for this sample are large, which permits greater variability in possible cooling trajectories. The output for this sample still shows rapid cooling from *ca.* 15 to 13 Ma followed by cooling to *ca.* 70˚C by *ca.* 9 Ma, similar to R02.

6.2. Exhumation Rates Through Time from Thermal-Kinematic Modeling

Calculation of transient exhumation histories that could produce the previous thermal histories is best done through thermal-kinematic modeling in which the advection-diffusion equation is solved for a range of temporally varying exhumation rates. For this we use a modified version of the *Pecube* software originally presented by Braun, (2003) and Braun et al., (2012). The modified version used here (Thiede and Ehlers, 2013; Adams et al., 2015) assumes one-dimensional heat transport (from depth toward Earth's surface, by both advection and conduction) and applies a smart-search Monte Carlo method to identify the range of all possible exhumation rates that could produce the observed cooling ages. Modeling parameters for our study follow those used by Thiede and Ehlers (2013) and Adams et al., (2015); see Appendix A for details.

Because many published applications of *Pecube* to problems in tectonics and landscape evolution employ two- or three-dimensional heat transport, our choice to use the 1-D approach of Thiede and Ehlers (2013) merits further explanation. While large-displacement normal faulting on moderately to steeply dipping structures can lead to significant lateral heat advection (Ruppel et al., 1988; Campani et al., 2010; Braun et al., 2012), which might be an argument for our using at least a 2-D model, these effects are actually minor for extremely low-angle structures like the Qomolangma detachment. For example, we can compare the nearly uniform ZrnHe dates obtained along the Rongbuk Valley transect with ZrnHe dates for samples collected over a similar distance along a dip-parallel transect beneath the more steeply dipping Snake Range detachment in Nevada (Evans et al., 2015). Those authors reported that ZrnHe apparent ages decreased from *ca.* 41 Ma to *ca.* 21 Ma in the dip direction of dip, roughly a factor of two. Had

there been considerable lateral heat advection during slip on the Qomolangma detachment faulting, we likely would have detected evidence for it in the form of a progressive younging of closure ages. In addition, previous work comparing the outcomes of 1-D and 3-D thermal-kinematic models suggest that rapid exhumation regardless of mechanism largely results in a vertical compression of isotherms and an essentially 1-D thermal field at the shallow depths where ZrnHe and ApHe chronometers pass through their partial retention zones; compare, for example, 1-D, 2-D, and 3-D modelling results reported by Thiede and Ehlers (2013). Concerns regarding the suitability of 1-D techniques for thermal-kinematic modeling of thermochronologic data are generally more valid for regions that experience low (<1 mm/a) exhumation rates, where lateral heat advection rates due to faulting may exceed vertical heat advection rates, especially for higher temperature chronometers like MsAr, as noted by Thiede and Ehlers (2013). As we show below, modeled exhumation rates for the Rongbuk samples at the time of MsAr closure are much higher. Due to its relative computational simplicity, a 1-D version of Pecube modeling has an important advantage of over multidimensional modeling: it permits the rapid testing of hundreds of thousands of theoretical exhumation histories for compatibility with observed cooling ages with relative computational ease and speed.

Our thermal-kinematic models for the Rongbuk samples show two general types of behavior (Figures 2.6 and A3). Models for six of the eight samples indicate high exhumation rates ($\geq$ 3.5 mm/a) persisting to as recently as 14.0-13.0 Ma and a rapid decrease in exhumation rate to $\leq$ 0.5 mm/a thereafter. Models for two samples (R01 and R06) also show a factor of two or more decrease in exhumation rate at 13.0 Ma, but

indicate moderate (*ca.* 1.0-1.5 mm/a) exhumation rates from 13.0 to 8.0 Ma that then decrease to ≤ 0.5 mm/a thereafter.

7. Tectonic Interpretations

The MsAr dates reported here indicate that the Qomolangma detachment footwall exposed in Rongbuk Valley maintained relatively high temperatures (*ca.* 450-500 ˚C) well after 15.6 Ma, the timing of the end of ductile activity on the structure as inferred from U/Pb monazite dates of Cottle et al. (2015b). Our thermal models indicate rapid cooling (*ca.* 262 - 72˚C/Ma) of the footwall commencing after MsAr closure at 15.420 ± 0.050 to 14.40 ± 0.060 Ma (Figures 2.5 and A2). The thermal-kinematic models imply that this cooling was accompanied by exhumation at rates of *ca.* 3-4 mm/a prior to ca. 13.0 Ma (Figures 2.6 and A3). Those rates are a factor of 3 higher than erosional exhumation rates during that same period as deduced from thermochronological data for the southern flank of the Himalaya (e.g., Thiede and Ehlers, 2013). It is improbable that the high 3 – 4 mm/a exhumation rates implied by our data reflect high precipitation-driven erosion, given that Mount Everest was near its present-day elevation in the Miocene, with the southern Tibetan Plateau likely already established and the current monsoonal precipitation pattern probably in place by 15.4-13.0 Ma (Coleman and Hodges, 1995; Blisniuk et al., 2001; Spicer et al., 2003; Harris, 2006; Clift et al., 2008; Gébelin et al., 2013). As a consequence, we might expect dryer, rather than wetter, conditions to have prevailed north of the Himalayan crest where our samples under study would have been at the time. We interpret the high modeled exhumation rates prior to *ca.* 13 Ma to be related to rapid slip on the Qomolangma detachment.

Our thermal-kinematic models further suggest that this early period of very rapid tectonic denudation ended at *ca.* 13 Ma. Modeling of two of our eight samples (R01 and R06) indicate at least a factor of two lowering of the exhumation rates from *ca.* 2.2-3.4 mm/a to 1.0-1.2 mm/a at this time, and the other six samples indicate an even higher (order of magnitude) decrease from 1.5-4 mm/a to <0.5 mm/a (Figures 2.6 and A3). The most reasonable interpretation of this behavior is that slip on the Qomolangma detachment effectively terminated or drastically slowed at *ca.* 13 Ma (within the ±1 Ma resolution of our models). By no later than 8 Ma, the exhumation rate of *ca.* <1 mm/a, indicated by our models was sufficiently low to be explained exclusively by erosional denudation similar to that currently operating on the Tibetan Plateau (e.g., Rades et al., 2015; Strobl et al., 2012).

7.1. Fault displacement estimations based on exhumation

Our thermal-kinematic modeling results inform a reconstruction of Qomolangma detachment footwall exhumation since the inferred cessation of ductile deformation at *ca.* 15.6 Ma. This reconstruction, along with a little simple trigonometry, permits an estimation of the displacement history of the fault.

For these calculations, we assumed that total exhumation was constant during each of the time steps shown in Figures 2.6 and A3. For example, we assumed that the total exhumation between 15.6 Ma and 15.0 Ma for sample R01 was 2.0 km based on the *ca.* 3 – 4 mm/a exhumation rate estimated by our 1-D thermo-kinematic model for this interval. From 15.0 to 14.0 Ma, a comparable calculation indicated an additional 2.8 km of exhumation. Continuing this process for all of the modeled increments from 15.6

through the 13.0 Ma interval indicated 7.7 km of cumulative exhumation. Modeled cumulative exhumation for the other seven samples ranged from 10.4 km for R05 to 6.3 km for R03 and the average for all eight samples is 8.3 km.

Given that we have no indication that the Qomolangma detachment has rotated significantly since it was active, or that its dip changes significantly between the summit pyramid of Everest and the north end of Rongbuk Valley where it disappears between the valley floor (over 30 km down dip), we estimate displacement values using a simple geometrical model: displacement = exhumation/(sin α), where α is fault dip (Figure 2.2). The detachment surface is not easily accessible for direct measurement in Rongbuk Valley, so its regional dip – between 5 and 10˚ – is estimated from its intersection with topography along the valley (Figure 2.1; Figure 2.2). Figure 2.7 illustrates detachment displacement histories over the 15.6 to 13.0 Ma time period as calculated from our exhumation histories (based on the alternative assumptions of a 5˚ or 10˚ dip) for the two samples with the most complete thermochronologic datasets (R01 and R02). By the cessation of fault slip (presumed to be *ca.* 13.0 Ma), data from both samples indicate a consistent 44 ± 11 km of slip assuming a 10˚ dip. If the dip is assumed to be 5˚, the amount of slip doubles to 88 ± 22 km. (In both cases, uncertainties reflect the cumulative effects of propagating the 2σ uncertainties in the *Pecube* models for successive time steps.) Calculations for all eight samples yielded average 10˚ fault slip estimates ranging from 60 ± 8 km (R05) to 36 ± 11 km (R03). For an assumed 5˚ dip, the range was from 119 ± 17 km to 72 ± 22 km.

The modeling results are most consistent with the cessation of slip by *ca.* 13.0 Ma, but we cannot completely rule out an alternative interpretation: that minor slip may

have persisted into the 13.0-8.0 Ma timeframe. Unfortunately, the lack of apatite crystals suitable for ApHe thermochronology in most samples precluded our examining this possibility in more detail. Smaller step thermal-kinematic modeling increments between 13.0 and 8.0 Ma would not have yielded robust results given the lack of quantitative constraints on temperature-time paths. The dotted lines in Figure 2.7 show modeled projections of the slip history for our R01 and R02 samples if we assume that detachment activity continued until 8.0 Ma. Of all the models, sample R01 would imply the most total slip in this case: 78 ± 21 km (for $\alpha = 10^{\circ}$) or 156 ± 42 km (for $\alpha = 5^{\circ}$).

8. Discussion

8.1 Comparisons with previous work

On the same timeframe as – but independent of – our thermochronologic work in the Rongbuk Valley, another team (Orme et al., 2015; Carrapa et al., 2016) also conducted low-temperature thermochronologic studies in the Rongbuk Valley. They reported ZrnHe, ApHe, and apatite fission-track (ApFT) dates for seven different bedrock samples (mostly leucogranites) from outcrops close to the collection localities for our samples. While providing more detailed insights, our analytical results and modeling generally support the interpretation of the other team that the injection complex cooled rapidly during the middle Miocene (Carrapa et al., 2016). However, neither our new data nor the monazite U/Pb data of Cottle et al. (2015b) are consistent with the contention of Orme et al. (2015) that the footwall of the Qomolangma detachment has not experienced temperatures greater than the nominal ApFT closure temperature (ca. 110-120˚C; (Reiners and Brandon, 2006)) since 16 Ma.

The ApFT results in Carrapa et al. (2016) are particularly challenging to interpret in a robust way. In theory, the ApFT chronometer should provide constraints on the timeframe of cooling of a sample through the partial annealing zone for apatite; a nominal closure temperature range for ApFT assuming a cooling rate of 10˚C/Ma is ca. 100-120˚C (Reiners and Brandon, 2006). The Rongbuk ApFT dates reported by Carrapa et al. (2016) were significantly over-dispersed in individual samples, and showed a sample-to-sample range of weighted mean dates from 12.7 ± 3.0 Ma to 15.6 ± 5.6 Ma, with a mean for all samples of 14.8 ± 6.4 Ma (uncertainties reported at the 2σ level). Some of the ApFT dates seem impossibly old, approaching or exceeding the U/Pb crystallization ages of leucogranite dikes in these collection outcrops (Cottle et al., 2015b). Five of the seven samples yielded mean ApFT dates as old or older than the MsAr dates reported here, even though the closure temperature range for MsAr is several hundred degrees higher than that for ApFT. Given that the ApFT dates reported by Carrapa et al. (2016) have low precision and are highly over-dispersed regardless, they do not provide very useful constraints on the thermal history of Rongbuk Valley.

Analyzing their zircons using methods essentially identical to ours, including the assumption of homogeneous U+Th in the crystals, Orme et al. (2015) obtained 25 single-crystal ZrnHe dates ranging from 14.70 ± 0.46 Ma to 9.87 ± 0.29 Ma, with all but two dates between ca. 12.8 and 9.9 Ma. Noting that Sakai et al. (2005) obtained 14-15 Ma ApFT and zircon fission track (ZrnFT) dates for a sample collected beneath the Qomolangma detachment near the summit of Everest and likely mindful of the team's own ApFT data from the Rongbuk Valley that would be published in Carrapa et al. (2016), Orme et al. (2015) questioned the reliability of their own ZrnHe dates since the

closure temperature for the ZrnHe chronometer is higher than that of the ApFT chronometer. Orme et al. (2015) also presented laser ablation ICPMS depth profiling data for five of their dated crystals, showing evidence for significant U and Th zonation, often featuring rims highly enriched in uranium. This sort of zoning, if not recognized and properly accounted for during the data reduction procedure, can result in improper alpha ejection corrections leading to substantial underestimates of the true ZrnHe ages (Hourigan et al., 2005). However, U-Th zoning in zircon is typically complex in three dimensions and can vary widely among zircons from the same sample (Corfu et al., 2003). This is why most (U-Th)/He researchers, without *a priori* comprehensive knowledge of zoning in a zircon, choose the simplifying assumption that the U-Th element distribution is homogeneous within the crystal as they correct raw (U-Th)/He zircon dates for alpha-particle ejection (Farley et al., 1996). Given their knowledge of zoning in at least one dimension at one place beneath the rims of the five profiled zircons, Orme et al. (2015) attempted a correction of their original ZrnHe dates for the five crystals, obtaining new estimates ranging from 17.00 ± 0.36 to 14.82 ± 0.31 Ma. These corrections assumed that the single 1-D profiles they obtained for each crystal could be extrapolated concentrically around the zircon.

As noted by Orme et al. (2015) and Bargnesi et al. (2016), such a correction exercise is not an exact science. Some knowledge of the magnitude of chemical zoning, such as that obtained by one-dimensional depth profiling measurements of U and Th, can provide useful information regarding the likelihood that the homogeneity assumption yields alpha ejection corrections that are too large or too small, but quantitative adjustments based on such data can be misleading. In the case of the samples analyzed by

Orme et al. (2015), it appears that the correction procedure used led to an over-correction of most or all of their ZrnHe dates. All of their corrected ZrnHe dates are as old as or older than our MsAr dates for the same structural horizons, which is inconsistent with published kinetic data indicating that the MsAr chronometer has a much higher nominal closure temperature than the ZrnHe thermochronometer. Our ZrnHe analytical procedures, like those used by Orme et al., (2015) for most of their samples, did not permit evaluation of parent element zoning, but we note that our dates are generally older than original dates obtained by Orme et al. (2015) (assuming parent element homogeneity), while still being appropriately younger than MsAr dates for the same samples.

In contrast to the low-temperature thermochronometry results published by Orme et al. (2015) and Carrapa et al. (2016), our ZrnHe and ApHe dates are appropriately younger than the higher-precision MsAr dates obtained for Rongbuk Valley samples. Moreover, our thermochronologic dataset is consistent with previously published data indicating that amphibolite facies metamorphic conditions were maintained in the Qomolangma detachment footwall until at least 15.6 Ma (Law et al., 2011; Cottle et al., 2015b). Thus, we regard our dataset and the thermal and thermal-kinematic models derived from it as robust indicators of the thermal evolution of the Qomolangma detachment footwall in Rongbuk Valley.

8.2. Tectonic ramifications of this Rongbuk Valley study

One popular model for the development and evolution of the South Tibetan detachment is that it represents a fundamental structural boundary at the top of a

southward extruding metamorphic infrastructure, the Greater Himalayan sequence (Nelson et al., 1996; Beaumont et al., 2001; Hodges et al., 2001; Grujic et al., 2002; Hodges, 2006; Cottle et al., 2015a). If correct, this interpretation would predict the compression of isotherms within the detachment-related mylonites of the detachment footwall. Indeed, Law et al. (2011) presented evidence of this having accompanied the development of mylonitic fabrics in the Qomolangma detachment footwall in Rongbuk Valley: a systematic variation in quartz c-axis fabric opening angles that serves as a proxy for geothermal gradient (Law, 2014). Law et al. (2011) used two particle-path geometric models, with one particle assigned to the 475˚C isotherm and another to the 675˚C isotherm, to infer displacement on the detachment of 25-170 km during mylonite development, with estimates toward the low and high ends of this range derived assuming a 10˚ or 5˚ detachment dip, respectively.

Importantly, Law et al. (2011) also estimated the range of mylonitization temperatures in the Hermit's Gorge area as increasing from *ca.* 480-490 ˚C immediately near the detachment to *ca.* 625-680˚C at a structural level *ca.* 480 m beneath the brittle fault trace. The fact that this entire temperature range is at or above the nominal closure temperature of MsAr indicates strongly that the cooling history reported in this paper reflects footwall exhumation subsequent to the ductile deformation responsible for the footwall mylonites. Thus, an important – and somewhat unanticipated – finding of our work is that the amount of brittle-ductile to brittle displacement on the Qomolangma detachment (36 ± 11 to 119 ± 17 km) was similar to the amount of ductile displacement when the mylonites predominantly developed (Law et al., 2011). Our estimates (*ca.* 36 to *ca.* 119 km) and those of Law et al. (2011) (25 to 170 km) can be combined to arrive at

an estimate for the total STDS offset in the Everest area of *ca.* 61 to 289 km. This total compares reasonably well with the very rough estimate of 90 to 216 km calculated by Searle et al. (2006) based in the inference that such displacements (varying depending on fault dip) were necessary to juxtapose high-grade rocks from the detachment footwall to the upper crust.

Our preferred interpretation that slip on the Qomolangma detachment terminated at ca. 13 Ma is consistent with an emerging consensus estimate for the end of STDS displacement from the Everest region eastward to Sikkim, India (Leloup et al., 2010; Cottle et al., 2011; Kellett et al., 2013; Braun, 2016). Farther east – across the Yadong cross-structure (Figure 2.1) in Bhutan and adjacent areas of Tibet – STDS activity appears to have continued for another 1-2 Ma; whether or not this inconsistency is tectonically significant remains unclear (Cooper et al., 2015). Our estimate of many tens to perhaps more than two hundred kilometers of total slip on the Qomolangma detachment adds to a growing body of evidence (e.g., Cooper et al., 2012; 2013) that the South Tibetan detachment system played a major role in the Miocene tectonic evolution of the Himalaya.

9. Conclusions

Multisystem, medium- to low-temperature thermochronology (MsAr, ZrnHe, and ApHe) of samples collected along a footwall transect parallel to the displacement direction of the Qomolangma detachment have been used to constrain the brittle-ductile and brittle slip history of this important strand of the South Tibetan detachment system. Collectively, the thermochronologic data indicate cooling from the ≥ 480˚C temperatures

that pertained during ductile deformation on the detachment as recently as 15.6 Ma, followed by cooling through MsAr closure (*ca.* 15.4 – 14.4 Ma), ZrnHe closure (14.3 – 11.0 Ma), and lastly ApHe closure (*ca.* 9.3 – 7.8 Ma).

QTQt thermal modeling of the data suggests monotonic rapid cooling from MsAr closure at *ca.* 490°C and 15.4-14.4 Ma to ZrnHe closure at *ca.* 200˚C (closure temperatures re-calculated from the resulting *QTQt* cooling histories) by no later than 12 Ma. Thermal-kinematic (1-D *Pecube*) modeling indicates that this rapid cooling accompanied rapid exhumation from at least *ca.* 15.6 (nominally the end of ductile deformation on the detachment; (Cottle et al., 2015b) to *ca.* 13.0 Ma. We interpret this exhumation to have been caused by brittle-ductile to brittle slip on the detachment subsequent to footwall mylonitization. Our preferred interpretation of the models is that Qomolangma detachment activity effectively ceased *ca.* 13.0 Ma, but we cannot completely rule out the possibility of minor displacements as recently as *ca.* 8 Ma.

Reconstructions of the exhumation history between *ca.* 15.6 Ma and 13.0 Ma for two samples containing all three thermochronometers indicate brittle-ductile to brittle displacements of 44 ± 11 km assuming a 10˚ fault dip and 88 ± 11 km assuming a 5˚ fault dip. Six other samples are consistent with fault offsets between 36 ± 11 km and 119 ± 17 km with fault dips of 5 and 10°. When added to previously published estimates for ductile displacement on the detachment (Law et al., 2011), these model results indicate total displacements of *ca.* 61 to 289 km.

STDS displacements of this magnitude appear to favor tectonic models that feature significant channel flow of the Greater Himalayan metamorphic infrastructure of the range, with the STDS as the upper bounding structure of the core. This interpretation

seems inconsistent, however, with models that assign small displacements to the STDS and relegate the structure to a minor role in Himalayan tectonics (Yin, 2006; Webb et al., 2007; Webb, 2013; Kohn, 2008; He et al., 2015).

10. Acknowledgments

This work was supported by National Science Foundation Tectonics Program grants EAR1007929 and EAR1346360 to K.V.H. The fieldwork in Tibet would not have been possible without the logistical assistance of Ding Lin (Institute of Tibetan Plateau Research, Chinese Academy of Sciences), Paul Kapp (University of Arizona), and Ross Waldrip (University of Arizona). Thanks to Kerry Gallagher (Geosciences Rennes, Université Rennes 1) for his help and guidance with the *QTQt* program. Many thanks to Willi Kappler and Byron Adams (Department of Geosciences, Universität Tübingen) for their assistance with running Monte Carlo version of *Pecube* used in this study. Comments and suggestions by Frances Cooper (School of Earth Sciences, University of Bristol) on earlier versions of this manuscript by are much appreciated. All analytical data presented in this study are provided in Appendix A in the Supplementary Materials.

11. Figure Captions

Figure 2.1. A) Map showing the position of the STDS along the crest of the Himalaya. The bold shaded box indicates the location of Fig. 2.1B and the boxes to the east indicate regions where the STDS has been previously studied (Cottle et al., 2011; Cooper et al., 2012; 2013; Kellett et al., 2013). The map is based on Cooper et al., (2012). B) Regional map of the Rongbuk Valley in the Everest region of Tibet. Geologic units are mapped

after Searle et al., (2003). Sample localities are shown with blue and red circles and the different colors represent different chronometric systems measured for each sample. See inset map for sample names. The base map is taken from the ArcGIS World Imagery catalogue.

Figure 2.2. Geologic cross-section of the Rongbuk Valley showing major geologic units and sample localities. The map is after Jessup et al*.,* (2008). This figure highlights the stuctural position of the samples in the footwall of the Qomolangma detachment. MsAr, ZrnHe, and ApHe ages of samples R01 and R02 are shown. All other age data can be found in Table 2.1.

Figure 2.3. Field photograph taken in the Rongbuk Valley looking east into the mouth of Hermit's Gorge. The photo clearly shows the leucogranitic dikes and sills of the injection complex, which makes up the immediate footwall of the STDS in this area. The large leucogranite sill near the base of the photo is about 2 m tall. The high-grade sillimanite gneisses are the surrounding dark-colored layers. The photo also highlights the mylonitic fabric and shows how thick the zone is, as the trace of the brittle, low-dipping Qomolangma detachment can be observed near the top of the northern gorge wall.

Figure 2.4. Muscovite $^{40}Ar/^{39}Ar$ release spectra for samples R01, R02, R05, and R08. All eight samples have well-defined plateau ages. See Table 2.1 for the rest of the plateau ages and the Supplementary Material for the individual heating steps.

Figure 2.5. Time-temperature histories output from the 1-D thermal model *QTQt* for samples R01 and R02 (with ApHe constraints) and R05 and R08 (without). The bold black line is the "Expected Model," which is the weighted mean of all best-fit thermal histories (Gallagher, 2012). Grey shading indicates the 95% credible confidence intervals. The input chronometer data (along with their 2σ uncertainties) are shown on the cooling curve.

Figure 2.6. Exhumation rate histories from thermal-kinematic modeling using a 1-D version of *Pecube* for samples R01 and R02 (with MsAr, ZrnHe, and ApHe constraints) and R05 and R08 (MsAr and ZrnHe only). The bold black lines indicate the mean exhumation rate history, and the horizontal grey boxes indicate two standard deviations from the mean. The input chronometer data (along with their 2σ uncertainties) are presented at the top of each figure pane. The number of acceptable fits to the data are noted. See Figures 2.1 and 2.2 for sample locality information. The dashed vertical line at ~15.6 Ma indicates the timing of transition from ductile shearing to ductile-brittle slip on the detachment according to Cottle et al. (2015).

Figure 2.7. Estimates of displacement on the Qomolangma detachment between 15.6 and 13.0 Ma for samples R01 and R02, which have the most thermochronometric information. These detachment displacement histories were calculated from *Pecube* exhumation history results (see Figure 2.6) and presume either a 5° or 10° dip on the

detachment. The shaded areas represent the uncertainties that reflect the propagation of the 2σ uncertainties in the *Pecube* models for successive time steps.

12. References

Adams, B.A., Hodges, K.V., Whipple, K.X., Ehlers, T.A., van Soest, M.C., and Wartho, J. (2015). Constraints on the tectonic and landscape evolution of the Bhutan Himalaya from thermochronometry, *Tectonics*. *32*(6), 1329-1347.

Bargnesi, E. A., Stockli, D. F., Hourigan, J. K., and Hager, C. (2016). Improved accuracy of zircon (U-Th)/He ages by rectifying parent nuclide zonation with practical methods, *Chemical Geology*. *426*, 158-169.

Beaumont, C., Jamieson, R. A., Nguyen, M.H., and Lee, B. (2001). Himalayan tectonics explained by extrusion of a low-viscosity crustal channel coupled to focused surface denudation. *Nature, 414*, 738-742.

Blisniuk, P. M., Hacker, B. R., Glodny, J., Ratschbacher, L., Bi, S., Wu, Z., McWilliams, M.O., and Calvert, A. (2001). Normal faulting in central Tibet since at least 13.5 Myr ago. *Nature*, *412*, 628-632.

Brady, R.J. (2002). Very high slip rates on continental extensional faults: new evidence from (U-Th)/He thermochronometry of the Buckskin Mountains, Arizona. *Earth and Planetary Science Letters, 197*, 95-104.

Braun, J. (2003). Pecube: A new finite-element code to solve the 3D heat transport equation including the effects of a time-varying, finite amplitude surface topography. *Computers & Geosciences*, *29*(6), 787-794.

Braun, J.P. (2016). Strong imprint of past orogenic events on the thermochronological record, *Tectonophysics*. *683, 325-332.*

Braun, J., van der Beek, P., Valla, P., Robert, X., Herman, F., Glotzbach, C., Pedersen, V., Perry, C., Simon-Labric, T., and Prigent, C. (2012). Quantifying rates of landscape evolution and tectonic processes by thermochronology and numerical modeling of crustal heat transport using PECUBE. *Tectonophysics*, *524–525*, 1-28.

Brichau, S. (2004). Constraining the tectonic evolution of extensional fault systems in the Cyclades (Greece) using low-temperature thermochronology. *PhD Dissertation*, University of Mainz and University of Montpelier.

Burchfiel, C. B., Chen, Z., Hodges, K. V., Liu, Y., Royden, L.H., Deng, C., and Xu J.

(1992). The South Tibetan detachment system, Himalayan orogen: extension contemporaneous with and parallel to shortening in a collisional mountain belt. *Geologic al Society of America Special Paper*, *269*, 41 p.

Campani, M., Herman, F., and Mancktelow, N. (2010). Two- and three-dimensional thermal modeling of a low-angle detachment; exhumation history of the Siplon fault zone, Central Alps. *Journal of Geophysical Research*, *115*, *B10.*

Carosi, R., Lombardo, B., Molli, G., Musumeci, G., and Pertusati, P.C. (1998). The South Tibetan detachment system in the Rongbuk Valley, Everest region. Deformation features and geological implications. *Journal of Asian Earth Sciences*, *16*, 299–311.

Carosi, R., Lombardo, B., Musumeci, G., and Pertusati, P.C. (1999). Geology of the Higher Himalayan Crystallines in Khumbu Himal (Eastern Nepal). *Journal of Asian Earth Sciences*, *17*, 785-803.

Carrapa, B., Robert, X., DeCelles, P.G., Orme, D.A., Thomson, S.N., and Schoenbohm, L.M. (2016). Asymmetric exhumation of the Mount Everest region: Implications for the tectono-topographic evolution of the Himalaya. *Geology*, doi: 10.1130/G37756.1.

Clift, P. D., Hodges, K. V., Heslop, D., Hannigan, R., Hoang, L. V., and Calves G. (2008). Correlation of Himalayan exhumation rates and Asian monsoon intensity. *Nature Geoscience*, *1*, 875-880.

Coleman, M., and Hodges, K. (1995). Evidence for Tibetan Plateau uplift before 14 Myr ago from a new minimum age for east-west extension. *Nature*, *374*(6517), 49-52.

Cooper, F. J., Adams, B. A., Edwards, C. S., and Hodges, K. V. (2012). Large normal-sense displacement on the South Tibetan fault system in the eastern Himalaya. *Geology*, *40*(11), 971-974.

Cooper, F. J., Hodges, K.V., and Adams, B.A. (2013). Metamorphic constraints on the character and displacement of the South Tibetan fault system, central Bhutanese Himalaya. *Lithosphere*, *5*, 67-81.

Cooper, F.J., Hodges, K.V., Parrish, R.R., Roberts, N.M.W., and Horstwood, M.S.A. (2015). Synchronous N-S and E-W extension at the Tibet-to-Himalaya transition in NW Bhutan, *Tectonics*. *34*(7), 1375-1395.

Copeland, P., Parrish, R.R., and Harrison, T.M. (1988). Identification of inherited radiogenic Pb in monazite and its implications for U-Pb systematics. *Nature*, *333*, 760-763.

Corfu, F., Ravna, E. J. K., and Kullerud, K. (2003). A Late Ordovician U-Pb age for the Tromsø Nappe eclogites, Uppermost Allocthon of the Scandinavian Caledonides.

Contrib. Mineral Petrol., *145*, 502-513.

Corthouts, T. L., Lageson, D. R., and Shaw, C. A. (2016). Polyphase deformation, dynamic metamorphism, and metasomatism of Mount Everest's summit limestone, east central Himalaya, Nepal/Tibet. *Lithosphere*, *8*, doi: 10.1130/l1473.1131.

Cottle, J. M., Jessup, M.J., Newell, D.L., Searle, M.P., Law, R.D., and Horstwood M.S.A., (2007). Structural insight into the ductile evolution of an orogen-scale detachment: the South Tibetan detachment system, Dzakaa Chu section, eastern Himalaya. *Journal of Structural Geology*, *29*, 1781-1797.

Cottle, J. M., Waters, D.J., Riley, D., Beyssac, O., and Jessup, M.J. (2011). Metamorphic history of the South Tibetan Detachment System, Mt. Everest region, revealed by RSCM thermometry and phase equilibria modelling. *Journal of Metamorphic Geology*, *29*(5), 561-582.

Cottle, J. M., Larson, K.P., and Kellett, D.A. (2015a). How does the mid-crust accommodate deformation in large, hot collisional orogens? A review of recent research in the Himalayan orogen. *Journal of Structural Geology*, *78*, 119-133.

Cottle, J. M., Searle, M. P., Jessup, M. J., Crowley, J. L., and Law, R. D. (2015b). Rongbuk re-visited: Geochronology of leucogranites in the footwall of the South Tibetan Detachment System, Everest Region, Southern Tibet. *Lithos*, *227*, 94-106.

Evans, S. L., Styron, R.H., van Soest, M.C., Hodges, K.V., and Hanson, A.D. (2015). Zircon and apatite (U-Th)/He evidence for Paleogene and Neogene extension in the Southern Snake Range, Nevada, USA. *Tectonics*, *34*(10), 2142-2164, doi: 10.1002/2015TC003913.

Farley, K.A., Wolf, R.A., and L.T. Silver, L.T. (1996). The effects of long alpha-stopping distances on (U-Th)/He ages. *Geochimica et Cosmochimica Acta*, *60*, 4223-4229.

Farley K.A. (2000). Helium diffusion from apatite: General behavior as illustrated by Durango fluorapatite. *Journal of Geophysical Research*, *105*, 2903–2914.

Flowers, R.M., Ketcham, R.A., Shuster, D.L., and Farley K.A. (2009). Apatite (U-Th)/He thermochronometry using a radiation damage accumulation and annealing model. *Geochimica et Cosmochimica Acta*, *73*, 2347-2365.

Gaetani, M., and Garzanti, E. (1991). Multicyclic history of the northern India continental margin (Northwestern Himalaya). *Bulletin of the American Association of Petroleum Geologists*, *75*, 1427-1446.

Gallagher, K. (2012). Transdimensional inverse thermal history modelling for quantitative thermochronology. *Journal of Geophysical Research*, *117*, B02408, doi:10.1029/2011JB00882.

Gébelin, A., Mulch, A., Teyssier, C., Jessup, M. J., Law, R. D., and Brunei M. (2013). The Miocene elevation of Mount Everest. *Geology*, *41*(7), 799-802.

Grujic, D., Hollister, L., and Parrish, R.R. (2002). Himalayan metamorphic sequence as an orogenic channel: insight from Bhutan. *Earth Planetary Science Letters*, *198*, 177–191.

Guenthner, W.R., Reiners, P.W., Ketcham, R.A., Nasdala, L., and Geister, G. (2013). Helium diffusion in natural zircon: Radiation damage, anisotropy, and the interpretation of zircon (U-Th)/He thermochronology. *American Journal of Science*, *313*, p. 145 – 198.

Harris, N. (2006). The elevation history of the Tibetan Plateau and its implications for the Asian monsoon. *Palaeogeography, Palaeoclimatology, Palaeoecology*, *241*, 4-15.

Harrison, T. M., Celerier, J., Aikman, A.B., Hermann, J., and Heizler, M.T. (2009). Diffusion of ^{40}Ar in muscovite. *Geochimica et Cosmochimica Acta*, *73*(4), 1039-1051.

He, D., Webb, A.A.G., Larson, K.P., Martin, A.J., and Schmitt, A.K. (2015). Extrusion vs. duplexing models of Himalayan mountain building 3: duplexing dominates from the Oligocene to Present. *International Geology Review*, *57*, 1-27.

Hodges, K. V. (2000). Tectonics of the Himalaya and southern Tibet from two perspectives. *Geological Society of America Bulletin*, *112*, 324-350.

Hodges, K. V. (2006). A synthesis of the Channel Flow-Extrusion hypothesis as developed for the Himalayan-Tibetan orogenic system, in *Channel Flow, Ductile Extrusion, and Exhumation of Lower-Middle Crust in Continental Collision Zones*, edited by R. Law, M. Searle and L. Godin, 71-90, Geological Society Special Publication 268, London.

Hodges, K. V., Parrish, R.R., Housh, T.B., Lux, D.R., Burchfiel, B.C., Royden, L.H., and Chen, Z. (1992). Simultaneous Miocene extension and shortening in the Himalayan orogen. *Science*, *258*, 1466–1470.

Hodges, K. V., Bowring, S., Davidek, K., Hawkins, D., and Krol, M. (1998). Evidence for rapid displacement on Himalayan normal faults and the importance of tectonic denudation in the evolution of mountain ranges. *Geology*, *26*, 483–486.

Hodges, K. V., Hurtado, J. M., and Whipple, K. X. (2001). Southward extrusion of Tibetan crust and its effect on Himalayan tectonics. *Tectonics*, *20*(6), 799-809.

Hourigan, J.K., Reiners, P.W., and Brandon, M.T. (2005). U-Th zonation dependent alpha-ejection in (U-Th)/He chronometry. *Geochimica et Cosmochimica Acta, 69*, 3349-3365.

Jessup, M. J., Law, R. D., Searle, M. P. and Hubbard, M.S. (2006). Structural evolution

and vorticity of flow during extrusion and exhumation of the Greater Himalayan Slab, Mount Everest Massif, Tibet/Nepal: implications for orogen-scale flow partitioning, *in Channel Flow, Ductile Extrusion, and Exhumation of Lower-Middle Crust in Continental Collision Zones*, edited by Law, R., Searle, M., and Godin, L., London, Geological Society Special Publication 268, p. 79-414.

Jessup, M. J., Cottle, J.M., Searle, M.P, Law, R.D., Newell, D.L., Tracy, R.J., and Waters, D.J. (2008). PT-t-D paths of Everest Series schist. Nepal, *Journal of Metamorphic Geology*, *26*, 717–739.

John, B.E., and Foster, D.A. (1993). Structural and thermal constraints on the initiation angle of detachment faulting in the southern Basin and Range: The Chemehuevi Mountains case study. *Geologic Society of America Bulletin, 105*, 1091-1108.

Kellett, D.A., Grujic, D., Coutand, I., Cottle, J., and Mukul M. (2013). The South Tibetan detachment system facilitates ultra rapid cooling of granulite-facies rocks in Sikkim Himalaya. *Tectonics*, *32*, 252 – 270.

Ketcham, R. A. (2005). Forward and inverse modeling of low-temperature thermochronometry data, in *Low-Temperature Thermochronology: Techniques, Interpretations, and Applications*, edited by P. W. Reiners and T. A. Ehlers, pp. 275-314, Mineralogical Society of America, Washington, DC.

Kohn, M. J. (2008). P-T-t data from central Nepal support critical taper and repudiate large-scale channel flow of the Greater Himalayan Sequence, *Geological Society of America Bulletin*. *120*(3-4), 259-273.

Law, R. D. (2014). Deformation thermometry based on quartz c-axis fabrics and recrystallization microstructures: A review. *Journal of Structural Geology*, *66*, 129-161.

Law, R.D., Searle, M.P., and Simpson, R.L. (2004). Strain, deformation temperatures and vorticity of flow at the top of the Greater Himalayan Slab, Everest Massif, Tibet. *Journal of the Geological Society of London*, *161*, 305-320.

Law, R.D., Jessup, M.J., Searle, M.P., Francis, M.K., Waters, D.J., and Cottle, J.M. (2011). Telescoping of isotherms beneath the South Tibetan Detachment System, Mount Everest Massif. *Journal of Structural Geology*, *33*, 1569-1594.

Le Breton, N., and Thompson, A.B. (1988). Fluid-absent (dehydration) melting of biotite in metapelites in the early stages of crustal anatexis. *Contributions to Mineralogy and Petrology*, *99*, 226-237.

Le Fort, P., Cuney, M., Deniel, C., France-Lanord, C., Sheppard, S.M.F., Upreti, B.N., and Vidal, P. (1987). Crustal generation of Himalayan leucogranites. *Tectonophysics*, *134*, 39-57.

Leloup, P.H., Maheo, G., Arnaud, N., Kali, E., Boutonnet, E., Liu, D., Xiaohan, L., and Haibing, L. (2010). The South Tibet detachment shear zone in the Dinggye area Time constraints on extrusion models of the Himalayas. *Earth and Planetary Science Letters*, *292*, 1-16.

Lombardo, B., Pertusati, P., and Borghi S., (1993). Geology and tectonomagmatic evolution of the eastern Himalaya along the Chomolungma-Makalu transect, in *Himalayan Tectonics*, edited by P. J. Treloar and M. P. Searle, pp. 341-355, Geological Society Special Publication, 47, London.

Murphy, M. A. and Harrison, T.M. (1999). Relationship between leucogranites and the Qomolangma Detachment in the Rongbuk Valley, South Tibet. *Geology*, *27*(9), 831-834, doi:10.1130/0091-7613(1999)027<0831:RBLATQ>2.3.CO;2.

Myrow, P. M., Hughes, N.C., Searle, M.P., Fanning, C.M., Peng, S.C., and Parcha, S.K. (2009). Stratigraphic correlation of Cambrian-Ordovician deposits along the Himalaya: Implications for the age and nature of rocks in the Mount Everest region. *Geological Society of America Bulletin*, *121*(3-4), 323-332.

Najman, Y., Appel, E., Boudagher-Fadel, M., Bown, P., Carter, A., Garzanti, E., Godin, L., Han, J.T., Liebke, U., Oliver, G., Parrish, R., and Vezzoli, G. (2010). Timing of India-Asia collision: Geological, biostratigraphic, and palaeomagnetic constraints. *Journal of Geophysical Research-Solid Earth*, *115*, doi: 10.1029/2010jb007673.

Nelson, K.D., Zhao, W., Brown, L.D., Kuo, J., Che, J., Xianwen, L., Klemperer, S., Makovsky, Y., Meissner, R., Mechie, J., Kind, R., Wenzel, F., Ni, J., Nabelek, J., Chen, L., Handong, T., Wenbo, W., Jones, A.G., Booker, J., Unsworth, N., Kidd, W.S.F., Hauk, M., Alsdorf, D., Ross, A., Cogan, M., Wu, C., Sandvol, E.A., and Edwards, M. (1996). Partially molten middle crust beneath southern Tibet: Synthesis of Project INDEPTH Results. *Science*, *274*, 1684-1688.

Orme, D.A., Reiners, P.W., Hourigan, J.K., and Carrapa, B. (2015). Effects of inherited cores and magmatic overgrowths on zircon (U-Th)/He ages and age-eU trends from Greater Himalaya sequence rocks, Mt. Everest region, Tibet. *Geochemistry, Geophysics, Geosystems*, DOI 10.1002/2015GC005818

Owen, L. A., Robinson, R., Benn, D.I., Finkel, R.C., Davis, N.K., Yi, C., Putkonen, J., Li, D.H., and Murray, A.S. (2009). Quaternary glaciation of Mount Everest. *Quaternary Science Reviews*, *28*, 1412-1433.

Parrish, R. R., and Hodges, K.V. (1996). Isotopic constraints on the age and provenance of the Lesser and Greater Himalayan sequences. Nepalese Himalaya, *Geological Society of America Bulletin*, *108*, 904-911.

Patiño-Douce, A. E., and Harris, N. (1998). Experimental constraints on Himalayan anatexis. *Journal of Petrology*, *39*, 689-710.

Pearson, R.K. (2011). *Exploring data in engineering, the sciences, and medicine*, Oxford University Press.

Pognante, U., and Benna, P. (1993). Metamorphic zonation, migmatization and leucogranites along the Everest transect of eastern Nepal and Tibet: record of an exhumation history, *in* Treloar, P. J., and Searle, M. P., eds., Himalayan Tectonics: London, The Geological Society, 323-340.

Rades, E. F., Hetzel, R., Strobl, M., Xu, Q., and Ding, L. (2015). Defining rates of landscape evolution in a south Tibetan graben with in situ-produced cosmogenic ^{10}Be. *Earth Surface Processes and Landforms*, *40*, 1862-1876.

Reiners, P. W., Spell, T. L., Nicolescu, S., and Zanetti K. A., (2004). Zircon (U-Th)/He thermochronometry: He diffusion and comparisons with ^{40}Ar/^{39}Ar dating. *Geochimica et Cosmochimica Acta*, *68*, 1857-1887.

Reiners, P.W. and Brandon, M.T. (2006). Using thermochronology to understand orogenic erosion. *Annual Review of Earth and Planetary Sciences*, *34*, 419-466.

Ruppel, C., Royden, L., and Hodges, K.V. (1988). Thermal modeling of extensional tectonics: Application to pressure-temperature-time histories of metamorphic rocks. *Tectonics*, *7*, 947 – 957.

Sakai, H., Sawada, M., Takigami, Y., Orihashi, Y., Danhara, T., Iwano, H., Kuwahara, Y., Dong, Q., Cai, H.W., and Li, J.G. (2005). Geology of the summit limestone of Mount Qomolangma (Everest) and cooling history of the Yellow Band under the Qomolangma detachment. *Island Arc*, *14*(4), 297-310.

Searle, M. P. (1999). Extensional and compressional faults in the Everest-Lhotse massif, Khumbu Himalaya, Nepal. *Journal of the Geological Society of London*, 156, 227–240.

Searle, M. P., Simpson, R., Law, R.D., Parrish, R.R., and Waters, D.J. (2003). The structural geometry, metamorphic and magmatic evolution of the Everest massif, High Himalaya of Nepal–South Tibet. *Journal of the Geological Society of London*, *160*, 345–366.

Searle, M. P., Law, R.D., and Jessup, M.J. (2006). Crustal structure, restoration and evolution of the Greater Himalaya: implication for channel flow and ductile extrusion of the middle crust. In Law, R. D.; Searle, M. P.; and Godin, L., eds. *Channel flow, extrusion, and exhumation in continental collision zones*, Geological Society of London Special Publications, *268*, 355–378.

Searle, M. P., Cottle, J.M., Streule, M.J., and Waters, D.J. (2010). Crustal melt granites and migmatites along the Himalaya: melt source, segregation, transport and granite emplacement mechanisms. *Earth and Environmental Science Transactions of the Royal Society of Edinburgh*, *100*, 219-233.

Shuster, D. L., Flowers, R. M., and Farley, K.A. (2006). The influence of natural radiation damage on helium diffusion kinetics in apatite. *Earth and Planetary Science Letters*, *249*, 148-161.

Spicer, R.A, Harris, N.B.W., Widdowson, M., Herman, A.B., Guo, S., Valdes, P.J.,

Wolfe, J.A., and Kelley, S.P. (2003). Constant elevation of southern Tibet over the past 15 million years. *Nature*, *421*, 622 – 624.

Stockli, D. (2005). Application of low-temperature thermochronometry to extensional tectonic settings, *in* Reiners, P. W., and Ehlers, T. A., eds., Low-Temperature Thermochronology, Techniques, Interpretations, ad Applications: Washington, DC, *Mineralogical Society of America, Reviews in Mineralogy and Geochemistry*, *58*, 411-448.

Stockli, D. F., Linn, J.K., Walker, J.D., and Dumitru, T. (2001). Miocene unroofing of the Canyon Range during extension along the Sevier Desert Detachment, west central Utah. *Tectonics*, *20*, 289-307.

Strobl, M., Hetzel, R., Niedermann, S., Ding, L., and Zhang, L. (2012). Landscape evolution of a bedrock peneplain on the southern Tibetan Plateau revealed by in situ-produced cosmogenic ^{10}Be and ^{21}Ne. *Geomorphology*, *153*, 192-204.

Thiede, R.C., and Ehlers, T.A. (2013). Large Spatial and Temporal Variations in Himalayan Denudation. *Earth and Planetary Science Letters*, 371-372, 278-293.

van Hinsbergen, D. J. J., Lippert, P.C., Dupont-Nivet, G., McQuarrie, N., Doubrovine, P.V., Spakman, W., and Torsvik, T.H. (2012). Greater India Basin hypothesis and a two-stage Cenozoic collision between India and Asia. *Proceedings of the National Academy of Sciences*, *109*, 7659-7664.

Vermeesch, P., Seward, D., Latkoczy, C., Wipf, M., Gunther, D., and Baur, H. (2007). Alpha-emitting mineral inclusions in apatite, their effect on (U-Th)/He ages, and how to reduce it. *Geochimica et Cosmochimica Acta*, *71*, 1737-1746.

Webb, A. A. G. (2013). Preliminary balanced palinspastic reconstruction of Cenozoic deformation across the Himachal Himalaya (northwestern India). *Geosphere*, *9*(3), 572-587.

Webb, A. A. G., Yin, A., Harrison, T.M., Celerier, J., and Burgess, W.P. (2007). The leading edge of the Greater Himalayan Crystalline complex revealed in the NW Indian Himalaya. Implications for the evolution of the Himalayan orogen, *Geology*, *35*(10), 955-958.

Wendt, I., and Carl, C. (1991). The statistical distribution of the mean squared weighted deviation. *Chemical Geology: Isotope Geoscience setion*, *86*, 275 – 285.

Yin, A. (2006). Cenozoic tectonic evolution of the Himalayan orogen as constrained by along-strike variation of structural geometry, exhumation history, and foreland sedimentation. *Earth Science Reviews*, *76*, 1-131.

Yin, C. H., and Kuo, S.T. (1978). Stratigraphy of the Mount Jolmo Lungma and its north slope. *Scientia Sinica*, *21*, 629-644.

TABLE 2.1. THERMOCHRONOLOGIC DATA FOR QOMOLANGMA DETACHMENT FOOTWALL SAMPLES, RONGBUK VALLEY, TIBET

Sample number	Latitude	Longitude	Elevation (m)	Structural depth beneath Qomolangma detachment (m)	Rock Type	**MsAr (Ma)**[1]	**ZrnHe (Ma)**[2]	**ApHe (Ma)**[2]
R01	28.14056° N	86.85194° E	5157	800	Leucogranite	15.37 ± 0.16 (98.8)	11.4 ± 2.4 (4)	9.3 ± 2.8 (6)
R02	28.17328° N	86.84003° E	5114	700	Mylonitized leucogranite	15.000 ± 0.060 (100)	13.0 ± 1.5 (4)	7.76 ± 0.52 (2)
R03	28.17300° N	86.84297° E	5089	600	Mylonitized leucogranite	15.25 ± 0.11 (99)	12.9 ± 1.7 (2)	-
R04	28.18148° N	86.83585° E	5025	600	Mylonitized leucogranite	15.420 ± 0.050 (99.8)	14.32 ± 0.21 (4)	-
R05	28.19000° N	86.83243° E	5019	500	Leucogranite	14.400 ± 0.060 (100)	13.1 ± 1.7 (4)	-
R06	28.20502° N	86.82913° E	5128	450	Mylonitized leucogranite	14.770 ± 0.070 (100)	11.0 ± 1.1 (4)	-
R07	28.20610° N	86.82580° E	4997	400	Leucogranite	14.450 ± 0.070 (99.9)	12.9 ± 1.9 (7)	-
R08	28.21285° N	86.82395° E	4961	300	Leucogranite	14.930 ± 0.080 (99)	13.66 ± 0.17 (5)	-

All uncertainties quoted at 2σ

[1]Numbers in parentheses indicates the total %^{39}Ar making up the plateau Ar-Ar age.

[2]Numbers in parentheses designates number of analyses contributing to the mean

FIGURE 2.1

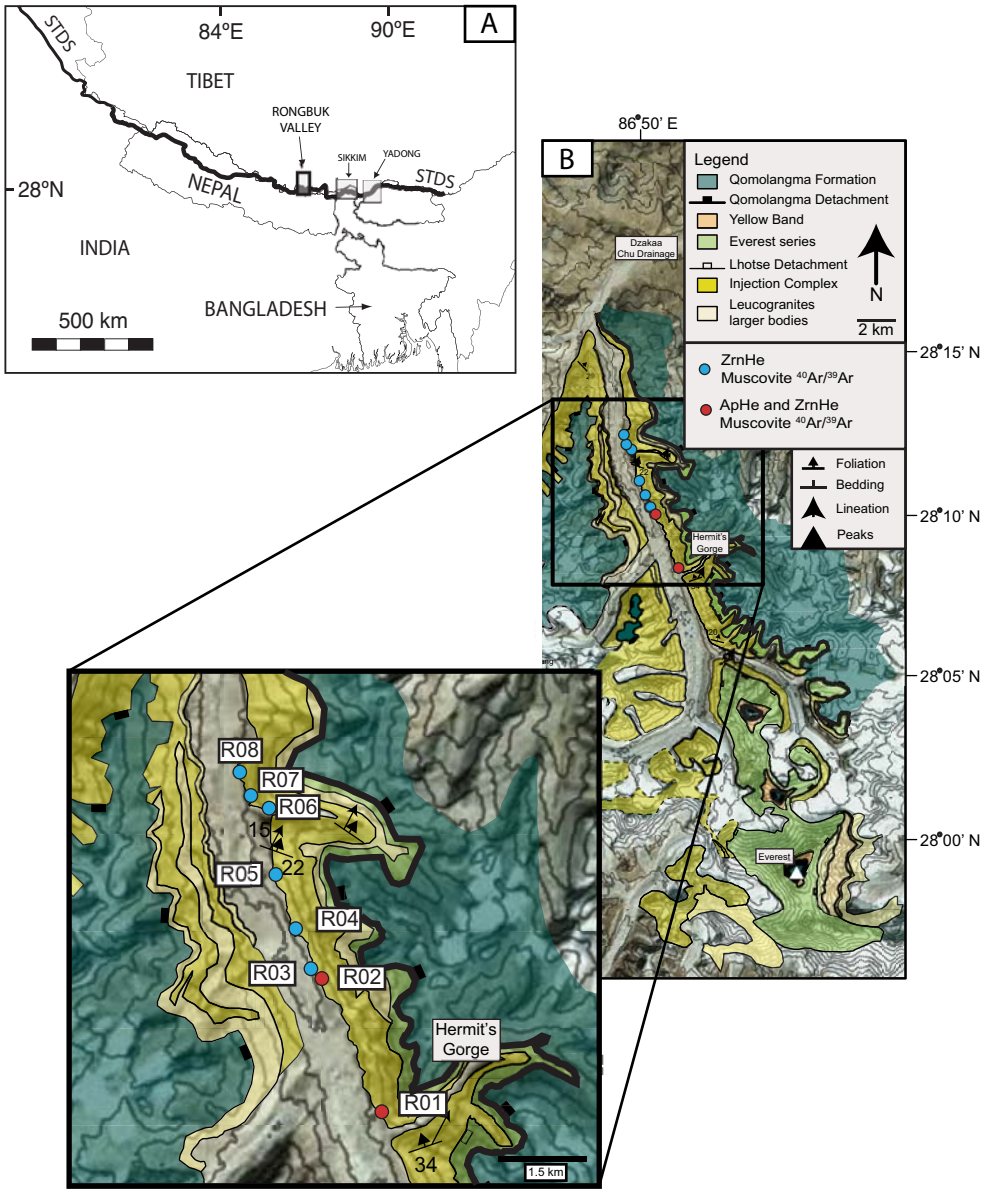
A
84°E
90°E
STDS
TIBET
RONGBUK VALLEY
SIKKIM
YADONG
STDS
28°N
NEPAL
INDIA
BANGLADESH
500 km
B
86°50' E
Legend
Qomolangma Formation
Qomolangma Detachment
Yellow Band
Everest series
Lhotse Detachment
Injection Complex
Leucogranites larger bodies
N
2 km
Dzakaa Chu Drainage
ZrnHe Muscovite 40Ar/39Ar
ApHe and ZrnHe Muscovite 40Ar/39Ar
Foliation
Bedding
Lineation
Peaks
Hermit's Gorge
Everest
28°15' N
28°10' N
28°05' N
28°00' N
R08
R07
R06
15
22
R05
R04
R03
R02
Hermit's Gorge
R01
34
1.5 km

FIGURE 2.2

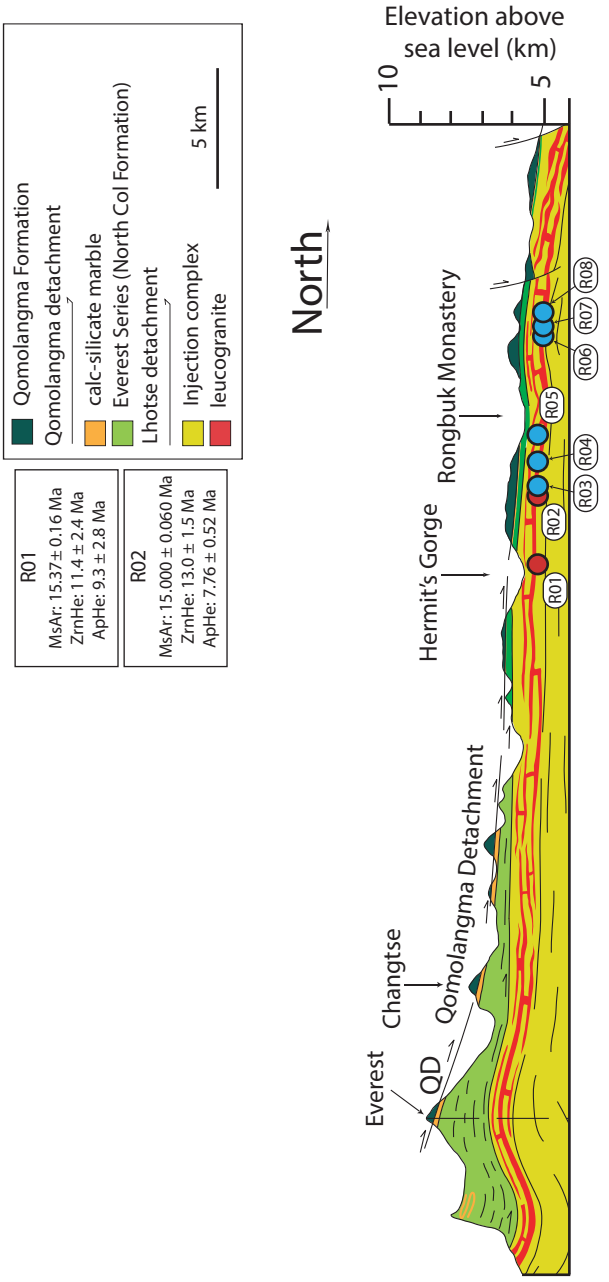
Qomolangma Formation
Qomolangma detachment
calc-silicate marble
Everest Series (North Col Formation)
Lhotse detachment
Injection complex
leucogranite
5 km
R01
MsAr: 15.37± 0.16 Ma
ZrnHe: 11.4 ± 2.4 Ma
ApHe: 9.3 ± 2.8 Ma
R02
MsAr: 15.000 ± 0.060 Ma
ZrnHe: 13.0 ± 1.5 Ma
ApHe: 7.76 ± 0.52 Ma
North
Elevation above sea level (km)
10
5
Rongbuk Monastery
Hermit's Gorge
Changtse
Qomolangma Detachment
Everest
QD
R01
R02
R03
R04
R05
R06
R07
R08

FIGURE 2.3

FIGURE 2.4

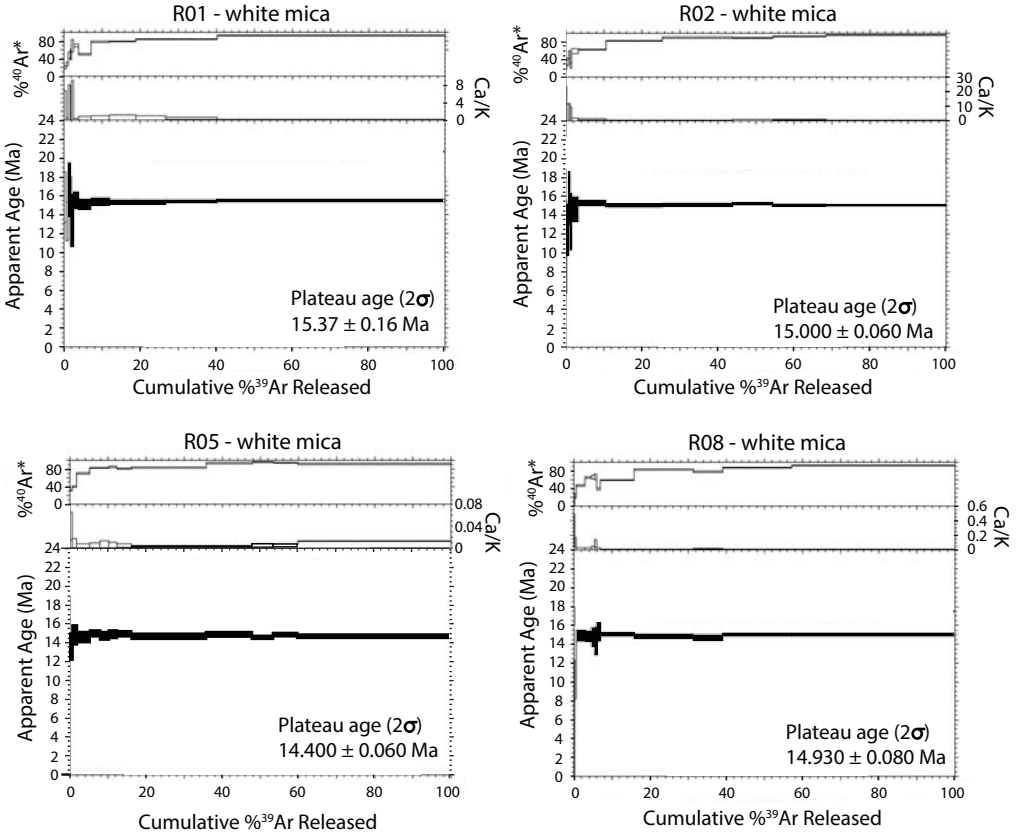
R01 - white mica
%40Ar*
Ca/K
Apparent Age (Ma)
Plateau age (2σ)
15.37 ± 0.16 Ma
Cumulative %39Ar Released
R02 - white mica
Plateau age (2σ)
15.000 ± 0.060 Ma
R05 - white mica
Plateau age (2σ)
14.400 ± 0.060 Ma
R08 - white mica
Plateau age (2σ)
14.930 ± 0.080 Ma

FIGURE 2.5

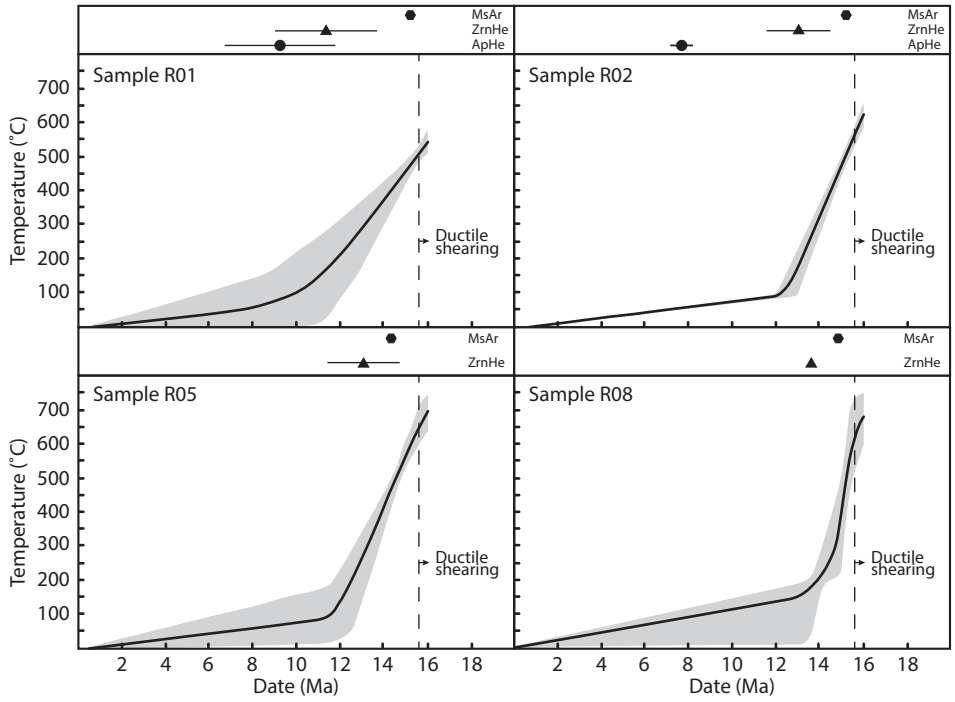
MsAr
ZrnHe
ApHe
Sample R01
Sample R02
Sample R05
Sample R08
Ductile shearing
Temperature (°C)
Date (Ma)
100
200
300
400
500
600
700
2
4
6
8
10
12
14
16
18

FIGURE 2.6

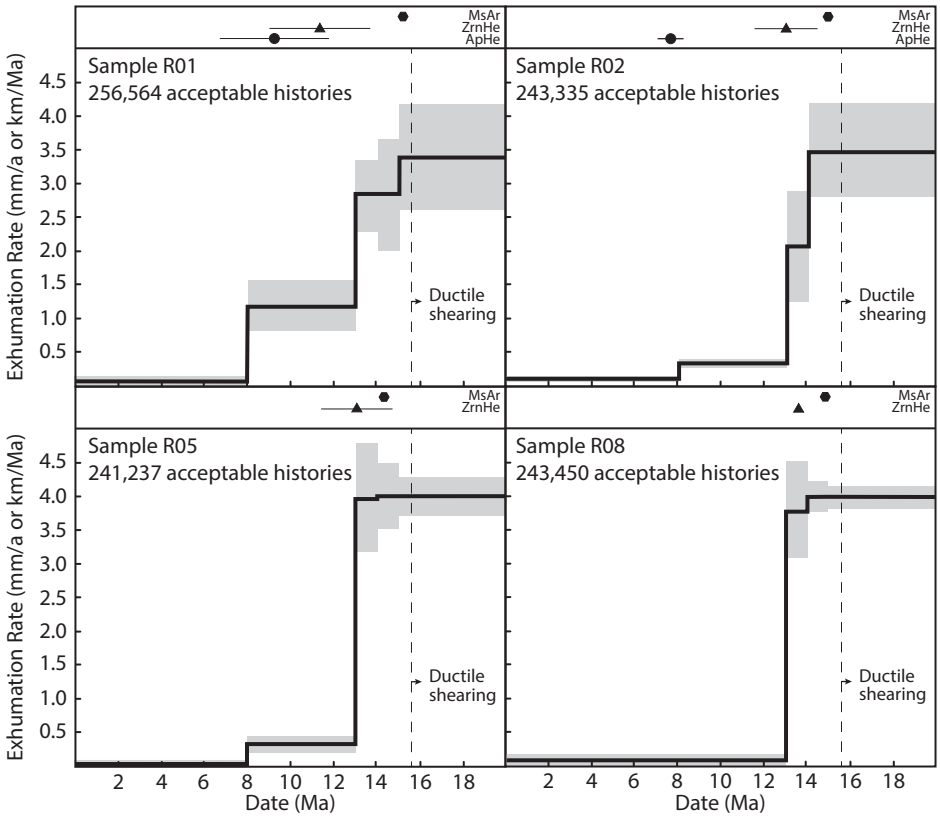
MsAr
ZrnHe
ApHe
Sample R01
256,564 acceptable histories
Ductile
shearing
Sample R02
243,335 acceptable histories
MsAr
ZrnHe
Sample R05
241,237 acceptable histories
Sample R08
243,450 acceptable histories
Exhumation Rate (mm/a or km/Ma)
0.5
1.0
1.5
2.0
2.5
3.0
3.5
4.0
4.5
2
4
6
8
10
12
14
16
18
Date (Ma)

FIGURE 2.7

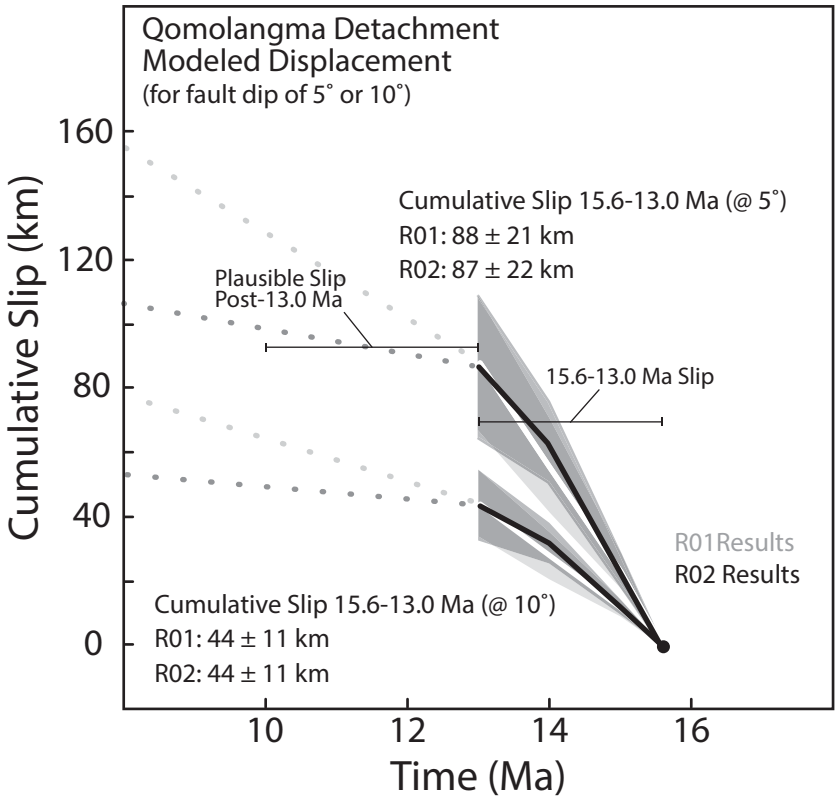
Qomolangma Detachment
Modeled Displacement
(for fault dip of 5˚ or 10˚)
Cumulative Slip (km)
160
120
80
40
0
10
12
14
16
Time (Ma)
Cumulative Slip 15.6-13.0 Ma (@ 5˚)
R01: 88 ± 21 km
R02: 87 ± 22 km
Plausible Slip
Post-13.0 Ma
15.6-13.0 Ma Slip
R01Results
R02 Results
Cumulative Slip 15.6-13.0 Ma (@ 10˚)
R01: 44 ± 11 km
R02: 44 ± 11 km

CHAPTER 3

TWO-DIMENSIONAL THERMAL-KINEMATIC MODELING OF THE SLIP HISTORY OF THE SOUTH TIBETAN DETACHMENT SYSTEM, EVEREST REGION, SOUTH-CENTRAL TIBET

1. Abstract

The South Tibetan detachment system includes numerous, north-dipping, low-angle extensional faults and shear zones exposed for over 1000 km along the length of the Himalaya. Here we present two-dimensional thermal-kinematic models of the slip history of the major displacement horizon of the system in south-central Tibet, north of Mount Everest. These models are constrained by previously published and new $^{40}Ar/^{39}Ar$ and (U-Th)/He thermochronologic data from gneisses and granites at three geographically dispersed exposures of the immediate footwall (Rongbuk, Ra Chu, and Dzakar Chu). These data are largely consistent with forward thermal-kinematic models which assume that the basal structure of the South Tibetan system in this region is a simple, planar, north-dipping detachment represented at the different study areas as a high-strain ductile shear zone often – but not always – capped by a discrete brittle fault surface depending on the depth at which the dominant tectonite fabrics developed. Best fits of models to thermochronologic data suggest between *ca.* 84 and 219 km of high-temperature slip between *ca.* 20 and 15.6 Ma and *ca.* 83 to 119 km of lower-temperature displacement between *ca.* 15.4 and 13 Ma, for a total displacement of *ca.* 167 to 338 km in this region. The broad consistency of these preliminary results with previously published one-dimensional modeling of the Rongbuk dataset alone suggests that much of

the essential thermal structure in regions of active tectonics can be deduced successfully using simpler, one-dimensional models when exhumation rates are high.

2. Introduction

The discovery a few decades ago of regional-scale, north-dipping, low-angle normal faults (detachments) in the Himalaya (Caby et al., 1983; Burg and Chen, 1984; Burchfiel and Royden, 1985; Burchfiel et al., 1992) profoundly altered the views of the earth science community regarding the possible importance of extensional faulting in the evolution of convergent orogenic systems. The South Tibetan detachment system (STDS), as Burchfiel and colleagues (1992) named that family of structures, can be traced along the spine of the Himalaya for over 1000 kilometers (Figure 3.1). While STDS faults have been studied in detail over the course of dozens of studies since their discovery, their origin and significance remain controversial; compare, for example, alternative interpretations in papers collected in Law et al. (2006). For example, many researchers – focusing on the distinctive north-vergent kinematics of the STDS faults as compared to the broadly coeval, south-vergent kinematics of major thrust faults of the Himalayan orogenic wedge – have interpreted the STDS as the upper boundary of a major Miocene, southward-extruding channel of middle or lower crust (e.g., Grujic et al., 1996; Nelson et al., 1996; Beaumont et al., 2001; Hodges et al., 2001; Hodges, 2006). Others have suggested that the STDS is little more than a reactivated earlier thrust fault in the upper part of the Himalayan orogenic wedge, with total normal-sense displacement of no more than a few kilometers (Yin 2006; Webb et al., 2007; Webb, 2013).

The area north of Mount Everest in south-central Tibet (Figure 3.2) offers an excellent opportunity to evaluate the evolution of a relatively large segment of the STDS and further evaluate the importance of the STDS in Himalayan tectonics. This part of the system was first mapped in reconnaissance fashion by Burchfiel et al. (1992) in their

foundational study of the STDS. They documented excellent exposures of the STDS in the walls of the Rongbuk valley, a glacio-fluvial catchment draining the north slopes of the Everest massif and noted that the system could be traced at the base of a series of klippen projecting southward to the Everest summit pyramid. These field relationships limited the regional NNE-dip of the major STDS detachment in the region – which they named the Qomolangma detachment – to no more than about 10˚. Noting that no footwall and hanging wall units could be matched across the Qomolangma detachment, they inferred a minimum displacement of 35 km on the structure. Although they did not trace the detachment beyond the mouth of the Rongbuk valley, the low dip of the structure, the moderate topography of the southern Tibetan Plateau, and its high desert climate favored the eventual identification of other segments of the STDS down dip to the north. Two were eventually discovered about 15 km north of the mouth of the Rongbuk valley and a few tens of kilometers to the east and west (Figure 3.2). Exposures to the west, along the banks of the Ra Chu ("chu" is the Tibetan word for small river) were characterized geologically by Jessup and Cottle (2010). Exposures to the east, along the banks of the Dzakar Chu, were characterized by Cottle et al. (2007). Together, the Rongbuk, Ra Chu, and Dzakar Chu outcrops define the best three-dimensional exposure of a single segment of the STDS known at present: roughly 50 km down dip and a comparable distance along strike.

Building on recent medium- and low-temperature thermochronometry of Qomolangma detachment footwall rocks in the Rongbuk valley (Schultz et al., 2017), we present here new $^{40}Ar/^{39}Ar$ and (U-Th)/He data for the Ra Chu and Dzakar Chu footwalls. We also report the results of a two-dimensional (2D) thermal-kinematic

modeling study of the STDS in the Everest area, done using the software package *Pecube* (Braun, 2003; Braun et al., 2012), and aimed at constraining better its probable time-integrated displacement and slip rate. The results support previous geometric (Searle et al., 2003; Law et al., 2004) and thermal-kinematic modeling (Schultz et al., 2017) arguments that the STDS was a major Miocene tectonic feature that likely played a fundamental role in Himalayan orogenesis.

3. Regional Geologic Setting

The Himalayan component of the Himalayan-Tibetan orogenic system, stretching from northeast India to northern Pakistan, developed as a consequence of the collision of Greater India with Eurasia at *ca.* 55 to 50 Ma (Hodges, 2000; Najman et al., 2010; van Hinsbergen et al., 2012). South of the Yarlung suture that marks the zone of initial collision, the central Himalayan orogenic wedge comprises several tectonostratigraphic elements separated by major, north-dipping, south-vergent thrust fault system and the STDS. South of the Himalayan range crest, the northernmost major contractional structure is the Main Central thrust system (MCT), which initiated in the latest Oligocene or early Miocene and was active concurrently (at least in part) with the STDS (Hodges et al., 1992). The tectonostratigraphic unit between the MCT and the STDS, commonly referred to as the Greater Himalayan sequence (GHS), represents the metamorphic core of the Himalaya. It is composed of Indian provenance high-grade metasedimentary and metaigneous gneisses with protolith ages that are lowermost Paleozoic-Neoproterozoic (Parrish and Hodges, 1996). Leucogranitic intrusions in the footwall rocks are a consequence of anatectic melting of the upper GHS that occurred during amphibolite-

granulite facies metamorphism in the Oligocene-Miocene (Le Fort, 1987; Searle et al., 2010). The STDS hanging wall instead consists of weakly metamorphosed to unmetamorphosed, Cambrian and younger strata of the Tibetan Sedimentary sequence (TSS) (Gaetani and Garzanti, 1991; Myrow et al., 2009).

3.1 Rongbuk valley

The Rongbuk valley extends about 35 km north from the base of the north face of Mount Everest to the confluence of its small river – the upper Dzakar Chu – with the Gyachung Chu merging from the southwest (Figure 3.2). GHS units, a large and complex leucogranite network that intrudes them, and TSS units are exposed in the valley, and the existence of a structural contact between the GHS and TSS had been postulated by Burg (1983) and Burg and Chen (1984) prior to the definition of the Qomolangma detachment by Burchfiel et al., (1992). In the central, accessible lower-elevation parts of the Rongbuk valley, the uppermost exposures of the GHS and its leucogranite dikes and sills constrain strong, high and medium temperature mylonitic fabrics (Burchfiel et al., 1992; Carosi et al., 1998; Law et al., 2004; Jessup et al., 2006). At the contact, which corresponds to a dramatic metamorphic discontinuity (upper amphibolite facies rocks in the footwall and lower greenschist facies or unmetamorphosed rocks in the hanging wall) lies a breccia zone oriented subparallel to the dominant mylonitic fabrics in the footwall. This fault zone is interpreted as the brittle expression of the Qomolangma detachment and the detachment as well as the underlying shear zone are mapped as the STDS in the valley.

In outcrops near the valley floor, the detachment hanging wall comprises fossiliferous, silty to relatively pure limestones of the Lower-Middle Ordovician Mt.

Qomolangma Formation (Yin and Kuo, 1978; Myrow et al., 2009). Sakai et al. (2005) confirmed the projection of the Qomolangma detachment to the Everest summit pyramid and documented that the Mt. Qomolangma Formation in its hanging wall there was indeed correlative to hanging wall lithologies in the Rongbuk valley (see also Corthouts et al., 2016). However, the immediate footwall rocks on the mountain are distinctive from those in the Rongbuk valley floor, and include metacarbonate and metaclastic rocks of the Cambrian Yellow Band and North Col Formation (Myrow et al., 2009). This relationship led to the proposition that a second, low-angle, north-dipping STDS structure – the Lhotse detachment – may occur beneath the North Col formation and above the GHS-leucogranite package as exposed on the southern flanks of Everest (Lombardo et al., 1993; Pognante and Benna, 1993; Carosi et al., 1998, 1999; Searle, 1999), even though the proposed structure has never been studied in detail. If this structural configuration is correct, the Qomolangma detachment must be a younger structure than the Lhotse detachment and must have a slightly steeper dip so as to cut out the Yellow Band and North Col Formation to the north between the mountain and the more accessible STDS exposures in the Rongbuk valley (Carosi et al., 1998; Jessup et al., 2008).

Studies of the Qomolangma detachment footwall mylonites in the Rongbuk valley imply that this structure, like similar, regional-scale detachments found in extensional terrains such as the Basin and Range province of western North America, shows evidence for progressive exhumation of the footwall in the form of overprinting textures and fabrics that formed at progressively lower temperatures with time. Based on quartz fabric opening angles, the primary mylonitic fabrics formed over a range of temperatures (Law

et al., 2011), ranging from ca. 625 ± 50˚C at the deepest structural levels exposed in the middle reaches of the valley, to chlorite grade near the brittle Qomolangma detachment. The temperature estimate of Law et al. (2011) for the highest temperature fabrics is nearly identical to that determined by Hodges et al. (1992) for the prograde GHS metamorphic assemblages at that structural level based on element partitioning thermobarometry. Based on the pressure estimated from the thermobarometric work, the depth of formation of the high-temperature mylonitic fabrics was ca. 17 km.

3.2 Ra Chu and Dzakar Chu Exposures

Jessup and Cottle (2010) noted the existence of several localities in the Everest region also thought to provide additional exposures of the STDS. We collected samples from two of these – which we will refer to as the Ra Chu and Dzakar Chu exposures (Figures 3.2 and 3.3) – for thermochronologic study in anticipation of the thermal-kinematic modeling presented here.

At the Ra Chu exposures, roughly 30 km to the northwest of Hermit's Gorge in the Rongbuk valley, Jessup and Cottle (2010) documented exposures of the STDS shear zone (Figure 3.2). Our samples were collected in a bedrock cliff section by the river bank that includes a *ca.* 30-m-thick section of the STDS shear zone (Figure 3.3). The outcrop consists largely of basal calc-silicate rocks and overlying marbles, which together represent the GHS. Both are intruded by foliated leucogranites that present as lenses concordant with the prominent mylonitic fabric in the outcrop. Jessup and Cottle (2010) documented a prominent pseudotachylite cutting the leucogranitic pods at high angles, which attests to the progressive ductile to brittle evolution of the STDS at this locality. A

sharp, low-angle, N-dipping fault separates the mylonitized GHS rocks from overlying Carbonaceous terrigenous sediments assigned to the TSS. Jessup and Cottle (2010) estimated deformation temperatures in the footwall mylonites of 200 to 400˚C.

Below the confluence of the Dzakar Chu and the Gyachung Chu at the north end of the Rongbuk valley, the combined flow is referred to as the Dzakar Chu. Roughly 40 km to the east of the Rongbuk valley along this drainage, Cottle et al. (2007) documented another exposure of the STDS, which they referred to as the Dzakaa Chu section (Figure 3.2). (There is much inconsistency on maps and in the literature regarding the English spelling of translations from the Tibetan. For the purposes of consistency, we conform to the Royal Geographical Society spelling convention, and thus will refer here to the section studied by Cottle et al. (2007) as the "Dzakar Chu" section rather than the "Dzakaa Chu" section.)

The STDS in the Dzakar Chu section manifests as a ~1000 m-thick shear zone containing at least three generations of centimeter to decimeter-scale leucogranitic sills and dykes that intrude into gneisses, metapelites, calc-silicates, and marbles of the GHS (Cottle et al., 2007; Figure 3.3). This section displays well-developed fabrics and mylonites, the intensity of which increases up-section. Cottle et al. (2007) suggested the lower exposed portions of the shear zone reached deformation temperatures >500˚C, based on the occurrence of syn-kinematic fibrolitic sillimanite. Cottle et al. (2007) also reported estimated *P-T* conditions of 705 ± 30˚C and 7.8 ± 1.5 kbar based on preliminary garnet-biotite thermometry and garnet-plagioclase-aluminosilicate-quartz barometry.

Unlike the Rongbuk and Ra Chu examples, the Dzakar Chu exposure appears not to feature a sharp, brittle fault at the transition between the GHS rocks below and TSS

rocks above. Instead, Cottle et al. (2007) describe a progressive drop in shear zone temperatures at higher structural levels. At the highest levels of the section, low-grade metaclastic rocks with weak cleavage were interpreted by Cottle and co-workers as Ordovician TSS rocks.

4. Previous estimates of the timing and magnitude of slip on the STDS in the Everest region

Great efforts have been made over the past 25 years to resolve the magnitude and duration of slip on the Qomolangma detachment. Hodges et al. (1992) argued that slip on the structure was on-going at the time of upper amphibolite facies metamorphism in the GHS mylonites at *ca.* 21-20 Ma based on the overlapping ages of U/Pb and $^{40}Ar/^{39}Ar$ dates of metamorphic titanite and hornblende, respectively. This interpretation was strengthened by the inference by Law et al. (2011) that at least some of the mylonitic fabrics in the shear zone were developed under upper amphibolite facies conditions. Subsequent (U-Th)/Pb work documented that mylonitic fabrics were developed in *ca*. 16.7 to 16.4 Ma leucogranite sills (Hodges et al., 1998; Murphy and Harrison, 1999; Cottle et al., 2015), but Cottle et al. (2015) showed that cross-cutting, post-mylonitization leucogranite dikes limited ductile STDS deformation to being older than 15.6 Ma.

Schultz et al. (2017) generated $^{40}Ar/^{39}Ar$ and (U-Th)/He data for eight leucogranite samples from the Rongbuk shear zone that placed additional constraints on their post-15.6 Ma exhumation history. Following the approach of Thiede and Ehlers (2013), they modeled footwall exhumation histories that implied a steep drop from exhumation rates of *ca.* 3 to 4 km/Ma to ≤0.5 km/Ma at roughly 13 Ma. Schultz et al.

(2017) inferred from these results that STDS activity continued on the brittle Qomolangma detachment between *ca.* 15.4 Ma and 13 Ma, but then ceased, with exhumation subsequent to *ca.* 13 Ma reflecting erosional processes rather than tectonic denudation by slip on the detachment. Projecting the modeled exhumation rates back in time, Schultz et al. (2017) estimated total brittle displacement on the detachment to be between *ca.* 36 and 119 km. Schultz et al. (2017) added these values to the ductile deformation estimates (*ca.* 25 to 170 km) presented by Law et al. (2011), indicating *ca.* 61 to 289 km of total slip occurred on the STDS in the Everest region during the Miocene.

Less is known regarding the age and slip magnitude for the STDS based on studies of the Ra Chu and Dzakar Chu exposures. Monazite from an unfoliated dyke that intruded almost orthogonal to the host rock foliation at Dzakar Chu yielded a $^{208}Pb/^{232}Th$ date of *ca.* 20.4 Ma, implying that the fabric of the shear zone at this locality developed prior to this time (Cottle et al., 2007). Cottle et al. (2007) also adopted a simple trigonometric model for STDS displacement at Dzakar Chu, using their *P–T* estimates of 705 ± 30˚C and 7.8 ± 1.5 kbar and the approximate 32˚ dip of the mylonitic foliation to calculate a minimum horizontal displacement of *ca.* 50 km. Noting that the detachment may have been rotated locally by subsequent faulting from its primary orientation, those authors repeated the calculation using what they regarded as the 15˚N regional dip of the STDS and hypothesized that the displacement may have been as high as *ca.* 80 to 120 km.

5. New Thermochronologic Data

Many of the thermochronologic studies that explored the slip histories of Basin and Range metamorphic core complexes in western North America observed a progressive younging of cooling ages in the footwall along the dip direction of the main detachments (John and Foster, 1993; Brady et al., 2002; Stockli, 2005; Brichau, 2004; Evans et al., 2015). For example, the ZrnHe apparent ages presented by Evans et al. (2015) show a *ca*. 20 Myr decrease along the Snake Range detachment in Nevada. Though Schultz et al. (2017) did not observe this trend in their Rongbuk data, it is possible that there was not enough down-dip length in the footwall exposures they studied to reveal such a distribution. The Ra Chu and Dzakar Chu exposures of the STDS proximal footwall offer the possibility to revisit the question of down-dip variability in closure dates. To that end, we collected footwall samples at both localities for both $^{40}Ar/^{39}Ar$ and (U-Th)/He thermochronology (Figure 3.2). From the Ra Chu section, we collected one sample (RC01) that contained both calc-silicate and amphibolite lithologies. From the Dzakar Chu exposures, we collected one leucogranite (DC01) and two biotite gneiss samples (DC02, DC03).

5.1 Methods

5.1.1 $^{40}Ar/^{39}Ar$ thermochronology

Muscovite and biotite crystals from the 250 to 500μm size fraction were handpicked and cleaned. Samples were individually wrapped in aluminum foil packets and loaded into small aluminum disks, which were interdispersed with grains of biotite standard HD-B1 (24.18 ± 0.09 Ma, uncertainty at 1σ, Schwarz et al., 2007) to monitor the

overall neutron flux. Synthetic and natural K and Ca salts were added to determine interfering nuclear production ratios. Ra Chu biotite and Dzakar Chu muscovites were irradiated in a Cd-shielded package at the Oregon State University CLICIT facility for 0.33 hours.

After irradiation, the unknowns, monitors, and standards were loaded into an ultrahigh-vacuum line for argon isotopic analysis. The analytical experiments involved incremental heating of individual crystals using a Photon Machines/Atlex ArF 193 nm excimer laser operated at successively high power levels ranging from 0.8 to 3 W for biotite sample RC01 and 0.6 to 10 W for muscovite sample DC01. Released gasses were purified by passing them over hot and cold SAES NP10 metal alloy 'getters' prior to Ar isotopic analysis with a Nu Instruments *Noblesse* magnetic sector mass spectrometer. For most release steps, signals were measured using an ETP ion counting detector, but a few ^{40}Ar signals were so large that a Faraday detector (fitted with a 10^{11} Ohm resistor) was used. The fully automated laser heating, automated valves operation, and data acquisition was computer controlled using Alan Deino's *MassSpec* software program.

Cooling age results were calculated using Isoplot 3.75 (Ludwig, 2012). Both the biotite and muscovite incremental heating analyses resulted in plateau ages, defined as three or more steps comprising 50% or more of the total ^{39}Ar in a sample, with individual calculated ages that overlap at the 2σ level without propagation of the *J*-value uncertainty (Fleck et al., 1977). The reported plateau dates and their 2σ uncertainties (inclusive of the *J*-value uncertainties) represent the ^{39}Ar-weighted means of the ages of all the steps defining each plateau. We also used the inverse-isochron method (Grove and Harrison, 1996) to determine if there was a presence of excess argon in the biotite of sample RC01.

While the inverse-isochron initially implied the presence of excess argon with a $^{40}Ar/^{36}Ar$ ratio, we removed three heating steps, B, E, and J that were not steps included in the calculation of the plateau age. The removal of these steps resulted in a $^{40}Ar/^{36}Ar$ ratio that lies statistically within the range of the atmospheric ratio of 295.5 and displays a MSWD of 0.65.

5.1.2 (U-Th)/He thermochronology

Using a binocular microscope, individual crystals of clear, euhedral, and apparently inclusion-free zircon and apatite were picked for (U-Th)/He dating from rough concentrates. We report dates for five individual crystals of apatite for sample DC03 and between four and six zircon grains per sample (Tables B2 and B3). Each crystal was measured to establish the necessary parameters for the alpha ejection corrections of the resulting dates using the approach of Farley et al. (1996) for apatite and Hourigan et al. (2005) for zircon. For both minerals, we assumed a homogeneous distribution of U and Th for determining correction factors. The grains were then loaded into small niobium tubes prior to analysis. All helium measurements were made with an Australian Scientific Instruments (ASI) *Alphachron* system, which features a 45 Watt, infrared (980 nm) diode laser for gas extraction and a Balzers *Prisma QMS 200* quadrupole mass spectrometer for isotopic measurements. Gasses including helium were released from apatite by laser heating for five minutes at 9A, and from zircon by laser heating for ten minutes at 20A. The released gasses were mixed with a known quantity of ^{3}He spike in preparation for isotope-dilution analysis, after which the mixture was purified of reactive gasses using a combination of hot and cold metal alloy getters. Along with sample unknowns, we also

analyzed aliquots of Fish Canyon zircon and Durango fluorapatite to monitor system performance, and empty Nb tubes to allow for blank correction of the resulting data.

After ^{4}He analysis, each sample packet was unloaded from the laser chamber and dissolved for U and Th analysis. Apatites were dissolved using 25 µl of 50% nitric (HNO_3) acid that contains a mixed spike of ~5 ng of ^{230}Th and ~15ng of ^{235}U. In contrast, zircons were digested at elevated temperatures and pressures in Parr vessels using concentrated hydrofluoric (HF), nitric (HNO_3), and hydrochloric (HCl) acids mixed with the U+Th spike. After dissolution, samples, together with specially prepared batches of spiked standard solutions, were analyzed for U and Th using a Thermo Scientific *ICAP-Q* inductively coupled, plasma source mass spectrometer.

The He, U, and Th data were used to calculate raw ages using an iterative approach to the (U-Th)/He age equation. Within this calculation, the concentration of ^{235}U is derived from the measured ^{238}U concentration using the known ratio of these isotopes in nature. The raw ages are then corrected for alpha ejection as described above. All uncertainties for ApHe and ZrnHe dates reflect the full propagation of analytical errors, but no errors were assigned to the alpha ejection correction calculations or propagated into the reported uncertainties.

5.2 Results

A biotite ^{40}Ar/^{39}Ar (BtAr) incremental release experiment was conducted on material separated from the Ra Chu sample RC01 (Tables 3.1 and B2; Figure 3.5). Although there was some apparent age variability in the first few steps of the experiment, many contiguous, high-temperature steps – representing 68.1% of the ^{39}Ar released

during the experiment – defined a statistically significant plateau (Fleck et al., 1977) indicative of a 13.39 ± 0.38 Ma BtAr closure age. While excess ^{40}Ar is a commonly encountered problem in Himalayan biotites (Hubbard and Harrison, 1989; Viskupic et al., 2005; Adams et al., 2015; Stübner et al., 2017), it can be difficult to detect and account for unambiguously in many cases due to the fact that high radiogenic yields are common in these biotites. The RC01 biotite, however, shows significant distribution on a $^{36}Ar/^{40}Ar$ vs. $^{39}Ar/^{40}Ar$ correlation diagram (Figure 3.5). Despite some scatter on such a diagram, the distribution is suggestive of an initial $^{40}Ar/^{36}Ar$ ratio close to atmospheric, so we infer that the ca. 13.4 Ma plateau date is robust.

Tables 3.1 and B2 show the (U-Th)/He zircon (ZrnHe) data for RC01. (We were unable to identify and separate sufficiently clean and large apatite crystals from this sample for (U-Th)/He analysis.) ZrnHe dates for five individual crystals range between 10.62 ± 0.33 Ma and 13.92 ± 0.41 Ma. This range is greater than would be expected from analytical imprecision alone. Unfortunately, attempts to identify outliers using the Hampel identifier method (Pearson, 2011) failed, so we conservatively estimate the ZrnHe closure date for RC01 as 11.9 ± 1.3 Ma, the inverse variance-weighted standard deviation of the weighted mean as magnified by the square root of the mean squared weighted deviation (MSWD) in accordance with common practice (Wendt and Carl, 1991).

DC01 muscovite $^{40}Ar/^{39}Ar$ step-heating age spectra can be found in Figure 3.5 and Tables 3.1 and B1. The DC01 muscovite yielded a plateau age of 13.693 ± 0.092 Ma and like the muscovite release spectra of the Rongbuk samples, displayed uncomplicated behavior. Based on the ample availability of micas, particularly muscovite, in the

Rongbuk valley samples, we expected to find similar yields in the Ra Chu and Dzakar Chu samples. Unfortunately, the leucogranites and calc-silicates collected from the footwall rocks at Ra Chu did not contain any muscovite and provided only biotite. Sample DC01 from Dzakar Chu produced muscovite, however, the other Dzakar Chu samples either did not contain micas or if they did, the biotite grains were unsuitable to send for irradiation.

Inverse-variance weighted mean ZrnHe for the Dzakar Chu samples DC01, DC02, and DC03 can be found in Tables 3.1 and B2. The Dzakar Chu ZrnHe dates are also over-dispersed. The Hampel method identified two individual ZrnHe dates from sample DC03: z04 (8.59 ± 0.26 Ma) and z06 (8.31 ± 0.25 Ma). Finding no other outliers, we multiplied each weighted mean's date 2σ uncertainties by the square-root of their individual MSWD values. ZrnHe dates for the Dzakar Chu samples range from 12.16 ± 0.35 Ma to 8.67 ± 0.54 Ma.

For all Ra Chu and Dzakar Chu samples, we plotted the individual ZrnHe dates of each sample against effective uranium (eU) values (where eU = 0.235[Th] + [U]) to determine if radiation damage could explain the younger ZrnHe dates, even though ZrnHe analyses from Rongbuk indicated no correlation between the cooling ages and eU (Guenthner et al., 2013; Schultz et al., 2017). These samples also did not display a correlation between cooling age and eU.

The ApHe inverse-variance weighted mean for five individual apatite grains in sample DC03 is 10.2 ± 2.6 Ma and can be found in Tables 3.1 and B3. The Hampel method identified no outliers and thus we expanded the uncertainty of its weighted mean as we did for the ZrnHe dates described above.

As has been observed in other low-angle detachment systems (e.g. Stockli et al., 2001; Brady, 2002; Brichau, 2004; Stockli, 2005; Evans et al., 2015), we expected to observe a younging trend in thermochronometric cooling ages from the Rongbuk valley down the dip of the detachment to the Ra Chu and Dzakar Chu sampling collection sites over ten kilometers to the north. Indeed, the MsAr plateau age for sample DC01 (13.963 ± 0.092 Ma) is younger than the youngest MsAr plateau age revealed for the Rongbuk valley (14.400 ± 0.060 Ma; Schultz et al. (2017)) even taking into account the uncertainties of each plateau age. ZrnHe cooling ages from Dzakar Chu samples DC01 and DC02 are also younger than what was revealed from the Rongbuk leucogranites to the south, although the weighted mean ZrnHe dates from the Ra Chu sample and sample DC03 compare very well with ZrnHe cooling ages from the Rongbuk samples, making our assessment of a down-dip younging of cooling ages more nebulous. One explanation for these contradicting ZrnHe cooling ages is that slip on this particular structure was very rapid, as shown by the thermal-kinematic modeling results of Schultz et al. (2017), resulting in nearly horizontal isotherms, differing from other low-angle normal fault systems with slower slip rates. A second potential causation for both younger and older ZrnHe cooling ages in the Ra Chu and Dzakar Chu samples is the possible enrichment of parent isotopes around the rims of these zircon crystals, as was reported by Orme et al. (2015) for zircons in the Rongbuk valley. As explained in Hourigan et al. (2005), zircon crystal rims with much higher eU values than the core may lead to an underestimate of the true ZrnHe date.

6. 2D Thermal-Kinematic Modeling

The addition of data from the Ra Chu and Dzakar Chu exposures to the Schultz et al. (2017) thermochronological dataset invites multi-dimensional thermal-kinematic modeling, the results of which can be compare with the simpler 1D modeling approach used by Schultz et al. (2017).

6.1 Methods

Our 2D approach took advantage of the widely used *Pecube software environment* of Braun (2003) and Braun et al. (2012). *Pecube* solves the three-dimensional advection-diffusion equation to predict thermochronometer cooling ages. The version of *Pecube* that we employed also incorporates the Neighborhood Algorithm (NA) presented in Sambridge (1999), which searches for optimal values of given parameters of the model that will minimize a misfit function defined by the difference between observed ages and predictions (Equation 3.1):

$$\Phi = \frac{1}{N}\sqrt{\sum_{i=1}^{N}\frac{(\alpha_{i,pred}-\alpha_{i,obs})^2}{\sigma_i^2}} \quad (3.1)$$

Prior values for our 2D thermal-kinematic inversion modeling are presented in Table 3.2 and the overall model setup can be seen in Figure 3.4. An ASTER Global Digital Elevation Model V002 (GDEM) covering the entire Everest region and valleys to the north (86.6˚E, 28.4˚N; 87.4˚E, 27.9˚N) was incorporated into *Pecube*. The model depth was set to 35 kilometers and the model ran through a total of 11 time steps based on our observed thermochronologic data. As is true for most thermal-kinematic models,

this version of *Pecube* requires a "spin-up" time. We set this to 40 Ma because earlier trials in which we prescribed a later spin-up time (i.e. 25 Ma), the model did not have enough time to adjust to the given scenario set by the thermal parameters. Following this time step, we had a single 5 million-year time step from 20 to 15 Ma. We set the topography half its value for the 40 and 20 Ma time steps as *Pecube* requires a similar start-up adjustment for topography. We implemented the topography as it appears today for every time step after 20 Ma, which we believe to be a sound decision based on the paleotopographic evidence presented in Gébelin et al. (2013) that argued the Mount Everest massif was close to its present-day elevation by *ca.* 15 to 13 Ma. After 15 Ma, we set the model to run one million-year time steps until 7 Ma. A final time step was set from 7 Ma to the present day as we do not have any thermochronological constraints following ApHe closure at *ca.* 8 Ma.

We modeled the STDS as a single shear surface, setting the intersection of the detachment with the surface to be [87.4˚E, 27.94˚N; 86.6˚E, 27.94˚N], constrained by its southern exposure on the Everest summit and the longitudinal range of the footwall exposures down-dip at the Ra Chu and Dzakar Chu (Figure 3.4). The Indus-Tsangpo suture zone marks the northern boundary of the detachment.

Pecube models fault movement as one half-space moving with respect to the other. We decided that the hanging wall should remain fixed, with displacement entirely due to the southward motion of the footwall. This assumption is supported by several former studies (Walker et al., 1999; Vannay and Grasemann, 2001; Searle et al., 2003; Law et al., 2004; Jessup et al., 2006; Cottle et al., 2007; Schultz et al., 2017), all of which interpreted the STDS as a passive roof fault to the southward-extruding GHS.

Based on what we know from the previous work at Rongbuk, we set two time intervals for slip on the detachment: T1 to reflect the duration of ductile deformation and T2 to encompass slip during brittle displacement. We set T1 to be between *ca.* 20 and 15.6 Ma, based on the geochronologic constraints in Cottle et al. (2015). We acknowledge that these constraints are only truly valid for the movement of footwall at Rongbuk and are only estimates for the other two localities. Cottle et al. (2007) pointed out that mylonite fabric development had ended by *ca.* 20.4 Ma at Dzakar Chu, however, there is no upper limit for that estimate. Thus, the amount of ductile deformation revealed by the modeling results will be treated as a minimum estimate. We set the timing for brittle displacement, T2, to range between 15.5 and 9 Ma, based on our thermochronological results and those of Schultz et al. (2017).

Pecube allows the user to implement changes in the dip angle of a fault and although the mylonitic fabric at Dzakar Chu dips more steeply than at Rongbuk, there is a possibility that the detachment rotated after displacement (Cottle et al., 2007). As there is no such evidence for a change in geometry down-dip of the detachment elsewhere in the region, we applied a constant dip to the detachment (Figure 3.4). Unfortunately, it is difficult to test different geometric scenarios as the *Pecube* software only allows the user to set the geometry of the structure before the model run begins. *Pecube* does, however, permit the variation of the structure's dip. We set the priors for the northernmost depth of the detachment to vary between 1 and 20 km for the inversion run to try to determine the depth of the detachment, however, this was not a primary goal of this study.

For the inversion, we ran 40 samples with 24 iterations for a total of 1000 models. We decided that the basal temperature and heat production should be free parameters

during the inversion runs as the published values for these parameters range widely. Estimated radiogenic heat production values for GHS rocks range between *ca.* 3 and 0.8 $\mu W/m^3$ (Ray et al., 2007; Whipp et al., 2007). We set the basal temperature to range between 600 and 1000˚C.

6.2. Predicted versus observed thermochronological data from forward modeling

Before beginning the inversion, we ran a forward model using the 1D thermal parameters in Schultz et al. (2017) to determine how thermochronological cooling ages predicted by *Pecube* would compare to the observed cooling ages. The input thermal parameter constraints from Schultz et al. (2017) are indicated in Table 3.4. For the forward model, we specified that ductile slip on the detachment should occur between *ca.* 20 and 15.6 Ma and the slip rate to be *ca.* 23 km/Ma – the average slip rate that would produce the average total ductile displacement estimate in Law et al. (2011). Based on the 1D thermal-kinematic results of Schultz et al. (2017), we specified the interval *ca.* 15.4 to 13 Ma for brittle displacement to occur the detachment and a faster slip rate of *ca.* 33 km/Ma. We also set the detachment dip to 10˚. The results of the forward model are presented in Table 3.3 and Figure 3.6. There is general agreement with the predicted and observed cooling ages, although the predicted dates for MsAr are ca. 0.5 to 1 Ma older than published MsAr plateau ages and the MsAr plateau age of sample DC01. Similarly, the observed plateau age for the RC01 biotite sample is slightly younger than the predicted BtAr cooling age. The predicted ZrnHe dates are also somewhat older than the observed dataset, although half of the modeled cooling ages fall within the 2σ uncertainties of the observed ZrnHe dates. Two of the exceptions, the *ca.* 24.6 Ma

predicted ZrnHe dates for samples DC01 and DC03 were unrealistic predictions made by the model, probably due to the fact that the simple, planar fault geometry we implemented would predict that samples at these locations would be in the hanging wall, rather than in the footwall where they were actually collected. Two of the predicted ApHe cooling ages (R01 and DC03) are within uncertainty of the observed dates, however the *ca.* 10.2 Ma predicted ApHe cooling age for sample R02 is *ca.* 2.4 Ma older than what is observed. Given these discrepancies, we also used the NA inversion option in *Pecube* software (see Section 6.1) to determine what thermal and structural parameters might yield better fits to the data.

6.3 2D thermal-kinematic NA inversion modeling results

The results of the NA inversion are shown in Figure 3.7 as six scatterplots in the parameter space. Each symbol represents a forward model and the type of symbol reveals the quality of fit to the data (using the misfit Φ). The inversion run resulted in misfit values between 5345 and 2.82 (see Equation 3.1). The ranges of parameter values revealing the lowest misfits from the inversion run can be found in Table 3.4 and the best fit model is indicated by a star on each of the plots in Figure 3.7. Results reveal a wide range of acceptable values for the temperature at the Moho (*ca.* 700 to 1000˚C) and high estimates for radiogenic heat production (*ca.* 2.6 to 1.48 $\mu W/m^3$). The best-fit northernmost detachment depth at the location of the suture zone is *ca.* 3.2 km below sea level, resulting in a very shallow detachment dip of *ca.* 5˚, which agrees with field observations that the detachment dips no more than 10˚ (Figure 3.7B). Preliminary best-fit slip rates for T1 (*ca.* 20 to 15.6 Ma) during ductile deformation range from *ca.* 19 to

50 km/Ma, with total ductile displacement estimates ranging from *ca.* 84 to 219 km (Figure 3.7D and E). Results suggest extension during lower-temperature brittle deformation (T2) occurred following MsAr closure at *ca.* 15.5 Ma until *ca.* 13 Ma with best-fit average slip rates even faster for those during ductile deformation ranging between *ca*. 33 and 48 km/Ma (Figure 3.7C and D). Best-fit estimates for total brittle slip from *ca.* 15.4 to 13 Ma are between *ca.* 83 and 119 km (Figure 3.7F). Adding the slip estimates for T1 and T2 implies *ca.* 167 to 338 km of total displacement on the STDS.

7. Discussion

7.1 Comparing 1D and 2D modeling approaches

New MsAr, BtAr, ZrnHe, and ApHe datasets from the Ra Chu and Dzakar Chu combined with the Rongbuk thermochronology results of Schultz et al. (2017) and 2D thermal-kinematic modeling indicate at least *ca.* 84 km of ductile displacement occurred on the STDS from *ca.* 20 to 15.6 Ma. Ductile deformation on the detachment was followed by at least *ca.* 83 km slip in the ductile-brittle to brittle realm from *ca.*15.4 to 13 Ma. Added together, these estimates suggest a minimum total displacement on the STDS of *ca.* 167 to 338 km in the Everest region.

The STDS slip histories revealed by our multidimensional modeling are directly comparable to those in Schultz et al. (2017) that suggested *ca.* 36 to 119 km of brittle displacement took place on the Qomolangma detachment in the Rongbuk valley between *ca.* 15.4 and 13 Ma based on exhumation histories produced by 1D thermal-kinematic modeling. The similarities of the results between the 2D modeling method presented here and 1D modeling scheme originally introduced by Thiede and Ehlers (2013) and used in

Schultz et al. (2017) suggest that, when tectonic denudation is rapid enough beneath a very shallowly dipping detachment, simpler 1D models may adequately reflect the basic physics of exhumation and cooling (Table 3.4). Previous workers, however, have emphasized the generally improved representation of orogenic thermal structures provided by multi-dimensional models (Whipp et al., 2007; Herman et al., 2010). Whipp et al. (2007), for example, employed a 3D thermal-kinematic model to explore exhumation in the Marsiyangdi region of central Nepal and argued that, because of extreme topography and non-vertical exhumation pathways, 1D-models could produce more misleading results than multi-dimensional models. We certainly agree that the effects of topography and lateral heat advection due to faulting can affect the thermal evolution of samples significantly in orogenic environments, but the degree to which these complications matter when denudation is dominantly controlled by tectonic denudation depends critically on the exhumation rate dictated by the slip rates and geometries of the major detachments involved (Ruppel et al., 1988). Apparently, the combination of a very shallow dip of the STDS and the rapid exhumation of the footwall prevented formation of a geometrically complex thermal field in our study area in southern Tibet. When one-dimensional modeling is a viable option for at least obtaining a first-order understanding of the thermal evolution of a region, it has a clear practical advantage over two-dimensional modeling: each of our 1D models developed for the Rongbuk samples (Schultz et al., 2017) represent hundreds of thousands of simulations that were completed over the course of a day, while the 1000 multidimensional models presented here required many weeks of computational time.

7.2 Tectonic significance

The 1D thermal-kinematic modeling results in Schultz et al. (2017) and results of the *Pecube* NA inversion run offer strong arguments that the STDS was a tectonically significant structure in the Miocene evolution of the Himalaya and likely accommodated a minimum of 160 km of slip. Observed MsAr dates from the region generally agree with predicted dates from forward modeling using *Pecube* and indicate closure through the *ca.* 490˚C isotherm from *ca.* 15.8 to 14.2 Ma, with slightly younger predicted MsAr and BtAr dates at Ra Chu and Dzakar Chu. Inversion modeling results suggest high-temperature detachment slip rates over the period of *ca.* 20 to 15.6 Ma were anywhere from *ca.* 19 to 50 km/Ma, the average of which are comparable to the ductile slip rates implied by the estimates of Law et al. (2011). Rapid exhumation of the footwall slowed drastically after ZrnHe closure at *ca.* 13 Ma, as indicated in both the observed ZrnHe bedrock dataset as well as the ZrnHe modeled dates. NA inversion results imply that brittle slip on the detachment, with more rapid slip rates between *ca.* 33 and 48 km/Ma, likely occurred over the period of *ca.* 15.4 to 13 Ma.

Estimated slip rates for the STDS, during both high-temperature ductile displacement and low-temperature brittle slip, are reasonable; they are, for example, comparable to moderate sea-floor spreading half-rates (Müller et al., 2008). However, we note that previously estimated slip rates on Basin and Range detachments are typically an order of magnitude lower (Brady, 2002; Evans et al., 2015). One reason for this discrepancy may be the unusual tectonic significance of the STDS. Unlike detachment systems in continental regions where the entire lithosphere is in extension, the STDS served as a roof structure for an evolving infrastructure within a collisional orogen

(Hodges, 2016), likely originating as a consequence of the dramatic gradient in gravitational potential energy between a Miocene Tibetan Plateau and the much lower elevation Indian craton to the south (Hodges et al., 2001).

The results of both the 1D (Schultz et al., 2017) and 2D thermal-kinematic modeling indicate substantial amounts of displacement on the STDS, possibly over 300 km, and favor the interpretation that the STDS represents the top boundary of the southward-extruding GHS (Hodges et al., 2001; Jamieson et al., 2004; Cottle et al., 2007). The timing of the cessation of slip at *ca.* 13 Ma is consistent with other estimates for the end of STDS displacement to the east in Sikkim and Bhutan (Leloup et al., 2010; Cooper et al., 2012, 2013; Kellett et al., 2013; Braun et al., 2016).

8. Conclusions

New and previously published thermochronological datasets including MsAr, BtAr, ZrnHe and ApHe, paired with results from multidimensional thermal-kinematic modeling of the data, constrain the Miocene slip history of the STDS in the Everest region of south-central Tibet. NA inversion modeling of the thermochronological datasets and free thermal parameters of the GHS footwall in this region reveal a minimum of *ca.* 84 to 219 km of ductile deformation taking place between *ca.* 20 and 15.6 Ma. Models with the lowest misfit values indicate that the transition from ductile to brittle slip on the detachment likely occurred following MsAr closure at *ca.* 15.4 Ma and that total brittle displacement on the STDS was *ca.* 83 to 119 km, almost as much movement as during ductile shearing. High radiogenic heat production values between *ca.* 2.6 and 1.48 $\mu W/m^3$ accompanied movement on the shallowly dipping detachment. STDS displacements this

large favor tectonic models that invoke channel flow of the Greater Himalayan sequence, with the STDS acting as the upper boundary. Models that suggest the STDS was a minor structure in the evolution of Himalayan tectonics are incompatible with our results (Yin, 2006; Webb et al., 2007; Webb, 2013; He et al., 2015).

9. Acknowledgments

This work was supported by National Science Foundation Tectonics Program grants EAR1007929 and EAR1346360 to K.V.H. Many thanks to Ding Lin (Institute of Tibetan Plateau Research), Paul Kapp (University of Arizona), and Ross Waldrip (University of Arizona) for their exceptional logistical assistance during fieldwork in Tibet. Many thanks to Jean Braun (Université Joseph Fourier – Grenoble, France) for guidance with the *Pecube* software. Thanks also to Adam Forte (Arizona State University) for great help and insightful discussions regarding the *Pecube* modeling setup.

10. Figure Captions

Figure 3.1. Map of the central Himalaya showing the E-W striking STDS. The trace of the detachment is after Hodges (2000).

Figure 3.2. Generalized geologic map of the Everest region in south-central Tibet showing the Rongbuk valley sampling localities of Schultz et al. (2017) and the sample collection sites of this study at Ra Chu and Dzakar Chu. The dark shading indicates the units of the Greater Himalayan Sequence, separated from the Tibetan Sedimentary Sequence above by the STDS (Qomolangma detachment at Rongbuk). Shapes and colors

of symbols indicated the chronometric systems analyzed in each sample. Abbreviations: MsAr = muscovite $^{40}Ar/^{39}Ar$, BtAr = biotite $^{40}Ar/^{39}Ar$, ZrnHe = zircon (U-Th)/He, and ApHe = apatite (U-Th)/He.

Figure 3.3. Field photographs of the STDS footwall shear zones at Ra Chu (3.3A and B) and Dzakar Chu (3.3C and D). The Ra Chu section exposes ~30m of calc-silicate and the tourmaline leucogranites. To the west is the spectacular ~1000 m exposure of the STDS zone at Dzakar Chu, consisting of biotite gneisses and leucogranitic sills and dykes of all sizes.

Figure 3.4. Forward and inversion 2-D thermal-kinematic modeling set-up. DEM (ASTER Global Digital Elevation Model V002) of the Everest region (86.6˚E, 28.4˚N; 87.4˚E, 27.9˚N) with the top layer indicating changes in elevation. The depth of the model is 35 km and the basal temperature was initially set to 650°C for the forward models, though was allowed to vary during the inversion. White circles indicate Rongbuk sampling localities of Schultz et al. (2017). The orange circle shows the locality of sample RC01 and the green circles to the west are the sample sites at Dzakar Chu.

Figure 3.5. $^{40}Ar/^{39}Ar$ results for biotite sample RC01 and muscovite sample DC01. The release spectra for DC01 and RC01 reveal plateau ages (all uncertainties quoted at 2σ) and the inverse-isochron for RC01 provides a $^{40}Ar/^{36}Ar$ ratio within statistical uncertainty of atmosphere and a low MSWD.

Figure 3.6. Plot of all measured and modeled cooling ages. Measured ages for MsAr, BtAr, ZrnHe and ApHe are represented by colored symbols (MsAr, hexagon; BtAr, square; ZrnHe, triangle; ApHe, circle) and error bars showing their 2σ uncertainties. Colored cross symbols represent the modeled cooling age resulting from forward modeling using the 1D parameters.

Figure 3.7. Results of the Neighborhood Algorithm (NA) inversion as scatter diagrams of the misfit between observations and predictions. Each symbol corresponds to a forward model run (1000 runs total). The position of the symbol is determined by the value of the model parameters (see Table 3.2). The symbol shape is proportional to the value of the misfit. Circles: misfits less than 3; Triangles: misfits between 3 and 20; Squares: misfits between 20 and 100; Diamonds: misfits greater than 100. The best-fit models are indicated by the stars.

11. References

Adams, B.A., Hodges, K.V., Whipple, K.X., Ehlers, T.A., van Soest, M.C., and Wartho, J. (2015). Constraints on the tectonic and landscape evolution of the Bhutan Himalaya from thermochronometry, *Tectonics*. *32*(6), 1329-1347.

Beaumont, C., Jamieson, R. A., Nguyen, M.H., and Lee, B. (2001). Himalayan tectonics explained by extrusion of a low-viscosity crustal channel coupled to focused surface denudation. *Nature, 414*, 738-742.

Brady, R.J. (2002). Very high slip rates on continental extensional faults: new evidence from (U-Th)/He thermochronometry of the Buckskin Mountains, Arizona. *Earth and Planetary Science Letters, 197*, 95-104.

Braun, J. (2003). Pecube: A new finite-element code to solve the 3D heat transport equation including the effects of a time-varying, finite amplitude surface topography. *Computers & Geosciences*, *29*(6), 787-794.

Braun, J. (2016). Strong imprint of past orogenic events on the thermochronological record. *Tectonophysics, 683,* 325-332.

Braun, J., van der Beek, P., Valla, P., Robert, X., Herman, F., Glotzbach, C., Pedersen, V., Perry, C., Simon-Labric, T., and Prigent, C. (2012). Quantifying rates of landscape evolution and tectonic processes by thermochronology and numerical modeling of crustal heat transport using PECUBE. *Tectonophysics*, *524–525*, 1-28.

Brichau, S. (2004). Constraining the tectonic evolution of extensional fault systems in the Cyclades (Greece) using low-temperature thermochronology. *PhD Dissertation*, University of Mainz and University of Montpelier.

Burchfiel, B.C., and Royden, L.H. (1985). North-south extension within the convergent Himalayan region. *Geology*, *13,* 679-682.

Burchfiel, C. B., Chen, Z., Hodges, K. V., Liu, Y., Royden, L.H., Deng, C., and Xu J. (1992). The South Tibetan detachment system, Himalayan orogen: extension contemporaneous with and parallel to shortening in a collisional mountain belt. *Geologic al Society of America Special Paper*, *269*, 41 p.

Burg, J.P. (1983). *Carte Geologique du Sud du Tibet*. Ministry of Geology, Peking and CNRS, Paris.

Burg J. P. and Chen, G. (1984). Tectonics and structural formation of southern Tibet, China. *Nature, 311,* 219-223.

Caby, R. Pêcher, A., and Le Fort, P. (1983). Le grand chevauchement central himalayen: nouvelles données sur le métamorphisme inverse à la base de la Dalle du Tibet. *Revue de Géologie Dynamique et de Géographie Physique*, *24,* 89-100.

Carosi, R., Lombardo, B., Molli, G., Musumeci, G., and Pertusati, P.C. (1998). The South Tibetan detachment system in the Rongbuk Valley, Everest region. Deformation features and geological implications. *Journal of Asian Earth Sciences*, *16*, 299–311.

Carosi, R., Lombardo, B., Musumeci, G., and Pertusati, P.C. (1999). Geology of the Higher Himalayan Crystallines in Khumbu Himal (Eastern Nepal). *Journal of Asian Earth Sciences*, *17*, 785-803.

Clift, P., Hodges, K.V., Heslop, D., Hannigan, R., Hoang, L.V., Calves, G. (2008). Correlation of Himalayan exhumation rates and Asian monsoon intensity. *Nature Geoscience*, *1,* 875-880.

Cooper, F. J., Adams, B. A., Edwards, C. S., and Hodges, K. V. (2012). Large normal-sense displacement on the South Tibetan fault system in the eastern Himalaya. *Geology*, *40*(11), 971-974.

Cooper, F. J., Hodges, K.V., and Adams, B.A. (2013). Metamorphic constraints on the

character and displacement of the South Tibetan fault system, central Bhutanese Himalaya. *Lithosphere*, *5*, 67-81.

Corthouts, T. L., Lageson, D. R., and Shaw, C. A. (2016). Polyphase deformation, dynamic metamorphism, and metasomatism of Mount Everest's summit limestone, east central Himalaya, Nepal/Tibet. *Lithosphere*, *8*, doi: 10.1130/l1473.1131.

Cottle, J. M., Jessup, M.J., Newell, D.L., Searle, M.P., Law, R.D., and Horstwood M.S.A., (2007). Structural insight into the ductile evolution of an orogen-scale detachment: the South Tibetan detachment system, Dzakaa Chu section, eastern Himalaya. *Journal of Structural Geology*, *29*, 1781-1797.

Cottle, J. M., Searle, M. P., Jessup, M. J., Crowley, J. L., and Law, R. D. (2015). Rongbuk re-visited: Geochronology of leucogranites in the footwall of the South Tibetan Detachment System, Everest Region, Southern Tibet. *Lithos*, *227*, 94-106.

Evans, S. L., Styron, R.H., van Soest, M.C., Hodges, K.V., and Hanson, A.D. (2015). Zircon and apatite (U-Th)/He evidence for Paleogene and Neogene extension in the Southern Snake Range, Nevada, USA. *Tectonics*, *34*(10), 2142-2164, doi: 10.1002/2015TC003913.

Farley, K.A., Wolf, R.A., and L.T. Silver, L.T. (1996). The effects of long alpha-stopping distances on (U-Th)/He ages. *Geochimica et Cosmochimica Acta*, *60*, 4223-4229.

Fleck, R. J., Sutter, J.F., and Elliot, D.H. (1977). Interpretation of discordant $^{40}Ar/^{39}Ar$ age spectra of Mesozoic tholeiites from Antarctica. *Geochimica et Cosmochimica Acta*, *41*, 15-32.

Gaetani, M., and Garzanti, E. (1991). Multicyclic history of the northern India continental margin (Northwestern Himalaya). *Bulletin of the American Association of Petroleum Geologists*, *75*, 1427-1446.

Gebelin, A., Mulch, A., Teyssier, C., Jessup, M. J., Law, R. D., and Brunei M. (2013). The Miocene elevation of Mount Everest. *Geology*, *41*(7), 799-802.

Grove, M. and Harrison, T.M. (1996). $^{40}Ar^*$ diffusion in Fe-rich biotite. *American Mineralogist*, *81*, 940-951.

Grujic, D., Casey, M., Davidson, C., Hollister, L. S., Kündig, R., Pavlis, R., and Schmid, S. (1996). Ductile extrusion of the Higher Himalayan crystalline in Bhutan: evidence from quartz microfabrics, *Tectonophysics*, *260*, 21-43.

Guenthner, W.R., Reiners, P.W., Ketcham, R.A., Nasdala, L., and Geister, G. (2013). Helium diffusion in natural zircon: Radiation damage, anisotropy, and the interpretation of zircon (U-Th)/He thermochronology. *American Journal of Science*, *313*, p. 145 – 198.

He, D., Webb, A.A.G., Larson, K.P., Martin, A.J., and Schmitt, A.K. (2015). Extrusion vs. duplexing models of Himalayan mountain building 3: duplexing dominates from the Oligocene to Present. *International Geology Review*, *57*, 1-27.

Herman, F., Copeland, P., Avouac, J-P., Bollinger, L., Mahéo, G., Le Fort, P., Rai, S., Foster, D., Pêcher, A., Stüwe, K., and Henry, P. (2010). Exhumation, crustal deformation, and thermal structure of the Nepal Himalaya derived from the inversion of thermochronological and thermobarometric data and modeling of the topography. *Journal of Geophysical Research – Solid Earth, 115*, doi:B0640710.1029/2008jb006126.

Hodges, K. V. (2000). Tectonics of the Himalaya and southern Tibet from two perspectives. *Geological Society of America Bulletin*, *112*, 324-350.

Hodges, K. V. (2006). A synthesis of the Channel Flow-Extrusion hypothesis as developed for the Himalayan-Tibetan orogenic system, in *Channel Flow, Ductile Extrusion, and Exhumation of Lower-Middle Crust in Continental Collision Zones*, edited by R. Law, M. Searle and L. Godin, 71-90, Geological Society Special Publication 268, London.

Hodges, K.V. (2016). Crustal decoupling in collisional orogenesis: Examples from the East Greenland Caledonides and Himalaya. *Annual Review of Earth and Planetary Sciences, 44*, 685-708.

Hodges, K.V., and Walker, J.D. (1992). Extension in the Cretaceous Sevier orogeny, North American Cordillera. *Geological Society of America Bulletin*, *104*, 560-569.

Hodges, K. V., Parrish, R.R., Housh, T.B., Lux, D.R., Burchfiel, B.C., Royden, L.H., and Chen, Z. (1992). Simultaneous Miocene extension and shortening in the Himalayan orogen. *Science*, *258*, 1466–1470.

Hodges, K. V., Bowring, S., Davidek, K., Hawkins, D., and Krol, M. (1998). Evidence for rapid displacement on Himalayan normal faults and the importance of tectonic denudation in the evolution of mountain ranges. *Geology*, *26*, 483–486.

Hodges, K. V., Hurtado, J. M., and Whipple, K. X. (2001). Southward extrusion of Tibetan crust and its effect on Himalayan tectonics. *Tectonics*, *20*(6), 799-809.

Hourigan, J.K., Reiners, P.W., and Brandon, M.T. (2005). U-Th zonation dependent alpha-ejection in (U-Th)/He chronometry. *Geochimica et Cosmochimica Acta, 69*, 3349-3365.

Hubbard, M., and Harrison, T.M. (1989). $^{40}Ar/^{39}Ar$ age constraints on deformation and metamorphism in the Main Central Thrust zone and Tibetan Slab, eastern Nepal Himalaya. *Tectonics*, *8*(4), 865 – 880.

Jamieson, R.A., Beaumont, C., Medvedev, S., and Nguyen, M.H. (2004). Crustal channel flows: 2. Numerical models with implications for metamorphism in the Himalayan-Tibetan orogeny. *Journal of Geophysical Research, 109*, B06406, doi:10.1029/2003JB002811.

Jessup, M. J., Law, R. D., Searle, M. P. and Hubbard, M.S. (2006). Structural evolution and vorticity of flow during extrusion and exhumation of the Greater Himalayan Slab, Mount Everest Massif, Tibet/Nepal: implications for orogen-scale flow partitioning, *in Channel Flow, Ductile Extrusion, and Exhumation of Lower-Middle Crust in Continental Collision Zones*, edited by Law, R., Searle, M., and Godin, L., London, Geological Society Special Publication 268, p. 79-414.

Jessup, M. J., Cottle, J.M., Searle, M.P, Law, R.D., Newell, D.L., Tracy, R.J., and Waters, D.J. (2008). PT-t-D paths of Everest Series schist. Nepal, *Journal of Metamorphic Geology*, *26*, 717–739.

Jessup, M.J. and Cottle, J.M. (2010). Progression from South-Directed Extrusion to Orogen-Parallel Extension in the Southern Margin of the Tibetan Plateau, Mount Everest Region, Tibet. *Journal of Geology*, *118*, 467-486.

John, B.E., and Foster, D.A. (1993). Structural and thermal constraints on the initiation angle of detachment faulting in the southern Basin and Range: The Chemehuevi Mountains case study. *Geologic Society of America Bulletin, 105*, 1091-1108.

Kellett, D.A., Grujic, D., Coutand, I., Cottle, J., and Mukul M. (2013). The South Tibetan detachment system facilitates ultra rapid cooling of granulite-facies rocks in Sikkim Himalaya. *Tectonics*, *32*, 252 – 270.

Law, R.D., Searle, M.P., and Simpson, R.L. (2004). Strain, deformation temperatures and vorticity of flow at the top of the Greater Himalayan Slab, Everest Massif, Tibet. *Journal of the Geological Society of London*, *161*, 305-320.

Law, R.D., Searle, M.P., and Godin, L., (Eds). (2006). Channel Flow, Ductile Extrusion and Exhumation in Continental Collision Zones. *Geological Society of London Special Publication, 268,* London. 632 pp.

Law, R.D., Jessup, M.J., Searle, M.P., Francis, M.K., Waters, D.J., and Cottle, J.M. (2011). Telescoping of isotherms beneath the South Tibetan Detachment System, Mount Everest Massif. *Journal of Structural Geology*, *33*, 1569-1594.

Le Fort, P., Cuney, M., Deniel, C., France-Lanord, C., Sheppard, S.M.F., Upreti, B.N., and Vidal, P. (1987). Crustal generation of Himalayan leucogranites. *Tectonophysics*, *134*, 39-57.

Leloup, P.H., Maheo, G., Arnaud, N., Kali, E., Boutonnet, E., Liu, D., Xiaohan, L., and Haibing, L. (2010). The South Tibet detachment shear zone in the Dinggye area Time constraints on extrusion models of the Himalayas. *Earth and Planetary Science Letters*, *292*, 1-16.

Lombardo, B., Pertusati, P., and Borghi S., (1993). Geology and tectonomagmatic evolution of the eastern Himalaya along the Chomolungma-Makalu transect, in *Himalayan Tectonics*, edited by P. J. Treloar and M. P. Searle, pp. 341-355, Geological Society Special Publication, 47, London.

Long, S.P., Thomson, S.N., Reiners, P.W., and Di Fiori, R.V. (2015). Synorogenic extension localized by upper-crustal thickening: An example from the Late Cretaceous Nevadaplano. *Geology, 43*(4), 351-354.

Ludwig, K.R. (2012). *User's manual for Isoplot 3.75: a geochronological toolkit for Microsoft Excel* (Vol. 5): Kenneth R. Ludwig.

Müller, R. D., Sdrolias, M., Gaina, C., and Roest, W.R. (2008). Age, spreading rates, and spreading asymmetry of the world's ocean crust. *Geochemistry Geophysics Geosystems*, *9*, doi: 10.1029/2007gc001743.

Murphy, M. A. and Harrison, T.M. (1999). Relationship between leucogranites and the Qomolangma Detachment in the Rongbuk Valley, South Tibet. *Geology*, *27*(9), 831-834, doi:10.1130/0091-7613(1999)027<0831:RBLATQ>2.3.CO;2.

Myrow, P. M., Hughes, N.C., Searle, M.P., Fanning, C.M., Peng, S.C., and Parcha, S.K. (2009). Stratigraphic correlation of Cambrian-Ordovician deposits along the Himalaya: Implications for the age and nature of rocks in the Mount Everest region. *Geological Society of America Bulletin*, *121*(3-4), 323-332.

Najman, Y., Appel, E., Boudagher-Fadel, M., Bown, P., Carter, A., Garzanti, E., Godin, L., Han, J.T., Liebke, U., Oliver, G., Parrish, R., and Vezzoli, G. (2010). Timing of India-Asia collision: Geological, biostratigraphic, and palaeomagnetic constraints. *Journal of Geophysical Research-Solid Earth*, *115*, doi: 10.1029/2010jb007673.

Nelson, K.D., Zhao, W., Brown, L.D., Kuo, J., Che, J., Xianwen, L., Klemperer, S., Makovsky, Y., Meissner, R., Mechie, J., Kind, R., Wenzel, F., Ni, J., Nabelek, J., Chen, L., Handong, T., Wenbo, W., Jones, A.G., Booker, J., Unsworth, N., Kidd, W.S.F., Hauk, M., Alsdorf, D., Ross, A., Cogan, M., Wu, C., Sandvol, E.A., and Edwards, M. (1996). Partially molten middle crust beneath southern Tibet: Synthesis of Project INDEPTH Results. *Science*, *274*, 1684-1688.

Orme, D.A., Reiners, P.W., Hourigan, J.K., and Carrapa, B. (2015). Effects of inherited cores and magmatic overgrowths on zircon (U-Th)/He ages and age-eU trends from Greater Himalaya sequence rocks, Mt. Everest region, Tibet. *Geochemistry, Geophysics, Geosystems*, DOI 10.1002/2015GC005818

Parrish, R. R., and Hodges, K.V. (1996). Isotopic constraints on the age and provenance of the Lesser and Greater Himalayan sequences. Nepalese Himalaya, *Geological Society of America Bulletin*, *108*, 904-911.

Pearson, R.K., (2011). *Exploring data in engineering, the sciences, and medicine*, Oxford University Press.

Pognante, U., and Benna, P. (1993). Metamorphic zonation, migmatization and leucogranites along the Everest transect of eastern Nepal and Tibet: record of an exhumation history, *in* Treloar, P. J., and Searle, M. P., eds., Himalayan Tectonics: London, The Geological Society, 323-340.

Ray, L., Bhattacharya, A., and Roy, S. (2007). Thermal conductivity of Higher Himalayan Crystallines from Garhwal Himalaya, India. *Tectonophysics*, *434*, 71-79.

Ruppel, C., Royden, L. and Hodges, K.V. (1988). Thermal modeling of extensional tectonics: application to pressure-temperature-time histories of metamorphic rocks. *Tectonics*, *7*, 947-957.

Sakai, H., Sawada, M., Takigami, Y., Orihashi, Y., Danhara, T., Iwano, H., Kuwahara, Y., Dong, Q., Cai, H.W., and Li, J.G. (2005). Geology of the summit limestone of Mount Qomolangma (Everest) and cooling history of the Yellow Band under the Qomolangma detachment. *Island Arc*, *14*(4), 297-310.

Sambridge, M. (1999). Geophysical inversion with a Neighborhood Algorithm – I. Searching a parameter space. *Geophysical Journal International, 138,* 479-494.

Schultz, M.H., Hodges, K.V., Ehlers, T.A., van Soest, M.C., and Wartho, J-A. (2017). Thermochronologic constraints on the slip history of the South Tibetan detachment system, south-central Tibet, *Earth and Planetary Science Letters*, *459*, 105-117.

Schwarz, W.H., and Trielhoff, M. (2007). Intercalibration of ^{40}Ar-^{39}Ar age standards NL-25, HB3gr hornblende, GA1550, SB-3, HD-B1 biotite and BMus/2 muscovite. *Chemical Geology*, *242*, 218 – 231.

Searle, M. P. (1999). Extensional and compressional faults in the Everest-Lhotse massif, Khumbu Himalaya, Nepal. *Journal of the Geological Society of London*, 156, 227–240.

Searle, M. P., Simpson, R., Law, R.D., Parrish, R.R., and Waters, D.J. (2003). The structural geometry, metamorphic and magmatic evolution of the Everest massif, High Himalaya of Nepal–South Tibet. *Journal of the Geological Society of London*, *160*, 345–366.

Searle, M. P., Cottle, J.M., Streule, M.J., and Waters, D.J. (2010). Crustal melt granites and migmatites along the Himalaya: melt source, segregation, transport and granite emplacement mechanisms. *Earth and Environmental Science Transactions of the Royal Society of Edinburgh*, *100*, 219-233.

Stockli, D. (2005). Application of low-temperature thermochronometry to extensional tectonic settings, *in* Reiners, P. W., and Ehlers, T. A., (Eds.) Low-Temperature Thermochronology, Techniques, Interpretations, ad Applications: Washington, DC, *Mineralogical Society of America, Reviews in Mineralogy and Geochemistry*, *58*, 411-448.

Stübner, K., Warren, C., Ratschbacher, L., Sperner, B., Kleeberg, R., Pfänder, J., and Grujic, D. (2017). Anomalously old biotite $^{40}Ar/^{39}Ar$ ages in the NW Himalaya. *Lithosphere, 9,* DOI:10.1130/L1586.1131.

Thiede, R.C., and Ehlers, T.A. (2013). Large Spatial and Temporal Variations in Himalayan Denudation. *Earth and Planetary Science Letters*, 371-372, 278-293.

van Hinsbergen, D. J. J., Lippert, P.C., Dupont-Nivet, G., McQuarrie, N., Doubrovine, P.V., Spakman, W., and Torsvik, T.H. (2012). Greater India Basin hypothesis and a two-stage Cenozoic collision between India and Asia. *Proceedings of the National Academy of Sciences*, *109*, 7659-7664.

Vannay, J.- C. and Grasemann, B. (2001). Himalayan inverted metamorphism and syn-convergence extension as a consequence of a general shear extrusion. *Geological Magazine, 138*, 253-376.

Viskupic, K., Hodges, K.V., and Bowring S.A. (2005). Timescales of melt generation and the thermal evolution of the Himalayan metamorphic core, Everest region, eastern Nepal. *Contrib. Mineral. Petrol., 149,* p. 1-21.

Walker, J.D., Martin, M.W., Bowring, S.A., Searle, M.P., Waters, D.J., Hodges, K.V. (1999). Metamorphism, melting and extension: age constraints from the high Himalayan slab of southeastern Zanskar and northwestern Lahoul. *Journal of Geology, 107*, 473-495.

Webb, A. A. G. (2013). Preliminary balanced palinspastic reconstruction of Cenozoic deformation across the Himachal Himalaya (northwestern India). Geosphere, *9*(3), 572-587.

Webb, A. A. G., Yin, A., Harrison, T.M., Celerier, J., and Burgess, W.P. (2007). The leading edge of the Greater Himalayan Crystalline complex revealed in the NW Indian Himalaya. Implications for the evolution of the Himalayan orogen, *Geology*, *35*(10), 955-958.

Wendt, I., and Carl, C., (1991). The statistical distribution of the mean squared weighted deviation. *Chemical Geology: Isotope Geoscience setion*, *86*, 275 – 285.

Whipp, D. M., Ehlers, T.A., Blythe, A.E., Huntington, K.W., Hodges, K.V., Burbank, D.W. (2007). Plio-Quaternary exhumation history of the central Nepalese Himalaya: 2. Thermo-kinematic and thermochronometer age prediction model. *Tectonics, 26*, doi:10.1029/2006TC001991.

Yin, A. (2006). Cenozoic tectonic evolution of the Himalayan orogen as constrained by along-strike variation of structural geometry, exhumation history, and foreland sedimentation. *Earth Science Reviews*, *76*, 1-131.

Yin, C. H., and Kuo, S.T. (1978). Stratigraphy of the Mount Jolmo Lungma and its north slope. *Scientia Sinica*, *21*, 629-644.

TABLE 3.1: THERMOCHRONOLOGIC DATA FOR THE RONGBUK VALLEY, RA CHU, AND DZAKAR CHU

Sample	Location	Elevation m	Rock Type	MsAr (Ma)*	BtAr (Ma)*	ZrnHe (Ma)**	ApHe (Ma)**
RONGBUK❖							
R01	28.14056 N 86.85194 E	5157	Leucogranite	15.37 ± 0.16 (98.8)	-	11.4 ± 2.4 (4)	9.3 ± 2.8 (6)
R02	28.17328 N 86.84003 E	5114	Mylonitized leucogranite	15.000 ± 0.060 (100)	-	13.0 ± 1.5 (4)	7.76 ± 0.52 (2)
R03	28.17300 N 86.84297 E	5089	Mylonitized leucogranite	15.25 ± 0.11 (99)	-	12.9 ±1.7 (2)	-
R04	28.18148 N 86.83585 E	5025	Mylonitized leucogranite	15.420 ± 0.050 (99.8)	-	14.32 ± 0.21 (4)	-
R05	28.19000 N 86.83243 E	5019	Leucogranite	15.400 ± 0.060 (100)	-	13.1 ± 1.7 (4)	-
R06	28.20502 N 86.82913 E	5128	Mylonitized leucogranite	14.400 ± 0.070 (100)	-	11.0 ± 1.1 (4)	-
R07	28.20610 N 86.82580 E	4997	Leucogranite	14.770 ± 0.070 (99.9)	-	12.9 ± 1.9 (7)	-
R08	28.21285 N 86.82395 E	4961	Leucogranite	14.450 ± 0.080 (99)	-	13.66 ± 0.17 (5)	-
RA CHU							
RC01	28.35530 N 86.67233 E	3942	Calc-silicate and Amphibolite	-	13.39 ± 0.38 (68.1)	11.9 ± 1.3 (5)	
DZAKAR CHU							
DC01	28.34593 N 87.22805 E	3907	Mylonitic leucogranite	13.963 ± 0.092 (89)	-	10.05 ± 0.74 (4)	-
DC02	28.33858 N 87.25626 E	3885	Biotite Gneiss	-	-	8.67 ± 0.54 (7)	-
DC03	28.33664 N 87.27357 E	4380	Leucogranite and Biotite Gneiss	-	-	12.16 ± 0.35 (7)	10.2 ± 2.6 (5)

All uncertainties are quoted at 2σ

❖Rongbuk valley samples can be found in *Schultz et al. (2017)*

* Numbers in parentheses indicate the total $\%^{39}Ar$ making up the plateau Ar-Ar age.

** Numbers in parentheses designate number of analyses contributing to the mean.

TABLE 3.2: NA INVERSION 2D MODELING INPUT PARAMETERS

PARAMETER	VALUE
FIXED PARAMETERS	
Model dimensions	45 km N-S 80 km E-W
DEM node spacing (x, y, z directions)	50 m
Thermal diffusivity[a]	29 km Myr^{-1}
Moho depth[b]	35 km
Surface temperature[b]	5°C
Atmospheric lapse rate	6.69°C km^{-1}
PRIOR PARAMETERS	
Thermal	
Basal T temperatures	600 - 1000°C
Radiogenic heat production	0.4 to 3 $\mu W/m^3$
Fault	
T2 span of brittle slip	15.5 to 9 Ma
T1 (ca. 20 to 15.6 Ma) slip rates	5 to 50 km Ma^{-1}
T2 (ca. 15.5 to 9 Ma) slip rates	5 to 50 km Ma^{-1}

[a] From Ray et al. (2007); Whipp et al. (2007)

[b] From Thiede and Ehlers (2013)

TABLE 3.3: OBSERVED VERSUS EXPECTED THERMOCHRONOLOGIC COOLING AGES FOR THE RONGBUK VALLEY, RA CHU, AND DZAKAR CHU FROM FORWARD MODELING

Sample	Valley	Location	Elevation (m) (Observed)	MsAr ± 2σ (Observed)	MsAr (Predicted)	BtAr ± 2σ (Observed)	BtAr (Predicted)	ZrnHe ± 2σ (Observed)	ZrnHe (Predicted)	ApHe ± 2σ (Observed)	ApHe (Predicted)
R01	Rongbuk	28.14056 N 86.85194 E	5157	15.37 ± 0.16	15.61	-	-	11.4 ± 2.4	13.8	9.3 ± 2.8	10.5
R02	Rongbuk	28.17328 N 86.84003 E	5114	15.000 ± 0.060	15.550	-	-	13.0 ± 1.5	13.9	7.76 ± 0.52	10.20
R03	Rongbuk	28.17300 N 86.84297 E	5089	15.25 ± 0.11	15.65	-	-	12.9 ± 1.7	13.8	-	-
R04	Rongbuk	28.18148 N 86.83585 E	5025	15.420 ± 0.050	15.758	-	-	14.32 ± 0.21	14.24	-	-
R05	Rongbuk	28.19000 N 86.83243 E	5019	14.400 ± 0.060	15.051	-	-	13.1 ± 1.7	13.7	-	-
R06	Rongbuk	28.20502 N 86.82913 E	5128	14.770 ± 0.070	15.044	-	-	11.0 ± 1.1	13.7	-	-
R07	Rongbuk	28.20610 N 86.82580 E	4997	14.450 ± 0.070	14.933	-	-	12.9 ± 1.9	13.8	-	-
R08	Rongbuk	28.21285 N 86.82395 E	4961	14.930 ± 0.080	15.075	-	-	13.66 ± 0.17	13.98	-	-
RC01	Ra Chu	28.35530 N 86.67233 E	3952	-	-	13.39 ± 0.38	13.98	11.9 ±1.3	13.9	-	-
DC01	Dzakaa Chu	28.34593 N 87.22805 E	3907	13.693 ± 0.092	14.241	-	-	10.05 ± 0.74	24.62	-	-
DC02	Dzakaa Chu	28.33858 N 87.25626 E	3885	-	-	-	-	8.67 ± 0.54	11.80	-	-
DC03	Dzakaa Chu	28.33664 N 87.27357 E	4380	-	-	-	-	12.16 ± 0.35	24.62	10.2 ± 2.6	9.5

TABLE 3.4: COMPARISON OF 1D AND 2D THERMAL-KINEMATIC MODELING PARAMETERS AND RESULTS

PARAMETER	1D MODEL[a]	2D MODEL
Basal Temperature	650°C	700 - 1000°C
Heat Production	23°C/Ma	*ca.* 17 to 30°C/Ma
DUCTILE DISPLACEMENT ca. 20 to 15.6 Ma	*ca*. 25 to 170 km[b]	*ca.* 84 to 219 km
BRITTLE DISPLACEMENT ca. 15.5 to 13 Ma	*ca.* 36 to 119 km	*ca.* 83 to 119 km
TOTAL STDS DISPLACEMENT	*ca.* 61 to 289 km	*ca.* 167 to 338 km

[a]1D modeling parameters and results are from Schultz et al. (2017)

[b]Ductile displacement estimate from Law et al. (2011)

FIGURE 3.1

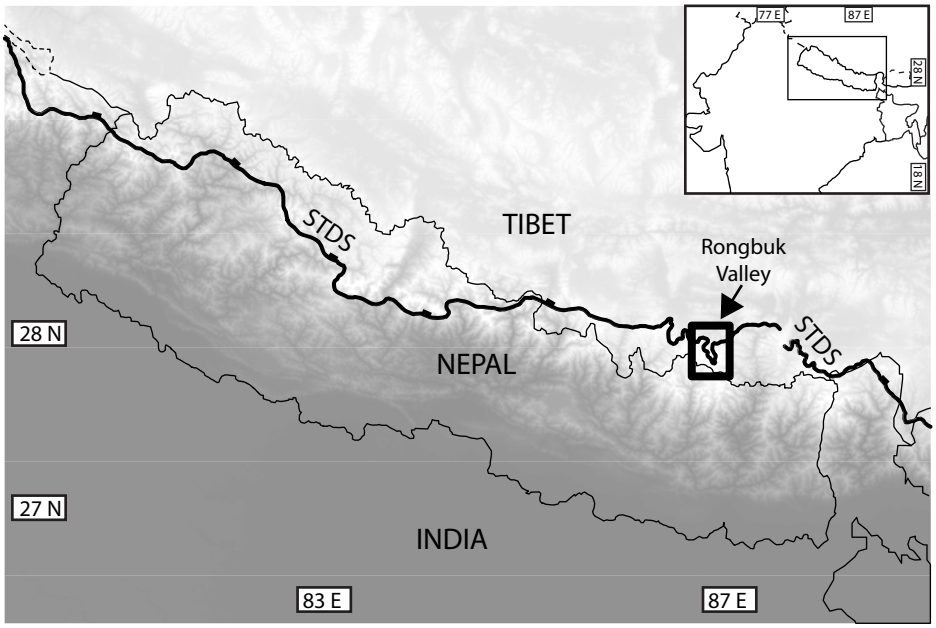
77 E
87 E
28 N
18 N
STDS
TIBET
Rongbuk
Valley
STDS
28 N
NEPAL
27 N
INDIA
83 E
87 E

FIGURE 3.2

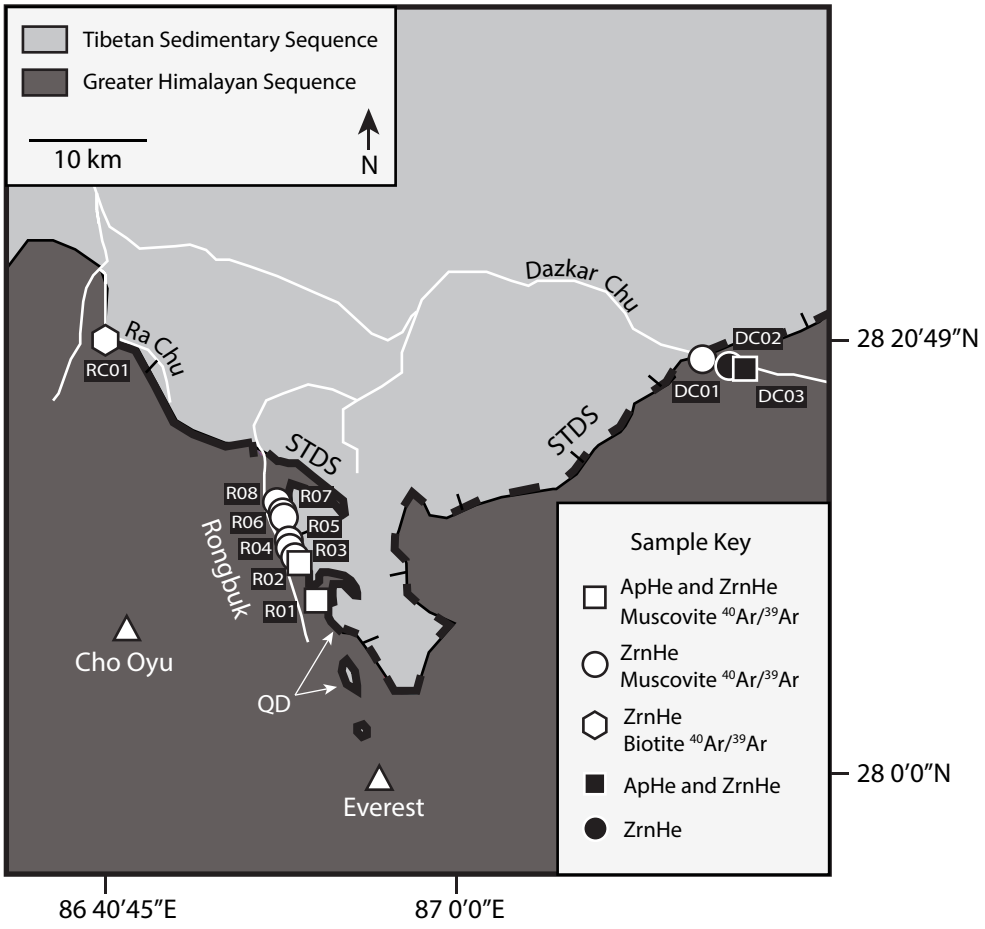
Tibetan Sedimentary Sequence
Greater Himalayan Sequence
10 km
N
Dazkar Chu
Ra Chu
RC01
DC02
DC01
DC03
STDS
STDS
R08
R07
R06
R05
R04
R03
R02
R01
Rongbuk
Cho Oyu
QD
Everest
Sample Key
ApHe and ZrnHe
Muscovite $^{40}Ar/^{39}Ar$
ZrnHe
Muscovite $^{40}Ar/^{39}Ar$
ZrnHe
Biotite $^{40}Ar/^{39}Ar$
ApHe and ZrnHe
ZrnHe
28 20′49″N
28 0′0″N
86 40′45″E
87 0′0″E

FIGURE 3.3

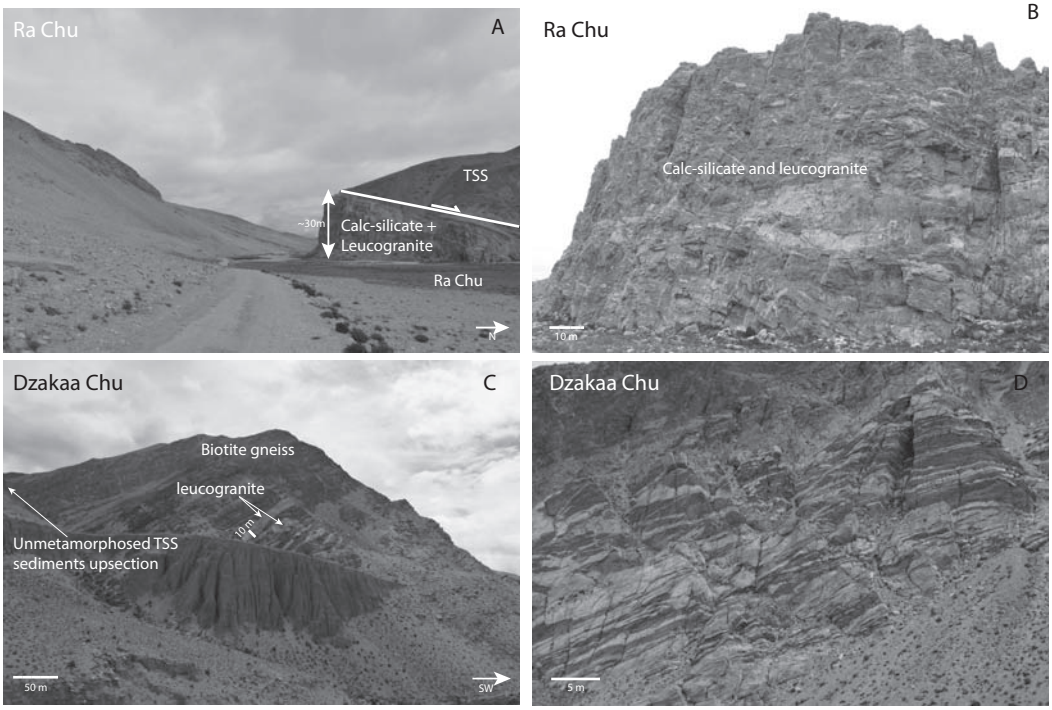
Ra Chu
A
TSS
~30m
Calc-silicate +
Leucogranite
Ra Chu
N
Ra Chu
B
Calc-silicate and leucogranite
10 m
Dzakaa Chu
C
Biotite gneiss
leucogranite
10m
Unmetamorphosed TSS
sediments upsection
50 m
SW
Dzakaa Chu
D
5 m

FIGURE 3.4

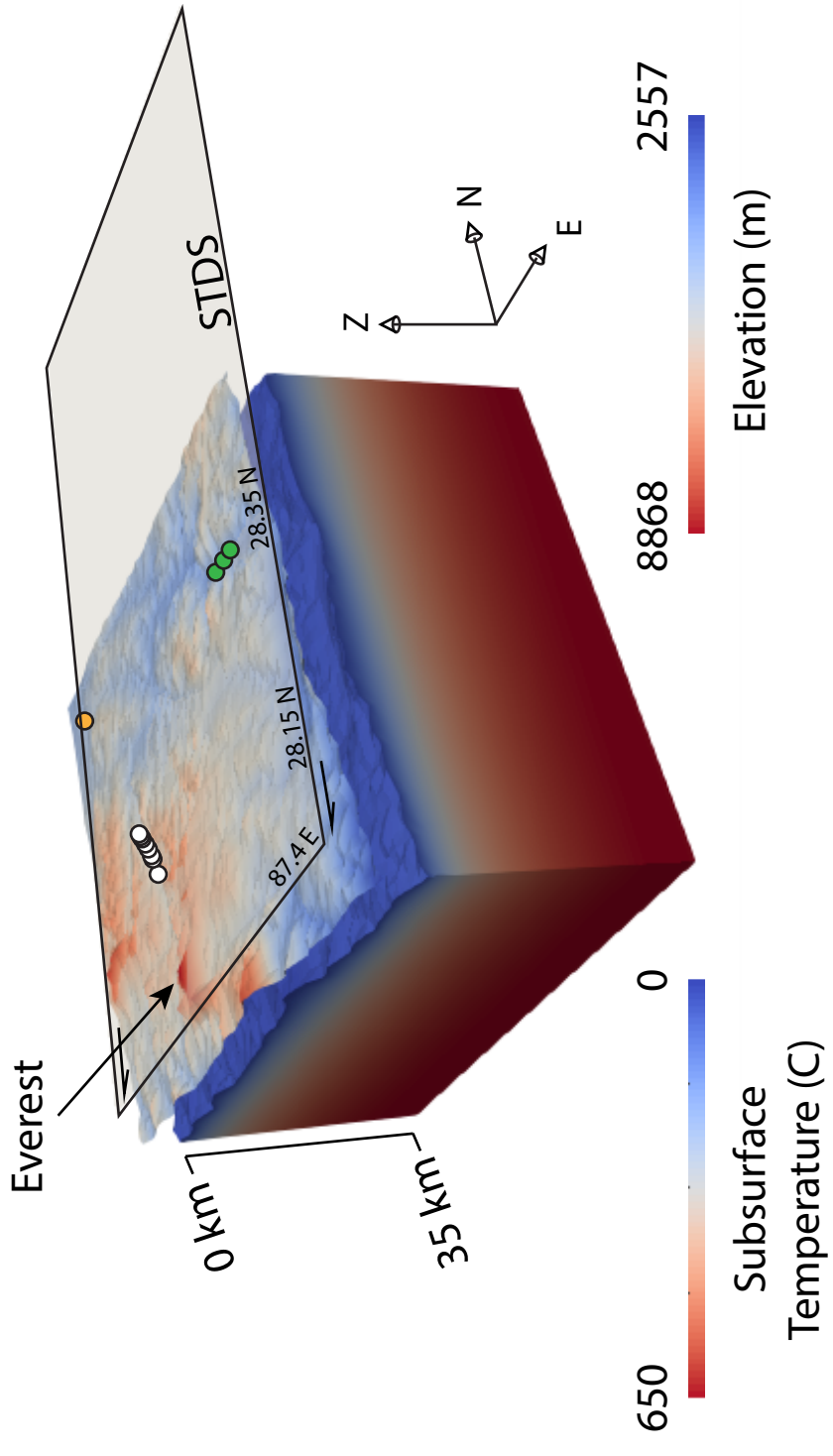
STDS
N
E
Z
28.35 N
28.15 N
87.4 E
Everest
0 km
35 km
2557
8868
Elevation (m)
0
650
Subsurface
Temperature (C)

FIGURE 3.5

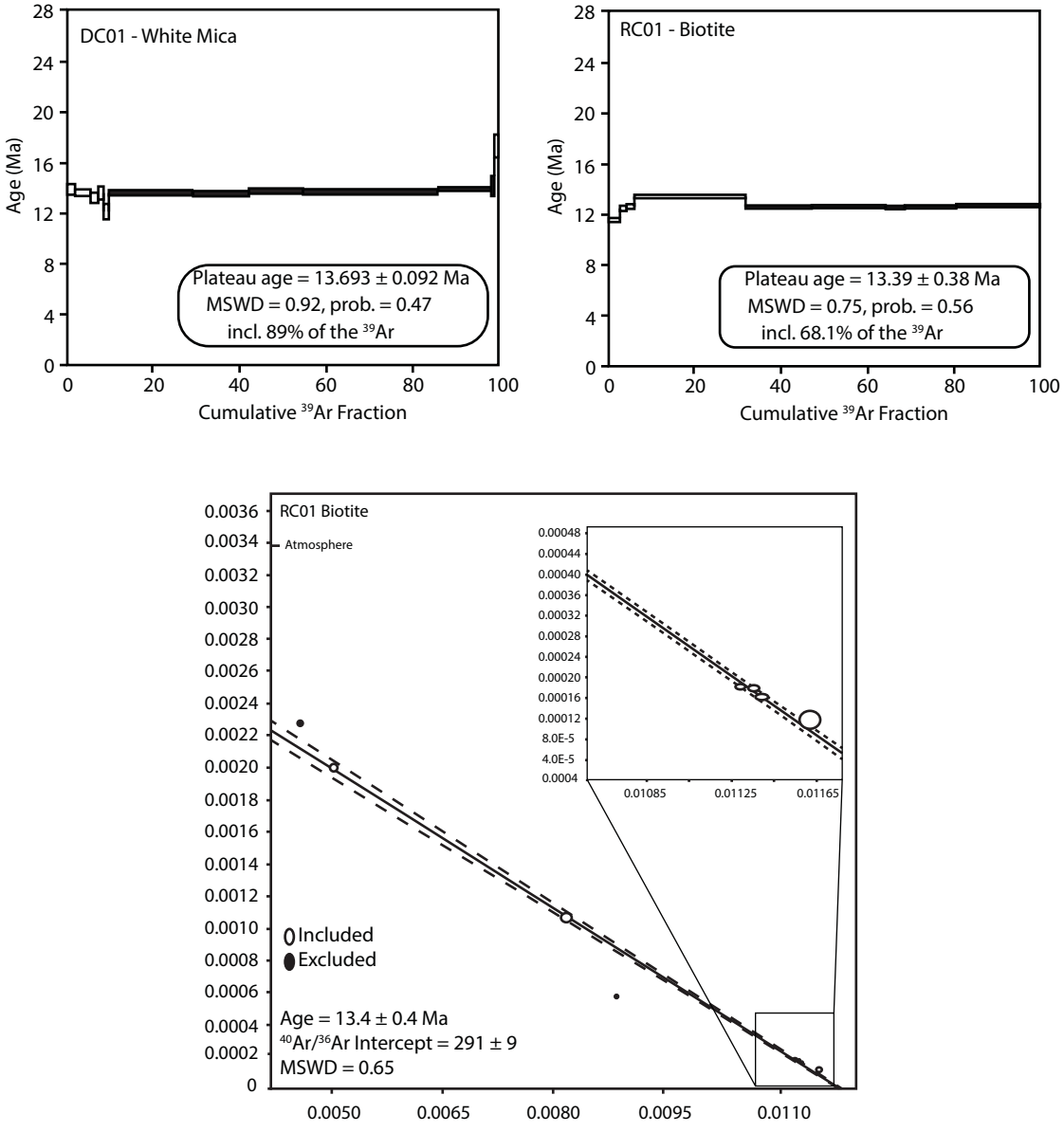
DC01 - White Mica
Age (Ma)
Cumulative ^{39}Ar Fraction
Plateau age = 13.693 ± 0.092 Ma
MSWD = 0.92, prob. = 0.47
incl. 89% of the ^{39}Ar
RC01 - Biotite
Plateau age = 13.39 ± 0.38 Ma
MSWD = 0.75, prob. = 0.56
incl. 68.1% of the ^{39}Ar
RC01 Biotite
Atmosphere
Included
Excluded
Age = 13.4 ± 0.4 Ma
^{40}Ar/^{36}Ar Intercept = 291 ± 9
MSWD = 0.65

FIGURE 3.6

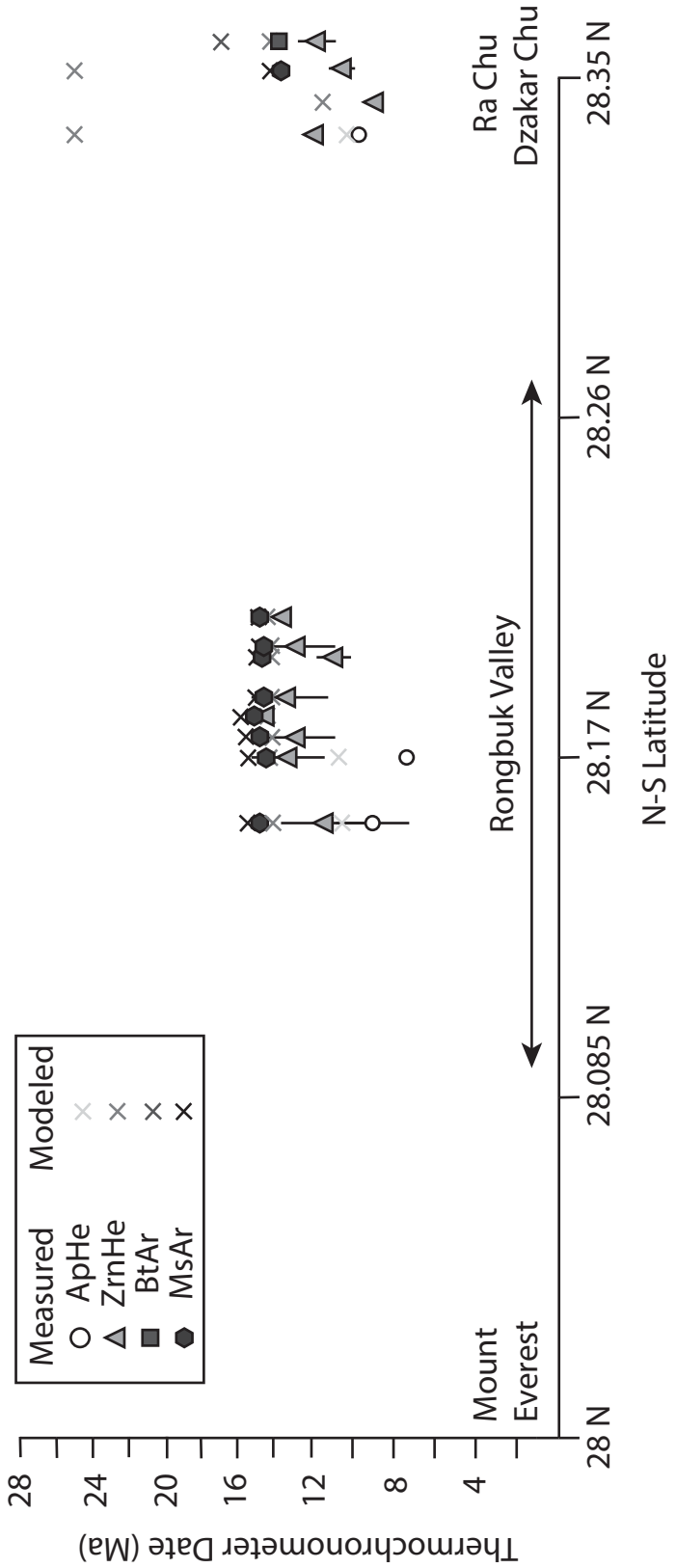
Thermochronometer Date (Ma)
28
24
20
16
12
8
4
Measured
Modeled
ApHe
ZrnHe
BtAr
MsAr
Mount Everest
Rongbuk Valley
Ra Chu
Dzakar Chu
28 N
28.085 N
28.17 N
28.26 N
28.35 N
N-S Latitude

FIGURE 3.7

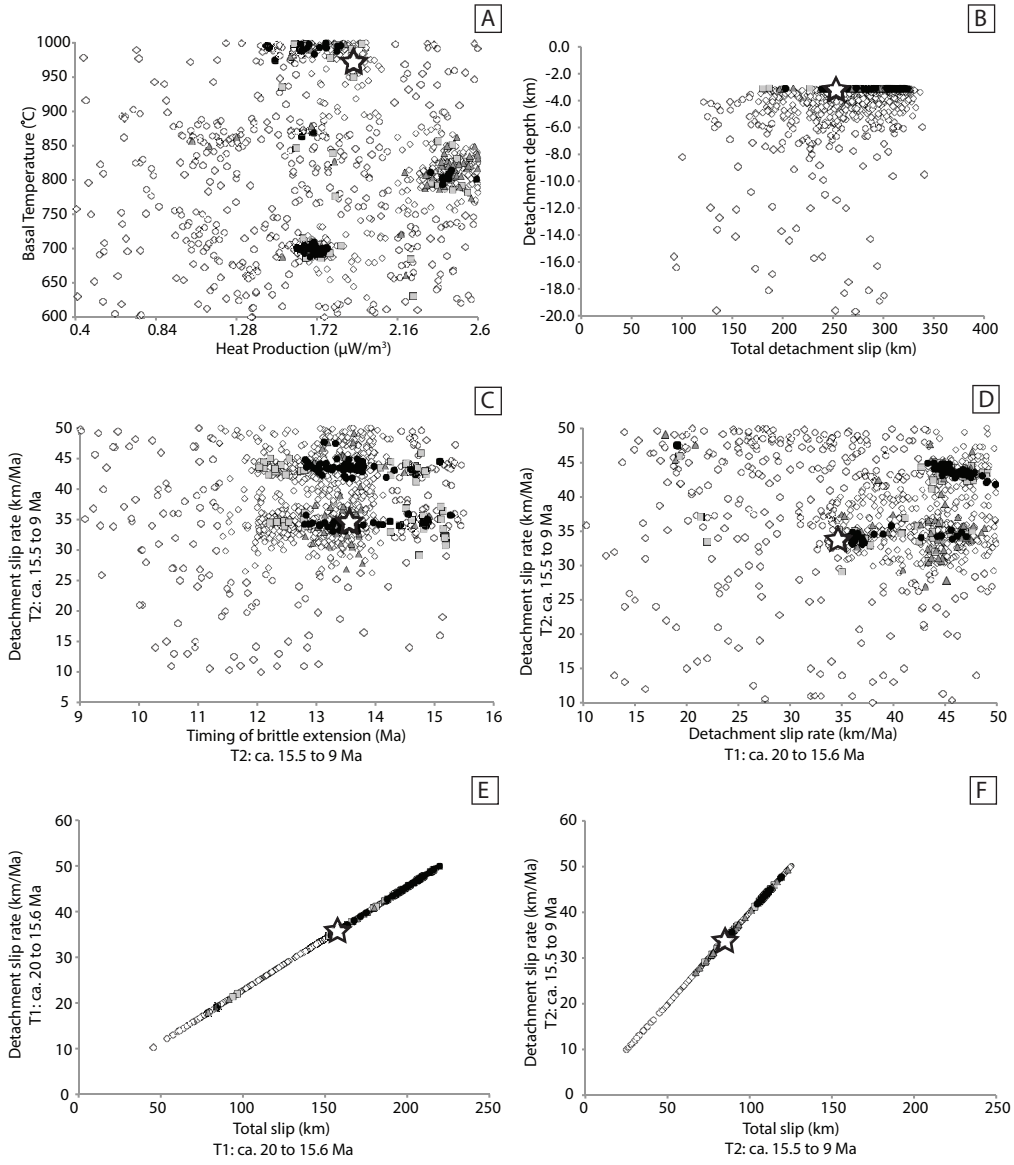

Misfit values: ◇ 100 < Φ □ 20 < Φ < 100 ▲ 3 < Φ < 20 ● Φ < 3

Best-fit model: ☆

CHAPTER 4

CONSTRAINING LONG-TERM EXHUMATION HISTORIES NORTH AND SOUTH OF THE HIMALAYAN RAIN SHADOW

1. Abstract

The Himalayan ranges of South Asia form one of the world's most impressive rain shadows. Data from the NASA – Japan Aerospace Exploration Agency Tropical Rainfall Measurement Mission (TRMM) suggest that precipitation in the central Himalaya drops from more than four meters per year along the southern flanks of the Higher Himalaya to about half a meter per year north of the range crest on the southern Tibetan Plateau. How long this rain shadow has existed remains poorly understood. In order to establish whether or not the million-year timescale signature of exhumation mimics the modern precipitation pattern, we present comparative thermochronologic datasets collected along a transect that crosses the precipitation transition in the Everest area of southern Tibet and Nepal. Zircon and apatite (U-Th)/He dates for Greater Himalayan Sequence (GHS) bedrock samples from the southern flank are about ten million years younger than ages for samples to the north of the transition. Modeled exhumation rates for samples north of the range crest were high ($\geq$ 3.5 mm/a) from $\geq$ 20 Ma until *ca.* 13 Ma, when they decreased rapidly. In sharp contrast, modeled exhumation rates for samples south of a major knickpoint in the Dudh Kosi river profile were low (*ca.* 0.5 to 1 mm/a) until *ca.* 4 Ma, when rates increased rapidly to *ca.* 4 mm/a until *ca.* 2 Ma. These results are consistent with the initiation of the Himalayan rain shadow in roughly its current configuration backward to at least Pliocene time.

2. Introduction

Mountain landscapes are shaped by the complex interactions between climate and plate tectonics, yet the precise nature of this relationship, particularly on million-year timescales, remains ambiguous. The Himalayan Mountains are among the best localities on Earth to investigate such interactions because they construct one of the world's starkest rain shadows (Figure 4.1). The oceans surrounding India and the elevated Tibetan Plateau produce a temperature and pressure gradient that results in the annual Indian summer monsoon (ISM), which is generally active from June until September (Bookhagen and Burbank, 2006). Data from NASA/Japan Aerospace Agency's joint Tropical Rainfall Measurement Mission (TRMM) for the period 1998 – 2005 reveal a drastic rainfall disparity across the Himalaya (Figure 4.1). Regions of the central Himalaya directly south of the range front may receive a mean of four meters of rainfall per year, while southern Tibet north of the range crest receives less than half a meter of rainfall annually (Bookhagen and Burbank, 2006). It is widely inferred that a modern-day feedback exists between precipitation and bedrock erosion in the Himalaya, with higher rates of erosion in regions that experience the annual ISM (Bookhagen et al., 2005a; Bookhagen et al., 2005b; Gabet et al., 2008; Wulf et al., 2010). The geomorphology of the central Himalaya provides compelling support for such feedback, with the strongest evidence residing in the topographic and river profiles across the width of the range. Precipitation-erosion feedback invites one approach to evaluating the longevity of the Himalayan rain shadow: if it persisted far back into deep time, we should see evidence for differential erosion north and south of the range preserved in thermochronologic datasets. This notion has inspired a variety of previous studies with discrepant

conclusions (Burbank et al., 2003; Thiede et al., 2004, 2009; Blythe et al., 2007). We regard the differences as largely reflecting the fact that studies were conducted along 'Transhimalayan' rivers that breach the rain shadow and may affect local precipitation patterns (Barros et al., 2006). In this contribution, we present new data and exhumation rate models for a transect that is not along a Transhimalayan river but still crosses the steep ISM precipitation gradient in the Everest region of southern Tibet and Nepal (Figure 4.1), with the aim of reducing interpretive ambiguity.

3. Physiography, monsoon rainfall, and bedrock geology in the study transect

Figure 4.2 illustrates a topographic profile, at the approximate longitude of Mount Everest, from the Himalayan range front to the south to the Tibetan Plateau to the north. The physiographic edge of the plateau – referred to as PT_1 by Hodges et al. (2001) – roughly corresponds to the Himalayan range crest in such transects, but more useful markers of its position are prominent knickpoints in the Transhimalayan rivers, where lower stream gradients on the plateau abruptly give way to very steep stream gradients on the southern flank of the Himalaya (Figure 4.1). In the area of the transect shown, there is no Transhimalayan drainage, so a practical edge of the plateau is less easily defined. An argument could be made that it corresponds to the range crest, but an alternative interpretation is that it might pass through a major knickpoint on the Dudh Kosi river, which – while not Transhimalayan – has its source just south of the highest peaks in the transect (Figures 4.2 and 4.3).

However PT_1 is defined, the regions immediately to its south include the steepest river and stream gradients in the Himalaya, which are widely regarded to correspond with

the regions having the most aggressive, ISM-driven, fluvial erosion along the southern flank of the range (Hodges et al., 2001; Wobus et al., 2006). This inference is supported by the N-S distribution of rainfall as measured by the TRMM data (Figure 4.1). In detail, maps of calibrated 1998 – 2005 data show two rainfall maxima. A minor maximum occurs in the Himalayan foothills, but the highest rainfall by far occurs at the approximate position of the Dudh Kosi knickpoint and tapers off abruptly to the north (Figure 4.2). Samples collected on either side of this abrupt transition in the Everest region are the focus of the current study (Figure 4.3). Thermochronologic data from these samples – combined with a previously published dataset (Schultz et al., 2017) for samples collected north of Mount Everest and clearly on the plateau – help constrain how long-term exhumation rates correlate with modern rainfall and erosion patterns. Stable isotope paleoaltimetry suggests that the Miocene elevation of Mount Everest was >5000 m (Gébelin et al., 2013), and thus it seems likely that at least the broad physiography of this region was not substantively different since that time than it is today.

The samples used in this study and that of Schultz et al. (2017) were collected from the Greater Himalayan sequence (GHS) of Hodges (2000): predominantly metapelitic and metaigneous rocks that represent the metamorphic core of the range and reached their highest upper amphibolite to granulite facies metamorphic conditions during the Miocene. Two samples in this study as well as all of the samples used in Schultz et al. (2017) were collected from small leucogranitic sills and dikes that intrude the GHS country rocks. Extensive (U-Th)/Pb geochronology of the leucogranites in the Everest area suggest they range in age from *ca.* 25 to *ca.* 15 Ma (Copeland et al., 1988; Hodges et al., 1992, 1998; Murphy and Harrison, 1999; Cottle et al., 2007, 2015). The

upper boundary of the GHS is a low-angle fault system with normal-sense kinematics: the north-dipping South Tibetan detachment system (STDS) of Burchfiel et al. (1992). In the Everest area, the structurally highest fault in the STDS has been named the Qomolangma detachment, which crops out at the base of a klippe high on the Everest summit pyramid, dipping a few degrees northward (Figure 4.3). The main trace of the detachment is exposed several tens of kilometers to the north near the floor of the Rongbuk valley in southern Tibet, where the samples studied by Schultz et al. (2017) were collected, in the proximal footwall of the Qomolangma detachment.

4. Previous thermochronologic work in the Mount Everest region

Streule et al. (2012) reported fission-track apatite and zircon dates for samples collected above and below the STDS in the Khumbu region of Nepal. Their results include extremely young apatite fission (ApFT) track cooling ages for GHS samples, ranging between *ca.* 3.1 Ma and *ca.* 0.9 Ma. Their fission-track zircon (ZrnFT) data set shows much greater variability. Samples collected closer to the crest of the range yielded dates much older (*ca.* 16 Ma) than those for samples collected 10 – 20 km to the south (*ca.* 3 Ma). The very young ApFT and ZrnFT dates reported by Streule et al. (2012) are consistent with previous results for samples collected at similar structural levels elsewhere in the Himalaya (Blythe et al., 2007; Thiede and Ehlers, 2013). Streule et al. (2012) interpreted their very young dates as a response to rapid erosion by glaciation in the Pliocene.

More recently, Orme et al. (2015) and Carrapa et al. (2016) published zircon (U-Th)/He (ZrnHe) and ApFT dates for samples collected in the Rongbuk valley. The

weighted mean ZrnHe dates of Orme et al., (2015) ranged from *ca.* 12 to 10 Ma; however, those dates were considered by the authors to be "too young" due to high concentrations of parent isotopes [U+Th] in the rims of the zircon crystals, which resulted in incorrect alpha ejection corrections of raw (U-Th)/He dates (cf., Hourigan et al., 2005). They reported "corrected" ages of *ca.* 17 to 14 Ma. The ApFT dates of Carrapa et al. (2016), ranging from ca. 15.6 Ma to 12.7 Ma, are much older than those of Streule et al. (2012). Comparing the two datasets, Carrapa et al. (2016) interpreted them as collectively implying a difference in million-year timescale exhumation rates on either side of the central Himalayan range crest. While our data support and better quantify this basic interpretation, we disagree with Carrapa and co-workers with regard to where the transition takes place and its root cause, as we discuss in detail below.

Schultz et al. (2017) presented a dataset including muscovite $^{40}Ar/^{39}Ar$ laser step heating (MsAr) and zircon and apatite (U-Th)/He from the Rongbuk valley. MsAr laser step heating resulted in plateau ages ranging from *ca.* 15.42 to *ca.* 14.4 Ma. ZrnHe dates were younger than the MsAr plateau ages and ranged from *ca.* 14.32 to *ca.* 11.0 Ma. ApHe dates from two samples were younger still, ranging from *ca.* 9.3 to *ca.* 7.76 Ma. The range of reported ZrnHe dates of Schultz et al. (2017) are older than the uncorrected dates of Orme et al. (2015) but significantly younger than their corrected dates. Noting that the correction approach used by Orme et al. (2015) is often imperfect due to the common geometric complexity of zircon zoning, and that many of their corrected helium dates are older than reported crystallization ages of zircons in the Rongbuk valley leucogranites (Cottle et al., 2015), Schultz et al. (2017), suggested that the Orme et al. (2015) corrected dates are likely too old due to over-correction.

5. New thermochronologic results

Here we report new MsAr, biotite $^{40}Ar/^{39}Ar$ (BtAr), ZrnHe, and ApHe cooling ages for bedrock samples collected south of the Everest massif (see Table 4.1 and Appendix Tables C1, C2, and C3 for the complete thermochronologic dataset). All work was done in the Group 18 Laboratories at Arizona State University, using methods described in the Supplementary Materials.

5.1 MsAr and BtAr

Muscovite and biotite $^{40}Ar/^{39}Ar$ laser step heating data were generated for single mica crystals for six biotite gneiss and leucogranite samples (Tables 4.1 and C1). Only two of our samples contained muscovite: leucogranites K07 and K08. Both yielded incremental release spectra (Figure 4.4) with statistically defined plateaus (Fleck, 1977) indicative of similar middle Miocene closure ages of 16.413 ± 0.074 Ma (K07) and 16.77 ± 0.16 Ma (K08). Of the six analyzed biotites, only two yielded plateaus: K01 (12.80 ± 0.19 Ma) and K07 (16.461 ± 0.059 Ma). Both BtAr plateaus are illustrated in Figure 4.4. The remaining four biotite spectra each were relatively flat but did not yield statistically defined plateaus (Figure C1). In general, such behavior may reflect contamination by excess ^{40}Ar (Kelley, 2002), and corrected ages sometimes can be deduced for contaminated biotites by analyzing the data using so-called "inverse isochron" plots (Roddick et al., 1980). For biotites K02, K03, K04, and K08, however, such analysis did not yield statistically acceptable linear arrays, so it is impossible to reliably estimate the contaminated, non-radiogenic $^{40}Ar/^{36}Ar$ necessary for robust corrections. In Table 4.1 we

simply report the "total gas" apparent ages for these grains, each of which represents the inverse variance- and percent ^{39}Ar-weighted mean for all incremental heating steps. While noting that excess ^{40}Ar is a relatively common issue in studies of Himalayan biotites (e.g., Hubbard and Harrison, 1989; Viskupic et al., 2005; Adams et al., 2015; Stübner et al., 2017), we regard these total gas dates as the best available estimates for the ^{40}Ar/^{39}Ar closure ages of our more problematic biotites. In general, the BtAr cooling dates decrease gradually from north to south: 17.18 ± 0.56 Ma for K08 to 12.80 ± 0.19 Ma for K01 (Figure 4.3).

5.2 ApHe and ZrnHe

Apatites lacking inclusions, of sufficient size, and with sufficiently good crystal morphology for single-crystal (U-Th)/He dating were found in samples K01, K02, K03, K04, and K08. The number of good candidates for ApHe dating limited in these samples, and we were only able to analyze between 1 and 5 grains from each of the samples (Table 4.2). The single crystal analyzed for K03 yielded an ApHe date of 1.33 ± 0.13 Ma. For samples K01 and K04, multiple crystals from each sample yielded statistically indistinguishable ApHe dates and we report the inverse-variance weighted mean date (with its analytically derived 2σ uncertainty) for these samples as the best estimates for ApHe closure. For the other samples containing acceptable apatite, several analyses were "over-dispersed", meaning that analytical imprecision alone cannot explain the dispersion. Unfortunately, none of the over-dispersed dates for a single sample was a statistically identifiable outlier. For each over-dispersed set of dates for a single sample, we report the inverse variance-weighted mean along with the analytically derived

multiplied by the square-root of the mean square weighted deviation (MSWD) of the data from that mean. These are interpreted as the best available estimates of the ApHe closure ages of the analyzed samples. The ApHe inverse-variance weighted mean dates (and single date for K03) range from 8.1 ± 3.4 Ma to 1.33 ± 0.13 Ma, but only sample K08 – collected north of the Dudh Kosi knickpoint (Figure 4.3) – is older than *ca.* 3.4 Ma.

Our ZrnHe dates – for samples K02 through K08 – show a similar pattern. We were able to separate and date between 3 and 8 zircon crystals from each sample. For any given sample, the ZrnHe dates were over-dispersed with no obvious outliers. As we did for the samples with over-dispersed ApHe dates, we report in Table 4.1 the inverse variance-weighted mean dates, with uncertainties magnified by the square-root of the MSWD, as the best estimates of the timing of ZrnHe closure for samples K02 through K08. These dates decrease steadily south of the Dudh Kosi knickpoint (Figure 4.3) from 4.14 ± 0.77 to 2.43 ± 0.23 Ma, but samples K07 and K08 to north yield much older ZrnHe mean dates of 12.1 ± 1.4 Ma and 13.5 ± 0.93 Ma respectively.

6. Thermal-kinematic modeling

$^{40}Ar/^{39}Ar$ mica data for the Khumbu samples collectively indicate that the entire region south of the Himalayan range crest cooled through the elevated closure temperature intervals for the MsAr and BtAr chronometers in middle Miocene time, but the lower-temperature ZrnHe and ApHe chronometers yield markedly different dates north and south of the Dudh Kosi knickpoint. A general similarity between the $^{40}Ar/^{39}Ar$ and (U-Th)/He datasets for samples collected to the north of the knickpoint (but south of the range crest) and samples studied by Schultz et al. (2017), which were collected north

of the range crest. imply that bedrock exhumation histories for the Rongbuk and uppermost Dudh Kosi drainages were similar. The data from south of the knickpoint strongly argue that bedrock exhumation histories on million-year timescales were much different south of the knickpoint. Below we present the results of thermal-kinematic modeling of samples K02, K03, K04, K07, and K08 and compare them with the modeling results we published previously for the Rongbuk valley samples (Schultz et al., 2017). With the exception of K07, these samples were chosen for modeling because they yielded ApHe, ZrnHe, and either MsAr or BtAr dates and thus produced the best-constrained models over the entire time interval of interest. Although we do not have ApHe data for it, we also modeled K07 to better refine the geographic position a major thermochronologic transition identified using K02, K03, K04, and K08.

6.1 Methods

Two- and three-dimensional thermal-kinematic models are powerful tools to evaluate plausible tectonic scenarios that might explain the patterns of mineral cooling ages in orogenic systems, and the widespread availability of software packages such as *Pecube* (Braun, 2003; Braun et al., 2012) have encouraged many such efforts in recent years. Multidimensional models are especially useful when the broad topographic and structural configuration of a study area is well-established, and the constraints sought are principally structural in nature (e.g., the ages and magnitudes of fault slip events, etc.). Computationally simpler one-dimensional models can be more enlightening when structural information is not the principal goal. For our purposes, we want to know how sample-to-sample variations in thermochronologic results for samples collects across a

landscape might reflect geographic variations in exhumation rate. One-dimensional models are very well suited to such studies, and their simplicity offers valued opportunities to explore a broad range of plausible exhumation histories before settling on the most probable range of histories (Thiede and Ehlers, 2013; Adams et al., 2015; Schultz et al., 2017).

The thermal-kinematic modeling approach we used for the Dudh Kosi samples was introduced by Thiede and Ehlers (2013). Based on a modified, one-dimensional version of the *Pecube* software package, it employs a smart-search Monte Carlo method to determine the range of exhumation models that could reasonably reproduce the thermochronometric dataset obtained for each sample given an assumed set of thermo-physical properties and boundary conditions. (See Supplementary Materials for details on specific assumptions made in this study.) For each sample, we conducted 500,000 forward modeling runs of thermal histories over the past 20 Ma using an initial temperature increments of 3 million years between 20 and 17 Ma, one million year increments between 17 and 3 Ma, and a last increment between 3 Ma and the present. During each increment, the software allowed exhumation rates to vary randomly between 0.01 and 4.00 mm/a and computed the times of cooling through the nominal closure temperatures of all chronometers applied to the sample (based on values from Hodges (2014)). A specific modeling run was deemed acceptable if it matched all thermochronologic results within appropriate uncertainty bounds. All acceptable runs from among the 500,000 tries were then used to determine a best-fit exhumation rate and its 2σ uncertainty range for each time increment.

6.2 Modeling Results

Our modeling results for the Dudh Kosi samples are shown in Figure 4.5 along with that for the southernmost of samples from the Rongbuk valley studied by Schultz et al. (2017): R01. Comparing their thermochronologic results from the Rongbuk valley with those of other workers from the southern flank of the Himalaya, Carrapa et al. (2016) concluded that the Himalayan range crest in the Everest region marked a major transition in thermochronologic ages that corresponded with a major transition in exhumation history. In detail, our data are inconsistent with this conclusion. All thermal-kinematic models for samples we collected in the Rongbuk valley north of Everest – as illustrated by the R01 model reproduced in Figure 4.5 – feature a dramatic drop in exhumation rate at *ca.* 13 Ma and very low exhumation rates after *ca.* 8 Ma (Schultz et al., *2*017). The models for samples K08 and K07– collected south of the Himalayan crest (Figure 4.2) – are similar in many ways to models of the Rongbuk valley samples; they show a steeply declining exhumation rate from *ca.* 17 to *ca.* 12 Ma, and exhumation rates remain very low (*ca.* 0.75 km/Ma or less) between *ca.* 12 Ma and the present. These results indicate that essentially the same pattern of Miocene-Recent exhumation rate evolution persists roughly 12 km south of the Himalayan range crest. However, a dramatic transition in exhumation rate evolution occurs farther south in the Dudh Kosi valley. Models for samples K04, K03, and K02 display a late, post-5 Ma acceleration in exhumation rate up to values of 3.5-4.0 km/Ma (Figure 4.5).

7. Alternative interpretations

Comparison of the patterns of modern precipitation, thermochronologic data, and derived exhumation rate models demonstrate that exhumation rates at the million-year timescale in the Dudh Kosi valley correlate spatially with modern precipitation rates (Figure 4.3). The latitudes over which the transition in exhumation rate history occur appear constrained by our modeling exercise to be between 27.95˚ N and 27.87˚ N, a map distance of roughly 8.3 km. Although the paucity of datable micas or apatite in samples K06 and K05 preclude better location through thermal-kinematic modeling, a major determining factor of the topology of the models we did produce was the ZrnHe date. Samples that indicated accelerated Pliocene and younger exhumation (K04, K03, and K02) yielded Plio-Pleistocene ZrnHe dates, whereas the ZrnHe dates in K08 and K07 were much older (middle Miocene; Table 4.1). The fact that K06 and K05 zircons yielded Pliocene (U-Th)/He dates suggests strongly that the break in million-year timescale exhumation rate patterns likely occurs between the latitudes of the K07 and K06 collection sites, over a distance of no more than 2.5 km

This distance interval includes the major knickpoint in the Dudh Kosi river (the likely local PT_1) discussed in Section 2 above. It also includes the steepest precipitation gradient along the valley based on the 1998-2005 TRMM dataset: south of the K07-K06 transition, the TRMM-estimated annual rainfall is ≥ 3 m/a, but annual rainfall is ≤ 0.5 m/a north of the K07 locality. Given these correlations, at least four interpretations are possible for the observed spatial variations in million-year timescale exhumation rates across the range.

7.1 Progressive Northward Migration of the Tibetan Plateau Margin

Carrapa et al. (2016) suggested that a "protoplateau" once extended much farther south than the modern southern edge of the Tibetan Plateau in the Everest region, and that very young exhumation rates on the southern flank of the Himalaya reflect erosionally driven northward retreat of the plateau over the last *ca.* 5 Ma. This idea, which can be traced back through similar inferences regarding Himalayan thermochronometric data (e.g., Wang et al., 2010), has its origins in models designed to explain topographic evolution of the Tibetan and Andean plateaus (e.g., Masek et al., 1994). While there is no doubt that northward retreat of the Tibetan Plateau could have produced a northward-propagating signal of very young exhumation, there must be a lag between the time the edge of the plateau passes a certain point on an antecedent drainage and the time that this signal is recorded by thermochronometers (McDermott et al., 2013). At any given time during retreat, the edge of the plateau should be marked by a distinctive knickpoints; we infer that the knickpoint we identified on the Dudh Kosi marks the edge of the plateau today. While the differential precipitation across such a knickpoint is large, there is effectively no difference in the total erosion immediately to either side of the knickpoint. It is only after the knickpoint migrates upstream that the higher precipitation downstream has time to result in significant erosional exhumation. The result of this is a very gradual change in thermochronometric cooling ages. To illustrate this point, we used the approach of Whipple et al. (2016) to model the 1D evolution of a bedrock channel over a period of two million years and have considered the implications of the results in light of our 1D thermal-kinematic modeling of the

exhumation rate history for sample K07, the southernmost of our samples lying north of the modern knickpoint.

The Whipple et al. (2016) finite-element method employs the popular detachment-limited stream power river incision model (Howard, 1994; Whipple and Tucker, 1999):

$$\frac{dz}{dt} = U - KA^m S^n \tag{4.1}$$

to examine how a stream profile evolves over time. In Equation 4.1, $\frac{dz}{dt}$ is the rate of change of channel elevation, K is the erosion coefficient (set by climate and rock properties), A is the drainage area, U is rock uplift rate defined relative to erosional base level, K is an erodability coefficient, and S is the channel gradient. For our purposes, we assumed the parameters K = 5E-10 yr^{-1}, m/n = ½, and n = 2. For our initial condition, we modeled an initial proto-plateau margin uplifting *(U)* at a rate of *ca.* 1.3 km/Myr, the average exhumation rate for the past ca. 2 Ma south of the knickpoint. To determine the amount of knickpoint retreat and the predicted position of a *ca.* 4 Ma (the ZrnHe date of K06), we ran the model for another 2 Ma and decreased the uplift rate to zero. The resulting progressive change in stream profile – as well as the progressive erosion of rock south of the northward-migrating knickpoint – is illustrated in Figure 4.6. Using the chosen parameters, the model predicts roughly 25 km of northward retreat of the knickpoint over the past two million years. We wish to add that if we ran the channel model since the onset of rapid incision (i.e. for *ca.* 5), the position of the proto-plateau would have to be much farther to the south (close the modern range front) in order for the

model to yield the right amount of migration so that the position of the knickpoint resembles that of the present-day.

Since ZrnHe closure at 12.1 Ma, the average exhumation rate for sample K07 has been 0.34 km/Ma. We take this as a reasonable estimate of the exhumation rate on the southern margin of the plateau at any time during plateau retreat. Noting that sample K06, collected <7 km south of the knickpoint, has a much younger ZrnHe cooling age of 4.14 Ma, we conducted simple thought experiment: can how deep below the present-day collection elevation of K07 would a sample need to be to yield a 4.14 Ma cooling age? Using the average exhumation rate for K07, we can estimate the depth at *ca.* 2.7 km. The projection of that horizon southward to the modern topographic profile shown in Figure 4.6 indicates the predicted locality for a sample collected today with a 4.14 Ma ZrnHe date: roughly 9.3 km south of the modern knickpoint, much farther south than the K06 collection locality. This discrepancy provides strong evidence that plateau margin retreat alone cannot explain the observed thermochronologic data. It also should be stressed that the distance estimate of *ca.* 9.3 km is an absolute minimum estimate as we did not factor in the relaxation of the ZrnHe isotherm below the plateau following the cessation of activity on the STDS into our calculations. ZrnHe isotherm relaxation after the *ca*.12 Ma ZrnHe closure of sample K07 only makes the projected depth of a 4.14 Ma ZrnHe cooling age deeper and thus, farther to the south of the knickpoint.

7.2 Progressive Northward Growth of a Duplex System at Depth

A second possibility is suggested by previous tectonic studies and thermal-kinematic modeling of the Himalayan orogenic wedge (e.g., Cattin and Avouac, 2000;

Decelles et al., 2001; Lavé and Avouac, 2001; Bollinger et al., 2004; Bollinger et al., 2006; Herman et al., 2010; Robinson and Pearson, 2013). Many researchers have suggested the existence of a late Cenozoic structural duplex in the Lesser Himalayan tectonostratigraphic zone structurally beneath the Greater Himalayan gneisses and related to a northward-dipping ramp in the basal thrust of the wedge (Main Himalayan Thrust, or Himalayan Sole Thrust). Kinematic and thermal-kinematic models predict patterns of the cooling ages from low-temperature thermochronometers characterized by: 1) an abrupt decrease in cooling age for a specific thermochronometer (like ZrnHe) from south to north above the top of the ramp (on the south side of the duplex); 2) a broad zone of young cooling ages above the duplex; and 3) an abrupt increase in cooling age from south to north above the base of the ramp on the north side of the duplex (Herman et al., 2010). The sort of abrupt south-to-north increase in cooling age predicted by such models was observed by Adams et al. (2013) in the Bhutan Himalaya, roughly coincident with the physiographic transition that occurs where the high-relief Higher Himalaya meet the more subdued Lower Himalayan ranges (Hodges et al., 2001). Noting that this disruption in cooling age pattern coincided with a steeply northward dipping structure they referred to as the Lhuntse fault, Adams et al. (2013), suggested that the fault is a normal-sense structure localized by the back of the duplex. However, this position for the back of the duplex lies far south of PT_1 in the Bhutan Himalaya, and most published interpretations of tectonic architecture of the orogenic wedge place the Lesser Himalayan duplex too far south to explain an abrupt transition in cooling ages near PT_1 such as that observed in our Khumbu transect (e.g., Lavé and Avouac, 2001). A notable exception is the geometry inferred by Herman et al. (2010) for the base of the ramp in the Himalayan Sole Thrust,

although the viability of that geometry has been questioned on the basis of recent analyses of the geodetic signature of the 2015 Gorkha earthquake in central Nepal (Whipple et al., 2016).

7.3 Young Normal Faulting at the Position of the Dudh Kosi Knickpoint

Recent work elsewhere in the central Himalaya has provided evidence for the existence of Pliocene-Pleistocene low-angle (north-dipping) normal faults (detachments) – with geometries similar to faults of the Miocene South Tibetan detachment system – at the position of major PT_1 knickpoints on Transhimalayan rivers. For example, McDermott et al. (2013, 2015) documented both field and thermochronologic evidence for such structures in the Nyalam area of southern Tibet (in the Bhote Kosi drainage) and the Annapurna-Dhaulagiri regions of central Nepal (in the Kali Gandaki and Myagdi Khola drainages). As articulated by McDermott et al. (2013), sustained activity on such a detachment would cause rock uplift rates to be higher in the footwall, leading to a sharp knickpoint in the river profile. High rates of tectonic denudation would also result in a sharp break in the pattern of dates from low-temperature thermochronometers, with much younger cooling ages south of the fault trace at the knickpoint. Similarity of the relationships between thermochronometric patterns and major knickpoints in the Bhote Kosi, Kali Gandaki, and Myagdi Khola drainages to the relationship observed in the Dudh Kosi drainage suggest that a similar structure could exist in our study area between the collection sites of K07 and K06. However, although we did not undertake detailed geologic mapping in the vicinity of the Dudh Kosi knickpoint, we saw no field evidence to support the existence of a detachment of appropriate geometry there, and study of

landforms in the area using Google Earth imagery revealed no obvious geomorphic expression of a detachment. Nevertheless, our past experience suggests that such evidence is often subtle, and thus more detailed fieldwork would be needed to test further the hypothesis that the observed thermochronometric pattern is related to young normal faulting.

7.4 Differential Erosion Due to Precipitation Patterns Persistent on Million-Year Timescales

Finally, the discrepant cooling age patterns and implied bedrock exhumation histories could be explained simply by a geographically sharp drop in monsoon rainfall on million-year timescales that mimics the current sharp drop in monsoon rainfall as constrained by TRMM satellite data (Bookhagen and Burbank, 2006). As noted in Section 1, such an inference is consistent with some previous studies of relationships between thermochronologic data and precipitation patterns elsewhere in the Himalaya and inconsistent with others (Burbank et al., 2003; Thiede et al., 2004, 2009; Blythe et al., 2007). We suggest that the discrepancies may reflect local precipitation pattern anomalies related to the channeling of monsoon storms up Transhimalayan drainages. Our study, designed to compare thermochronometric results across the Himalayan rain shadow outside a Transhimalayan drainage, avoids the possibility of ambiguity. ZrnHe and ApHe cooling age patterns and a major change in bedrock exhumation histories correspond closely to the modern-day rainfall transition (Figures 4.2 and 4.3). All of our bedrock samples collected immediately south of the rainfall transition, where mean annual rainfall amounts are typically higher than 4 m/yr, yield Plio-Pleistocene ZrnHe

and ApHe dates. These young dates persist southward along the transect even though the annual rainfall amounts decrease. We suggest this is due to the large amount of rain falling upstream, which contributes to the total flow of the Dudh Kosi downstream; erosional efficiency would be just as high in these southernmost areas as farther north where there is more annual rainfall.

The precipitous north-to-south drop in ZrnHe dates is easily explained if only the position of the Dudh Kosi knickpoint has remained geographically fixed since the Pliocene and did not retreat northward as modeled in Figure 4.6. Understanding why this might be true is challenging. Such a steady-state condition would likely require a balance of rock uplift south of the knickpoint with accelerated erosion south of the knickpoint so as to prevent upstream knickpoint migration. Such uplift might reflect accelerating growth of a ramp-related duplex, or southward extrusion of the Greater Himalayan infrastructure today beneath detachments such as those mapped by McDermott et al. (2013, 2015) in a manner similar to models southward channel flow of the Himalayan infrastructure beneath the South Tibetan detachment system (Nelson et al., 1996; Beaumont et al., 2001; Hodges et al., 2001; Grujic et al., 2002).

8. Conclusions

Contrasting modeled exhumation histories and cooling ages of GHS bedrock samples across a major erosional knickpoint in the Dudh Kosi river profile, well to the south of the range crest, suggest a strong correlation with central Himalayan rainfall patterns on million-year timescales, which is perhaps acting in concert with Pliocene extensional faulting and/or duplex growth in the Himalayan orogenic wedge. Exhumation

histories well to the north of the knickpoint in the Rongbuk valley indicate high erosion rates (*ca.* 3 mm/a) in the early Miocene from at least *ca.* 20 Ma to *ca.* 13 Ma during slip on the overlying Qomolangma detachment, after which exhumation rates drop drastically (Schultz et al., 2017). Samples K07 and K08, collected north of the knickpoint but south of the range crest, display similar exhumation histories to Rongbuk valley samples, with high exhumation rates early ~2 mm/a from *ca.* 20 to 13 Ma and low rates (<0.5 mm/a) from 13 Ma to the present. Modeled exhumation histories for GHS bedrock samples collected south of the knickpoint were similar prior to *ca.* 4 Ma, but different thereafter. At *ca.* 4 Ma, exhumation rates for these lower-elevation samples increased to *ca.* 4 mm/a until the Pleistocene when ZrnHe closure, and only a million years later, ApHe closure, occur.

A retreating plateau margin (Carrapa et al., 2016) is not an efficient mechanism to explain the sharply contrasting exhumation histories. Though it is likely that increased erosion rates from the newly initiated monsoonal pattern beginning in the middle Miocene removed a large cover of material from the southern flank of the range, plateau incision alone would not result in a sharp transition in cooling ages as we observe, but rather a much broader decrease in cooling ages with increasing downstream distance from the modern-day location of the knickpoint. The likeliest explanations involve persistence of the current Himalayan rainfall effect backward in time until at least the Pliocene, plausibly accompanied by accelerated rock uplift related to underplating at the base of the orogenic wedge and/or southward extrusion of rocks beneath a detachment at the Dudh Kosi knickpoint.

9. Acknowledgments

This work was supported by National Science Foundation Tectonics Program grant EAR1346360 to K.V.H. The fieldwork in Nepal would not have been possible without the logistical assistance of Bhim Chand (Earth's Paradise Treks and Expeditions, Kathmandu) and Bir Tamang (Earth's Paradise Treks and Expeditions, Kathmandu). M.H.S. would like to thank Alexandra Horne (Arizona State University) for her great assistance in the field. Many thanks to Willi Kappler and Byron Adams (Department of Geosciences, Universität Tübingen) for their assistance with running the Monte Carlo version of *Pecube* used in this study. Thanks also to Adam Forte (Arizona State University) for help with the topography tools in *Matlab*.

10. Figure captions

Figure 4.1. Shaded relief map of the central Himalaya with TRMM rainfall data overlay. The range crest is shown as are hexagons revealing the locations of major knickpoints of Transhimalayan rivers as described by McDermott et al. (2013, 2015). The inset shows our study area (Figure 4.3). Major peaks (>8000 m) are indicated by triangles (DH = Dhaulagiri; A = Annapurna I, and EV = Everest).

Figure 4.2. Topographic and TRMM swath profiles at the longitude of Mount Everest. Light grey shading indicates topography (scale on left of diagram) and dark grey shading is the TRMM profile (scale on right of diagram). The bedrock sampling locations of Schultz et al. (2017) are indicated by the black circles and the white circles show the bedrock sampling localities of this study. The major knickpoint in the Dudh Kosi river

profile is indicated by the hexagon. Note the extreme vertical exaggeration of this figure.

Figure 4.3. Map of the Mount Everest region with an overlay of TRMM rainfall data showing all GHS bedrock sampling localities (circles). Schultz et al. (2017) collected samples R01 through R08 and samples K01 through K08 were collected for this study. Lighter shading indicates higher amounts annual rainfall, whereas low annual rainfall amounts are shown with darker shading. The hexagon indicates a major knickpoint in the Dudh Kosi profile.

Figure 4.4. A and B) Muscovite $^{40}Ar/^{39}Ar$ release spectra for samples K07 and K08. Both samples yielded relatively uncomplicated plateau ages. Age information can be found in Table 4.1 and C1) Biotite $^{40}Ar/^{39}Ar$ release spectra samples K01 and K07. These are the only two biotite samples that yielded plateau ages. Age information found in Table 4.1 and C1. The biotite release spectra for samples K02, K03, K04, and K08 can be found in Appendix Figure C1.

Figure 4.5. Exhumation rate histories from thermal-kinematic modeling using a 1D version of *Pecube.* The modeled exhumation rates for sample R01 (with MsAr, ZrnHe, and ApHe constraints) are from Schultz et al. (2017). The 1D modeling results for samples K08 (MsAr, ZrnHe, and ApHe), K07 (BtAr and ZrnHe), K04, K03, and K02 (BtAr, ZrnHe, and ApHe) are from this study. The bold black lines indicate the mean exhumation rate history and the horizontal grey boxes indicate two standard deviations from the mean. The input chronometer data (along with their 2σ uncertainties) are

presented at the top of each figure pane. The number of acceptable fits to the data are noted. See Figure 4.3 for sample locality information.

Figure 4.6. Output of a simple 1D channel evolution model (e.g. Whipple et al., 2016) showing a retreating knickpoint. The solid black profile shows the channel's present-day location. The dashed profile indicates the location of the channel at 2 Ma. The dashed line is the approximate position of where a ZrnHe date of *ca.* 4.14 Ma would be based on the modeled exhumation rates of sample K07 (see Section 7.1 for explanation). Model results indicate that at least 2.7 km of material had to be removed to produce sample K04's ZrnHe date of *ca.* 4.14 Ma. If plateau incision was the sole mechanism at work, a ZrnHe date this young would not be observed until reaching a location of ca. 9.3 km downstream from the modern-day position of the knickpoint.

11. References

Adams, B. A., Hodges K.V., van Soest M.C., and Whipple, K.X. (2013). Evidence for Pliocene-Quaternary normal faulting in the hinterland of the Bhutan Himalaya. *Lithosphere*, *5*, 438-449.

Adams, B.A., Hodges, K.V., Whipple K.X., Ehlers T.A., van Soest M.C., and Wartho, J. (2015). Constraints on the tectonic and landscape evolution of the Bhutan Himalaya from thermochronometry. *Tectonics*, *32*(6), 1329-1347.

Barros, A. P., Chiao, S., Lang, T.J., Burbank, D., and Putkonen, J. (2006). In *Tectonics, Climate, and Landscape Evolution* Vol. Geological Society of America Special Paper *398* (eds S.D. Willett, N. Hovius, M.T. Brandon, & D.M. Fisher), 17-38 (Geological Society of America).

Beaumont, C., Jamieson, R. A., Nguyen M. H., and Lee, B. (2001). Himalayan tectonics explained by extrusion of a low-viscosity crustal channel coupled to focused surface denudation. *Nature, 414*, 738-742.

Blythe, A. E., Burbank, D. W., Carter, A., Schmidt, K., and Putkonen J. (2007). Plio-Quaternary exhumation history of the central Nepalese Himalaya: 1. Apatite and zircon fission track and apatite U-Th /He analyses. *Tectonics, 26*,

doi:Tc300210.1029/2006tc001990.

Bollinger, L., Avouac, J. P., Beyssac, O., Catlos, E. J., Harrison, T. M., Grove, M., Goffe, B., and Sapkota, S. (2004). Thermal structure and exhumation history of the Lesser Himalaya in central Nepal. *Tectonics*, *23*(5).

Bollinger, L., Henry, P., and Avouac, J. P. (2006). Mountain building in the Nepal Himalaya: Thermal and kinematic model. *Earth And Planetary Science Letters*, *244*, 58-71.

Bookhagen, B. and Burbank, D.W. (2006). Topography, relief, and TRMM-derived rainfall variations along the Himalaya. *Geophysical Research Letters, 33*, doi:L0840510.1029/2006gl026037.

Bookhagen, B. and Burbank, D.W. (2010). Toward a complete Himalayan hydrological budget: Spatiotemporal distribution of snowmelt and rainfall and their impact on river discharge. *J. Geophys. Res., 115*, F03019, doi:10.1029/2009jf001426

Bookhagen, B., Thiede, R.C., and Strecker, M.R. (2005a). Late Quaternary intensified monsoon phases control landscape evolution in the northwest Himalaya. *Geology 33*, 149-152.

Bookhagen, B., Thiede, R.C., and Strecker, M.R. (2005b). Abnormal monsoon years and their control on erosion and sediment flux in the high, arid northwest Himalaya. *Earth and Planetary Science Letters, 231*, 131-146.

Bookhagen, B. and Burbank, D.W. (2010). Toward a complete Himalayan hydrological budget: Spatiotemporal distribution of snowmelt and rainfall and their impact on river discharge. *J. Geophys. Res., 115*, F03019, doi:10.1029/2009jf001426

Braun, J. (2003). Pecube: A new finite-element code to solve the 3D heat transport equation including the effects of a time-varying, finite amplitude surface topography. *Computers & Geosciences*, *29*(6), 787-794.

Braun, J., van der Beek, P., Valla, P., Robert, X., Herman, F., Glotzbach, C., Pedersen, V., Perry, C., Simon-Labric, T., and Prigent, C. (2012). Quantifying rates of landscape evolution and tectonic processes by thermochronology and numerical modeling of crustal heat transport using PECUBE. *Tectonophysics*, *524–525*, 1-28.

Brewer, I. D., Burbank, D. W., and Hodges, K. V. (2003). Modelling detrital cooling-age populations: insights from two Himalayan catchments. *Basin Research, 15*, 305-320.

Burbank, D. W., Blythe, A. E., Putkonen, J., Pratt-Sitaula, B., Gabet, E., Oskin, M., Barros, A., and Ojha, T.P. (2003). Decoupling of erosion and precipitation in the Himalayas, *Nature, 426*, 652-655, doi:10.1038/nature02187.

Burchfiel, C. B., Chen, Z., Hodges, K.V., Liu, Z.Y., Royden, L.H., Deng, C., and Xu, J. (1992), The South Tibetan detachment system, Himalayan orogen: extension contemporaneous with and parallel to shortening in a collisional mountain belt. *Geological Society of America Special Paper*, *269*, 41 p.

Carrapa, B., Robert, X.,. DeCelles, P.G., Orme, D.A., Thomson, S.N., and Schoenbohm, L.M. (2016). Asymmetric exhumation of the Mount Everest region: Implications for the tectono-topographic evolution of the Himalaya. *Geology*, doi: 10.1130/G37756.1.

Cattin, R., and Avouac, J.P. (2000). Modeling mountain building and the seismic cycle in the Himalaya of Nepal. *Journal of Geophysical Research*, *105*(13), 13,389-13,407.

Copeland, P., Parrish, R. R., and Harrison, T. M. (1988). Identification of inherited radiogenic Pb in monazite and its implications for U-Pb systematics. *Nature*, *333*, 760-763.

Cottle, J.M., Jessup, M.J., Newell, D.L., Searle, M.P., Law, R.D., and Horstwood, M.S.A. (2007). Structural insights into the early stages of exhumation along an orogen-scale detachment: The South Tibetan Detachment System, Dzakaa Chu section, Eastern Himalaya. *Journal of Structural Geology, 29,* p. 1781-1797.

Cottle, J. M., Searle, M. P., Jessup, M. J., Crowley, J. L., and Law, R. D. (2015). Rongbuk re-visited: Geochronology of leucogranites in the footwall of the South Tibetan Detachment System, Everest Region, Southern Tibet. *Lithos*, *227*, 94-106.

DeCelles, P. G., et al. (2001). Stratigraphy, structure, and tectonic evolution of the Himalayan fold-thrust belt in western Nepal. Tectonics 20, 487-509.

Fleck, R. J., Sutter, J.F., and Elliot, D.H. (1977). Interpretation of discordant $^{40}Ar/^{39}Ar$ age spectra of Mesozoic tholeiites from Antarctica. *Geochimica et Cosmochimica Acta*, *41*, 15-32.

Gabet, E. J., Burbank, D.W., Pratt-Sitaula, B., Putkonen, J., and Bookhagen, B. (2008). Modern erosion rates in the High Himalayas of Nepal. *Earth and Planetary Science Letters, 267*, 482-494, doi:10.1016/j.epsl.2007.11.059.

Gébelin, A., Mulch, A., Teyssier, C., Jessup, M.J., Law, R.D., and Brunel, M. (2013). The Miocene elevation of Mount Everest. *Geology*, *41*(7), 799-802.

Grujic, D., Hollister, L. S., and Parrish, R. R. (2002). Himalayan metamorphic sequence as an orogenic channel; insight from Bhutan. *Earth And Planetary Science Letters*, *198*, 177-191.

Herman, F., Copeland, P., Avouac, J-P., Bollinger, L., Mahéo, G., Le Fort, P., Rai, S., Foster, D., Pêcher, A., Stüwe, K., and Henry, P. (2010). Exhumation, crustal deformation, and thermal structure of the Nepal Himalaya derived from the inversion of thermochronological and thermobarometric data and modeling of the topography. *Journal of Geophysical Research – Solid Earth, 115*, doi:B0640710.1029/2008jb006126.

Hodges, K.V. (2000). Tectonics of the Himalaya and southern Tibet from two perspectives. *Geological Society of America Bulletin*, *112*, 324-350.

Hodges, K.V. (2014). Thermochronology in Orogenic Systems, in: Holland, H.D., Turekian, K.K. (Eds.), *Treatise on Geochemistry, Second Edition, 4,* Elsevier, Oxford, 281-308.

Hodges, K. V., Hurtado, J.M., and Whipple, K.X. (2001). Southward extrusion of Tibetan crust and its effect on Himalayan tectonics. *Tectonics, 20*, 799-809.

Hodges, K. V., Parrish, R.R., Housh, T.B., Lux, D.R., Burchfiel, B.C., Royden, L.H., and Chen, Z. (1992). Simultaneous Miocene extension and shortening in the Himalayan orogen. *Science*, *258*, 1466–1470.

Hodges, K. V., Bowring, S., Davidek, K., Hawkins, D., and Krol, M. (1998). Evidence for rapid displacement on Himalayan normal faults and the importance of tectonic denudation in the evolution of mountain ranges. *Geology*, *26*, 483–486.

Hourigan, J.K., Reiners, P.W., and Brandon, M.T. (2005). U-Th zonation dependent alpha-ejection in (U-Th)/He chronometry. *Geochimica et Cosmochimica Acta, 69*, 3349-3365.

Hubbard, M., and Harrison, T.M. (1989). $^{40}Ar/^{39}Ar$ age constraints on deformation and metamorphism in the Main Central Thrust zone and Tibetan Slab, eastern Nepal Himalaya. *Tectonics*, *8*(4), 865 – 880.

Kelley, S. (2002). Excess argon in K-Ar and Ar-Ar geochronology. *Chemical Geology, 188*(1-2), 1-22.

Lavé, J., and Avouac, J.P. (2001). Fluvial incision and tectonic uplift across the Himalayas of central Nepal. *Journal of Geophysical Research, 106*(26), 26,561-26,591.

Masek, J.G., Isacks, B.L., Gubbels, T.L., and Fielding, E.J. (1994). Erosion and tectonics at margins of continental plateaus. J. Geophysical Research, *99*, 13941-13956.

McDermott, J.A., Whipple, K.X., Hodges, K.V., and van Soest, M.C. (2013). Evidence for Plio-Pleistocene north-south extension at the southern margin of the Tibetan Plateau, Nyalam region. *Tectonics, 32*, 317-333, doi:10.1002/tect.20018.

McDermott, J.A., Hodges, K.V., Whipple, K.X., van Soest, M.C., and Hurtado, J.M. (2015). Evidence for Pleistocene Low-Angle Normal Faulting in the Annapurna-Dhaulagiri Region, Nepal. *Journal of Geology*, *123*(2), 133 – 151.

Murphy, M.A. and Harrison, T.M. (1999). Relationship between leucogranites and the Qomolangma detachment in the Rongbuk Valley, south Tibet. *Geology, 27*(9), p. 831-834.

Nelson, K.D., Zhao, W., Brown, L.D., Kuo, J., Che, J., Xianwen, L., Klemperer, S., Makovsky, Y., Meissner, R., Mechie, J., Kind, R., Wenzel, F., Ni, J., Nabelek, J., Chen, L., Handong, T., Wenbo, W., Jones, A.G., Booker, J., Unsworth, N., Kidd, W.S.F., Hauk, M., Alsdorf, D., Ross, A., Cogan, M., Wu, C., Sandvol, E.A., and Edwards, M. (1996). Partially molten middle crust beneath southern Tibet: Synthesis of Project INDEPTH Results. *Science*, *274*, 1684-1688.

Orme, D.A., Reiners, P.W., Hourigan, J.K., and Carrapa, B. (2015). Effects of inherited cores and magmatic overgrowths on zircon (U-Th)/He ages and age-eU trends from Greater Himalaya sequence rocks, Mt. Everest region, Tibet. *Geochemistry, Geophysics, Geosystems*, DOI 10.1002/2015GC005818

Robinson, D. M. and Pearson, O.N. (2013). Was Himalayan normal faulting triggered by initiation of the Ramgarh-Munsiari thrust and development of the Lesser Himalayan duplex? *International Journal of Earth Sciences, 102*(7), 1773-1790.

Roddick, J.C., Cliff, R.A. and Rex, D.C. (1980). The evolution of excess argon in Alpine biotites – A ^{40}Ar-^{39}Ar analysis. *Earth and Planetary Science Letters*, *48*, 185-208.

Schultz, M.H., Hodges, K.V., Ehlers, T.A., van Soest, M.C., and Wartho, J-A. (2017). Thermochronologic constraints on the Miocene slip history of the South Tibetan detachment system, south-central Tibet. *Earth and Planetary Science Letters*, *459*, 105-117.

Streule, M. J., Carter, A., Searle, M.P., and Cottle, J.M. (2012). Constraints on brittle field exhumation of the Everest-Makalu section of the Greater Himalayan Sequence: Implications for models of crustal flow. *Tectonics, 31*, doi:Tc301010.1029/2011tc003062.

Stübner, K., Warren, C., Ratschbacher, L., Sperner, B., Kleeberg, R., Pfänder, J., and Grujic, D. (2017). Anomalously old biotite 40Ar/39Ar ages in the NW Himalaya. *Lithosphere,* doi: https://doi.org/10.1130/L586.1.

Thiede, R.C., Bookhagen, B., Arrowsmith, J.R., Sobel, E.R., and Strecker, M.R. (2004). Climatic control on rapid exhumation along the Southern Himalayan Front. *Earth and Planetary Science Letters*, *222*, 791-806.

Thiede, R.C., and Ehlers, T.A. (2013). Large Spatial and Temporal Variations in Himalayan Denudation. *Earth and Planetary Science Letters*, *371-372*, 278-293.

Viskupic, K., Hodges, K.V. and Bowring, S.A. (2005). Timescales of melt generation and the thermal evolution of the Himalayan metamorphic core, Everest region, eastern Nepal. *Contrib. Mineral. Petrol., 149,* p. 1-21.

Wang, A., Garver, J.I., Wang, G., Smith, J.A., and Zhang, K. (2010). Episodic exhumation of the Greater Himalayan Sequence since the Miocene constrained by fission track thermochronology in Nyalam central Himalaya. *Tectonophysics*, *495*, 315-323.

Whipple, K.X., and Tucker, G.E. (1999). Dynamics of the stream-power river incision model: Implications for height limits of mountain ranges, landscape response timescales, and research needs. *Journal of Geophysical Research-Solid Earth, 104*(B8), 17661-17674. Doi:10.1029/1999jb900120

Whipple, K.X., DiBiase, R.A., Ouimet, W.B., and Forte, A.M. (2016). Preservation or piracy: Diagnosing low-relief, high-elevation surface formation mechanism. *Geology,* doi: 10.1130/G38490.1.

Whipple, K. X., Shirzaei, M., Hodges, K.V., and Arrowsmith, J.R. (2016). Active shortening within the Himalayan orogenic wedge implied by the 2015 Gorkha earthquake. *Nature Geoscience*, *9*(9), 711-716.

Willett, S. D. (1999). Orogeny and orography: the effects of erosion on the structure of mountain belts. *Journal of Geophysical Research, 104*, 28957-28981.

Wobus, C. W., Whipple, K.X., and Hodges, K.V. (2006). Neotectonics of the central Nepalese Himalaya: Constraints from geomorphology, detrital 40Ar/39Ar thermochronology, and thermal modeling. *Tectonics, 25*, doi:10.1029/2005TC001935.

Wulf, H., Bookhagen, B., and Scherler D. (2010). Seasonal precipitation gradients and their impact on fluvial sediment flux in the Northwest Himalaya. *Geomorphology, 118*, 13-21, doi:10.1016/j.geomorph.2009.12.003.

TABLE 4.1. THERMOCHRONOLOGIC DATA FOR GREATER HIMALAYAN SEQUENCE SAMPLES, KHUMBU REGION, NEPAL

Sample number	Latitude	Longitude	Elevation (m)	Rock Type	**MsAr Date (Ma)**	**BtAr Date (Ma)**	**ZrnHe Date (Ma)[c]**	**ApHe Date (Ma)[c]**
K01	27.69531°N	86.72565°E	2766	Biotite Gneiss	-	12.80 ± 0.19 (61)[a]	-	2.03 ± 0.25 (3)
K02	27.790297°N	86.718155°E	2901	Biotite Gneiss	-	13.813 ± 0.089[b]	2.43 ± 0.23 (6)	3.4 ± 1.3 (5)
K03	27.84623°N	86.74149°E	3663	Biotite Gneiss	-	13.00 ± 0.13[b]	2.57 ± 0.39 (7)	1.33 ± 0.13 (1)
K04	27.87391°N	86.73954°E	3999	Biotite Gneiss	-	16.85 ± 0.12[b]	3.33 ± 0.25 (6)	2.32 ± 0.11 (2)
K05	27.89237°N	86.71404°E	4396	Biotite Gneiss	-	-	3.39 ± 0.29 (8)	-
K06	27.92701°N	86.70844°E	4596	Biotite Gneiss	-	-	4.14 ± 0.77 (4)	-
K07	27.94913°N	86.69547°E	4766	Leucogranite	16.413 ± 0.074 (90)[a]	16.461 ± 0.059 (69)[a]	12.1 ± 1.4 (6)	-
K08	27.99920°N	86.84812°E	5295	Leucogranite	16.77 ± 0.16 (76)[a]	17.18 ± 0.56[b]	13.50 ± 0.93 (4)	8.1 ± 3.4 (3)

[a]Plateau dates, quoted at two standard deviations of the ^{39}Ar and inverse variance-weighted mean for all steps. Numbers in parentheses indicates the cumulative $\%^{39}Ar$ for all steps on each plateau.

[b]Total-gas dates, quoted at two standard deviations of the ^{39}Ar- and inverse variance-weighted means multiplied by $MSWD^{0.5}$ (to account for over-dispersion)

[c]Inverse-variance weighted mean dates, quoted at two standard deviations of the weighted means and multiplied by $MSWD^{0.5}$ when necessary to account for over-dispersion. Numbers in parentheses indicate number of crystal dates averaged for the weighted mean.

FIGURE 4.1

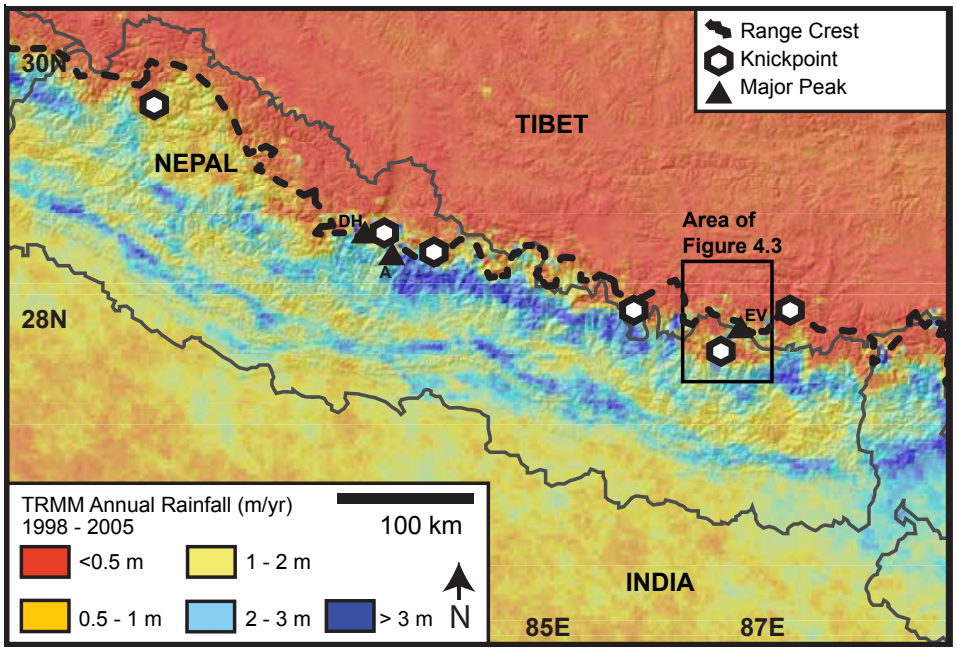
Range Crest
Knickpoint
Major Peak
30N
TIBET
NEPAL
DH
A
Area of
Figure 4.3
EV
28N
TRMM Annual Rainfall (m/yr)
1998 - 2005
100 km
<0.5 m
1 - 2 m
0.5 - 1 m
2 - 3 m
> 3 m
N
INDIA
85E
87E

FIGURE 4.2

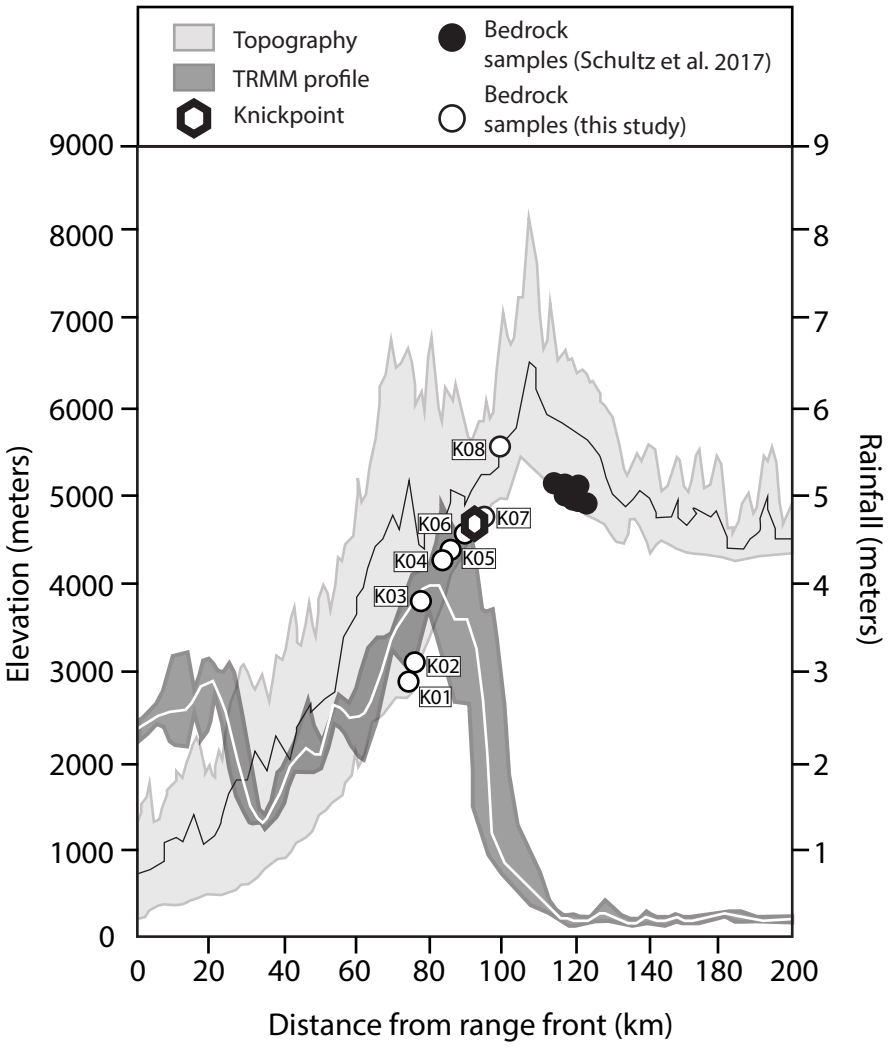
Topography
TRMM profile
Knickpoint
Bedrock samples (Schultz et al. 2017)
Bedrock samples (this study)
K08
K07
K06
K05
K04
K03
K02
K01
Elevation (meters)
Rainfall (meters)
Distance from range front (km)
0
1000
2000
3000
4000
5000
6000
7000
8000
9000
1
2
3
4
5
6
7
8
9
0
20
40
60
80
100
120
140
180
200

FIGURE 4.3

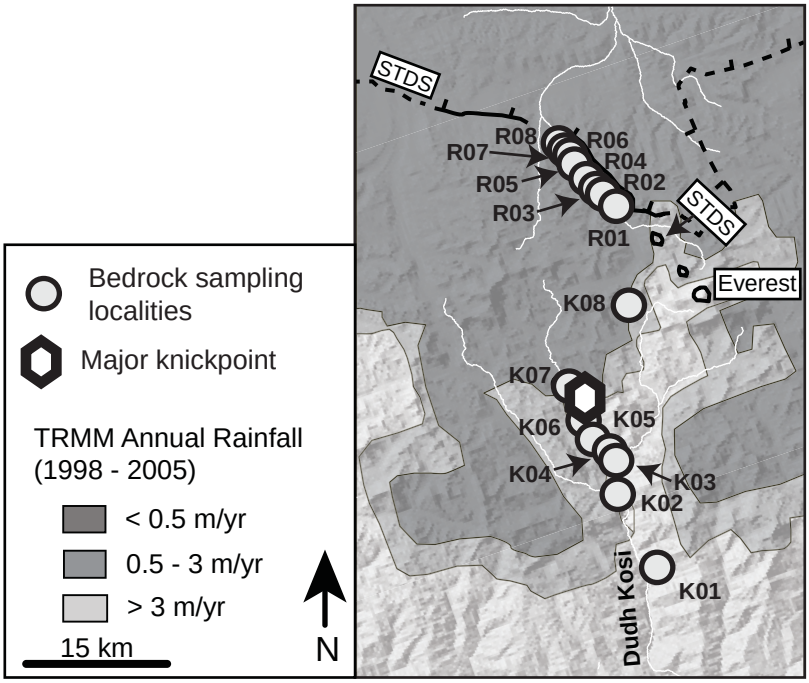
STDS
R08
R06
R07
R04
R05
R02
R03
STDS
R01
Everest
K08
K07
K06
K05
K04
K03
K02
K01
Dudh Kosi
Bedrock sampling localities
Major knickpoint
TRMM Annual Rainfall (1998 - 2005)
< 0.5 m/yr
0.5 - 3 m/yr
> 3 m/yr
15 km
N

FIGURE 4.4

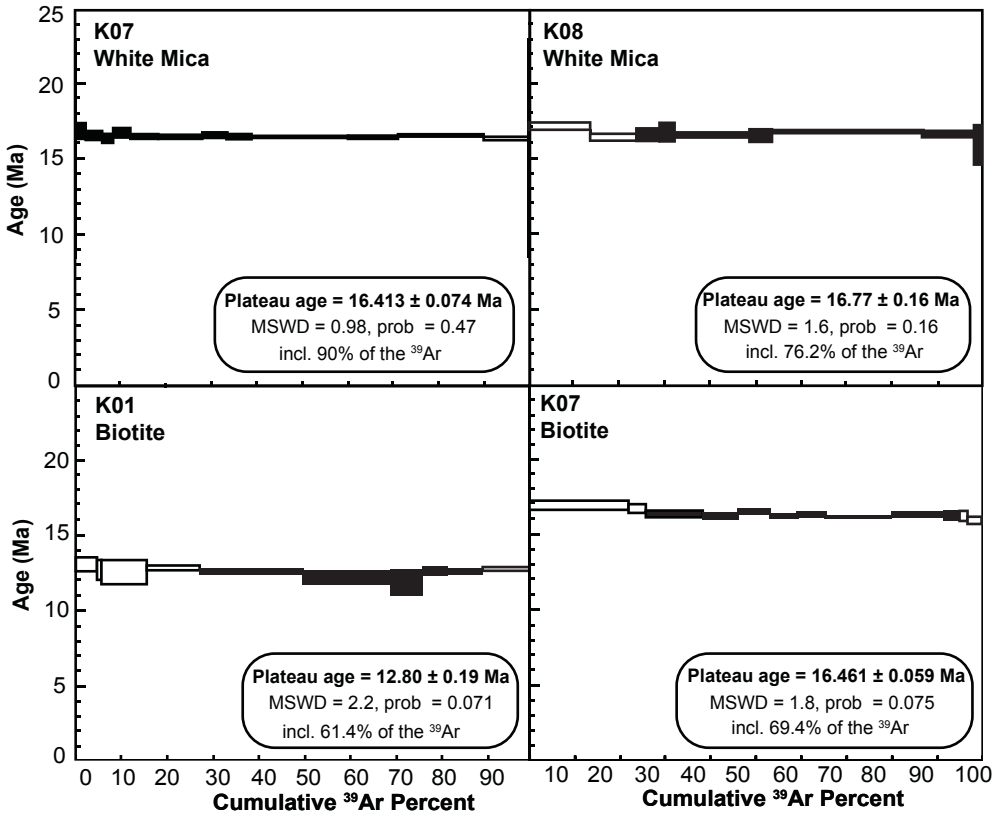
K07
White Mica
Plateau age = 16.413 ± 0.074 Ma
MSWD = 0.98, prob = 0.47
incl. 90% of the 39Ar
K08
White Mica
Plateau age = 16.77 ± 0.16 Ma
MSWD = 1.6, prob = 0.16
incl. 76.2% of the 39Ar
K01
Biotite
Plateau age = 12.80 ± 0.19 Ma
MSWD = 2.2, prob = 0.071
incl. 61.4% of the 39Ar
K07
Biotite
Plateau age = 16.461 ± 0.059 Ma
MSWD = 1.8, prob = 0.075
incl. 69.4% of the 39Ar
Age (Ma)
Cumulative 39Ar Percent

FIGURE 4.5

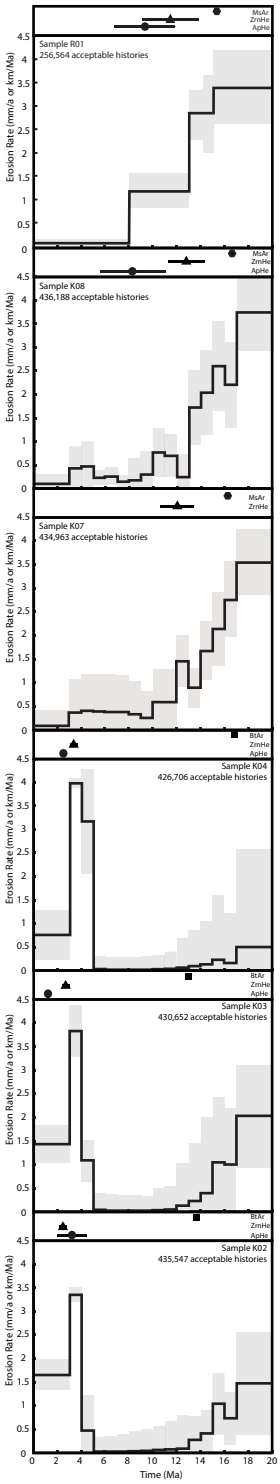
MsAr
ZrnHe
ApHe
Sample R01
256,564 acceptable histories
Sample K08
436,188 acceptable histories
Sample K07
434,963 acceptable histories
BtAr
Sample K04
426,706 acceptable histories
Sample K03
430,652 acceptable histories
Sample K02
435,547 acceptable histories
Erosion Rate (mm/a or km/Ma)
Time (Ma)

FIGURE 4.6

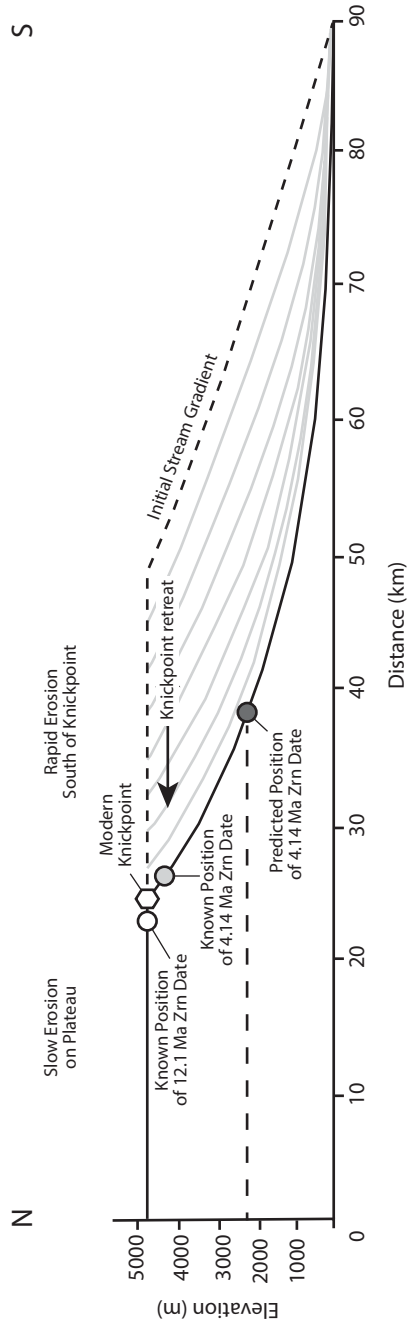
N
S
Slow Erosion
on Plateau
Rapid Erosion
South of Knickpoint
Modern
Knickpoint
Knickpoint retreat
Initial Stream Gradient
Known Position
of 12.1 Ma Zrn Date
Known Position
of 4.14 Ma Zrn Date
Predicted Position
of 4.14 Ma Zrn Date
Elevation (m)
5000
4000
3000
2000
1000
0
10
20
30
40
50
60
70
80
90
Distance (km)

CHAPTER 5

QUANTIFYING EROSION AND SEDIMENT MIXING OF THE RONGBUK GLACIAL CATCHMENT IN SOUTH-CENTRAL TIBET BY LASER ABLATION U/Pb and (U-Th)/He DOUBLE DATING

1. Abstract

The world's most recognizable mountain peaks and impressive valleys have been carved by the strong erosive power of glaciers. The central Himalayan Mountains of south-central Asia, containing many of the world's highest summits, have been heavily glaciated for the past *ca.* 2 Ma. Although much work has been done in recent years exploring the properties of modern-day glaciers in the High Himalaya as well as determining the timing of various major glacial retreats and advances, no study has yet examined the long-term spatial and temporal variation of erosion in a glaciated Himalayan catchment. Here we address this issue, applying the recently developed laser ablation U/Pb and (U-Th)/He double dating (LADD) technique to detrital zircons from mid-Holocene glacial moraine and outwash sediments from the modern-day glacier to help constrain how various glacial erosive processes shaped the Rongbuk glacial valley in the Everest region of south-central Tibet. Geologic mapping of the Rongbuk catchment has demonstrated that possible sources of these sediments include carbonate and siliciclastic rocks of the weakly metamorphosed and unmetamorphosed Tibetan Sedimentary sequence and high-grade metasedimentary and metaigneous rocks of the Greater Himalayan sequence and associated leucogranites. Many U/Pb detrital zircon dates from the ca. 8 to 2 ka Samdupo glacial moraine and modern outwash sediments are

consistent with derivation from the Greater Himalayan sequence and leucogranites due to the significant overlap of the previously reported distribution of detrital zircons from nearby bedrock exposures. In particular, (U-Th)/He dates for the moraine samples are similar to previously published helium dates for metamorphic and igneous bedrock samples from intermediate elevations of the valley near the mid-Holocene equilibrium line altitude for the Samdupo stage of the Rongbuk glacial system. In contrast, many zircons from the Dzakar Chu outwash detritus yielded significantly older Tertiary (U-Th)/He dates, implying that the outwash carries a much higher percentage of material eroded from upper elevations in the catchment than the Rongbuk glacial system did in the relatively recent past.

2. Introduction

The Himalayan orogenic wedge, constructed by the collision of Greater India with Eurasia at ca. 50 Ma (van Hinsbergen et al., 2012), continues to be shaped by the extreme erosional capacity of both its glaciers and extensive fluvial systems. Though recent thermochronologic contributions using conventional bedrock techniques have greatly increased our understanding of the exhumation history throughout the High Himalaya, (Burbank et al., 2003; Blythe et al., 2007; Whipp et al., 2007; Streule et al., 2012; Carrapa et al., 2016; Schultz et al., 2017), datasets continue to be scarce, mostly due to the paucity of accessible outcrop at very high elevations and in very rugged terrain. The advent of new and improved techniques for detrital thermochronology, coupled with more established bedrock methods, have provided effective tools for understanding sediment mixing as well as the uplift and erosion of entire catchments, some of which are up to several hundred square kilometers in area (Brewer et al., 2003; Ruhl and Hodges, 2005; Reiners et al., 2007; Whipp et al., 2009). Although detrital thermochronology has primarily been used thus far to explore spatial erosion in fluvial catchments, several investigations in western North America and the Alps have shown the usefulness of applying detrital thermochronology techniques to glacial moraine and outwash sediments (Stock et al., 2006; Tranel et al., 2011; Ehlers et al., 2015; Enkelmann and Ehlers, 2015; Wangenheim and Glotzbach, 2015). Despite the fact that the closure temperatures of most thermochronometric systems are too high to be sensitive to topographic fluctuations in the landscape during glacial-interglacial cycles, thermochronometric analyses of older glacial moraine sediments have the useful ability to show temporal changes in erosion over longer timescales (Enkelmann and Ehlers, 2015). These applications also revealed

that the distributions of thermochronologic cooling ages from grains in moraine sediments may expose cooling age populations not evident from sampling non-glaciated bedrock localities alone and, importantly, that the non-uniformity of erosion in glacial catchments may lead to very different spatial patterns of erosion as opposed to fluvial catchments, most of which are assumed to erode comparatively uniformly (Ruhl and Hodges, 2005).

Efficient, high-resolution dating of detrital sediments has been made possible by the recent creation and subsequent development of the laser ablation (U-Th)/He and U/Pb double dating (LADD) technique (Evans et al., 2015; Horne et al., 2016). The LADD method is powerful as it can determine both a mineral's crystallization age as well as its cooling history during exhumation.

In this study, we present new detrital zircon laser ablation $^{206}Pb/^{238}U$ and (U-Th)/He datasets of outwash and glacial moraine sediments in the Rongbuk valley, a moderately-sized glacial catchment in the Everest region of south-central Tibet, to determine the spatial and temporal evolution of erosion and sediment mixing in a Himalayan glacial catchment as well as to better understand how distinct glacial processes of erosion may compare and contrast in the High Himalaya. We compare our detrital datasets to previously published bedrock (U-Th)/He zircon mean ages of the Greater Himalayan Sequence (GHS) from the Rongbuk valley (Schultz et al., 2017) to test the reliability of cooling and exhumation histories determined from bedrock data alone and we also expand on the advantages and caveats of the LADD technique.

3. Geographic and Geologic Setting

The Rongbuk valley in south-central Tibet (28.063159°N 86.865197°E to 28.273212°N 86.805560°E) is a glaciofluvial catchment with an area of *ca.* 430 km^2 that extends northward from the base of Mount Everest for about 35 km (Figures 5.1 and 5.2a). The West and East Rongbuk glaciers and other unnamed tributary glaciers are found in the upper reaches of the valley, and they merge to the north as the Rongbuk glacier. The northern, lower elevations of the valley are drained by the Dzakar Chu, which emanates from beneath the Rongbuk glacier. (The word "chu" in Tibetan is equivalent to "small river" in English.) The end of the valley corresponds to the confluence of the Dzakar Chu and the Gyachung Chu merging from the southwest.

Bedrock in the Rongbuk valley walls includes three basic units. High on the ridges surrounding the valley are Cambrian-Ordovician clastic and carbonate sedimentary – and, in some places, metasedimentary – rocks of the Tibetan sedimentary sequence (TSS; Myrow et al., 2009). Structurally beneath them lie Precambrian high-grade metasedimentary rocks of the Greater Himalayan sequence (GHS; Burchfiel et al., 1992; Searle et al., 2003). GHS units in the valley are intruded by abundant, locally derived dikes and sills of leucogranite, ranging in dimension up to several tens of meters (Searle, 1999). In the Rongbuk valley, both high-grade metamorphism and the anatectic melting responsible for the leucogranites are of predominantly middle Miocene age (e.g., Hodges et al., 1998; Murphy and Harrison, 1999; Cottle et al., 2015). Separating the TSS from the GHS and the leucogranites within it are low-angle faults with normal-sense displacement, which represent the South Tibetan detachment system in the Everest area (Burchfiel et al., 1992); Figure 5.1 depicts the trace of the structurally highest of these

faults – the Qomolangma detachment.

3.1 Glacial Geology

The Rongbuk valley is semi-arid and cold, with the extreme elevations of the Everest massif sheltering the valley from the heavy precipitation that falls during the Indian summer monsoon on the southern flank of the range. The glaciers in this region are polythermal with isolated areas of basal melting (Huang, 1990; Mann et al., 1996; Owen et al., 2009) and the modern ice terminus is situated ~10 km north of the base of Everest. Owen et al. (2009) identified six major glacial advances during the Quaternary in the Rongbuk valley through optically stimulated luminescence (OSL) and ^{10}Be terrestrial cosmogenic nuclide (TCN) dating techniques. The oldest dated moraine, the Tingri moraine, located near the north end of the valley, dates to before 330 ka, while the youngest Xarlungnama moraine that is situated less than a kilometer north of the modern ice terminus, was determined to be ca. 1.6 ka (Owen et al., 2009).

Perhaps the most prominent moraines in the Rongbuk valley are the hummocky Samdupo moraines that are found near the mouth of Hermit's Gorge (Figures 5.1 and 5.3). Owen et al. (2009) ascertained the dates of the Samdupo moraines to be mid-Holocene, between *ca.* 8 and 2 Ma, with two separate glacial advances occurring over that interval. Owen et al. (2009) estimated the equilibrium line-altitude (ELA), or the altitude at which there is a mass balance between accumulation and abrasion, during the Samdupo glacial advance to be ca. 6140 m, only slightly lower than the modern-day estimated ELA on Everest of ca. 6200 m. These authors also pointed out that, though the vertical change in the ELA is on the order of tens of meters, the length of glacial retreat

up-valley is on the kilometer scale, highlighting both the low gradient of the lower Rongbuk valley as well as the extremity in elevation at the southernmost regions of the catchment.

4. Previous Work

4.1 Geochronology and low-temperature thermochronology

Many previous geochronologic and thermochronologic studies have been conducted on the leucogranites and gneisses of the GHS in the Rongbuk valley due to the uniquely impressive exposure of the STDS in the valley as well as the relative ease of access compared to other regions of the Himalaya. Protolith ages for the GHS are lowermost Paleozoic-Neoproterozoic with Indian provenance, as determined from detrital samples collected in Nepal (Parrish and Hodges, 1996; DeCelles, 2000). The GHS underwent intense amphibolite to granulite facies metamorphism during the Oligocene and Miocene, resulting in anatectic melting at the highest structural levels (Simpson et al., 2000; Searle et al., 2003). Although (U-Th)/Pb systematics of the GHS accessory minerals are complex, formation ages of the leucogranites range between ca. 20 and 15 Ma with a dominant cluster of ages surrounding ca. 16.5 Ma (Hodges et al., 1998; Murphy and Harrison, 1999; Cottle et al., 2015).

The Mt. Qomolangma Formation TSS carbonates have Indian provenance and U/Pb zircon crystallization ages are Cambrian and younger (Myrow et al., 2009). The Cretaceous U/Pb dates are thought to reflect zircons that were deposited during the rifting of the northern margin of India from Gondwana (Myrow et al., 2009).

Bedrock thermochronologic datasets collected from GHS and leucogranite

samples the middle reaches of the Rongbuk valley at *ca.* 5000 m elevations have been published by Hodges et al. (1992), Orme et al. (2015), Carrapa et al. (2016), and Schultz et al. (2017). Collectively, these data suggest that the bedrock at these elevations cooled from peak metamorphic and igneous temperatures relatively rapidly to the ca. 400-600˚C temperatures recorded by medium-temperature isotopic thermochronometers (U/Pb titanite, $^{40}Ar/^{39}Ar$ hornblende, $^{40}Ar/^{39}Ar$ muscovite) between ca. 20.0 and 14.5 Ma, then cooled very rapidly through the nominal ca. 180˚C (U-Th)/He zircon closure temperature zone between 14.3 and 11 Ma. Much of this cooling is thought to be related to tectonic denudation through slip on the immediately overlying Qomolangma detachment (Cottle et al., 2015; Schultz et al., 2017).

The only previously published detrital thermochronology work in this region was that of Carrapa et al. (2016). They reported $^{40}Ar/^{39}Ar$ dates for detrital muscovites from modern sediment collected on the banks of the Dzakar Chu, near the sampling locality of the outwash sediment data we report below. (Note that Carrapa et al. (2016) referred to the Dzakar Chu as the "Rongbuk river".) Their muscovite dates are narrowly dispersed over *ca.* 3 million years, with a primary mode at *ca.* 16 Ma. Some are within the range of $^{40}Ar/^{39}Ar$ muscovite dates from bedrock samples collected at roughly the same elevation in the valley walls (Schultz et al., 2017), but *ca.* 82% are older, suggesting transport of the detritus from significantly higher elevations further upstream. Carrapa and co-workers found that fission-track analyses for detrital apatites from this sample were more widely dispersed than bedrock apatite fission-track dates from the same area, with many dates considerably older than those from the bedrock samples. They also reported detrital apatite dates from a modern sediment sample from the Gyachung Chu collected just

above its confluence with the Dzakar Chu (Figure 5.1); the results, less widely dispersed than those from the Dzakar Chu, were slightly younger for the most part. The bedrock geology of the Gyachung catchment has been mapped in far less detail than that of the Rongbuk catchment, but one possible interpretation of the younger fission track date population from the Carrapa et al. (2016) Gyachung Chu sample is that most of the Gyachung catchment is likely underlain by apatite-poor Tibetan sedimentary sequence units.

5. Methods

Detrital sediments were collected from near the headwaters of the modern Dzakar Chu (M05) and from four locations spread *ca.* 100 m apart, near the lowermost lateral moraine of the mid-Holocene Samdupo system (M01-M04). We chose to sample this moraine because it has been dated and is old enough to potentially uncover spatial and temporal variations in erosion, following the methods of Enkelmann and Ehlers (2015). All five detrital samples were collected proximal to the bedrock sampling transect of Schultz et al. (2017). Each included ~5 to 10 kg of fine-to-pebble-sized sediment (Figures 5.2b and 5.3).

5.1 Laser ablation zircon U/Pb geochronology and (U-Th)/He thermochronometry

All analyses reported below were obtained using a relatively new method of U/Pb and (U-Th)/He dating of zircon that employs focused ultraviolet lasers to extract material for parent and daughter isotopic analysis. A natural extension of laser ablation U/Pb and (U-Th)/He dating techniques developed earlier (Feng et al., 1993; Kosler et al., 2002;

Boyce et al., 2006; Gehrels, 2012; Tripathy-Lang et al., 2013), the "laser ablation double dating" (LADD) technique was recently described in two papers to which the reader is directed for more extensive descriptions of methodologies (Evans et al., 2015; Horne et al., 2016). All analyses were performed in the Group 18 Laboratories at Arizona State University.

We followed the general LADD protocols outlined in Horne et al. (2016) with some modifications designed to improve analytical precision. The Samdupo moraine and Dzakar Chu outwash samples were prepared for zircon extraction using conventional magnetic and heavy liquid techniques. Zircon grains were picked under a microscope without bias concerning shape and inclusions because our laser microprobe analyses would target domains within grain interiors. Precise targeting allowed us to avoid crystal margins and thus the need for alpha ejection corrections of raw (U-Th)/He dates (Farley et al., 1996; Hourigan et al., 2005), and to avoid inclusions that might compromise dating results (Tripathy-Lang et al., 2013). One source of sampling bias, however, may be the size of zircons picked for analysis: only crystals larger than ca. 60 μm were picked due to the need to have sufficient zircon for relatively high-precision dating. Picked zircons, along with natural and synthetic zircon standards, were mounted in low vapor-pressure epoxy (*Torr seal*) and polished prior to isotopic analysis. For LADD of zircon, both composition and isotopic standards are necessary. For the former, we used an in-house 'SynZircon' (^{238}U = 426 ± 14 ppm; ^{232}Th = 206 ± 19 ppm; Monteleone et al., 2009). For the latter, we used Fish Canyon Tuff for samples M01, M03, and M06 (28.3 ± 3.1 Ma; Dobson et al., 2008) and in-house Sri Lankan zircon for samples M02 and M04 (555 ± 11 Ma; Nasdala et al., 2004).

Isotopic analyses were done in two stages, the first designed to enable the measurement of ^{4}He concentrations and the second to enable U and Th concentrations and the necessary isotopic ratios for U/Pb geochronology. The first stage involved *in vacuuo* ablation of material destined for helium analysis using a Photon Machines (now Teledyne CETAC) *Analyte G2* ArF (193 nm) excimer laser microprobe. Although we used a 25 μm diameter spot size for most helium extractions, a few of the grains required a smaller, 15μm spot size instead. During the extractions, we applied 5 mJ of laser energy at 50% output power and a pulse frequency of 5 Hz for a total of 80 shots. This resulted in typical ablation depths for each analysis comparable to its spot diameter. After gas purification using reactive metal getters and a cryogenic trap, ^{4}He abundance for the ablated material was determined with a Thermo Scientific *Helix SFT* (split flight tube) magnetic mass spectrometer based on predetermined sensitivity for the ion counting detector employed for the measurement. Following the helium analyses, the pucks were extracted from the system and the volume of the ^{4}He ablation pits were measured using an ADE PhaseShift *MicroXAM* interferometric microscope. The best-fit volumes are then calculated using an in-house *Matlab* script. Assuming a nominal density, this information and the ^{4}He abundances determined by mass spectrometry were used to calculate ^{4}He concentrations.

The second analytical stage involved mounting the puck in a Photon Machines (now Teledyne CETAC) *HelEx Active*, two-volume ablation cell for U, Th, Sm, and Pb analysis by laser ablation, inductively coupled plasma-source mass spectrometry (LA-ICPMS). For each zircon with a 25μm-diameter ablation pit for Step 1 ^{4}He determination, a second 65μm-diameter pit, centered on the first, was ablated for the Step 2 analysis.

(For the zircons with 15 μm-diameter ablation pits, the Step 2 pit diameters were reduced to 50 μm.) During the extractions, we applied 5 mJ of laser energy at 100% output power and a pulse frequency of 5 Hz for a total of 565 seconds. This resulted in typical ablation depths for each analysis ≥ 20 μm deeper than the Step 1 ablation pits so that the analyzed U and Th would be more representative of the volume of zircon that may have contributed to the ^{4}He measured during Step 1. The Step 2 ablated material was streamed into a Thermo Scientific *iCap Q* quadrupole mass spectrometer for abundance measurements based on predetermined detector sensitivity. Afterwards, the puck was returned to the interferometric microscope for measurement of the Step 2 ablation pits, and the results could be used with the LA-ICPMS results to determine U and Th concentrations.

Step 1 and Step 2 concentration data were combined to calculate (U-Th)/He dates. Zircon ^{206}Pb/^{238}U dates were calculated from the Step 2 data using the *Iolite* software package (Hellstrom et al., 2008) that runs using the Wavemetrics *Igor Pro* data analysis environment. We used the *U-Pb Geochronology* data reduction scheme (DRS) included in *Iolite* (Paton et al., 2010). We did not apply a common Pb correction to Phanerozoic zircon because of its low fractional common Pb; common Pb corrections would not change the apparent ^{206}Pb/^{238}U dates beyond the reported precision limits. All uncertainties in our zircon ^{206}Pb/^{238}U (ZrnPb) and (U-Th)/He (ZrnHe) dates quoted at the 2σ confidence level.

6. Results

Based on the yield of zircon crystals from bedrock samples in the Rongbuk

valley, we anticipated each of the moraine samples as well as the modern outwash sediment sample to contain abundant zircons. Each of the samples, however, yielded only ~60 to 70 crystals, and a significant number of those were too small to be dated effectively using the LADD method given the young (U-Th)/He dates we anticipated based on our experience with nearby bedrock samples. Moraine sample M02 contained the largest number of datable grains at 34, with samples M01 and M03 having 25 each, and M04 having 26. Only 22 zircons from the Dzakar Chu sample could be dated.

6.1 Dzakar Chu Outwash Sand (M05)

Zircons from the Dzakar Chu sample yielded ZrnPb dates ranging from 842 ± 41 Ma to 324.1 ± 5.3 Ma, and ZrnHe dates ranging from 53.8 ± 1.9 Ma to 10.31 ± 0.52 Ma (Table 5.1). Given the sizes of the Stage 2 ablation pits used to acquire the $^{206}Pb/^{238}U$ dates and the documented complexity of zircon U-Pb systematics in at least the Miocene leucogranite zircons from the Rongbuk valley (Hodges et al., 1998; Orme et al., 2015), it is likely that each of the Dzakar Chu detrital ZrnPb dates represent mixtures of an inherited Precambrian-Paleozoic core with a Tertiary igneous or metamorphic zircon rim. (The sizes of these zircons precluded higher spatial resolution dating by LA-ICPMS using the Thermo Scientific *iCap Q* instrument.) Despite the large dispersion of ZrnPb dates in this sample, there is a preponderance of ca. 500 Ma dates as shown in Figure 5.4a, a plot of the summed probability distribution functions (SPDF) for each date assuming normal (Gaussian) uncertainties. Orthogneisses of this approximate age have been documented in the GHS in many parts of the Himalaya (Le Fort, 1975; Parrish and Hodges, 1996; Cawood et al., 2007), but are also found in the TSS (Gehrels et al., 2011).

Figure 5.5, which compares SPDFs from this study with the SPDFs for GHS and TSS units throughout the Himalaya and southern Tibet (Gehrels et al., 2011), illustrates that the Dzakar Chu detrital ZrnPb dates do not clearly distinguish between the two potential zircon sources in the Rongbuk catchment.

Figure 5.6a shows the SPDF for the Dzakar Chu detrital ZrnHe dates. They are also widely dispersed, but the youngest overlap with substantially with nearby bedrock ZrnHe dates reported by Schultz et al. (2017). We suspect that these zircons are locally derived from the GHS and Miocene leucogranites. However, a high percentage of the dates are significantly older than the local bedrock dates, ranging up to early Eocene. The significance of these older ZrnHe dates with regard to detrital provenance is unclear, but many could be derived from the GHS and Miocene leucogranites at higher elevations in the catchment, while others are likely from higher-elevation exposures of the TSS.

The distribution of GHS and Miocene leucogranites in the catchment (Figure 5.1) is such that they are together exposed over 3000 m of relief. One way to predict the possible range of GHS + leucogranite ZrnHe dates that might be encountered in a detrital sample like M05 is to model ZrnHe dates as a function of elevation based on the range of dates obtained in local outcrops at *ca*. 5000 m and exhumation rates from the thermal-kinematic models for those samples as presented by Schultz et al. (2017). For this exercise, we used the average exhumation rate modeled for each bedrock sample between 22 Ma and 10 Ma and predicted the range of dates at various higher elevations from the range of single-crystal ZrnHe dates acquired for each sample: a total of 34 dates from 8 samples. (A maximum age of 22 Ma was assumed based on existing constraints on the ages of prograde metamorphism and leucogranite magmatism; see Schultz et al. (2017)

for a review.) The shaded region shown in Figure 5.7 indicates the total range of plausibly anticipated GHS + leucogranite ZrnHe dates from 5000 m to 8500 m elevations, presuming that the modeled exhumation rates from the Schultz et al. (2017) over the 22 - 10 Ma interval hold for the entire catchment. (The trace of the Qomolangma detachment on the Everest summit pyramid, at ca. 8500 m, marks the highest possible elevation from which a GHS zircon could be derived (Sakai et al., 2005)). This exercise predicts that virtually any detrital zircon from M05 that yields a ZrnHe date between ca. 10 and 21 Ma plausibly could have come from GHS + leucogranite exposed in the catchment above the detrital sample collection locality. Sixteen of the twenty-two crystals fall into that category, and all but the three youngest would have had to be derived from GHS + leucogranite presently exposed at 5500 m or higher.

The remaining six ZrnHe dates seem implausibly old to be derived from the Greater Himalayan sequence or the leucogranites based on our present knowledge of the bedrock cooling history in the area. Detrital zircons are known to occur in some bedrock units of the TSS. Given that the dominant Miocene cooling of the high-grade metamorphic GHS rocks and leucogranites in the Rongbuk valley was a consequence of tectonic denudation by slip on the Qomolangma detachment (Cottle et al., 2015; Carrapa et al., 2016; Schultz et al., 2017), we might reasonably expect that TSS rocks – restricted to the detachment hanging wall – would yield older cooling ages. Although we know of no ZrnHe dates for the TSS in this area, Bergman et al. (1993) and Streule et al. (2012) report Paleogene apatite fission-track dates for samples collected above the Qomolangma detachment on Everest. Since the nominal closure temperature of the apatite fission-track chronometer is substantially lower than that of the zircon (U-Th)/He chronometer (e.g.,

Hodges, 2014), we would expect even older ZrnHe dates from TSS samples. Thus, we tentatively suggest that the pre-21 Ma ZrnHe dates in the modern sediment sample derive from TSS units in the Rongbuk catchment.

One important advantage of LADD data is each crystal provides paired ZrnPb and ZrnHe dates. Figure 5.8 illustrates these relationships for both the Dzakar Chu and Samdupo datasets. For the outwash sample, there is no simple correlation between ZrnPb and ZrnHe dates from sample to sample; for example, zircons with ca. 500 Ma ZrnPb dates have the entire observed range of ZrnHe dates in the dataset. This implies that the source rocks for the dominant 500 Ma zircon component are broadly distributed at many elevations in the Rongbuk catchment, which reinforces the notion that our outwash sample – despite the relatively small number of dated zircons – received detritus from over much of the catchment.

6.2 Samdupo Moraine Sand (M01-M04)

Inter-sample comparisons of the dates obtained from each of our four Samdupo samples (M01-M04) suggest no significant differences in ZrnHe populations, and only limited differences in the ZrnPb populations (Table 5.2). Sample M01 yielded two very old zircons – with $^{206}Pb/^{238}U$ dates of 2267 ± 25 Ma and 2152 ± 20 Ma – while sample M01 and M02 yielded the youngest zircons (26.67 ± 0.24 Ma, 22.01 ± 0.20 Ma, and 21.80 ± 0.75 Ma). Overall, however, the distributions were quite similar for all samples, which leads us to conclude that each of the different sand samples are relatively well mixed and largely representative of the detrital zircon ZrnPb and ZrnHe dates found in at least this part of the Samdupo lateral moraine. Hereafter, we simply discuss all of the

Samdupo results collectively.

Overall, the Samdupo zircons yield a much broader range of $^{206}Pb/^{238}U$ dates than the Dzakar Chu zircons (Figure 5.4b). Although the moraine samples also include a large number of ca. 500 Ma dates, some are as old as Paleoproterozoic and some are as young as Miocene. The youngest dates reflect zircon growth in GHS and leucogranite source rocks during main-stage Himalayan orogenesis. As was the case for the Dzakar Chu zircons, we suspect that many of our Samdupo ZrnPb dates represent mixtures of varying proportions of very old cores and young overgrowth, making it difficult to assign them unambiguous geologic significance. Comparison of the Samdupo ZrnPb distribution with regional composites of the GHS and TSS suggest that both may have contributed zircons to M01-M04, but only the Miocene zircons clearly indicate GHS and/or leucogranite sources for at least some of the detritus.

Compared to the Dzakar Chu zircons, the Samdupo zircons yield a much more restricted range of ZrnHe dates (19.02 ± 0.69 Ma to 4.02 ± 0.17 Ma; Figure 5.6b). Forty-six percent of these dates lie within the rage those obtained by Schultz et al. (2017) for bedrock samples from essentially the same elevation range as the collection sites of M01-M04, suggesting local derivation. Nearly 32% of the ZrnHe dates are sufficiently old to require derivation from higher-elevation sources ranging to at least as high as 6500 m and perhaps somewhat higher (Figure 5.7) if we assume, as is likely, derivation from GHS + leucogranite sources.

The most surprising Samdupo ZrnHe dates – accounting for almost 22% of the dataset – are those that are younger than any of the nearby bedrock ZrnHe dates reported by Schultz et al. (2017). One possible interpretation is that the young dates reflect up-

valley excavation of deeper structural levels than presently exposed in the middle reaches of the Rongbuk valley by the glacier(s) responsible for the Samdupo moraine. However, some of the very young ZrnHe dates would likely require exceptionally deep glacial excavation. A second possibility is that the young ZrnHe dates are unreliable. Orme et al. (2015) documented that some zircons in the bedrock near our Samdupo sampling locality are characterized by internally complex U-Th zoning, and that thin, high U-Th zircon rims are relatively common. As those authors noted, conventional single-crystal ZrnHe dates for such crystals can be erroneously young because the typical correction factor for alpha ejection applied to ZrnHe dates presumes no significant parent element zoning (Farley et al., 1996). While the laser ablation ZrnHe method does not require alpha ejection corrections and generally accounts for the effects of intra-crystalline U-Th zoning, extremely complex zoning can be problematic. For example, it is possible that very different parent element concentrations in the part of a zircon that is polished away after mounting for LADD work could result in erroneously young (or old) laser ablation dates. Detailed, three-dimensional mapping of U-Th zoning in the young Samdupo zircons and appropriate correction schemes for its effects of apparent age calculations (Hourigan et al., 2005; Bargnesi et al., 2016) would be required to test this possibility further.

7. Spatial and Temporal Variations of Erosion in Rongbuk Catchment

The distinctive ZrnPb vs. ZrnHe patterns of detrital zircons from the modern Dzakar Chu outwash sand and mid-Holocene Samdupo moraine sands (Figure 5.8) suggest that the Samdupo glacier transported zircon grains from different regions of the

catchment than the modern glacial outwash system. We hypothesize that the glacier(s) responsible for the Samdupo moraine glacier primarily eroded material from GHS rocks and Miocene leucogranites from the middle elevations of the catchment, close to the estimated ELA of ~6140 m during the Samdupo glacial advance in the mid-Holocene (Owen et al., 2009). This result makes sense, as glacial sliding velocities may be higher near the ELA, resulting in more localized erosion at these elevations (Anderson et al., 2006). This finding is also consistent with similar results presented by Ehlers et al. (2015) in their detrital apatite (U-Th)/He distribution study of the outwash of a modern glacier in British Columbia.

The older ZrnHe dates for many Dzakar Chu outwash zircons implies derivation of a significant fraction of the sediment from higher elevations within the catchment, including GHS, TSS, and Miocene leucogranitic sources. This result may be somewhat puzzling, as sediments from the highest elevations in glacial systems tend to get trapped in cirques and overdeepened areas, although that tends to be much more of a problem where glaciers have retreated upstream from those overdeepenings, which is not the case here. One possibility to explain why the modern outwash system is preferentially sampling sediment from higher elevations is that previous glaciers in the valley from the Last Glacial Maximum (LGM) could have left behind earlier lateral moraines that insulate the lower zones of the modern glacier from hillslope and other supraglacial processes as has been observed in the Nepal Himalaya (Heimsath and McGlynn, 2008). In the Rongbuk valley, the LGM is manifested by the Jilong advance at *ca.* 27 to 24 ka and reveals an estimated ELA of *ca.* 6050 m (Owen et al., 2009). Assuming that the maximum elevation of the lateral moraines of the Jilong advance were close to the *ca.*

6050 m LGM ELA, then the sediment of the modern glacier would be preferentially sourced from elevations above *ca.* 6050 m. These high elevations comprise of TSS sediments at the location of Hermit's Gorge near the sample collection site mid-valley and consist of uppermost GHS rocks and Miocene leucogranites in the southern valley in addition to the TSS units.

A second possibility is that intense folding and deformation of moraine sediment – something that has been documented in glacier systems that persist over several glacial-interglacial cycles – was intense enough to provide the outwash river with extremely well-mixed sediment over time (Hambrey et al., 2009; Hambrey and Glasser, 2012).

8. Conclusions

New detrital zircon laser ablation (U-Th)/He and $^{206}Pb/^{238}U$ datasets for the ca. 8 to 2 ka Samdupo moraine and modern outwash sand from the Rongbuk valley in the Everest region of south-central Tibet yield evidence for different erosional focusing by valley glaciers and the modern upper Dzakar Chu outwash system. Although both datasets contain detrital zircons that are likely derived from Greater Himalayan sequence rocks and Miocene leucogranites in the middle elevations of the catchment, the Dzakar Chu outwash dataset from the modern glacier also contains many zircons apparently sourced from the Greater Himalayan sequence rocks, Miocene leucogranites, and Tibetan Sedimentary sequence rocks at much higher elevations. Some zircons from the Samdupo sediment yield ZrnHe dates that are anomalously young and not easily explained. It is possible that these dates reflect: 1) extremely aggressive downcutting by the Samdupo glacier(s); 2) an unusually high degree of parent element zoning that was not properly

accounted for by the laser ablation double dating protocol; or 3) a combination of the two.

9. Acknowledgments

This work was supported by National Science Foundation Tectonics Program grants EAR1007929 and EAR1346360 to K.V.H. Many thanks to Ding Lin (Institute of Tibetan Plateau Research, Chinese Academy of Sciences), Paul Kapp (University of Arizona) and Ross Waldrip (University of Arizona) for their excellent logistical assistance during fieldwork in Tibet. Many thanks to Cameron Mercer (Arizona State University) for providing the in-house *Matlab* code for calculating the ablation pit volumes. Thanks to Alexandra Horne (Arizona State University) for insightful discussions regarding the LADD technique and to Michelle Aigner, Anna Brunner, and Alyssa Anderson (Arizona State University) who assisted with the analyses. Arjun Heimsath and Kelin Whipple provided invaluable insights regarding glacial erosional processes that helped sharpen our interpretations.

10. Figure Captions

Figure 5.1. Regional map of the Rongbuk catchment in the Everest region of Tibet. Geologic units are mapped after Searle et al. (2003). Blue circles indicate the GHS bedrock sampling localities of Schultz et al. (2017). The red hexagon is the detrital sampling collection site for the Samdupo moraine and Dzakar Chu modern outwash sediment samples for this study. The white dashed lines outline moraines of various ages in the valley and are from oldest to youngest: T – Tingri (>300 ka), S – Samdupo (ca. 8 to

2 ka), X – Xarlungnama (ca. 1.6 ka), and M – Modern glacier terminus. Moraine names and dates are from Owen et al. (2009). The main strand of the STDS in the Rongbuk valley, the Qomolangma detachment, is indicated by a thick black line.

Figure 5.2. A) Depiction of the Rongbuk catchment looking up-valley to the south. GHS bedrock sampling localities of Schultz et al. (2017) are indicated by black circles. The moraine detrital sampling localities, M01 through M04, are shown with a grey circle and a white circle indicates the Dzakar Chu outwash detrital sample collection site, M05. B) A close-up view of the central Rongbuk catchment, showing the general geology as well as the Samdupo moraine (M01 through M04) and Dzakar Chu (M05) detrital sampling localities.

Figure 5.3. Field photographs of the Rongbuk catchment and the Samdupo moraines. A) A view above the modern outwash looking to the north down-valley. B) Rocks of the GHS, seen in the background, make up the majority of the elevations in the catchment with sediments deposited by the Samdupo glacial advance and retreat shown in the foreground. C) A wider view of the hummocky Samdupo moraines.

Figure 5.4. Summed probability density functions (SPDFs) of detrital zircon U/Pb dates by the LADD method are outlined with black. A) The SPDF of ZrnPb dates from the Dzakar Chu outwash sample (n = 22). B) the SPDF distribution of ZrnPb dates from the Samdupo moraine sediment (n = 110). Note that there are two >2.1 Ga zircon U/Pb dates from the moraine sample that are far older than the majority of the analyses and are off-

scale for this figure. Also note the prominent mode of zircon U/Pb dates in the moraine distribution at ca. 25 to 20 Ma.

Figure 5.5. The Samdupo moraine zircon U/Pb SPDFs of this study compared with zircon U/Pb composite distributions of primary units of the Himalaya (GHS and TSS) presented in Gehrels et al. (2011). The SPDF of the Dzakar Chu ZrnPb dates is shown in light blue and the SPDF of the Samdupo moraine ZrnPb dates is shown in red. The SPDF for TSS ZrnHe dates is in green and the GHS distribution (including the ZrnPb GHS pluton dates of Cawood et al. (2007)) is in dark blue.

Figure 5.6. SPDFs of detrital zircon (U-Th)/He dates shown in black. The SPDF for the ZrnHe bedrock dates of Schultz et al. (2017) are indicated by grey shading and are displayed in each panel for comparison. A) The SPDF of ZrnHe dates from the Dzakar Chu sand (n = 22). B) The SPDF of ZrnHe dates from the Samdupo moraine sediment.

Figure 5.7. Relationships between LADD ZrnPb and ZrnHe dates for Dzakar Chu outwash and Samdupo moraine zircons. Uncertainties are shown at the 2σ level. Note that the ZrnPb scale is logarithmic, whereas the ZrnHe scale is linear.

Figure 5.8. Modeled field (gray shading) for anticipated Greater Himalayan sequence (GHS) dates as a function of elevation in the Rongbuk catchment. The range of ZrnHe dates along the y-axis (at an elevation of 5000 m) represents the range of reported bedrock ZrnHe dates at that elevation in the valley by Schultz et al. (2017). Note that the

Dzakar Chu outwash and Samdupo moraine samples were collected at approximately this elevation as well. The gray field shows the range of dates that might be anticipated at a specific elevation higher in the catchment based on an assumption of uniform bedrock exhumation at rates calculated by Schultz et al. (2017) for the bedrock samples over the 22 to 10 Ma interval.

11. References

Anderson, R.S., Molnar, P. and Kessler, M.A. (2006). Features of glacial valley profiles simply explained, *Journal of Geophysical Research*. *111*, doi:10.1029/2005JF000334.

Bargnesi, E. A., Stockli, D. F., Hourigan, J. K., and Hager, C., (2016). Improved accuracy of zircon (U-Th)/He ages by rectifying parent nuclide zonation with practical methods. *Chemical Geology, 426*, 158-169.

Bergman, S. C., Coffield, D. Q., Donelick, R., Corrigan, J., Talbot, J., Cerveny, P., and Kelley, S., (1993). Late Cenozoic compressional & extensional cooling & exhumation of the Qomolangma (Mt. Everest) region, Nepal. *Geological Society of America Abstracts with Programs, 25*, 176.

Brewer, I.D., Burbank, D.W., and Hodges, K.V. (2003). Modelling detrital cooling-age populations: Insights from two Himalayan catchments. *Basin Research, 15,* 305-320.

Blythe, A. E., Burbank, D. W., Carter, A., Schmidt, K., and Putkonen, J. (2007). Plio-Quaternary exhumation history of the central Nepalese Himalaya: 1. Apatite and zircon fission track and apatite U-Th /He analyses. *Tectonics, 26*, doi:Tc300210.1029/2006tc001990.

Boyce, J.W., Hodges, K.V., Olszewski, W.J., Jercinovic, M.J., Carpenter B.D., and Reiners, P.W. (2006). Laser microprobe (U-Th)/He geochronology. *Geochimica Cosmochimica Acta, 70,* 3031-3039.

Burbank, D. W., Blythe, A. E., Putkonen, J., Pratt-Sitaula, B., Gabet, E., Oskin, M., Barros, A., and Ojha, T.P. (2003). Decoupling of erosion and precipitation in the Himalayas. *Nature, 426*, 652-655, doi:10.1038/nature02187.

Burchfiel, C. B., Chen, Z., Hodges, K. V., Liu, Y., Royden, L.H., Deng, C., and Xu, J. (1992). The South Tibetan detachment system, Himalayan orogen: extension

contemporaneous with and parallel to shortening in a collisional mountain belt. *Geologic al Society of America Special Paper*, *269*, 41 p.

Carrapa, B., Robert, X., DeCelles, P.G., Orme, D.A., Thomson, S.N., and Schoenbohm, L.M. (2016). Asymmetric exhumation of the Mount Everest region: Implications for the tectono-topographic evolution of the Himalaya. *Geology*, doi: 10.1130/G37756.1.

Cawood, P. A., Johnson, M. R. W., and Nemchin, A. A. (2007). Early Paleozoic orogenesis along the Indian margin of Gondwana: Tectonic response to Gondwana assembly. *Earth and Planetary Science Letters*, *255*, 70–84, doi:10.1016/j.epsl.2006.12.006.

Cottle, J. M., Searle, M.P., Jessup, M.J., Crowley, J.L., and Law, R.D. (2015). Rongbuk re-visited: Geochronology of leucogranites in the footwall of the South Tibetan Detachment System, Everest Region, Southern Tibet. *Lithos*, *227*, 94-106.

DeCelles, P. G., Gehrels, G.E., Quade, J., Lareau, B., and Spurlin M. (2000). Tectonic implications of U–Pb zircon ages of the Himalayan orogenic belt in Nepal. *Science*, *288*, 497–499, doi:10.1126/science.288.5465.497.

Dobson, K.J., Stuart, F.M., and Dempster, T.J. (2008). U and Th zonation in Fish Canyon Tuff zircons: implications for a zircon (U-Th)/He standard. *Geochimica Cosmochimica Acta, 72,* 4745-4755.

Ehlers, T.A., Szameitat, A., Enkelmann, E., Yanites, B.J., and Woodsworth, G.J. (2015). Identifying spatial variations in glacial erosion with detrital thermochronology, Coast Mountains British Columbia. *Journal of Geophysical Research: Earth Surface*, doi: 10.1002/2014JF003432.

Enkelmann, E. and Ehlers, T.A. (2015). Evaluation of detrital thermochronology for quantification of glacial catchment denudation and sediment mixing, *Chemical Geology*. *411,* 299-309.

Evans, N.J., McInnes, B.I.A., McDonald, B., Danisik, M., Becker, T., Vermeesch, P., Shelley, M., Marillo-Sialer, E., and Patterson, D.B. (2015). An *in situ* technique for (U-Th-Sm)/He and U-Pb double dating. *Journal of Analytical Atomic Spectrometry, 30,* 1636-1645.

Farley, K. A., Wolf, R. A., and Silver, L. T., (1996). The effects of long alpha-stopping distances on (U-Th)/He ages. *Geochimica et Cosmochimica Acta, 60*, 4223-4229.

Feng, R., Nuno, M., Ludden, J. (1993). Lead geochronology of zircon by laserprobe-inductively coupled plasma mass spectrometry (LA-ICPMS). *Geochimica et Cosmochimica Acta*, *57*(14), 3479-3486.

Gehrels, G. (2012). Detrital zircon U-Pb geochronology: Current methods and new opportunities. In: Busby, C. and Perez, A. A. Eds.). *Tectonics of Sedimentary Basins: Recent Advances*, Blackwell, Oxford, U.K.

Gehrels, G., Kapp, P., DeCelles, P., Pullen, A., Blakey, R., Weislogel, A., Ding, L., Guynn, J., Martin, A., McQuarrie, N., and Yin, A. (2011). Detrital zircon geochronology of pre-Tertiary strata in the Tibetan-Himalayan orogen. *Tectonics*, *30*, doi:10.1029/2011TC002868.

Hambrey, M.J., Quincey, D.J., Glasser, N.F., Reynolds, J.M., Richardson, S.J., and Clemmens, S. (2008). Sedimentological, geomorphological and dynamic context of debris-mantled glaciers, Mount Everest (Sagarmatha) region, Nepal. *Quaternary Science Reviews*, *27*, 2361-2389.

Hambrey, M.J., and Glasser, N.F. (2012). Discriminating glacier thermal and dynamic regimes in the sedimentary record. *Sedimentary Geology*, *251-252,* 1-33.

Heimsath, A. M. and McGlynn, R. (2008). Quantifying periglacial erosion in the Nepal high Himalaya. *Geomorphology*, *97*, 5-23.

Hellstrom, J., Paton, C., Woodhead, J., & Hergt, J. (2008). Iolite: software for spatially resolved LA-(quad and MC) ICPMS analysis. *Mineralogical Association of Canada short course series*, *40*, 343-348.

Hodges, K.V., Parrish, R.R., Housh, T.B., Lux, D.R., Burchfiel, B.C., Royden, L.H., and Chen, Z. (1992). Simultaneous Miocene extension and shortening in the Himalayan orogen. *Science, 258*, 1466–1470.

Hodges, K.V., Bowring, S., Davidek, K., Hawkins, D., and Krol, M. (1998). Evidence for rapid displacement on Himalayan normal faults and the importance of tectonic denudation in the evolution of mountain ranges. *Geology*, *26*, 483–486.

Horne, A.M, van Soest, M.C., Hodges, K.V., Tripathy-Lang, A., and Hourigan, J.K. (2016). Integrated Single Crystal Laser Ablation U/Pb and (U-Th)/He Dating of Detrital Accessory Minerals – Proof-of-Concept Studies of Titanites and Zircons from the Fish Canyon Tuff. *Geochimica et Cosmochimica Acta*, *178*, 106 – 123.

Hourigan, J.K., Reiners, P.W., and Brandon, M.T. (2005). U-Th zonation dependent alpha-ejection in (U-Th)/He chronometry. *Geochimica et Cosmochimica Acta, 69*, 3349-3365.

Huang, M. (1990). On the temperature distribution of glaciers in China. *Journal of Glaciology*, *36*, 210-216.

Kosler, J., Fonneland, H., Sylvester, P., Tubrett, M., Pedersen, R-B. (2002). U-Pb dating of detrital zircons for sediment provenance studies; a comparison of laser ablation ICPMS and SIMS techniques. *Chemical Geology, 182,* 605-618.

Le Fort, P. (1975). Himalayas: the collided range. Present knowledge of the continental arc. *American Journal of Science, 275-A,* 1-44.

Mann, D.H., Sletten, R.S. and Reanier, R.E. (1996). Quaternary glaciation of the Rongbuk valley, Tibet. *Journal of Quaternary Science*, *11,* 267-280.

Monteleone, B.D., van Soest, M.C., Hodges, K.V., Moore, G.M., Boyce, J.W., and Hervig, R.L. (2009). Assessment of Alternative [U] and [Th] Zircon Standards for SIMS. Paper presented at American Geophysical Union Fall Meeting, San Francisco, CA, USA.

Murphy, M.A. and Harrison, T.M. (1999). Relationship between leucogranites and the Qomolangma detachment in the Rongbuk Valley, South Tibet. *Geology 27*(9), 831–834. http://dx.doi.org/:10.1130/0091-7613.

Myrow, P. M., Hughes, N.C., Searle, M.P., Fanning, C.M., Peng, S.C., and Parcha, S.K. (2009). Stratigraphic correlation of Cambrian-Ordovician deposits along the Himalaya: Implications for the age and nature of rocks in the Mount Everest region. *Geological Society of America Bulletin*, *121*(3-4), 323-332.

Nasdala, L., Reiners, P.W., Garver, J.I., Kennedy, A.K., Stern, R.A., Balan, E., and Wirth, R. (2004). Incomplete retention of radiation damage in zircon from Sri Lanka. *American Mineralogist*, *89,* 219-231.

Orme, D.A., Reiners, P.W., Hourigan, J.K., and Carrapa, B. (2015). Effects of inherited cores and magmatic overgrowths on zircon (U-Th)/He ages and age-eU trends from Greater Himalaya sequence rocks, Mt. Everest region, Tibet. *Geochemistry, Geophysics, Geosystems*, DOI 10.1002/2015GC005818

Owen, L.A., Robinson, R., Benn, D., Finkel, R.C., Davis, N.K., Yi, C., Putkonen, J., Li, D.H., and Murray, A.S. (2009). Quaternary glaciation of Mount Everest. *Quaternary Science Reviews*, *28*, 1412–1433.

Parrish, R.R. and Hodges, K.V. (1996). Isotopic constraints on the age and provenance of the Lesser and Greater Himalayan sequences, Nepalese Himalaya. *Geol. Soc. Am. Bull.*,*108*, 904–911.

Paton, C., Woodhead, J.D., Hellstrom, J.C., Hergt, J.M., Greig, A., Maas, R., (2010). Improved laser ablation U-Pb zircon geochronology through robust downhole fractionation correction. *Geochemistry Geophysics Geosystems*, *11*, doi:10.1029/2009gc002618.

Reiners, P. W., Thomson, S.N., McPhillips, D., Donelick, R.A., and Roering, J.J. (2007). Wildfire thermochronology and the fate and transport of apatite in hillslope and fluvial environments. *Journal of Geophysical Research, 112*, F04001, doi:10.1029/2007JF000759.

Ruhl., K.W. and Hodges, K.V. (2005). The use of detrital mineral cooling ages to evaluate steady state assumptions in active orogens: An example from the central Nepalese Himalaya. *Tectonics*, *24*, doi: 10.1029/2004TC001712

Sakai, H., Sawada, M., Takigami, Y., Orihashi, Y., Danhara, T., Iwano, H., Kuwahara, Y., Dong, Q., Cai, H.W., and Li, J.G. (2005). Geology of the summit limestone of Mount Qomolangma (Everest) and cooling history of the Yellow Band under the Qomolangma detachment. *Island Arc*, *14*(4), 297-310.

Schultz, M.H., Hodges, K.V., Ehlers, T.A., van Soest, M.C., and Wartho, J-A. (2017). Thermochronologic constraints on the Miocene slip history of the South Tibetan detachment system, south-central Tibet. *Earth and Planetary Science Letters*, *459*, 105-117.

Searle, M.P. (1999). Extensional and compressional faults in the Everest-Lhotse massif, Khumbu Himalaya, Nepal. *Journal of the Geological Society of London, 156,* 227-240.

Searle, M. P., Simpson, R., Law, R.D., Parrish, R.R., and Waters, D.J. (2003). The structural geometry, metamorphic and magmatic evolution of the Everest massif, High Himalaya of Nepal–South Tibet. *Journal of the Geological Society of London*, *160*, 345–366.

Simpson, R.L., Parrish, R.R., Searle, M.P., and Waters, D.J. (2000). Two episodes of monazite crystallization during metamorphism and crustal melting in the Everest region of the Nepalese Himalaya. *Geology*, *28*, 403-406.

Stock, G.M., Ehlers, T.A., and Farley, K.A. (2006). Where does sediment come from? Quantifying catchment erosion with detrital apatite (U-Th)/He thermochronology. *Geology*, *34*, 725-728.

Streule, M. J., Carter, A., Searle, M.P., and Cottle, J.M. (2012). Constraints on brittle field exhumation of the Everest-Makalu section of the Greater Himalayan Sequence: Implications for models of crustal flow. *Tectonics, 31*, doi:Tc301010.1029/2011tc003062.

Tranel, L.M., Spotila, J.A., Kowalewski, M.J., and Waller, C.M. (2011). Spatial variation of erosion in a small, glaciated basin in the Teton Range, Wyoming, based on detrital apatite (U-Th)/He thermochronology. *Basin Research*, *23*, 571-590.

Tripathy-Lang, A., Hodges, K.V., Monteleone, B., and van Soest, M.C. (2013). Laser (U-Th)/He thermochronology of detrital zircons as a tool for studying surface processes in modern catchments. *Journal of Geophysical Research Earth Surface*, *118*, 1333–1341, doi:10.1002/jgrf.20091.

van Hinsbergen, D. J. J., Lippert, P.C., Dupont-Nivet, G., McQuarrie, N., Doubrovine, P.V., Spakman, W., and Torsvik, T.H. (2012). Greater India Basin hypothesis and

a two-stage Cenozoic collision between India and Asia. *Proceedings of the National Academy of Sciences*, *109*, 7659-7664.

Wangenheim, C. and Glotzbach, C. (2015). Quantifying glacial erosion in the European Alps using apatite fission-track dating. *Geophysical Research Abstracts, 17,* EGU2015-1729, 2015.

Whipp, D. M., Ehlers, T.A., Blythe, A.E., Huntington, K.W., Hodges, K.V., Burbank, D.W. (2007). Plio-Quaternary exhumation history of the central Nepalese Himalaya: 2. Thermo-kinematic and thermochronometer age prediction model. *Tectonics, 26*, doi:10.1029/2006TC001991.

Whipp, D. M., Ehlers, T.A., Braun, J., and Spath, C.D. (2009). Effects of exhumation kinematics and topographic evolution on detrital thermochronometer data. *Journal of Geophysical Research*, *114*, F04014, doi:10.1029/2008JF001195.

TABLE 5.1: MODERN DZAKAR CHU FLUVIAL SYSTEM DETRITAL ZIRCON LASER ABLATION (U-Th)/He and U/Pb DATA TABLE

Sample	Grain	^{4}He pit volume (μ^3)	Error (2σ)	^{4}He (nmole/g)	Error (2σ)	U-Th-Pb pit volume (μ3)	Error (2σ)	^{238}U (ppm)	Error (2σ)	^{232}Th (ppm)	Error (2σ)	eU (ppm)	^{232}Th/^{238}U	(U-Th)/He Date (Ma)	Error (2σ)	^{206}Pb/^{238}U	Error (2σ)	^{238}U/^{206}Pb Date (Ma)	Error (2σ)
M05	z01	1298.3	2.8	33.3	1.2	40325	33	322	11	275	23	389	0.8784	15.88	0.75	0.07894	0.00054	489.8	3.2
M05	z02	1317.5	3.9	62.6	1.3	44763	23	325	12	82.4	7.3	347	0.2598	33.4	1.3	0.0922	0.0021	569	13
M05	z03	1136.8	2.4	45.9	1.2	44462	31	438	15	130	11	471	0.3049	18.05	0.76	0.074	0.0021	460	13
M05	z04	1416.4	1.7	29.35	0.87	44731	33	273.1	9.2	99.8	8.8	298	0.3750	18.22	0.79	0.07902	0.00041	490.2	2.4
M05	z05	1470.6	3.3	37.28	0.99	47314	29	316	11	62.8	5.5	333	0.2036	20.71	0.87	0.0836	0.0014	517.7	8.3
M05	z06	1477.4	3.2	36.56	0.94	42176	38	599	20	139	12	636	0.2387	10.66	0.44	0.05157	0.00086	324.1	5.3
M05	z07	1236.7	1.9	144.8	2.0	44232	57	423	14	302	26	497	0.7319	53.8	1.9	0.0779	0.00041	483.6	2.4
M05	z08	1374.8	1.5	102.5	1.5	43853	47	584	20	68.2	6.0	604	0.1198	31.4	1.2	0.07	0.0024	436	14
M05	z09	1282.0	2.6	92.3	1.6	45598	33	756	26	275	26	826	0.3725	20.70	0.77	0.0569	0.0026	356	16
M05	z10	1392.3	1.7	77.9	1.5	45595	44	574	20	249	22	637	0.4444	22.66	0.84	0.07894	0.00081	489.8	4.9
M05	z11	1278.7	2.5	37.00	0.94	45293	48	330	11	146	13	366	0.4553	18.70	0.77	0.11921	0.00099	726	5.7
M05	z12	1239.6	3.7	75.7	1.5	46085	41	267.0	9.0	160	14	307	0.6149	45.6	1.7	0.1152	0.00099	702.8	5.7
M05	z13	1281.55	0.59	35.30	0.91	46540	36	362	12	126	11	394	0.3581	16.59	0.68	0.14	0.0073	842	41
M05	z14	1304.8	3.2	32.32	0.84	44321	34	299	10	92.7	8.1	323	0.3182	18.56	0.77	0.08065	0.00082	499.9	4.9
M05	z15	1315.3	2.7	24.60	0.83	44217	36	243.7	8.2	102.0	9.0	269	0.4292	16.91	0.78	0.079	0.0017	490.2	9.9
M05	z16	1223.2	2.3	27.28	0.84	44686	45	409	14	281	26	478	0.7048	10.58	0.46	0.08378	0.00081	518.6	4.8
M05	z17	1225.3	2.4	19.61	0.76	44353	48	279.4	9.4	302	28	352	1.1090	10.31	0.52	0.0809	0.0021	501	12
M05	z18	1209.6	3.3	15.20	0.71	45149	39	138.7	4.7	88.8	7.8	161	0.6568	17.53	0.99	0.12015	0.00077	731.4	4.5
M05	z19	1310.0	2.4	33.64	0.83	45787	48	320	11	107.6	9.5	348	0.3448	17.92	0.72	0.07986	0.00055	495.3	3.3
M05	z20	1362.7	1.6	58.1	1.0	45387	32	611	21	114	10	642	0.1913	16.77	0.62	0.1273	0.0042	771	24
M05	z21	1212.162	0.020	46.3	1.1	47056	35	531	18	115	10	562	0.2222	15.28	0.61	0.0716	0.0016	445.4	9.8
M05	z22	1386.5	2.1	29.58	0.95	43533	33	177.5	6.0	81.3	7.1	198	0.4699	27.7	1.2	0.08041	0.00065	499.1	3.8

TABLE 5.2: SAMDUPO MORAINE DETRITAL ZIRCON LASER ABLATION (U-Th)/He DATA TABLE

Sample	Grain	^{4}He pit volume (μ^3)	Error (2σ)	^{4}He (nmole/g)	Error (2σ)	U-Th-Pb pit volume (μ^3)	Error (2σ)	^{238}U (ppm)	Error (2σ)	^{232}Th (ppm)	Error (2σ)	eU (ppm)	^{232}Th/^{238}U	(U-Th)/He Date (Ma)	Error (2σ)	^{206}Pb/^{238}U	Error (2σ)	^{238}U/^{206}Pb Date (Ma)	Error (2σ)
M01	z01	1146.1	1.1	29.59	0.93	43695	60	443	15	67.8	6.0	462	0.16	11.89	0.54	0.0753	0.0010	468.3	6.0
M01	z02	3171.2	1.6	45.17	0.76	166164	200	951	33	43.8	3.9	968	0.047	8.66	0.34	0.0291	0.0029	185	18
M01	z03	1241.0	1.1	7.12	0.49	65615	24	93.7	3.1	41.7	3.7	104	0.46	12.67	0.96	0.4219	0.0055	2267	25
M01	z04	1155.9	1.1	15.04	0.70	45726	50	267.3	9.0	83.8	7.4	289	0.32	9.65	0.54	0.1225	0.0031	744	18
M01	z05	1169.9	1.1	28.0	1.1	47219	37	450	15	81.1	7.1	472	0.18	11.01	0.55	0.07835	0.00056	486.3	3.3
M01	z06	3184.7	1.6	18.70	0.43	84325	170	181.2	6.2	146	13	217	0.83	15.96	0.63	0.0719	0.0016	447	10
M01	z07	3186.3	1.6	8.44	0.29	73648	63	72.8	2.4	133	12	105	1.9	14.90	0.73	0.07981	0.00058	495.0	3.5
M01	z08	1122.3	1.1	28.44	0.86	45976	68	279.7	9.5	323	28	358	1.2	14.72	0.66	0.1907	0.0025	1125	14
M01	z09	3180.6	1.7	13.41	0.37	47877	58	581	20	142	13	619	0.25	4.02	0.17	0.1586	0.0012	949.1	6.9
M01	z10	1122.6	1.0	137.5	2.3	47185	53	1132	38	843	74	1339	0.76	19.02	0.69	0.0709	0.0013	441.6	8.0
M01	z11	2682.9	1.6	23.26	0.49	88291	180	272.5	9.3	133	12	306	0.50	14.10	0.54	0.3966	0.0043	2152	20
M01	z12	1198.2	1.1	73.9	1.5	47951	63	1279	43	474	42	1400	0.38	9.80	0.37	0.10348	0.00072	634.7	4.2
M01	z13	1169.9	1.1	61.1	1.3	48407	49	605	21	100.4	8.8	633	0.17	17.90	0.70	0.1197	0.0047	727	27
M01	z14	3161.5	1.7	44.33	0.72	53625	51	502	17	72.8	6.4	523	0.15	15.72	0.58	0.03245	0.0005	205.9	3.1
M01	z15	3018.0	1.7	21.30	0.55	47271	42	747	26	145	13	787	0.20	5.02	0.21	0.057	0.0048	355	29
M01	z16	955.2	1.0	65.6	1.4	47279	58	1057	36	136	12	1097	0.13	11.10	0.44	0.0543	0.0037	339	23
M01	z17	1175.8	1.1	335.2	4.1	49968	57	4709	159	22.2	2.0	4748	0.0048	13.10	0.47	0.004146	0.000037	26.67	0.24
M01	z18	1008.6	1.0	41.5	1.1	45697	52	494	17	50.2	4.4	509	0.10	15.13	0.65	0.0832	0.0010	515.1	6.2
M01	z19	1065.9	1.1	97.2	1.9	49218	42	1360	50	184	16	1413	0.14	12.76	0.51	0.0567	0.0051	354	31
M01	z20	1158.0	1.1	14.16	0.64	65339	63	182.1	6.1	62.5	5.5	198	0.35	13.24	0.73	0.08254	0.00069	511.2	4.1
M01	z21	1103.3	1.1	184.0	3.0	43626	47	2283	76	92.6	8.1	2321	0.042	14.70	0.54	0.0115	0.0019	73	12
M01	z22	1152.7	1.1	42.1	1.1	44209	52	494	17	577	51	633	1.2	12.30	0.51	0.07661	0.00082	475.8	4.9
M01	z23	1077.5	1.1	41.09	0.98	93179	62	615	21	213	19	670	0.36	11.37	0.45	0.0780	0.0022	484	13
M01	z24	1006.1	1.0	31.9	1.1	45415	49	420	14	82.7	7.3	442	0.20	13.37	0.63	0.07876	0.00083	488.6	5.0
M01	z25	919.9	1.0	28.4	1.0	45924	54	808	29	376	32	903	0.48	5.83	0.28	0.0839	0.0015	519.3	9.1
M02	z01	1237.18	0.39	438.6	5.4	49776	100	4617	157	45.6	4.0	4661	0.0101	17.45	0.63	0.003421	3.20E-05	22.01	0.20
M02	z02	1238.82	0.38	33.17	0.87	47141	81	412	14	50.8	8.6	427	0.1267	14.42	0.61	0.01684	0.00072	107.6	4.6
M02	z03	1286.65	0.53	21.49	0.71	47151	120	207.2	7.0	131	12	239	0.6479	16.62	0.76	0.07901	0.00077	490.1	4.6
M02	z04	1319.04	0.23	34.59	0.90	47433	82	454	15	367	32	543	0.8298	11.80	0.48	0.08146	0.00059	504.8	3.5
M02	z05	1223.076	0.077	311.9	3.9	44167	72	3973	133	35.1	3.1	4010	0.0091	14.43	0.52	0.00339	0.00012	21.80	0.75
M02	z06	1282.3	1.1	25.31	0.67	47003	80	283	10	191	17	330	0.6916	14.19	0.59	0.0775	0.0016	481.2	9.5
M02	z07	1244.48	0.99	42.51	0.95	45232	71	523	18	120	11	555	0.2363	14.21	0.56	0.07388	0.00047	459.5	2.8
M02	z08	1192.69	0.34	34.08	0.99	44722	74	545	18	89.6	7.9	570	0.1687	11.09	0.48	0.07705	0.0007	478.4	4.2
M02	z09	1147.75	0.14	31.85	0.87	44391	78	433	15	444	39	541	1.0527	10.91	0.46	0.07906	0.00058	490.5	3.4
M02	z10	1192.83	0.54	36.29	0.92	45652	45	448	15	135	12	483	0.3087	13.93	0.57	0.0767	0.002	476	12
M02	z11	1216.01	0.48	51.7	1.2	47288	72	572	19	116	10	604	0.2081	15.88	0.63	0.07433	0.00071	462.2	4.2
M02	z12	1174.47	0.67	102.7	1.6	44775	66	1353	45	392	35	1455	0.2975	13.08	0.46	0.1154	0.0054	701	32
M02	z13	1266.982	0.037	36.27	0.94	46498	54	407	14	132	12	441	0.3313	15.24	0.62	0.07804	0.00061	484.4	3.6
M02	z14	1219.93	0.25	25.45	0.70	47053	65	355	12	60.9	5.3	372	0.1759	12.69	0.54	0.07832	0.00073	486	4.4
M02	z15	1286.974	0.073	52.8	1.0	53088	140	790	26	46.8	4.1	807	0.0608	12.14	0.47	0.03109	0.00067	197.3	4.2
M02	z16	1107.91	0.48	19.81	0.65	45671	58	357	12	173	16	401	0.4957	9.17	0.42	0.0658	0.0031	410	19
M02	z17	1138.73	0.60	37.6	1.0	45553	65	439	15	282	26	508	0.6585	13.70	0.57	0.07773	0.00059	482.5	3.5
M02	z18	1127.75	0.56	29.21	0.90	46029	76	382	13	89.0	7.8	406	0.2390	13.34	0.60	0.0572	0.0011	358.7	7
M02	z19	1092.82	0.56	34.65	0.97	46262	82	345	12	62.4	5.5	362	0.1856	17.74	0.76	0.07973	0.00088	494.4	5.2
M02	z20	1178.28	0.58	62.8	1.1	43285	76	590	20	401	35	688	0.6965	16.88	0.61	0.1328	0.006	801	34
M02	z21	1011.59	0.97	96.6	1.6	46199	86	869	29	1044	93	1120	1.2323	15.96	0.58	0.07986	0.00067	495.3	4
M02	z22	1009.7	1.8	25.02	0.85	49856	71	541	18	83.7	7.4	565	0.1588	8.22	0.39	0.079	0.0013	490.3	7.9
M02	z23	1041.02	0.18	28.81	0.85	46462	77	295	10	212	19	347	0.7355	15.37	0.66	0.07851	0.00075	487.2	4.5
M02	z24	968.32	0.58	17.86	0.62	45508	260	221.7	7.5	117	10	251	0.5436	13.19	0.62	0.07899	0.00071	490.1	4.2
M02	z25	857.96	0.74	50.7	1.3	46579	82	555	19	83.3	7.3	579	0.1538	16.22	0.67	0.07558	0.00071	469.7	4.3
M02	z26	1046.06	0.37	44.1	1.2	45991	88	475	16	74.7	6.6	496	0.1616	16.49	0.71	0.07248	0.0007	451	4.2
M02	z27	1196.29	0.90	22.73	0.75	47752	45	225.1	7.5	133	12	258	0.6056	16.33	0.74	0.07738	0.00079	480.4	4.7
M02	z28	1191.95	0.29	49.2	1.2	44450	100	674	23	76.3	6.7	697	0.1162	13.09	0.54	0.1139	0.0027	695	16
M02	z29	1264.128	0.034	23.62	0.72	46504	69	293	10	101.7	9.0	319	0.3560	13.73	0.61	0.07932	0.00069	492.1	4.1
M02	z30	1194.95	0.31	362.6	4.5	46226	100	4075	138	260	44	4165	0.0655	16.14	0.57	0.05551	0.00093	348.9	5.5
M02	z31	1088.36	0.83	68.9	1.4	47470	100	789	26	168	28	834	0.2186	15.32	0.60	0.0546	0.0042	341	26
M02	z32	1011.13	0.907	74.4	1.4	47873	73	943	31	435	37	1052	0.4730	13.09	0.48	0.0795	0.00098	493.1	5.9
M02	z33	1075.2	1.4	27.76	0.87	44415	73	296	10	101.7	8.9	322	0.3520	15.96	0.71	0.08155	0.00073	505.3	4.3
M02	z34	992.67363	0.00010	76.4	1.4	46632	68	716	24	310	28	794	0.4439	17.83	0.65	0.1859	0.0028	1098	15

Sample	Grain	^{4}He pit volume (μ^3)	Error (2σ)	^{4}He (nmole/g)	Error (2σ)	U-Th-Pb pit volume (μ^3)	Error (2σ)	^{238}U (ppm)	Error (2σ)	^{232}Th (ppm)	Error (2σ)	eU (ppm)	^{232}Th/^{238}U	(U-Th)/He Date (Ma)	Error (2σ)	^{206}Pb/^{238}U	Error (2σ)	^{238}U/^{206}Pb Date (Ma)	Error (2σ)
M03	z01	899.6	1.0	109.6	2.8	44976	64	1248	43	346	30	1339	0.2844	15.18	0.63	0.0843	0.0014	521.7	8.5
M03	z02	926.4	1.0	51.3	1.7	46768	54	1601	52	108.5	9.5	1638	0.0695	5.82	0.27	0.08075	0.00063	500.5	3.7
M03	z03	1023.2	1.1	52.8	1.7	42843	48	1075	36	55.9	4.9	1096	0.0533	8.94	0.42	0.1399	0.0046	842	26
M03	z04	907.8	1.0	23.6	1.3	47580	69	283	10	133	12	316	0.4804	13.84	0.89	0.1807	0.002	1070	11
M03	z05	1071.6	1.1	12.5	1.0	44414	61	202.6	7.1	70.5	6.2	221	0.3570	10.55	0.92	0.0726	0.002	453	12
M03	z06	2792.5	1.7	109.6	2.8	79846	140	692	24	52.5	4.6	710	0.0779	9.13	0.36	0.01805	0.00097	115.2	6.1
M03	z07	2634.0	1.6	51.3	1.7	70293	160	391	13	188	17	438	0.4926	13.68	0.58	0.0595	0.0022	373	13
M03	z08	904.0	1.0	52.8	1.7	44053	48	655	22	320	28	735	0.5015	12.76	0.57	0.1744	0.0014	1036.5	7.6
M03	z09	947.0	1.1	23.6	1.3	44944	50	260.3	8.8	182	16	305	0.7185	14.79	0.94	0.07946	0.00071	492.9	4.3
M03	z10	939.8	1.0	12.5	1.0	46428	46	576	19	333	30	658	0.5935	13.90	0.65	0.05571	0.00066	349.4	4
M03	z11	1033.2	1.1	34.92	0.76	46061	60	525	18	130	12	559	0.2539	9.69	0.52	0.1271	0.005	769	29
M03	z12	985.7	1.1	32.33	0.90	47644	77	1208	40	131	12	1247	0.1116	17.46	0.69	0.0889	0.0014	548.8	8.3
M03	z13	2752.3	1.7	50.6	1.6	87098	180	285	10	68.1	6.0	303	0.2455	7.85	0.41	0.0782	0.001	485.4	6.2
M03	z14	2809.2	1.7	24.3	1.3	48149	66	235.2	7.9	64.3	5.7	252	0.2803	17.13	0.73	0.1021	0.0013	626.3	7.7
M03	z15	1096.4	1.1	49.4	1.7	43804	62	413	14	55.4	4.9	429	0.1377	11.15	0.68	0.1937	0.0045	1141	24
M03	z16	990.0	1.0	29.2	1.3	46521	49	2668	100	2218	200	3209	0.8528	10.94	0.41	0.0646	0.002	403	12
M03	z17	1050.8	1.1	117.4	2.5	47312	62	469	16	140	12	505	0.3066	10.94	0.55	0.117	0.0018	713	11
M03	z18	911.6	1.0	21.3	1.2	47428	76	358	12	164	14	399	0.4707	9.89	0.65	0.0684	0.0011	426.3	6.4
M03	z19	818.5	1.0	41.4	1.8	46319	58	426	14	155	14	465	0.3727	16.50	0.89	0.1029	0.0015	631.4	8.9
M03	z20	812.2	1.0	151.4	3.1	46503	42	2660	90	760	67	2858	0.2932	9.83	0.38	0.08314	0.00068	514.8	4.1
M03	z21	1045.6	1.1	113.0	2.1	47858	58	2702	95	394	35	2814	0.1495	7.45	0.29	0.0543	0.0023	340	14
M03	z22	2987.8	1.7	48.8	1.0	85797	240	542	19	549	49	675	1.0401	13.38	0.51	0.1284	0.0013	778.8	7.2
M03	z23	975.3	1.1	37.0	2.6	51677	69	538	18	530	46	667	1.0104	10.27	0.79	0.07407	0.0009	460.5	5.4
M03	z24	1000.2	1.1	29.6	1.7	56617	57	356	12	111.7	9.9	385	0.3222	14.24	0.95	0.1162	0.0069	706	40
M03	z25	999.8	1.1	39.5	1.5	46382	59	930	31	510	44	1056	0.5626	6.93	0.34	0.08092	0.00078	501.6	4.7
M04	z01	853.94	2.00	45.7	1.6	44429	80	953	33	79.8	7.1	979	0.086	8.42	0.43	0.017	0.076	471.2	7.6
M04	z02	867.11	1.80	25.2	1.5	45843	69	500	17	112	10	530	0.23	8.83	0.61	0.024	0.062	386	18
M04	z03	917.60	2.00	54.1	1.7	40480	73	611	21	508	44	735	0.85	13.66	0.64	0.017	0.085	524.5	5.4
M04	z04	983.41	2.00	29.8	1.3	40620	69	453	15	149	13	491	0.34	11.28	0.61	0.009	0.079	489.2	3.9
M04	z05	772.01	1.80	31.9	1.5	42176	95	390	13	43.9	3.9	403	0.12	14.52	0.88	0.016	0.074	461.5	8.6
M04	z06	746.21	1.80	52.1	1.8	40128	90	540	18	111.0	9.9	570	0.21	17.03	0.83	0.018	0.061	383	12
M04	z07	807.38	2.00	28.4	1.5	39758	52	413	14	66.7	5.9	432	0.17	12.24	0.77	0.019	0.070	433	12
M04	z08	823.33	1.80	14.7	1.3	47932	88	187.1	6.3	78.1	6.9	207	0.43	13.5	1.2	0.017	0.079	487.7	6.3
M04	z09	830.35	1.80	35.5	1.5	36723	75	402	14	167	15	444	0.43	14.80	0.81	0.015	0.085	526.0	4.1
M04	z10	817.32	1.80	19.6	1.5	37909	63	200.3	6.7	147	13	236	0.75	15.4	1.3	0.07	0.26	1469	20
M04	z11	841.35	1.80	14.8	1.2	36717	84	216.8	7.3	98.0	8.6	241	0.46	12.4	1.1	0.014	0.081	502.4	5.6
M04	z12	811.11	1.80	24.5	2.6	38541	100	348	12	108.3	9.5	376	0.32	13.5	1.4	0.015	0.077	480.8	5.4
M04	z13	835.50	2.00	35.6	1.6	40650	79	205.1	7.6	14.7	1.3	210	0.074	9.10	0.52	0.015	0.076	472.7	6.7
M04	z14	779.18	1.80	54.0	1.8	40305	83	860	29	42.4	3.7	876	0.051	11.31	0.56	0.013	0.025	160	11
M04	z15	768.32	1.80	19.9	1.2	33773	67	205.7	6.9	174	15	248	0.87	14.8	1.1	0.016	0.082	510.3	5.8
M04	z16	807.33	1.80	112.1	2.5	43286	100	531	22	26.4	2.4	541	0.051	10.70	0.45	0.02	0.10	622.9	9.6
M04	z17	898.49	2.00	51.6	1.7	38064	88	671	23	131	12	707	0.20	13.54	0.65	0.013	0.076	474.3	4.9
M04	z18	775.70	1.80	46.8	1.7	33630	83	721	24	251	22	785	0.36	11.06	0.55	0.011	0.075	464.2	6.2
M04	z19	879.42	2.00	29.7	1.5	40501	92	436	15	36.9	3.3	448	0.087	12.28	0.76	0.022	0.058	361	11
M04	z20	815.79	1.80	30.4	1.6	37306	86	1158	40	498	44	1283	0.44	4.41	0.27	0.019	0.079	487	10
M04	z21	825.50	2.00	69.4	1.9	36455	100	729	24	317	28	808	0.45	15.98	0.71	0.04	0.22	1257	12
M04	z22	820.25	2.00	28.6	1.4	34759	77	819	29	421	37	924	0.53	5.99	0.36	0.014	0.077	475.4	6.6
M04	z23	949.98	2.20	36.1	1.4	32957	72	698	24	392	35	796	0.58	7.91	0.41	0.009	0.072	449.6	3.7
M04	z24	831.56	2.00	19.5	1.5	35498	64	239.4	8.0	94.5	8.3	263	0.40	12.9	1.1	0.010	0.080	493.9	3.0
M04	z25	802.51	1.80	42.2	2.0	35660	75	176.7	6.3	56.5	6.1	191	0.33	10.89	0.63	0.014	0.080	498.8	5.7
M04	z26	809.41	1.80	22.9	1.3	34217	72	399	13	117	10	429	0.30	9.94	0.66	0.012	0.079	489.3	4.2

FIGURE 5.1

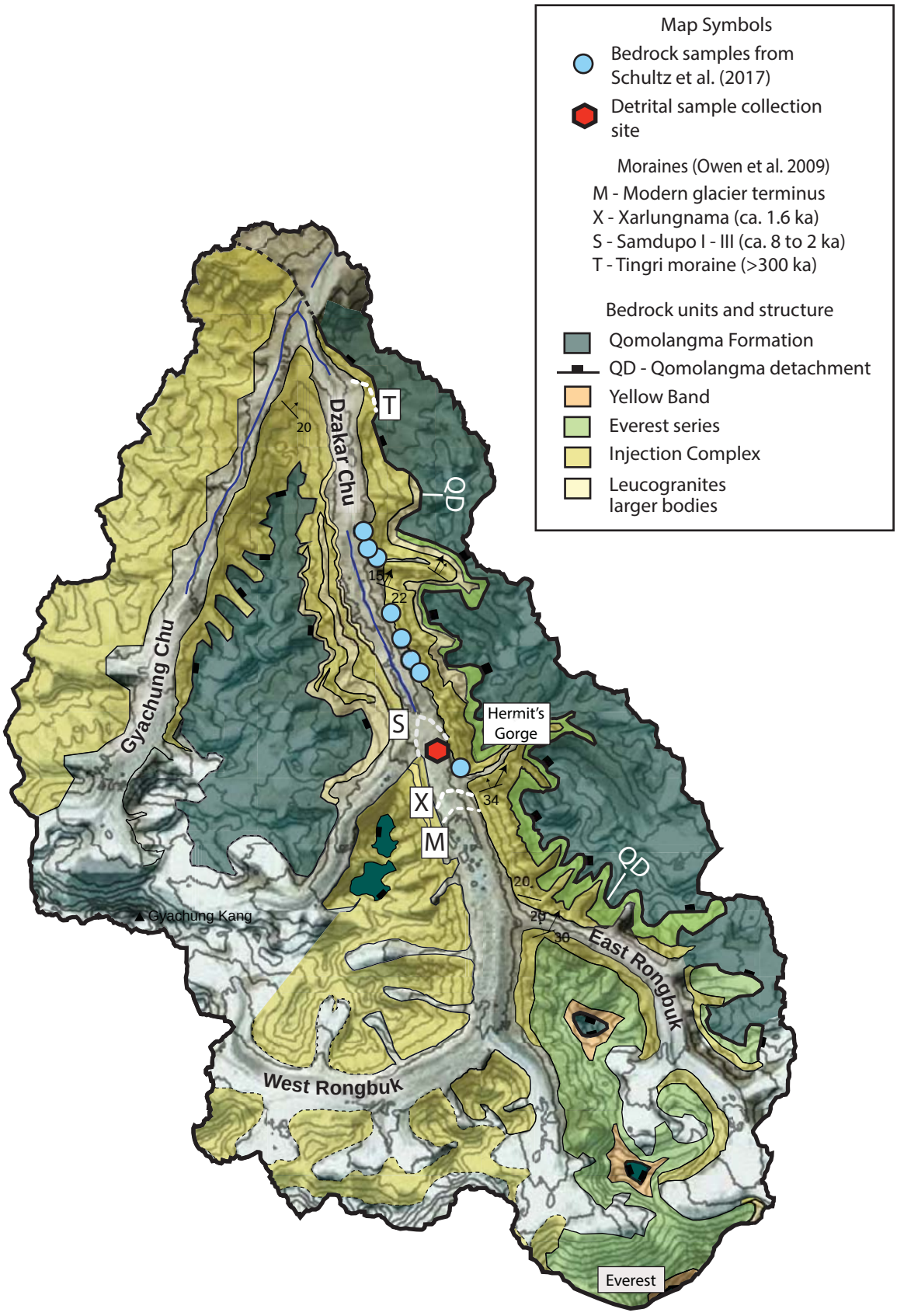
Map Symbols
Bedrock samples from Schultz et al. (2017)
Detrital sample collection site
Moraines (Owen et al. 2009)
M - Modern glacier terminus
X - Xarlungnama (ca. 1.6 ka)
S - Samdupo I - III (ca. 8 to 2 ka)
T - Tingri moraine (>300 ka)
Bedrock units and structure
Qomolangma Formation
QD - Qomolangma detachment
Yellow Band
Everest series
Injection Complex
Leucogranites larger bodies
Dzakar Chu
Gyachung Chu
Gyachung Kang
West Rongbuk
East Rongbuk
Hermit's Gorge
Everest
T
S
X
M
QD
20
15
22
34
20
29
30

FIGURE 5.2

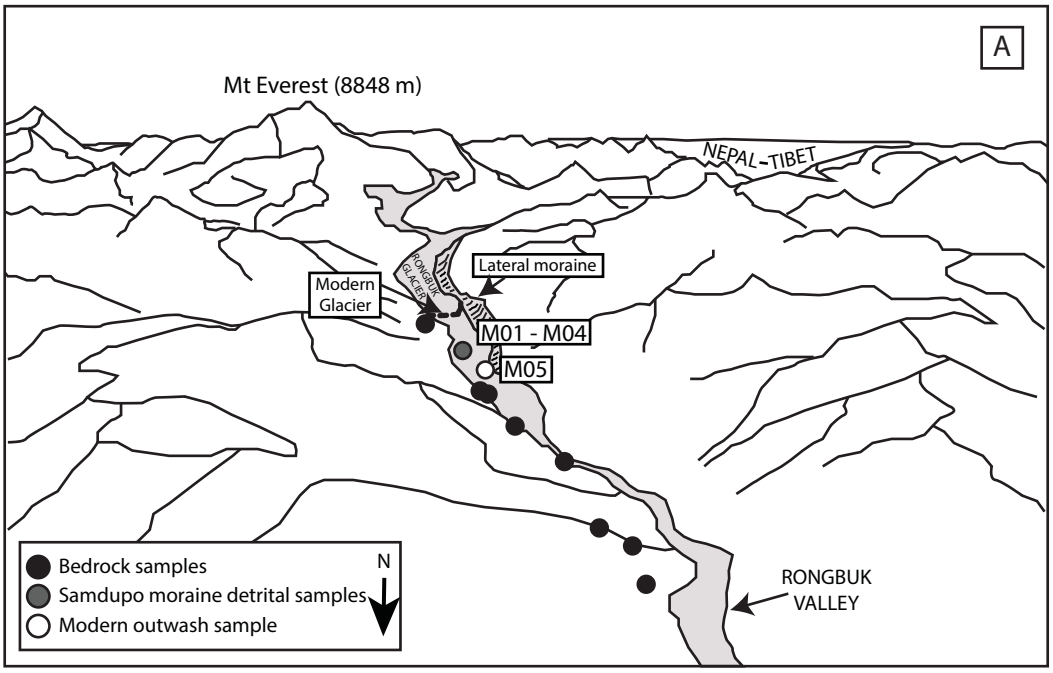
A
Mt Everest (8848 m)
NEPAL–TIBET
RONGBUK GLACIER
Modern Glacier
Lateral moraine
M01 - M04
M05
Bedrock samples
Samdupo moraine detrital samples
Modern outwash sample
N
RONGBUK VALLEY

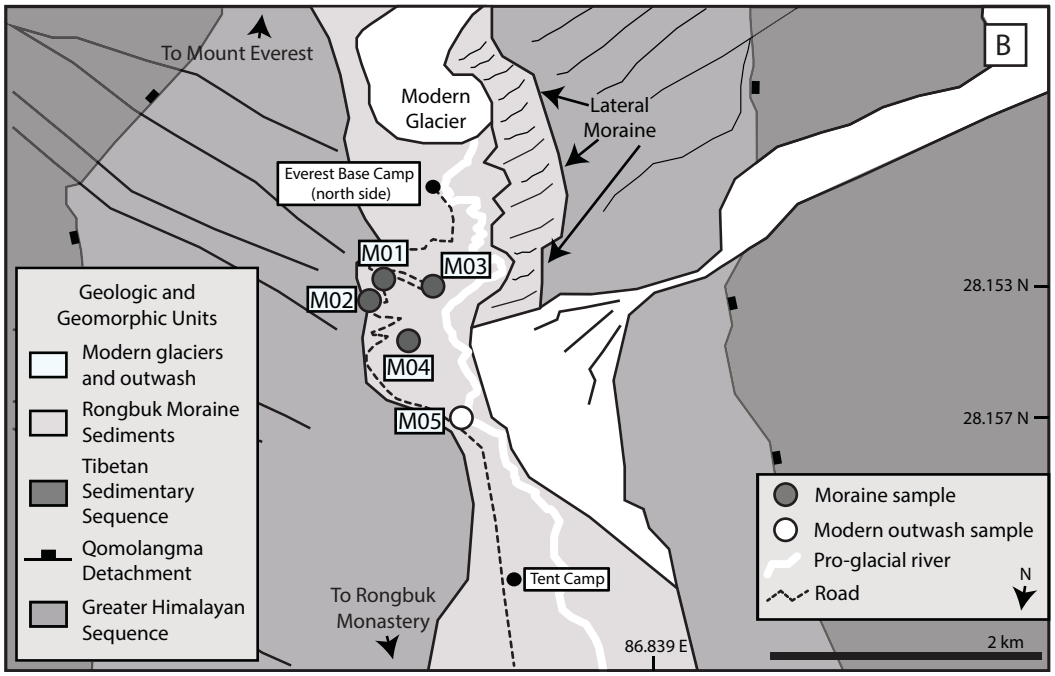
B
To Mount Everest
Modern Glacier
Lateral Moraine
Everest Base Camp (north side)
M01
M02
M03
M04
M05
Geologic and Geomorphic Units
Modern glaciers and outwash
Rongbuk Moraine Sediments
Tibetan Sedimentary Sequence
Qomolangma Detachment
Greater Himalayan Sequence
28.153 N
28.157 N
Moraine sample
Modern outwash sample
Pro-glacial river
Road
N
Tent Camp
To Rongbuk Monastery
86.839 E
2 km

FIGURE 5.3

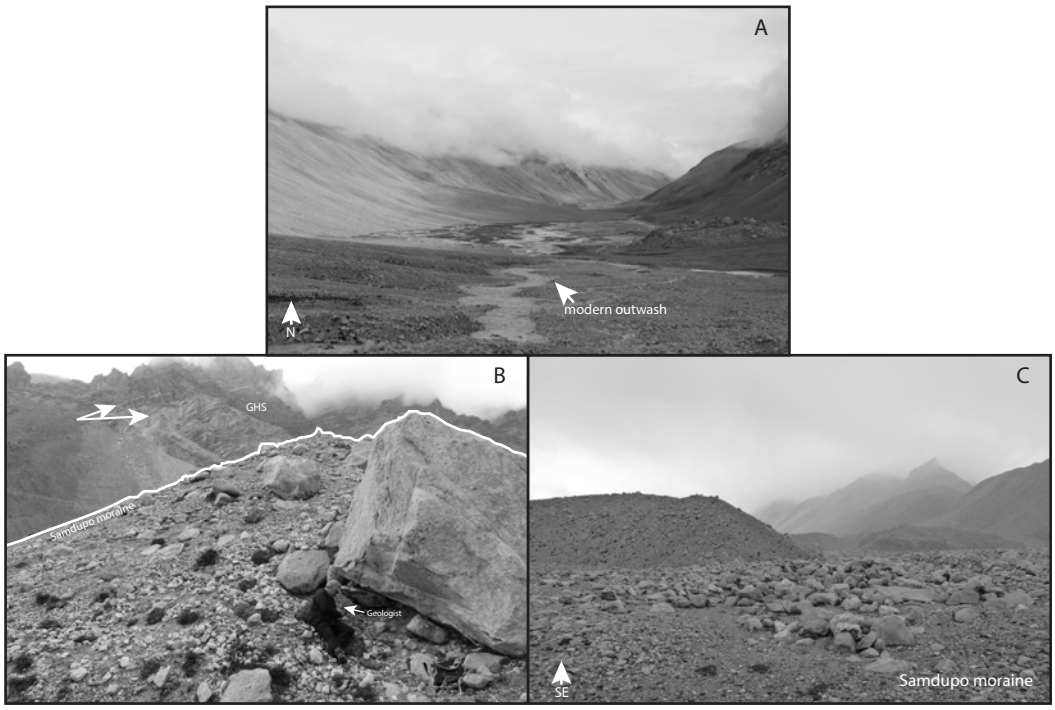
A
modern outwash
N
B
GHS
Samdupo moraine
Geologist
C
SE
Samdupo moraine

FIGURE 5.4

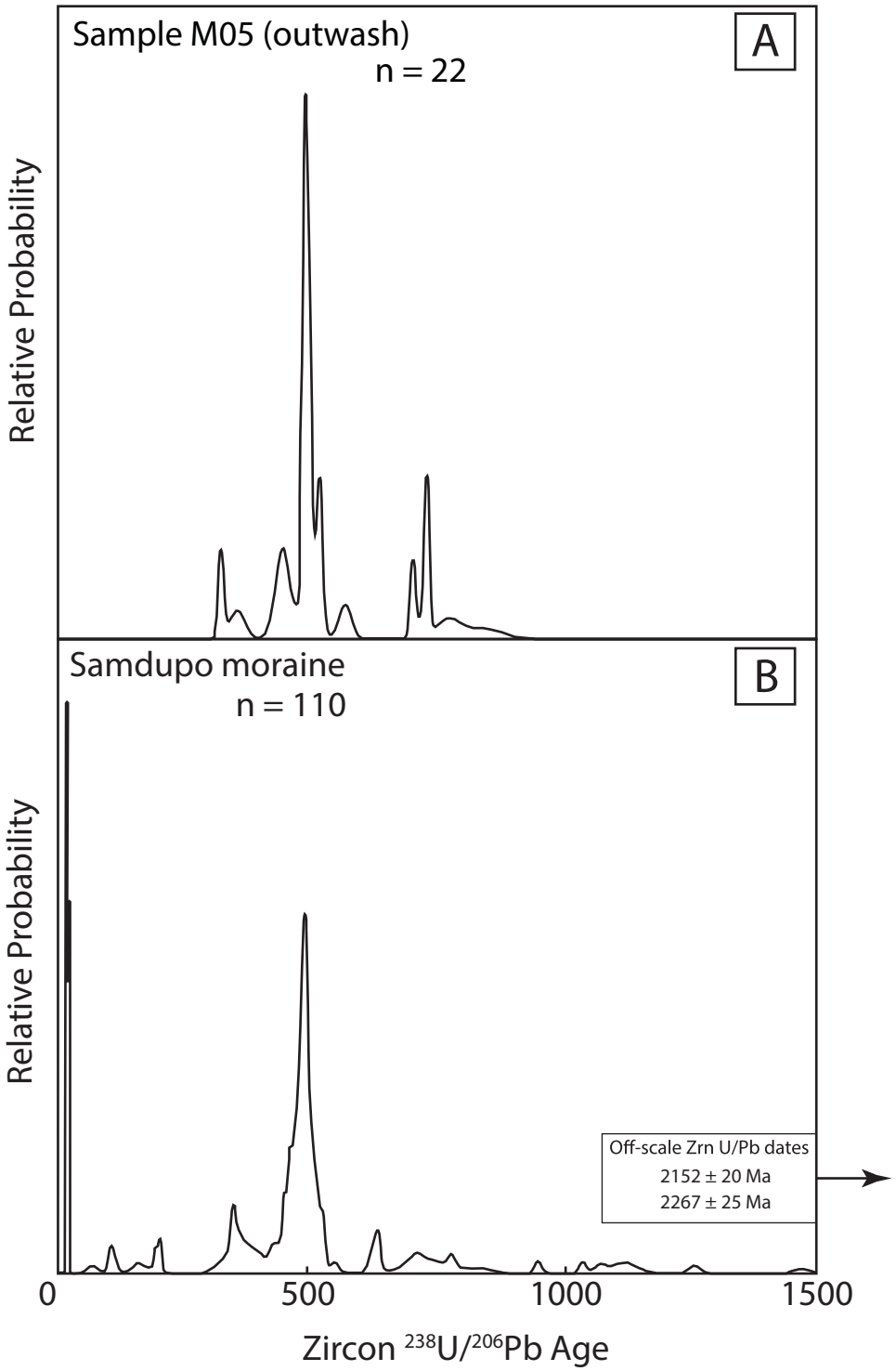
Sample M05 (outwash)
n = 22
A
Relative Probability
Samdupo moraine
n = 110
B
Relative Probability
Off-scale Zrn U/Pb dates
2152 ± 20 Ma
2267 ± 25 Ma
0
500
1000
1500
Zircon 238U/206Pb Age

FIGURE 5.5

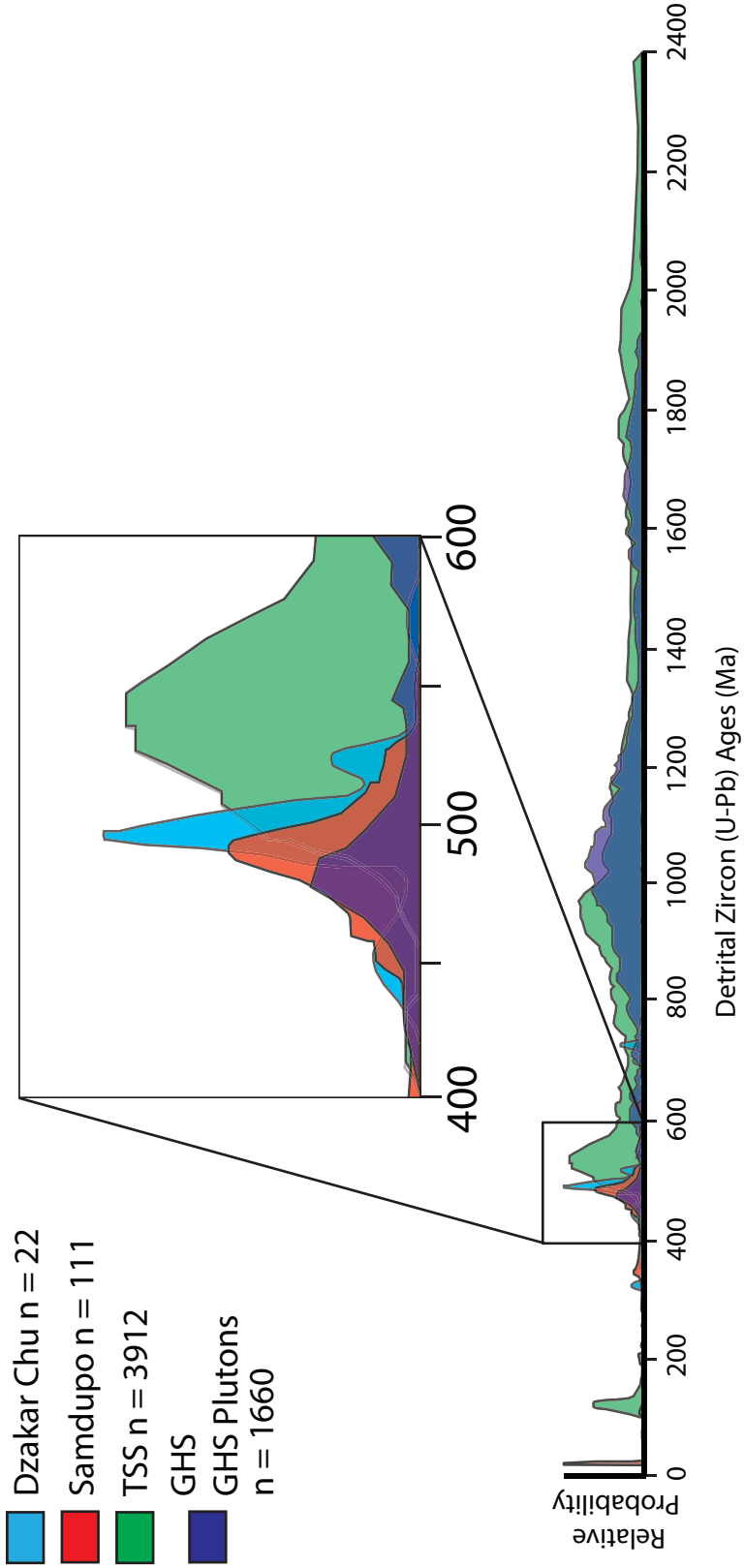
Dzakar Chu n = 22
Samdupo n = 111
TSS n = 3912
GHS
GHS Plutons
n = 1660
Relative Probability
0
200
400
600
800
1000
1200
1400
1600
1800
2000
2200
2400
Detrital Zircon (U-Pb) Ages (Ma)
400
500
600

FIGURE 5.6

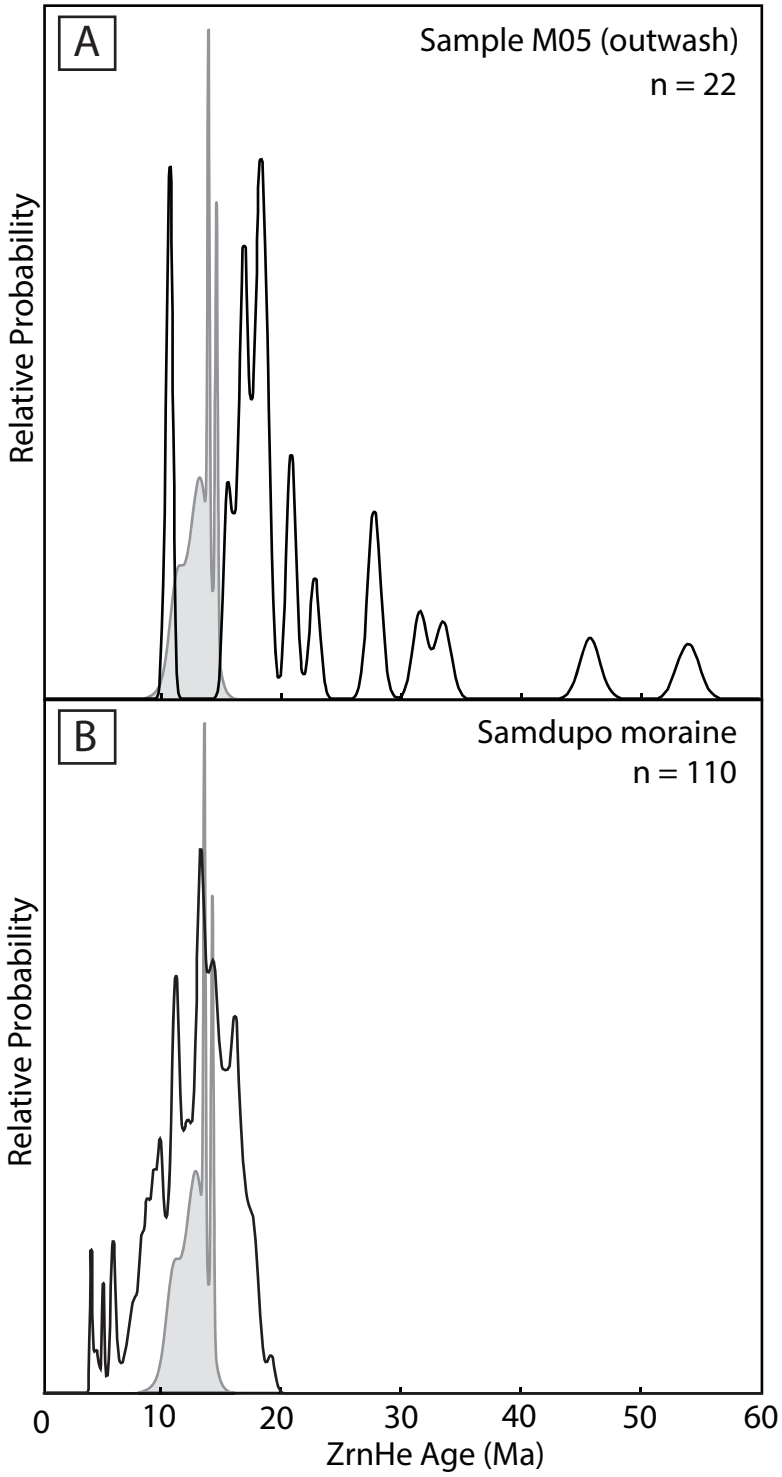
A
Sample M05 (outwash)
n = 22
Relative Probability
B
Samdupo moraine
n = 110
Relative Probability
0
10
20
30
40
50
60
ZrnHe Age (Ma)

FIGURE 5.7

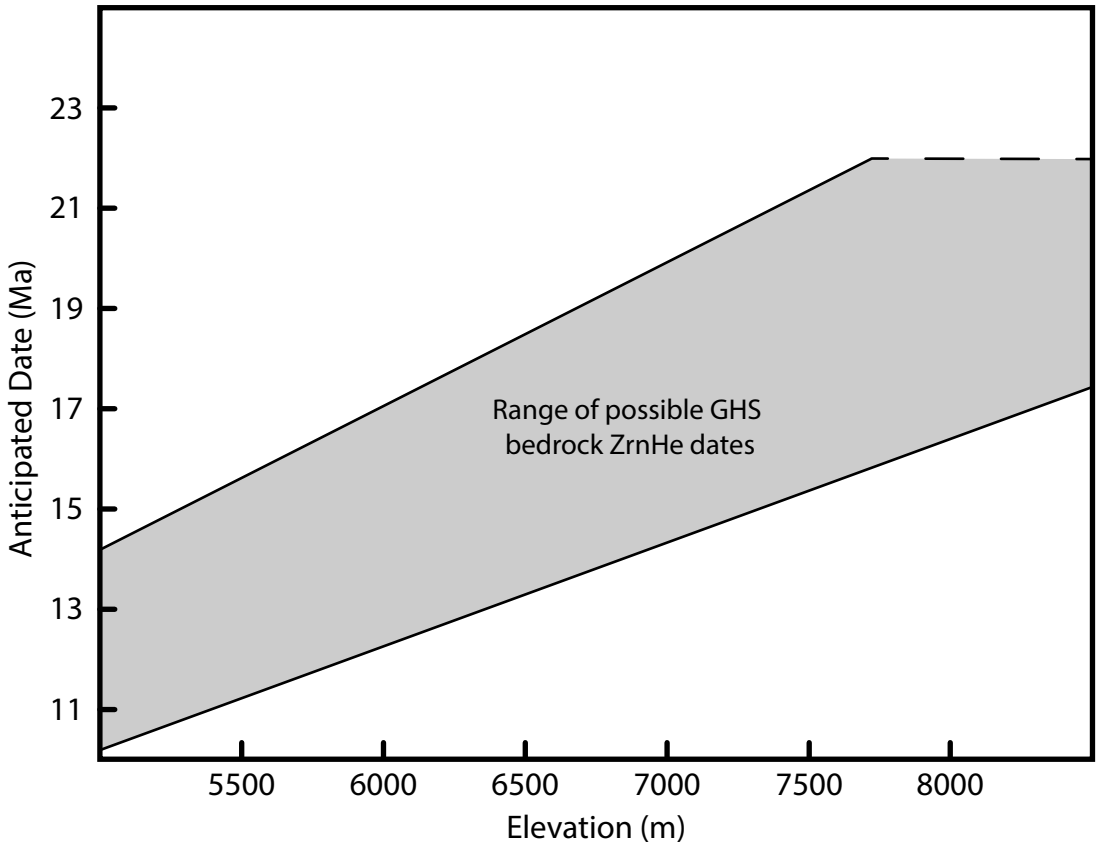
Anticipated Date (Ma)
23
21
19
17
15
13
11
Range of possible GHS
bedrock ZrnHe dates
5500
6000
6500
7000
7500
8000
Elevation (m)

FIGURE 5.8

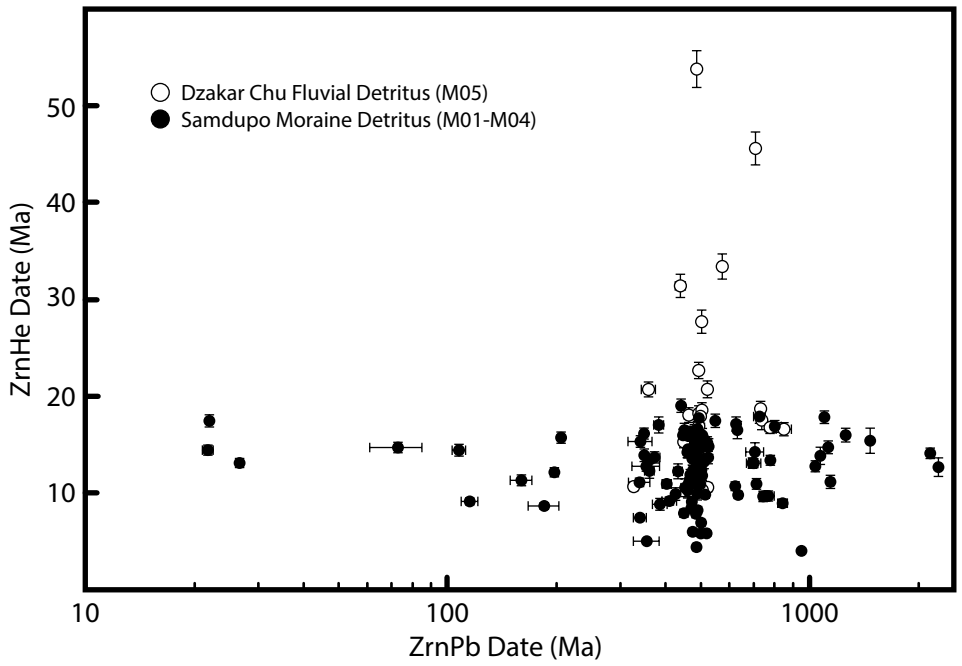
Dzakar Chu Fluvial Detritus (M05)
Samdupo Moraine Detritus (M01-M04)
ZrnHe Date (Ma)
50
40
30
20
10
10
100
1000
ZrnPb Date (Ma)

CHAPTER 6

SYNTHESIS

The chapters above explored the Late Cenozoic climatic and tectonic evolution of the Everest region in the central Himalaya using a variety of approaches and techniques. In this final chapter, I summarize the major contributions of this work and the opportunities for further research.

1. The tectonic significance of the South Tibetan detachment system

The magnitude of displacement on the STDS and continues to be a topic of great debate in Himalayan tectonics. In Chapters 2 and 3, we presented new low-temperature thermochronologic datasets, including muscovite and biotite $^{40}Ar/^{39}Ar$ step heating and zircon and apatite (U-Th)/He analyses, of Greater Himalayan Sequence rocks of the STDS footwall in the Rongbuk valley and two exposures of the STDS about 15 km down dip: on the Ra Chu and Dzakar Chu. We explored the implications of these data for detachment evolution using 1D and preliminary 2D thermal-kinematic models. Our results suggest that total slip on the STDS was ca. 61 to 289 km between at least ca. 20 and 13 Ma, with ca. 36 to 119 km of the displacement occurring in the brittle realm. Our findings imply that the STDS acted as the upper bound of a thick southward extruding channel of rocks of the GHS (Nelson et al., 1996; Beaumont et al., 2001; Hodges et al., 2001; Grujic et al., 2002) and are inconsistent with models that state the STDS played a minor role in Himalayan tectonic evolution (Yin, 2006; Webb et al., 2007; Webb, 2013).

2. Constraining Exhumation Rates North and South of the Himalayan Rain Shadow

Chapter 4 focused on exploring the variations of Late Cenozoic exhumation histories across the Himalayan rain shadow using TRMM data, muscovite and biotite $^{40}Ar/^{39}Ar$ and zircon and apatite (U-Th)/He thermochronometry, and 1D thermal-kinematic modeling. Unlike the uniformly young cooling ages that were revealed for sampling transects along major Transhimalayan rivers (Burbank et al., 2003; Blythe et al., 2007; McDermott, 2012), our results from Chapter 4 show sharp transitions in both cooling ages and modeled exhumation rates that also correspond to the rainfall transition, suggesting that rainfall and bedrock erosion are correlated on million-year timescales.

3. Spatial and Temporal Variations in Sediment Mixing in the Rongbuk Glacial Catchment

In Chapter 5, we used the recently developed laser ablation U/Pb and (U-Th)/He double dating (LADD) technique on detrital zircon crystals from modern outwash sediment of the Dzakar Chu and from sediment of a Holocene glacial moraine to examine how different glacial processes of erosion have acted on the Rongbuk valley. Our results reveal that erosion from older glacial advances affects different areas of the catchment than those of the outwash system of the modern glacier. The source regions of the modern-day Dzakar Chu inferred from our detrital zircon LADD dates are much higher in elevation than the source regions for the Holocene glacial moraine.

4. Future Research Opportunities

4.1 Structural mapping of the Everest transect

Chapter 4 presented the very first comprehensive thermochronologic dataset across a non-Transhimalayan drainage, which revealed a very sharp transition in both cooling ages and exhumation histories. McDermott et al. (2013, 2015) presented evidence of very young, low-angle normal detachments to the east in the Nyalam and Dhaulagiri regions of southern Tibet and central Nepal, respectively and as stated in Chapter 4, our own data may be explained by the existence of such a detachment. Though we did not find evidence for a structural control along the Everest transect, detailed structural mapping of the catchment may prove otherwise. If not, then we must assume that a steady-state precipitation profile exists, perhaps aided by downstream uplift via duplexing to inhibit knickpoint migration.

4.2 Additional sampling of the Dzakar Chu modern fluvial outwash system

Chapter 5 presented (U-Th)/He and U/Pb detrital datasets from Holocene glacial moraine and modern glacial outwash sediment samples. Somewhat unexpectedly, the data from the outwash sample revealed sediment source regions that are much higher in elevation than for the moraine sample. Although there are geomorphic scenarios that could explain this outcome, the number of zircon crystals analyzed from the modern outwash sample was much lower than from the moraine sample, potentially hiding younger ZrnHe populations (in other words, those that point to sourcing from lower elevations). Future work should include the collection of a higher volume of the outwash

detritus that results in a larger number of dated zircons to see if additional ZrnHe date populations are revealed.

5. References

Beaumont, C., Jamieson, R. A., Nguyen, M.H., and Lee, B. (2001). Himalayan tectonics explained by extrusion of a low-viscosity crustal channel coupled to focused surface denudation. *Nature, 414*, 738-742.

Blythe, A. E., Burbank, D. W., Carter, A., Schmidt, K., and Putkonen J. (2007). Plio-Quaternary exhumation history of the central Nepalese Himalaya: 1. Apatite and zircon fission track and apatite U-Th /He analyses. *Tectonics, 26*, doi:Tc300210.1029/2006tc001990.

Burbank, D. W., Blythe, A. E., Putkonen, J., Pratt-Sitaula, B., Gabet, E., Oskin, M., Barros, A., and Ojha, T.P. (2003). Decoupling of erosion and precipitation in the Himalayas, *Nature, 426*, 652-655, doi:10.1038/nature02187.

Ehlers, T.A., A. Szameitat, E. Enkelmann, B.J. Yanites, and G.J. Woodsworth (2015), Identifying spatial variations in glacial erosion with detrital thermochronology, Coast Mountains British Columbia, *Journal of Geophysical Research: Earth Surface*, doi: 10.1002/2014JF003432.

Enkelmann, E. and T.A. Ehlers (2015), Evaluation of detrital thermochronology for quantification of glacial catchment denudation and sediment mixing, *Chemical Geology*, *411,* 299-309.

Grujic, D., Hollister, L., and Parrish, R. R. (2002). Himalayan metamorphic sequence as an orogenic channel: insight from Bhutan. *Earth Planetary Science Letters*, *198*, 177–191.

Herman, F., P. Copeland, J-P. Avouac, L. Bollinger, G. Mahéo, P. Le Fort, S. Rai, D. Foster, A. Pêcher, K. Stüwe, and P. Henry (2010), Exhumation, crustal deformation, and thermal structure of the Nepal Himalaya derived from the inversion of thermochronological and thermobarometric data and modeling of the topography, *Journal of Geophysical Research – Solid Earth, 115*, doi:B0640710.1029/2008jb006126.

Hodges, K. V., Hurtado, J.M., and Whipple, K.X. (2001). Southward extrusion of Tibetan crust and its effect on Himalayan tectonics. *Tectonics, 20*, 799-809.

McDermott, J. A. (2012). Plio-Pleistocene North-South and East-West Extension at the Southern Margin of the Tibetan Plateau. Ph.D. thesis, Arizona State University.

McDermott, J.A., Whipple, K.X., Hodges, K.V., and van Soest, M.C. (2013). Evidence for Plio-Pleistocene north-south extension at the southern margin of the Tibetan Plateau, Nyalam region. *Tectonics, 32*, 317-333, doi:10.1002/tect.20018.

McDermott, J.A., Hodges, K.V., Whipple, K.X., van Soest, M.C., and Hurtado, J.M. (2015). Evidence for Pleistocene Low-Angle Normal Faulting in the Annapurna-Dhaulagiri Region, Nepal. *Journal of Geology*, *123*(2), 133 – 151.

Nelson, K.D., Zhao, W., Brown, L.D., Kuo, J., Che, J., Xianwen, L., Klemperer, S., Makovsky, Y., Meissner, R., Mechie, J., Kind, R., Wenzel, F., Ni, J., Nabelek, J., Chen, L., Handong, T., Wenbo, W., Jones, A.G., Booker, J., Unsworth, N., Kidd, W.S.F., Hauk, M., Alsdorf, D., Ross, A., Cogan, M., Wu, C., Sandvol, E.A., and Edwards, M. (1996). Partially molten middle crust beneath southern Tibet: Synthesis of Project INDEPTH Results. *Science*, *274*, 1684-1688.

Stock, G.M., Ehlers, T.A. and Farley, K.A. (2006). Where does sediment come from? Quantifying catchment erosion with detrital apatite (U-Th)/He thermochronology. *Geology*, *34*, 725-728.

Tranel, L.M., Spotila, J.A., Kowalewski, M.J., and Waller, C.M. (2011). Spatial variation of erosion in a small, glaciated basin in the Teton Range, Wyoming, based on detrital apatite (U-Th)/He thermochronology. *Basin Research*, *23*, 571-590.

Webb, A. A. G. (2013). Preliminary balanced palinspastic reconstruction of Cenozoic deformation across the Himachal Himalaya (northwestern India). *Geosphere*, *9*(3), 572-587.

Webb, A. A. G., Yin, A., Harrison, T.M., Celerier, J. and Burgess, W.P. (2007). The leading edge of the Greater Himalayan Crystalline complex revealed in the NW Indian Himalaya: Implications for the evolution of the Himalayan orogen. *Geology*, *35*(10), 955-958.

Yin, A. (2006). Cenozoic tectonic evolution of the Himalayan orogen as constrained by along-strike variation of structural geometry, exhumation history, and foreland sedimentation. *Earth Science Reviews*, *76*, 1-131.

REFERENCES

Adams, B. A., Hodges K.V., van Soest M.C., and Whipple, K.X. (2013). Evidence for Pliocene-Quaternary normal faulting in the hinterland of the Bhutan Himalaya. *Lithosphere*, *5*, 438-449.

Adams, B.A., Hodges, K.V., Whipple, K.X., Ehlers, T.A., van Soest, M.C., and Wartho, J. (2015). Constraints on the tectonic and landscape evolution of the Bhutan Himalaya from thermochronometry, *Tectonics*. *32*(6), 1329-1347.

Anderson, R.S., Molnar, P. and Kessler, M.A. (2006). Features of glacial valley profiles simply explained, *Journal of Geophysical Research*. *111*, doi:10.1029/2005JF000334.

Bargnesi, E. A., Stockli, D. F., Hourigan, J. K., and Hager, C. (2016). Improved accuracy of zircon (U-Th)/He ages by rectifying parent nuclide zonation with practical methods, *Chemical Geology*. *426*, 158-169.

Barnard, P.L., Owen, L.A., Finkel, R.C., (2006). Quaternary fans and terraces in the Khumbu Himal south of Mount Everest: their characteristics, age and formation. *Journal of Geological Society of London, 163,* 383-399.

Barros, A. P., Chiao, S., Lang, T.J., Burbank, D., and Putkonen, J. (2006). In *Tectonics, Climate, and Landscape Evolution* Vol. Geological Society of America Special Paper *398* (eds S.D. Willett, N. Hovius, M.T. Brandon, & D.M. Fisher), 17-38 (Geological Society of America).

Beaumont, C., Jamieson, R. A., Nguyen, M.H., and Lee, B. (2001). Himalayan tectonics explained by extrusion of a low-viscosity crustal channel coupled to focused surface denudation. *Nature, 414*, 738-742.

Benn, D.I., and Owen, L.A. (2002). Himalayan glacial sedimentary environments: a framework for reconstructing and dating former glacial extents in high mountain regions. *Quaternary International, 97/98,* 3-26.

Bergman, S. C., Coffield, D. Q., Donelick, R., Corrigan, J., Talbot, J., Cerveny, P., and Kelley, S., (1993). Late Cenozoic compressional & extensional cooling & exhumation of the Qomolangma (Mt. Everest) region, Nepal. *Geological Society of America Abstracts with Programs, 25*, 176.

Blisniuk, P. M., Hacker, B. R., Glodny, J., Ratschbacher, L., Bi, S., Wu, Z., McWilliams, M.O., and Calvert, A. (2001). Normal faulting in central Tibet since at least 13.5 Myr ago. *Nature*, *412*, 628-632.

Blythe, A. E., Burbank, D. W., Carter, A., Schmidt, K., and Putkonen J. (2007). Plio-Quaternary exhumation history of the central Nepalese Himalaya: 1. Apatite and zircon fission track and apatite U-Th /He analyses. *Tectonics, 26*,

doi:Tc300210.1029/2006tc001990.

Bollinger, L., Avouac, J. P., Beyssac, O., Catlos, E. J., Harrison, T. M., Grove, M., Goffe, B., and Sapkota, S. (2004). Thermal structure and exhumation history of the Lesser Himalaya in central Nepal. *Tectonics*, *23*(5).

Bollinger, L., Henry, P., and Avouac, J. P. (2006). Mountain building in the Nepal Himalaya: Thermal and kinematic model. *Earth And Planetary Science Letters*, *244*, 58-71.

Bookhagen, B. and Burbank, D.W. (2006). Topography, relief, and TRMM-derived rainfall variations along the Himalaya. *Geophysical Research Letters, 33*, doi:L0840510.1029/2006gl026037.

Bookhagen, B. and Burbank, D.W. (2010). Toward a complete Himalayan hydrological budget: Spatiotemporal distribution of snowmelt and rainfall and their impact on river discharge. *J. Geophys. Res., 115*, F03019, doi:10.1029/2009jf001426

Bookhagen, B., Thiede, R.C., and Strecker, M.R. (2005a). Late Quaternary intensified monsoon phases control landscape evolution in the northwest Himalaya. *Geology 33*, 149-152.

Bookhagen, B., Thiede, R.C., and Strecker, M.R. (2005b). Abnormal monsoon years and their control on erosion and sediment flux in the high, arid northwest Himalaya. *Earth and Planetary Science Letters, 231*, 131-146.

Bookhagen, B. and Burbank, D.W. (2010). Toward a complete Himalayan hydrological budget: Spatiotemporal distribution of snowmelt and rainfall and their impact on river discharge. *J. Geophys. Res., 115*, F03019, doi:10.1029/2009jf001426

Boyce, J.W., Hodges, K.V., Olszewski, W.J., Jercinovic, M.J., Carpenter B.D., and Reiners, P.W. (2006). Laser microprobe (U-Th)/He geochronology. *Geochimica Cosmochimica Acta, 70,* 3031-3039.

Brady, R.J. (2002). Very high slip rates on continental extensional faults: new evidence from (U-Th)/He thermochronometry of the Buckskin Mountains, Arizona. *Earth and Planetary Science Letters, 197*, 95-104.

Braun, J. (2003). Pecube: A new finite-element code to solve the 3D heat transport equation including the effects of a time-varying, finite amplitude surface topography. *Computers & Geosciences*, *29*(6), 787-794.

Braun, J.P. (2016). Strong imprint of past orogenic events on the thermochronological record, *Tectonophysics*. *683, 325-332.*

Braun, J., van der Beek, P., Valla, P., Robert, X., Herman, F., Glotzbach, C., Pedersen, V., Perry, C., Simon-Labric, T., and Prigent, C. (2012). Quantifying rates of

landscape evolution and tectonic processes by thermochronology and numerical modeling of crustal heat transport using PECUBE. *Tectonophysics*, *524–525*, 1-28.

Brewer, I. D., Burbank, D. W., and Hodges, K. V. (2003). Modelling detrital cooling-age populations: insights from two Himalayan catchments. *Basin Research, 15*, 305-320.

Brichau, S. (2004). Constraining the tectonic evolution of extensional fault systems in the Cyclades (Greece) using low-temperature thermochronology. *PhD Dissertation*, University of Mainz and University of Montpelier.

Burbank, D. W., Blythe, A. E., Putkonen, J., Pratt-Sitaula, B., Gabet, E., Oskin, M., Barros, A., and Ojha, T.P. (2003). Decoupling of erosion and precipitation in the Himalayas, *Nature, 426*, 652-655, doi:10.1038/nature02187.

Burchfiel, B.C., and Royden, L.H. (1985). North-south extension within the convergent Himalayan region. *Geology*, *13,* 679-682.

Burchfiel, C. B., Chen, Z., Hodges, K. V., Liu, Y., Royden, L.H., Deng, C., and Xu J. (1992). The South Tibetan detachment system, Himalayan orogen: extension contemporaneous with and parallel to shortening in a collisional mountain belt. *Geologic al Society of America Special Paper*, *269*, 41 p.

Burg, J.P. (1983). *Carte Geologique du Sud du Tibet*. Ministry of Geology, Peking and CNRS, Paris.

Burg J. P. and Chen, G. (1984). Tectonics and structural formation of southern Tibet, China. *Nature, 311,* 219-223.

Caby, R. Pêcher, A., and Le Fort, P. (1983). Le grand chevauchement central himalayen: nouvelles données sur le métamorphisme inverse à la base de la Dalle du Tibet. *Revue de Géologie Dynamique et de Géographie Physique*, *24,* 89-100.

Campani, M., Herman, F., and Mancktelow, N. (2010). Two- and three-dimensional thermal modeling of a low-angle detachment; exhumation history of the Siplon fault zone, Central Alps. *Journal of Geophysical Research*, *115*, *B10.*

Carosi, R., Lombardo, B., Molli, G., Musumeci, G., and Pertusati, P.C. (1998). The South Tibetan detachment system in the Rongbuk Valley, Everest region. Deformation features and geological implications. *Journal of Asian Earth Sciences*, *16*, 299–311.

Carosi, R., Lombardo, B., Musumeci, G., and Pertusati, P.C. (1999). Geology of the Higher Himalayan Crystallines in Khumbu Himal (Eastern Nepal). *Journal of Asian Earth Sciences*, *17*, 785-803.

Carrapa, B., Robert, X., DeCelles, P.G., Orme, D.A., Thomson, S.N., and Schoenbohm, L.M. (2016). Asymmetric exhumation of the Mount Everest region: Implications for the tectono-topographic evolution of the Himalaya. *Geology*, doi: 10.1130/G37756.1.

Cattin, R., and Avouac, J.P., (2000). Modeling mountain building and the seismic cycle in the Himalaya of Nepal. *Journal of Geophysical Research: Solid Earth*. doi: 10.1029/2000JB90032.

Cawood, P. A., Johnson, M. R. W., and Nemchin, A. A. (2007). Early Paleozoic orogenesis along the Indian margin of Gondwana: Tectonic response to Gondwana assembly. *Earth and Planetary Science Letters*, *255*, 70–84, doi:10.1016/j.epsl.2006.12.006.

Clift, P. D., Hodges, K. V., Heslop, D., Hannigan, R., Hoang, L. V., and Calves G. (2008). Correlation of Himalayan exhumation rates and Asian monsoon intensity. *Nature Geoscience*, *1*, 875-880.

Coleman, M., and Hodges, K. (1995). Evidence for Tibetan Plateau uplift before 14 Myr ago from a new minimum age for east-west extension. *Nature*, *374*(6517), 49-52.

Cooper, F. J., Adams, B. A., Edwards, C. S., and Hodges, K. V. (2012). Large normal-sense displacement on the South Tibetan fault system in the eastern Himalaya. *Geology*, *40*(11), 971-974.

Cooper, F. J., Hodges, K.V., and Adams, B.A. (2013). Metamorphic constraints on the character and displacement of the South Tibetan fault system, central Bhutanese Himalaya. *Lithosphere*, *5*, 67-81.

Cooper, F.J., Hodges, K.V., Parrish, R.R., Roberts, N.M.W., and Horstwood, M.S.A. (2015). Synchronous N-S and E-W extension at the Tibet-to-Himalaya transition in NW Bhutan, *Tectonics*. *34*(7), 1375-1395.

Copeland, P., Parrish, R.R., and Harrison, T.M. (1988). Identification of inherited radiogenic Pb in monazite and its implications for U-Pb systematics. *Nature*, *333*, 760-763.

Corfu, F., Ravna, E. J. K., and Kullerud, K. (2003). A Late Ordovician U-Pb age for the Tromsø Nappe eclogites, Uppermost Allocthon of the Scandinavian Caledonides. *Contrib. Mineral Petrol.*, *145*, 502-513.

Corthouts, T. L., Lageson, D. R., and Shaw, C. A. (2016). Polyphase deformation, dynamic metamorphism, and metasomatism of Mount Everest's summit limestone, east central Himalaya, Nepal/Tibet. *Lithosphere*, *8*, doi: 10.1130/l1473.1131.

Cottle, J. M., Jessup, M.J., Newell, D.L., Searle, M.P., Law, R.D., and Horstwood

M.S.A., (2007). Structural insight into the ductile evolution of an orogen-scale detachment: the South Tibetan detachment system, Dzakaa Chu section, eastern Himalaya. *Journal of Structural Geology*, *29*, 1781-1797.

Cottle, J. M., Waters, D.J., Riley, D., Beyssac, O., and Jessup, M.J. (2011). Metamorphic history of the South Tibetan Detachment System, Mt. Everest region, revealed by RSCM thermometry and phase equilibria modelling. *Journal of Metamorphic Geology*, *29*(5), 561-582.

Cottle, J. M., Larson, K.P., and Kellett, D.A. (2015a). How does the mid-crust accommodate deformation in large, hot collisional orogens? A review of recent research in the Himalayan orogen. *Journal of Structural Geology*, *78*, 119-133.

Cottle, J. M., Searle, M. P., Jessup, M. J., Crowley, J. L., and Law, R. D. (2015b). Rongbuk re-visited: Geochronology of leucogranites in the footwall of the South Tibetan Detachment System, Everest Region, Southern Tibet. *Lithos*, *227*, 94-106.

DeCelles, P. G., Gehrels, G.E., Quade, J., Lareau, B., and Spurlin M. (2000). Tectonic implications of U–Pb zircon ages of the Himalayan orogenic belt in Nepal. *Science*, *288*, 497–499, doi:10.1126/science.288.5465.497.

DeCelles, P. G., et al. (2001). Stratigraphy, structure, and tectonic evolution of the Himalayan fold-thrust belt in western Nepal. Tectonics 20, 487-509.

Dobson, K.J., Stuart, F.M., and Dempster, T.J. (2008). U and Th zonation in Fish Canyon Tuff zircons: implications for a zircon (U-Th)/He standard. *Geochimica Cosmochimica Acta, 72,* 4745-4755.

Ehlers, T.A., Szameitat, A., Enkelmann, E., Yanites, B.J., and Woodsworth, G.J. (2015). Identifying spatial variations in glacial erosion with detrital thermochronology, Coast Mountains British Columbia. *Journal of Geophysical Research: Earth Surface*, doi: 10.1002/2014JF003432.

Enkelmann, E. and Ehlers, T.A. (2015). Evaluation of detrital thermochronology for quantification of glacial catchment denudation and sediment mixing. *Chemical Geology*, *411,* 299-309.

Evans, N.J., McInnes, B.I.A., McDonald, B., Danisik, M., Becker, T., Vermeesch, P., Shelley, M., Marillo-Sialer, E., and Patterson, D.B. (2015). An *in situ* technique for (U-Th-Sm)/He and U-Pb double dating. *Journal of Analytical Atomic Spectrometry, 30,* 1636-1645.

Evans, S. L., Styron, R.H., van Soest, M.C., Hodges, K.V., and Hanson, A.D. (2015). Zircon and apatite (U-Th)/He evidence for Paleogene and Neogene extension in the Southern Snake Range, Nevada, USA. *Tectonics*, *34*(10), 2142-2164, doi: 10.1002/2015TC003913.

Farley, K.A., Wolf, R.A., and L.T. Silver, L.T. (1996). The effects of long alpha-stopping distances on (U-Th)/He ages. *Geochimica et Cosmochimica Acta*, *60*, 4223-4229.

Farley K.A. (2000). Helium diffusion from apatite: General behavior as illustrated by Durango fluorapatite. *Journal of Geophysical Research*, *105*, 2903–2914.

Feng, R., Nuno, M., Ludden, J. (1993). Lead geochronology of zircon by laserprobe-inductively coupled plasma mass spectrometry (LA-ICPMS). *Geochimica et Cosmochimica Acta*, *57*(14), 3479-3486.

Finkel, R.C., Owen, L.A., Barnard, P.L., Caffee, M.W., (2003). Beryllium-10 dating of Mount Everest moraines indicates a strong monsoonal influence and glacial synchroneity throughout the Himalaya. *Geology, 31,* 561-564.

Fleck, R. J., Sutter, J.F., and Elliot, D.H. (1977). Interpretation of discordant $^{40}Ar/^{39}Ar$ age spectra of Mesozoic tholeiites from Antarctica. *Geochimica et Cosmochimica Acta*, *41*, 15-32.

Flowers, R.M., Ketcham, R.A., Shuster, D.L., and Farley K.A. (2009). Apatite (U-Th)/He thermochronometry using a radiation damage accumulation and annealing model. *Geochimica et Cosmochimica Acta*, *73*, 2347-2365.

Gabet, E. J., Burbank, D.W., Pratt-Sitaula, B., Putkonen, J., and Bookhagen, B. (2008). Modern erosion rates in the High Himalayas of Nepal. *Earth and Planetary Science Letters, 267*, 482-494, doi:10.1016/j.epsl.2007.11.059.

Gaetani, M., and Garzanti, E. (1991). Multicyclic history of the northern India continental margin (Northwestern Himalaya). *Bulletin of the American Association of Petroleum Geologists*, *75*, 1427-1446.

Gallagher, K. (2012). Transdimensional inverse thermal history modelling for quantitative thermochronology. *Journal of Geophysical Research*, *117*, B02408, doi:10.1029/2011JB00882.

Gayer, E., Lavé, J., Pik, R., and France-Lanord, C. (2006). Monsoonal forcing of Holocene glacier fluctuations in Ganesh Himal (Central Nepal) constrained by cosmogenic ^{3}He exposure of garnets. *Earth and Planetary Science Letters*, *252*(3-4), 275-288.

Gébelin, A., Mulch, A., Teyssier, C., Jessup, M. J., Law, R. D., and Brunei M. (2013). The Miocene elevation of Mount Everest. *Geology*, *41*(7), 799-802.

Gehrels, G. (2012). Detrital zircon U-Pb geochronology: Current methods and new opportunities. In: Busby, C. and Perez, A. A. Eds.). *Tectonics of Sedimentary Basins: Recent Advances*, Blackwell, Oxford, U.K.

Gehrels, G., Kapp, P., DeCelles, P., Pullen, A., Blakey, R., Weislogel, A., Ding, L., Guynn, J., Martin, A., McQuarrie, N., and Yin, A. (2011). Detrital zircon

geochronology of pre-Tertiary strata in the Tibetan-Himalayan orogen. *Tectonics*, *30*, doi:10.1029/2011TC002868.

Grove, M. and Harrison, T.M. (1996). ^{40}Ar* diffusion in Fe-rich biotite. *American Mineralogist*, *81*, 940-951.

Grujic, D., Casey, M., Davidson, C., Hollister, L. S., Kündig, R., Pavlis, R., and Schmid, S. (1996). Ductile extrusion of the Higher Himalayan crystalline in Bhutan: evidence from quartz microfabrics, *Tectonophysics*, *260*, 21-43.

Grujic, D., Hollister, L., and Parrish, R. R. (2002). Himalayan metamorphic sequence as an orogenic channel: insight from Bhutan. *Earth Planetary Science Letters*, *198*, 177–191.

Guenthner, W.R., Reiners, P.W., Ketcham, R.A., Nasdala, L., and Geister, G. (2013). Helium diffusion in natural zircon: Radiation damage, anisotropy, and the interpretation of zircon (U-Th)/He thermochronology. *American Journal of Science*, *313*, p. 145 – 198.

Hambrey, M.J., Quincey, D.J., Glasser, N.F., Reynolds, J.M., Richardson, S.J., and Clemmens, S. (2008). Sedimentological, geomorphological and dynamic context of debris-mantled glaciers, Mount Everest (Sagarmatha) region, Nepal. *Quaternary Science Reviews*, *27*, 2361-2389.

Hambrey, M.J., and Glasser, N.F. (2012). Discriminating glacier thermal and dynamic regimes in the sedimentary record. *Sedimentary Geology*, *251-252,* 1-33.

Harris, N. (2006). The elevation history of the Tibetan Plateau and its implications for the Asian monsoon. *Palaeogeography, Palaeoclimatology, Palaeoecology*, *241*, 4-15.

Harrison, T. M., Celerier, J., Aikman, A.B., Hermann, J., and Heizler, M.T. (2009). Diffusion of ^{40}Ar in muscovite. *Geochimica et Cosmochimica Acta*, *73*(4), 1039-1051.

He, D., Webb, A.A.G., Larson, K.P., Martin, A.J., and Schmitt, A.K. (2015). Extrusion vs. duplexing models of Himalayan mountain building 3: duplexing dominates from the Oligocene to Present. *International Geology Review*, *57*, 1-27.

Heimsath, A. M. and McGlynn, R. (2008). Quantifying periglacial erosion in the Nepal high Himalaya. *Geomorphology*, *97*, 5-23.

Hellstrom, J., Paton, C., Woodhead, J., & Hergt, J. (2008). Iolite: software for spatially resolved LA-(quad and MC) ICPMS analysis. *Mineralogical Association of Canada short course series*, *40*, 343-348.

Herman, F., Copeland, P., Avouac, J-P., Bollinger, L., Mahéo, G., Le Fort, P., Rai, S., Foster, D., Pêcher, A., Stüwe, K., and Henry, P. (2010). Exhumation, crustal deformation, and thermal structure of the Nepal Himalaya derived from the

inversion of thermochronological and thermobarometric data and modeling of the topography. *Journal of Geophysical Research – Solid Earth, 115*, doi:B0640710.1029/2008jb006126.

Hodges, K. V. (2000). Tectonics of the Himalaya and southern Tibet from two perspectives. *Geological Society of America Bulletin*, *112*, 324-350.

Hodges, K. V. (2006). A synthesis of the Channel Flow-Extrusion hypothesis as developed for the Himalayan-Tibetan orogenic system, in *Channel Flow, Ductile Extrusion, and Exhumation of Lower-Middle Crust in Continental Collision Zones*, edited by R. Law, M. Searle and L. Godin, 71-90, Geological Society Special Publication 268, London.

Hodges, K.V. (2014). Thermochronology in Orogenic Systems, in: Holland, H.D., Turekian, K.K. (Eds.), *Treatise on Geochemistry, Second Edition, 4,* Elsevier, Oxford, 281-308.

Hodges, K.V. (2016). Crustal decoupling in collisional orogenesis: Examples from the East Greenland Caledonides and Himalaya. *Annual Review of Earth and Planetary Sciences, 44*, 685-708.

Hodges, K. V., Parrish, R.R., Housh, T.B., Lux, D.R., Burchfiel, B.C., Royden, L.H., and Chen, Z. (1992). Simultaneous Miocene extension and shortening in the Himalayan orogen. *Science*, *258*, 1466–1470.

Hodges, K.V., and Walker, J.D. (1992). Extension in the Cretaceous Sevier orogeny, North American Cordillera. *Geological Society of America Bulletin*, *104*, 560-569.

Hodges, K. V., Bowring, S., Davidek, K., Hawkins, D., and Krol, M. (1998). Evidence for rapid displacement on Himalayan normal faults and the importance of tectonic denudation in the evolution of mountain ranges. *Geology*, *26*, 483–486.

Hodges, K. V., Hurtado, J.M., and Whipple, K.X. (2001). Southward extrusion of Tibetan crust and its effect on Himalayan tectonics. *Tectonics, 20*, 799-809.

Horne, A.M, van Soest, M.C., Hodges, K.V., Tripathy-Lang, A., and Hourigan, J.K. (2016). Integrated Single Crystal Laser Ablation U/Pb and (U-Th)/He Dating of Detrital Accessory Minerals – Proof-of-Concept Studies of Titanites and Zircons from the Fish Canyon Tuff. *Geochimica et Cosmochimica Acta*, *178*, 106 – 123.

Hourigan, J.K., Reiners, P.W., and Brandon, M.T. (2005). U-Th zonation dependent alpha-ejection in (U-Th)/He chronometry. *Geochimica et Cosmochimica Acta, 69*, 3349-3365.

Huang, M. (1990). On the temperature distribution of glaciers in China. *Journal of Glaciology*, *36*, 210-216.

Hubbard, M., and Harrison, T.M. (1989). $^{40}Ar/^{39}Ar$ age constraints on deformation and metamorphism in the Main Central Thrust zone and Tibetan Slab, eastern Nepal Himalaya. *Tectonics*, *8*(4), 865 – 880.

Jamieson, R.A., Beaumont, C., Medvedev, S., and Nguyen, M.H. (2004). Crustal channel flows: 2. Numerical models with implications for metamorphism in the Himalayan-Tibetan orogeny. *Journal of Geophysical Research, 109*, B06406, doi:10.1029/2003JB002811.

Jessup, M. J., Law, R. D., Searle, M. P. and Hubbard, M.S. (2006). Structural evolution and vorticity of flow during extrusion and exhumation of the Greater Himalayan Slab, Mount Everest Massif, Tibet/Nepal: implications for orogen-scale flow partitioning, *in Channel Flow, Ductile Extrusion, and Exhumation of Lower-Middle Crust in Continental Collision Zones*, edited by Law, R., Searle, M., and Godin, L., London, Geological Society Special Publication 268, p. 79-414.

Jessup, M. J., Cottle, J.M., Searle, M.P, Law, R.D., Newell, D.L., Tracy, R.J., and Waters, D.J. (2008). PT-t-D paths of Everest Series schist. Nepal, *Journal of Metamorphic Geology*, *26*, 717–739.

Jessup, M.J. and Cottle, J.M. (2010). Progression from South-Directed Extrusion to Orogen-Parallel Extension in the Southern Margin of the Tibetan Plateau, Mount Everest Region, Tibet. *Journal of Geology*, *118*, 467-486.

John, B.E., and Foster, D.A. (1993). Structural and thermal constraints on the initiation angle of detachment faulting in the southern Basin and Range: The Chemehuevi Mountains case study. *Geologic Society of America Bulletin, 105*, 1091-1108.

Kellett, D.A., Grujic, D., Coutand, I., Cottle, J., and Mukul M. (2013). The South Tibetan detachment system facilitates ultra rapid cooling of granulite-facies rocks in Sikkim Himalaya. *Tectonics*, *32*, 252 – 270.

Kelley, S. (2002). Excess argon in K-Ar and Ar-Ar geochronology. *Chemical Geology, 188*(1-2), 1-22.

Ketcham, R. A. (2005). Forward and inverse modeling of low-temperature thermochronometry data, in *Low-Temperature Thermochronology: Techniques, Interpretations, and Applications*, edited by P. W. Reiners and T. A. Ehlers, pp. 275-314, Mineralogical Society of America, Washington, DC.

Kohn, M. J. (2008). P-T-t data from central Nepal support critical taper and repudiate large-scale channel flow of the Greater Himalayan Sequence, *Geological Society of America Bulletin*. *120*(3-4), 259-273.

Kosler, J., Fonneland, H., Sylvester, P., Tubrett, M., Pedersen, R-B. (2002). U-Pb dating of detrital zircons for sediment provenance studies; a comparison of laser ablation ICPMS and SIMS techniques. *Chemical Geology, 182,* 605-618.

Lavé, J. and Avouac, J.P. (2001). Fluvial incision and tectonic uplift across the Himalayas of central Nepal. *Journal of Geophysical Research, 106,* 26561-26591.

Law, R. D. (2014). Deformation thermometry based on quartz c-axis fabrics and recrystallization microstructures: A review. *Journal of Structural Geology*, *66*, 129-161.

Law, R.D., Searle, M.P., and Simpson, R.L. (2004). Strain, deformation temperatures and vorticity of flow at the top of the Greater Himalayan Slab, Everest Massif, Tibet. *Journal of the Geological Society of London*, *161*, 305-320.

Law, R.D., Searle, M.P., and Godin, L., (Eds). (2006). Channel Flow, Ductile Extrusion and Exhumation in Continental Collision Zones. *Geological Society of London Special Publication, 268,* London. 632 pp.

Law, R.D., Jessup, M.J., Searle, M.P., Francis, M.K., Waters, D.J., and Cottle, J.M. (2011). Telescoping of isotherms beneath the South Tibetan Detachment System, Mount Everest Massif. *Journal of Structural Geology*, *33*, 1569-1594.

Le Breton, N., and Thompson, A.B. (1988). Fluid-absent (dehydration) melting of biotite in metapelites in the early stages of crustal anatexis. *Contributions to Mineralogy and Petrology*, *99*, 226-237.

Le Fort, P., Cuney, M., Deniel, C., France-Lanord, C., Sheppard, S.M.F., Upreti, B.N., and Vidal, P. (1987). Crustal generation of Himalayan leucogranites. *Tectonophysics*, *134*, 39-57.

Leloup, P.H., Maheo, G., Arnaud, N., Kali, E., Boutonnet, E., Liu, D., Xiaohan, L., and Haibing, L. (2010). The South Tibet detachment shear zone in the Dinggye area Time constraints on extrusion models of the Himalayas. *Earth and Planetary Science Letters*, *292*, 1-16.

Lombardo, B., Pertusati, P., and Borghi S., (1993). Geology and tectonomagmatic evolution of the eastern Himalaya along the Chomolungma-Makalu transect, in *Himalayan Tectonics*, edited by P. J. Treloar and M. P. Searle, pp. 341-355, Geological Society Special Publication, 47, London.

Long, S.P., Thomson, S.N., Reiners, P.W., and Di Fiori, R.V. (2015). Synorogenic extension localized by upper-crustal thickening: An example from the Late Cretaceous Nevadaplano. *Geology, 43*(4), 351-354.

Ludwig, K.R. (2012). *User's manual for Isoplot 3.75: a geochronological toolkit for Microsoft Excel* (Vol. 5): Kenneth R. Ludwig.

Mahon, K. I. (1996). The new "York" regression: Application of an improved statistical method to geochemistry. *International Geology Review*, *38*, 293-303.

Mann, D.H., Sletten, R.S. and Reanier, R.E. (1996). Quaternary glaciation of the Rongbuk valley, Tibet. *Journal of Quaternary Science*, *11,* 267-280.

Masek, J.G., Isacks, B.L., Gubbels, T.L., and Fielding, E.J. (1994). Erosion and tectonics at margins of continental plateaus. J. Geophysical Research, *99*, 13941-13956.

McDermott, J. A. (2012). Plio-Pleistocene North-South and East-West Extension at the Southern Margin of the Tibetan Plateau. Ph.D. thesis, Arizona State University.

McDermott, J.A., Whipple, K.X., Hodges, K.V., and van Soest, M.C. (2013). Evidence for Plio-Pleistocene north-south extension at the southern margin of the Tibetan Plateau, Nyalam region. *Tectonics, 32*, 317-333, doi:10.1002/tect.20018.

McDermott, J.A., Hodges, K.V., Whipple, K.X., van Soest, M.C., and Hurtado, J.M. (2015). Evidence for Pleistocene Low-Angle Normal Faulting in the Annapurna-Dhaulagiri Region, Nepal. *Journal of Geology*, *123*(2), 133 – 151.

Monteleone, B.D., van Soest, M.C., Hodges, K.V., Moore, G.M., Boyce, J.W., and Hervig, R.L. (2009). Assessment of Alternative [U] and [Th] Zircon Standards for SIMS. Paper presented at American Geophysical Union Fall Meeting, San Francisco, CA, USA.

Müller, R. D., Sdrolias, M., Gaina, C., and Roest, W.R. (2008). Age, spreading rates, and spreading asymmetry of the world's ocean crust. *Geochemistry Geophysics Geosystems*, *9*, doi: 10.1029/2007gc001743.

Murphy, M. A. and Harrison, T.M. (1999). Relationship between leucogranites and the Qomolangma Detachment in the Rongbuk Valley, South Tibet. *Geology*, *27*(9), 831-834, doi:10.1130/0091-7613(1999)027<0831:RBLATQ>2.3.CO;2.

Myrow, P. M., Hughes, N.C., Searle, M.P., Fanning, C.M., Peng, S.C., and Parcha, S.K. (2009). Stratigraphic correlation of Cambrian-Ordovician deposits along the Himalaya: Implications for the age and nature of rocks in the Mount Everest region. *Geological Society of America Bulletin*, *121*(3-4), 323-332.

Najman, Y., Appel, E., Boudagher-Fadel, M., Bown, P., Carter, A., Garzanti, E., Godin, L., Han, J.T., Liebke, U., Oliver, G., Parrish, R., and Vezzoli, G. (2010). Timing of India-Asia collision: Geological, biostratigraphic, and palaeomagnetic constraints. *Journal of Geophysical Research-Solid Earth*, *115*, doi: 10.1029/2010jb007673.

Nelson, K.D., Zhao, W., Brown, L.D., Kuo, J., Che, J., Xianwen, L., Klemperer, S., Makovsky, Y., Meissner, R., Mechie, J., Kind, R., Wenzel, F., Ni, J., Nabelek, J., Chen, L., Handong, T., Wenbo, W., Jones, A.G., Booker, J., Unsworth, N., Kidd, W.S.F., Hauk, M., Alsdorf, D., Ross, A., Cogan, M., Wu, C., Sandvol, E.A., and Edwards, M. (1996). Partially molten middle crust beneath southern Tibet: Synthesis of Project INDEPTH Results. *Science*, *274*, 1684-1688.

Orme, D.A., Reiners, P.W., Hourigan, J.K., and Carrapa, B. (2015). Effects of inherited cores and magmatic overgrowths on zircon (U-Th)/He ages and age-eU trends from Greater Himalaya sequence rocks, Mt. Everest region, Tibet. *Geochemistry, Geophysics, Geosystems*, DOI 10.1002/2015GC005818

Owen, L.A., Robinson, R., Benn, D.I., Finkel, R.C., Davis, N.K., Yi, C., Putkonen, J., Li, D., and Murray, A.S. (2009). Quaternary glaciation of Mount Everest. *Quaternary Science Reviews*, *28,* 1412-1433.

Parrish, R. R., and Hodges, K.V. (1996). Isotopic constraints on the age and provenance of the Lesser and Greater Himalayan sequences. Nepalese Himalaya, *Geological Society of America Bulletin*, *108*, 904-911.

Patiño-Douce, A. E., and Harris, N. (1998). Experimental constraints on Himalayan anatexis. *Journal of Petrology*, *39*, 689-710.

Paton, C., Woodhead, J.D., Hellstrom, J.C., Hergt, J.M., Greig, A., Maas, R., (2010). Improved laser ablation U-Pb zircon geochronology through robust downhole fractionation correction. *Geochemistry Geophysics Geosystems*, *11*, doi:10.1029/2009gc002618.

Pearson, R.K. (2011). *Exploring data in engineering, the sciences, and medicine*, Oxford University Press.

Pognante, U., and Benna, P. (1993). Metamorphic zonation, migmatization and leucogranites along the Everest transect of eastern Nepal and Tibet: record of an exhumation history, *in* Treloar, P. J., and Searle, M. P., eds., Himalayan Tectonics: London, The Geological Society, 323-340.

Rades, E. F., Hetzel, R., Strobl, M., Xu, Q., and Ding, L. (2015). Defining rates of landscape evolution in a south Tibetan graben with in situ-produced cosmogenic ^{10}Be. *Earth Surface Processes and Landforms*, *40*, 1862-1876.

Ray, L., Bhattacharya, A., and Roy, S. (2007). Thermal conductivity of Higher Himalayan Crystallines from Garhwal Himalaya, India. *Tectonophysics*, *434*, 71-79.

Reiners, P. W., Spell, T. L., Nicolescu, S., and Zanetti K. A., (2004). Zircon (U-Th)/He thermochronometry: He diffusion and comparisons with ^{40}Ar/^{39}Ar dating. *Geochimica et Cosmochimica Acta*, *68*, 1857-1887.

Reiners, P.W. and Brandon, M.T. (2006). Using thermochronology to understand orogenic erosion. *Annual Review of Earth and Planetary Sciences*, *34*, 419-466.

Reiners, P. W., Thomson, S.N., McPhillips, D., Donelick, R.A., and Roering, J.J. (2007). Wildfire thermochronology and the fate and transport of apatite in hillslope and fluvial environments. *Journal of Geophysical Research, 112*, F04001, doi:10.1029/2007JF000759.

Robinson, D. M. and Pearson, O.N. (2013). Was Himalayan normal faulting triggered by initiation of the Ramgarh-Munsiari thrust and development of the Lesser Himalayan duplex? *International Journal of Earth Sciences, 102*(7), 1773-1790.

Roddick, J.C., Cliff, R.A. and Rex, D.C. (1980). The evolution of excess argon in Alpine biotites – A ^{40}Ar-^{39}Ar analysis. *Earth and Planetary Science Letters*, *48*, 185-208.

Ruhl., K.W. and Hodges, K.V. (2005). The use of detrital mineral cooling ages to evaluate steady state assumptions in active orogens: An example from the central Nepalese Himalaya. *Tectonics*, *24*, doi: 10.1029/2004TC001712

Ruppel, C., Royden, L., and Hodges, K.V. (1988). Thermal modeling of extensional tectonics: Application to pressure-temperature-time histories of metamorphic rocks. *Tectonics*, *7*, 947 – 957.

Sakai, H., Sawada, M., Takigami, Y., Orihashi, Y., Danhara, T., Iwano, H., Kuwahara, Y., Dong, Q., Cai, H.W., and Li, J.G. (2005). Geology of the summit limestone of Mount Qomolangma (Everest) and cooling history of the Yellow Band under the Qomolangma detachment. *Island Arc*, *14*(4), 297-310.

Sambridge, M. (1999). Geophysical inversion with a Neighborhood Algorithm – I. Searching a parameter space. *Geophysical Journal International, 138,* 479-494.

Schultz, M.H., Hodges, K.V., Ehlers, T.A., van Soest, M.C., and Wartho, J-A. (2017). Thermochronologic constraints on the slip history of the South Tibetan detachment system, south-central Tibet, *Earth and Planetary Science Letters*, *459*, 105-117.

Schwarz, W.H., and Trielhoff, M. (2007). Intercalibration of ^{40}Ar-^{39}Ar age standards NL-25, HB3gr hornblende, GA1550, SB-3, HD-B1 biotite and BMus/2 muscovite. *Chemical Geology*, *242*, 218 – 231.

Searle, M. P. (1999). Extensional and compressional faults in the Everest-Lhotse massif, Khumbu Himalaya, Nepal. *Journal of the Geological Society of London*, 156, 227–240.

Searle, M. P., Simpson, R., Law, R.D., Parrish, R.R., and Waters, D.J. (2003). The structural geometry, metamorphic and magmatic evolution of the Everest massif, High Himalaya of Nepal–South Tibet. *Journal of the Geological Society of London*, *160*, 345–366.

Searle, M. P., Law, R.D., and Jessup, M.J. (2006). Crustal structure, restoration and evolution of the Greater Himalaya: implication for channel flow and ductile extrusion of the middle crust. In Law, R. D.; Searle, M. P.; and Godin, L., eds. *Channel flow, extrusion, and exhumation in continental collision zones*, Geological Society of London Special Publications, *268*, 355–378.

Searle, M. P., Cottle, J.M., Streule, M.J., and Waters, D.J. (2010). Crustal melt granites and migmatites along the Himalaya: melt source, segregation, transport and granite emplacement mechanisms. *Earth and Environmental Science Transactions of the Royal Society of Edinburgh*, *100*, 219-233.

Steiger, R. H., and E. Jäger (1977). Subcommission on geochronology: convention on the use of decay constants in geo- and cosmochronology. *Earth and Planetary Science Letters*, *36*, 359-362.

Shuster, D. L., Flowers, R. M., and Farley, K.A. (2006). The influence of natural radiation damage on helium diffusion kinetics in apatite. *Earth and Planetary Science Letters*, *249*, 148-161.

Simpson, R.L., Parrish, R.R., Searle, M.P., and Waters, D.J. (2000). Two episodes of monazite crystallization during metamorphism and crustal melting in the Everest region of the Nepalese Himalaya. *Geology*, *28*, 403-406.

Spicer, R.A, Harris, N.B.W., Widdowson, M., Herman, A.B., Guo, S., Valdes, P.J., Wolfe, J.A., and Kelley, S.P. (2003). Constant elevation of southern Tibet over the past 15 million years. *Nature*, *421*, 622 – 624.

Stock, G.M., Ehlers, T.A. and Farley, K.A. (2006). Where does sediment come from? Quantifying catchment erosion with detrital apatite (U-Th)/He thermochronology. *Geology*, *34*, 725-728.

Stockli, D. (2005). Application of low-temperature thermochronometry to extensional tectonic settings, *in* Reiners, P. W., and Ehlers, T. A., eds., Low-Temperature Thermochronology, Techniques, Interpretations, ad Applications: Washington, DC, *Mineralogical Society of America, Reviews in Mineralogy and Geochemistry*, *58*, 411-448.

Stockli, D. F., Linn, J.K., Walker, J.D., and Dumitru, T. (2001). Miocene unroofing of the Canyon Range during extension along the Sevier Desert Detachment, west central Utah. *Tectonics*, *20*, 289-307.

Streule, M. J., Carter, A., Searle, M.P., and Cottle, J.M. (2012). Constraints on brittle field exhumation of the Everest-Makalu section of the Greater Himalayan Sequence: Implications for models of crustal flow. *Tectonics, 31*, doi:Tc301010.1029/2011tc003062.

Strobl, M., Hetzel, R., Niedermann, S., Ding, L., and Zhang, L. (2012). Landscape evolution of a bedrock peneplain on the southern Tibetan Plateau revealed by in situ-produced cosmogenic ^{10}Be and ^{21}Ne. *Geomorphology*, *153*, 192-204.

Stübner, K., Warren, C., Ratschbacher, L., Sperner, B., Kleeberg, R., Pfänder, J., and Grujic, D. (2017). Anomalously old biotite ^{40}Ar/^{39}Ar ages in the NW Himalaya. *Lithosphere, 9,* DOI:10.1130/L1586.1131.

Thiede, R.C., and Ehlers, T.A. (2013). Large Spatial and Temporal Variations in Himalayan Denudation. *Earth and Planetary Science Letters*, 371-372, 278-293.

Tranel, L.M., Spotila, J.A., Kowalewski, M.J., and Waller, C.M. (2011). Spatial variation

of erosion in a small, glaciated basin in the Teton Range, Wyoming, based on detrital apatite (U-Th)/He thermochronology. *Basin Research*, *23*, 571-590.

Tripathy-Lang, A., Hodges, K.V., Monteleone, B., and van Soest, M.C. (2013). Laser (U-Th)/He thermochronology of detrital zircons as a tool for studying surface processes in modern catchments. *Journal of Geophysical Research Earth Surface*, *118*, 1333–1341, doi:10.1002/jgrf.20091.

Turrin, B.D., Swisher III, C.C., and Deino, A. (2010). Mass discrimiation monitoring and intercalibration of dual collectors in noble gas mass spectrometer systems. *Geochemistry, Geophysics, Geosystems*, *11*, doi:10.1029/2009GC003013.

van Hinsbergen, D. J. J., Lippert, P.C., Dupont-Nivet, G., McQuarrie, N., Doubrovine, P.V., Spakman, W., and Torsvik, T.H. (2012). Greater India Basin hypothesis and a two-stage Cenozoic collision between India and Asia. *Proceedings of the National Academy of Sciences*, *109*, 7659-7664.

Vannay, J.- C. and Grasemann, B. (2001). Himalayan inverted metamorphism and syn-convergence extension as a consequence of a general shear extrusion. *Geological Magazine, 138*, 253-376.

Vermeesch, P., Seward, D., Latkoczy, C., Wipf, M., Gunther, D., and Baur, H. (2007). Alpha-emitting mineral inclusions in apatite, their effect on (U-Th)/He ages, and how to reduce it. *Geochimica et Cosmochimica Acta*, *71*, 1737-1746.

Viskupic, K., Hodges, K.V., and Bowring S.A. (2005). Timescales of melt generation and the thermal evolution of the Himalayan metamorphic core, Everest region, eastern Nepal. *Contrib. Mineral. Petrol., 149,* p. 1-21.

Walker, J.D., Martin, M.W., Bowring, S.A., Searle, M.P., Waters, D.J., Hodges, K.V. (1999). Metamorphism, melting and extension: age constraints from the high Himalayan slab of southeastern Zanskar and northwestern Lahoul. *Journal of Geology, 107*, 473-495.

Wang, A., Garver, J.I., Wang, G., Smith, J.A., and Zhang, K. (2010). Episodic exhumation of the Greater Himalayan Sequence since the Miocene constrained by fission track thermochronology in Nyalam central Himalaya. *Tectonophysics*, *495*, 315-323.

Wangenheim, C. and Glotzbach, C. (2015). Quantifying glacial erosion in the European Alps using apatite fission-track dating. *Geophysical Research Abstracts, 17,* EGU2015-1729, 2015.

Webb, A. A. G. (2013). Preliminary balanced palinspastic reconstruction of Cenozoic deformation across the Himachal Himalaya (northwestern India). *Geosphere*, *9*(3), 572-587.

Webb, A. A. G., Yin, A., Harrison, T.M., Celerier, J. and Burgess, W.P. (2007). The leading edge of the Greater Himalayan Crystalline complex revealed in the NW

Indian Himalaya: Implications for the evolution of the Himalayan orogen. *Geology*, *35*(10), 955-958.

Wendt, I., and Carl, C., (1991). The statistical distribution of the mean squared weighted deviation. *Chemical Geology: Isotope Geoscience setion*, *86*, 275 – 285.

Whipp, D. M., Ehlers, T.A., Blythe, A.E., Huntington, K.W., Hodges, K.V., Burbank, D.W. (2007). Plio-Quaternary exhumation history of the central Nepalese Himalaya: 2. Thermo-kinematic and thermochronometer age prediction model. *Tectonics, 26*, doi:10.1029/2006TC001991.

Whipp, D. M., Ehlers, T.A., Braun, J., and Spath, C.D. (2009). Effects of exhumation kinematics and topographic evolution on detrital thermochronometer data. *Journal of Geophysical Research*, *114*, F04014, doi:10.1029/2008JF001195.

Whipple, K.X., and Tucker, G.E. (1999). Dynamics of the stream-power river incision model: Implications for height limits of mountain ranges, landscape response timescales, and research needs. *Journal of Geophysical Research-Solid Earth, 104*(B8), 17661-17674. Doi:10.1029/1999jb900120

Whipple, K.X., DiBiase, R.A., Ouimet, W.B., and Forte, A.M. (2016). Preservation or piracy: Diagnosing low-relief, high-elevation surface formation mechanism. *Geology,* doi: 10.1130/G38490.1.

Whipple, K. X., Shirzaei, M., Hodges, K.V., and Arrowsmith, J.R. (2016). Active shortening within the Himalayan orogenic wedge implied by the 2015 Gorkha earthquake. *Nature Geoscience*, *9*(9), 711-716.

Willett, S. D. (1999). Orogeny and orography: the effects of erosion on the structure of mountain belts. *Journal of Geophysical Research, 104*, 28957-28981.

Wobus, C. W., Whipple, K.X., and Hodges, K.V. (2006). Neotectonics of the central Nepalese Himalaya: Constraints from geomorphology, detrital 40Ar/39Ar thermochronology, and thermal modeling. *Tectonics, 25*, doi:10.1029/2005TC001935.

Wulf, H., Bookhagen, B., and Scherler D. (2010). Seasonal precipitation gradients and their impact on fluvial sediment flux in the Northwest Himalaya. *Geomorphology, 118*, 13-21, doi:10.1016/j.geomorph.2009.12.003.

Yin, A. (2006). Cenozoic tectonic evolution of the Himalayan orogen as constrained by along-strike variation of structural geometry, exhumation history, and foreland sedimentation. *Earth Science Reviews*, *76*, 1-131.

Yin, C. H., and Kuo, S.T. (1978). Stratigraphy of the Mount Jolmo Lungma and its north slope. *Scientia Sinica*, *21*, 629-644.

APPENDIX A

CHAPTER 2 SUPPLEMENTARY MATERIALS

1. Analytical methods – $^{40}Ar/^{39}Ar$ thermochronology

Crushing and standard gravimetric and magnetic procedures were used to prepare rough grain concentrates prior to the final purification of mineral separates for thermochronology. In the case of muscovite for $^{40}Ar/^{39}Ar$ dating, this involved hand-picking of single muscovite grains and their cleaning in acetone, methanol, and deionized water. Samples were then individually wrapped in aluminum foil packets and loaded into small aluminum disks, which were stacked and secured together to make up package for neutron irradiation production of ^{39}Ar. Grains of biotite standard HD-B1 (24.18 ± 0.09 Ma, uncertainty at 1σ, Schwarz et al., 2007) were regularly interspersed in the aluminum disks with the samples to monitor the overall neutron flux, and synthetic and natural K and Ca salts were added to determine interfering nuclear production ratios. Rongbuk muscovites were irradiated in two different, Cd-shielded packages: one at the McMaster University Row 8 position (samples R01, R02, R04, and R05) and the other at the Oregon State University CLICIT facility for 1.7 hours (samples R06, R07, and R08).

After irradiation, the unknowns, monitors, and standards were loaded into an ultrahigh-vacuum line for argon isotopic analysis. The analytical experiments involved incremental heating of individual crystals using a 60W IPG Photonics infrared (970 nm) diode laser operated at successively high power levels ranging from 4 to 15 W. No attempt was made to monitor sample temperatures during the experiment. Released gasses were purified by passing them over hot and cold SAES NP10 metal alloy 'getters' prior to Ar isotopic analysis with a Nu Instruments *Noblesse* magnetic sector mass spectrometer. For most release steps, signals were measured using an ETP ion counting detector, but a few ^{40}Ar signals were so large that a Faraday detector (fitted with a 10^{11}

Ohm resistor) was used. The fully automated laser heating, automated valves operation, and data acquisition was computer controlled using Alan Deino's *MassSpec* software program.

Total system blanks for our experiments are estimated to have been 2.2E-18, 2.6E-20, 2.7E-21, 5.2E-20, 1.2E-20 moles STP (standard temperature and pressure) for ^{40}Ar, ^{39}Ar, ^{38}Ar, ^{37}Ar and ^{36}Ar, respectively. Unknown analyses were corrected for mass spectrometer discrimination and nuclear interference reactions (see Table A1). Air pipette shots were analyzed regularly to intercalibrate the Faraday and ion counting detector, using the ^{40}Ar peak, and intercalibrations were done using the 'isotopic reference ratio intercalibration' method of Turrin et al. (2010). Apparent ages were calculated using the ^{40}Ar decay constants and branching ratios of Steiger and Jäger (1977). To account for potential gradients in the reactor neutron flux in the irradiation package, J values and errors were calculated for the unknown samples (Table A1) by spatially interpolating J values obtained from age standard minerals (i.e., HD-B1 biotite) evenly distributed within the seven-hole Al irradiation planchettes.

All muscovite laser incremental heating analyses resulted in plateau ages, defined as three or more steps comprising 50% or more of the total ^{39}Ar in a sample, with individual calculated ages that overlap at the 2σ level without propagation of the *J*-value uncertainty (Fleck et al., 1977). The reported plateau dates and their 2σ uncertainties (inclusive of the *J*-value uncertainties) represent the ^{39}Ar-weighted means of the ages of all the steps defining each plateau.

2. Analytical methods – (U-Th)/He thermochronology

Using a binocular microscope, individual crystals of clear, euhedral, and apparently inclusion-free zircon and apatite were picked for (U-Th)/He dating from rough concentrates. We report dates for between 3 and 7 individual crystals of apatite and zircon per sample. Each crystal was measured to establish the necessary parameters for the alpha ejection corrections of the resulting dates using the approach of Farley et al. (1996) for apatite and Hourigan et al. (2005) for zircon. For both minerals, we assumed a homogeneous distribution of U and Th for determining correction factors; potential problems with this assumption are discussed in the main text of the paper. The grains were then loaded into small niobium tubes prior to analysis. All helium measurements were made with an Australian Scientific Instruments (ASI) *Alphachron* system, which features a 45 Watt, infrared (980 nm) diode laser for gas extraction and a Balzers *Prisma QMS 200* quadrupole mass spectrometer for isotopic measurements. Gasses including helium were released from apatite by laser heating for five minutes at 9 A, and from zircon by laser heating for ten minutes at 20 A. The released gasses were mixed with a known quantity of ^{3}He spike in preparation for isotope-dilution analysis, after which the mixture was purified of reactive gasses using a combination of hot and cold metal alloy getters. Along with sample unknowns, we also analyzed aliquots of Fish Canyon zircon and Durango fluorapatite to monitor system performance, and empty Nb tubes to allow for blank correction of the resulting data.

After ^{4}He analysis, each sample packet was unloaded from the laser chamber and dissolved for U and Th analysis. Apatites were dissolved using 25 µl of 50% nitric (HNO_3) acid that contains a mixed spike of ~5 ng of ^{230}Th and ~15ng of ^{235}U. In contrast,

zircons were digested at elevated temperatures and pressures in Parr vessels using concentrated hydrofluoric (HF), nitric (HNO_3), and hydrochloric (HCl) acids mixed with the U+Th spike. After dissolution, samples, together with specially prepared batches of spiked standard solutions, were analyzed for U and Th using a Thermo Scientific *ICAP-Q* inductively coupled, plasma source mass spectrometer.

The He, U, and Th data were used to calculate raw ages using an iterative approach to the (U-Th)/He age equation. Within this calculation, the concentration of ^{235}U is derived from the measured ^{238}U concentration using the known ratio of these isotopes in nature. The raw ages are then corrected for alpha ejection as described above. All uncertainties for ApHe and ZrnHe dates reflect the full propagation of analytical errors, but no errors were assigned to the alpha ejection correction calculations or propagated into the reported uncertainties.

As is frequently the case for (U-Th)/He data, the dispersion of zircon or apatite dates from a single sample from Rongbuk was often greater than would be anticipated from propagated analytical errors alone. The most probable causes of this overdispersion are unquantified, crystal-specific errors in the alpha ejection correction (often due to parent element zoning; Hourigan et al., 2005) or variable amounts of radiation damage that can affect the closure behavior of the zircon or apatite (Flowers et al., 2009; Guenthner et al., 2013). For this study, our approach to handling dispersion was as follows. First, we attempted to identify outliers in the measured zircon or apatite dates for each sample using the Hampel identifier method (e.g., Pearson, 2011), assuming that any date more than four median average deviations from the median could be reasonably discarded from further analysis. After removing any outliers present, we recalculated the

inverse variance-weighted mean of each ensemble of ApHe or ZrnHe dates, as well as: 1) the standard deviation of the weighted mean; 2) the mean squared weighted deviation (MSWD) of the distribution with outliers removed; and 3) the expected ca. 95% confidence range of MSWD for the ensemble based on the number of analyses in the weighted mean (Wendt and Carl, 1991; Mahon, 1996). In cases where the calculated MSWD was within the ca. 95% confidence range of its predicted value of 1.0, we report twice the standard deviation of the inverse-variance weighted mean as a realistic uncertainty for the calculated weighted mean ApHe or ZrnHe date. If the calculated MSWD was higher than this range, then we instead report two standard deviations of the population of dates as a realistic ca. 95% confidence-level estimate of the uncertainty in the inverse-variance weighted mean for that sample.

3. 1D Pecube thermal-kinematic modeling input parameters

Our approach to 1D thermal-kinematic modeling and choice of thermal physical properties and boundary conditions follows that used by previous work in neighboring regions of the Himalaya (e.g., Thiede and Ehlers, 2013; Adams et al., 2015). More specifically, we assumed a layer thickness – 30 km; a basal temperature of 650°C; a surface temperature of 5°C; a heat capacity of 800 J $kg^{-1}K^{-1}$; a crustal density of 2750 kg m^3; a thermal conductivity of 2.5 $Wm^{-1}K^{-1}$; and a heat production rate of 2 μWm^{-3}. With these assumptions, we conducted 300,000 forward models of thermal histories over the past 20 Ma predicted by randomly selected denudation rates between 0.01 and 4.0 mm/a. These rates were held constant for time steps of up to a few million years but were allowed to change between time steps. The ensemble of thermal histories produced

by this Monte Carlo scheme were then used to predict MsAr, ZrnHe, and ApHe closure ages (assuming diffusion parameters as described in the text), and these were compared with the actual dates for a sample using the misfit criteria as described in Thiede and Ehlers (2013). If a simulation reproduced all of a sample's closure ages within one standard deviation based on their analytical precisions, it was deemed acceptable. The ensemble of acceptable simulation was then used to calculate ca. 95% confidence ranges for modeled exhumation histories.

Based on the *QTQt* modeling results, we anticipated that the exhumation rates returned by thermo-kinematic modeling would decrease precipitously with time, but an important goal of this aspect of our modeling was to refine our understanding of when the steep decrease began and when it might have ended. To achieve this, the thermo-kinematic modeling began assuming relatively coarse time intervals of a few million years and we subsequently inserted increasingly shorter elements to improve our resolution of the variation in exhumation rates with time. Our intention in taking this approach was not to over-interpret the data – very small increments might suggest changes in exhumation rates that are modeling artefacts – but to establish the coarsest set of models that would still illuminate the most important exhumation rate transitions. The modeling results all are based on modeling increments of 20.0-15.0 Ma, 15.0-14.0 Ma, 14.0-13.0 Ma, 13.0-8.0 Ma, and 8.0 Ma to the present.

4. Supplementary Materials Figure Captions

Figure A1. Muscovite $^{40}Ar/^{39}Ar$ release spectra for samples R03, R04, R06, and R07. All eight samples have well-defined plateau ages. See Table 2.1 for the rest of the plateau ages and Appendix A for the individual heating steps.

Figure A2. Time-temperature histories output from the 1D thermal model *QTQt* for samples R03, R04, R06, and R07. The bold black line is the "Expected Model," which is the weighted mean of all acceptable thermal histories (Gallagher, 2012). Grey shading indicates the 95% credible confidence intervals. Dots mark the input thermochronometric system and vertical bars indicate uncertainty on the calculated closure temperatures. The input chronometer data (along with their 2σ uncertainties) are presented at the top of each figure pane.

Figure A3. Exhumation rate histories from thermal-kinematic modeling using a 1D version of *Pecube* for samples R03, R04, R06, and R07. Bold black line indicates the mean exhumation rate history. Horizontal grey bars indicate two standard deviations from the mean. Input chronometer data (along with their 2σ uncertainties) are presented at the top of each figure pane. The number of acceptable fits to the data is noted. See Figures 2.1 and 2.2 for sample locality information. A dashed vertical line at ~15.6 Ma indicates the transition from ductile shearing to ductile-brittle slip on the detachment.

5. References Cited in Supplementary Materials

Adams, B.A., Hodges, K.V., Whipple, K.X., Ehlers, T.A., van Soest, M.C., and Wartho, J. (2015). Constraints on the tectonic and landscape evolution of the Bhutan

Himalaya from thermochronometry, *Tectonics*. *32*(6), 1329-1347.

Farley, K.A., Wolf, R.A., and L.T. Silver, L.T. (1996). The effects of long alpha-stopping distances on (U-Th)/He ages. *Geochimica et Cosmochimica Acta*, *60*, 4223-4229.

Fleck, R. J., Sutter, J.F., and Elliot, D.H. (1977). Interpretation of discordant $^{40}Ar/^{39}Ar$ age spectra of Mesozoic tholeiites from Antarctica. *Geochimica et Cosmochimica Acta*, *41*, 15-32.

Flowers, R.M., Ketcham, R.A., Shuster, D.L., and Farley, K.A. (2009). Apatite (U-Th)/He thermochronometry using a radiation damage accumulation and annealing model. *Geochimica et Cosmochimica Acta*, *73*, 2347-2365.

Gallagher, K. (2012). Transdimensional inverse thermal history modelling for quantitative thermochronology. *Journal of Geophysical Research*, *117*, B02408, doi:10.1029/2011JB00882.

Guenthner, W.R., Reiners, P.W., Ketcham, R.A., Nasdala, L., and Geister, G. (2013). Helium diffusion in natural zircon: Radiation damage, anisotropy, and the interpretation of zircon (U-Th)/He thermochronology. *American Journal of Science*, *313*, p. 145 – 198.

Hourigan, J.K., Reiners, P.W., and Brandon, M.T. (2005). U-Th zonation dependent alpha-ejection in (U-Th)/He chronometry. *Geochimica et Cosmochimica Acta, 69*, 3349-3365.

Mahon, K. I. (1996). The new "York" regression: Application of an improved statistical method to geochemistry. *International Geology Review*, *38*, 293-303.

Pearson, R.K. (2011). *Exploring data in engineering, the sciences, and medicine*, Oxford University Press.

Schwarz, W.H., and Trielhoff, M. (2007). Intercalibration of ^{40}Ar-^{39}Ar age standards NL-25, HB3gr hornblende, GA1550, SB-3, HD-B1 biotite and BMus/2 muscovite, *Chemical Geology*, *242*, 218 – 231.

Steiger, R. H., and E. Jäger (1977). Subcommission on geochronology: convention on the use of decay constants in geo- and cosmochronology. *Earth and Planetary Science Letters*, *36*, 359-362.

Thiede, R.C., and Ehlers, T.A. (2013). Large Spatial and Temporal Variations in Himalayan Denudation. *Earth and Planetary Science Letters*, 371-372, 278-293.

Turrin, B.D., Swisher III, C.C., and Deino, A. (2010). Mass discrimiation monitoring and intercalibration of dual collectors in noble gas mass spectrometer systems. *Geochemistry, Geophysics, Geosystems*, *11*, doi:10.1029/2009GC003013.

Wendt, I., and Carl, C. (1991). The statistical distribution of the mean squared weighted deviation. *Chemical Geology: Isotope Geoscience setion*, *86*, 275 – 285.

TABLE A1: RONGBUK VALLEY WHITE MICA $^{40}Ar/^{39}Ar$ RESULTS

Sample: R01 Lab: Arizona State University Group 18 Laboratories J: 0.0005309 ± 2.65E-06
Mineral: White mica IGSN:

N	Power (W)	^{40}Ar (moles)	^{40}Ar	±σ$_{40}$	^{39}Ar	±σ$_{39}$	^{38}Ar	±σ$_{38}$	^{37}Ar	±σ$_{37}$	^{36}Ar	±σ$_{36}$	%^{40}Ar*	^{40}Ar*/^{39}Ar$_K$	±σ	Age (Ma)	±σ (Ma)	±2σ (Ma)	Ca/K	Δt^{c} (days)	Blank Type	^{40}Ar	±σ$_{40}$	^{39}Ar	±σ$_{39}$	^{38}Ar	±σ$_{38}$	^{37}Ar	±σ$_{37}$	^{36}Ar	±σ$_{36}$
622-01A		4	1.13E-17	66564	92	785.1	9.1	42.2	2.5	292	1200	181.3	3.6	12.7	11.1	2.2	15.8	1.3	3	0.714	150 LR	11403	29	123.9	4.0	11.0	1.1	263.5	5.0	59.1	1.7
622-01B		4.5	9.57E-18	47841	71	937	11	37.5	2.3	-2506	1300	117.1	3.3	40.3	18.4	1.4	13.2	1.0	2.0	-5.141	150 LR	11122	32	122.1	4.8	11.0	1.2	268.5	5.7	58.0	2.0
622-01C		5	4.58E-18	22899	65	609.4	9.2	17.5	1.9	-376	1400	41.4	3.0	38.0	18.07	0.63	16.6	1.4	2.9	-1.187	150 LR	10875	34	121.4	5.2	11.5	1.3	271.1	6.1	57.4	2.2
622-01D		5.1	2.88E-18	14413	60	458.6	8.7	12.6	1.8	-2701	1400	24.7	3.0	55.2	16.70	0.31	14.3	1.8	3.7	-11.322	150 LR	10895	31	122.8	4.6	12.2	1.2	268.5	5.5	57.9	2.0
622-01E		5.15	2.19E-18	10931	50	538.0	8.6	7.6	1.8	-32	1300	11.5	2.6	55.7	15.97	0.32	13.3	1.4	2.8	-0.0115	150 LR	10939	28	124.3	4.1	13.0	1.1	265.5	5.1	58.5	1.8
622-01F		5.17	8.79E-18	43926	72	1875	14	32.8	2.1	-2237	1300	44.8	2.9	40.2	16.10	0.20	15.48	0.45	0.90	-2.294	150 LR	10940	27	125.7	3.8	13.7	1.0	262.9	4.9	59.0	1.7
622-01G		5.5	2.77E-17	138651	104	4323	19	99.5	3.4	-712	1200	237.4	4.0	65.9	16.201	0.091	15.08	0.27	0.54	-0.317	150 LR	10980	27	127.0	3.6	14.3	1.0	260.3	5.0	59.5	1.8
622-01H		7	2.64E-17	132142	106	6356	22	90.5	3.3	7	1400	100.4	3.8	80.1	16.616	0.074	15.36	0.18	0.36	0.002	150 LR	11017	35	133.4	4.1	16.5	1.3	252.1	6.5	60.9	2.2
622-01I		8	3.72E-17	186056	212	9151	29	126.4	3.9	2064	1400	134.1	3.5	80.2	15.997	0.061	15.26	0.12	0.24	0.434	150 LR	10990	30	135.0	3.7	15.9	1.2	254.1	5.8	60.3	2.0
622-01J		8.5	4.00E-17	200153	113	10423	30	133.4	4.1	2331	1300	112.1	3.4	82.5	16.104	0.071	15.29	0.10	0.21	0.430	150 LR	10963	28	136.6	3.5	15.4	1.1	256.1	5.4	59.7	1.8
622-01K		11	6.89E-17	344595	162	17879	40	247.5	5.2	2758	1300	189.7	3.8	87.2	15.975	0.053	15.389	0.070	0.14	0.297	150 LR	10931	27	138.4	3.6	14.7	1.1	258.5	5.5	59.0	1.8
622-01L		15	2.63E-16	1390000*	6050*	78808	71	987.3	8.8	1401	1400	389.5	5.1	92.3	16.392	0.055	15.462	0.076	0.15	0.034	150 LR	11150*	600*	140.1	4.0	14.2	1.2	260.6	6.0	58.3	1.9

Plateau Age (steps C - L): 15.37 ± 0.16 Ma

Standard: HD-B1 Age: 24.18 ± 0.09 Ma Swartz and Trieloff (2007)

Explanations
Δt^{c}: Time interval (days) between end of irradiation and beginning of analysis
Blank Type: Ave = average; LR = linear regression versus time
*: Analyzed on the Faraday
Constants used
Atmospheric argon ratios
(^{40}Ar/^{36}Ar)$_A$ 295.5 ± 0.5 Nier (1950)
(^{38}Ar/^{36}Ar)$_A$ 1575 ± 2 Nier (1950)
Interfering isotope production ratios
(^{40}Ar/^{39}Ar)$_K$ 0.0184383 0.0023199
(^{38}Ar/^{39}Ar)$_K$ 0 0
(^{37}Ar/^{39}Ar)$_K$ 0 0
(^{36}Ar/^{37}Ar)$_{Ca}$ 0.0007096 2.5E-06
(^{38}Ar/^{37}Ar)$_{Ca}$ 0 0
(^{40}Ar/^{37}Ar)$_{Ca}$ 0.000281 1.5E-06
(^{38}Cl/^{37}Cl)$_{Cl}$ 316 0
Decay constants
^{40}K λ$_e$ (5.81E-11 ± 0.00)E-11 a^{-1} Steiger and Jäger (1977)
^{40}K λ$_β$ (4.962E-10 ± 0.00)E-10 a^{-1} Steiger and Jäger (1977)
^{37}Ar (2.58 ± 0.03)E-03 a^{-1} Stoenner et al. (1965)
^{39}Ar (0.019725 ± 0.000) a^{-1} Stoenner et al. (1965)
^{36}Cl (2.35 ± 0.02)E-06 a^{-1} Endt (1998)

Sample: R02 Lab: Arizona State University Group 18 Laboratories J: 0.0005462 ± 1.68E-06
White mica

N	Power (W)	^{40}Ar (moles)	^{40}Ar	±σ$_{40}$	^{39}Ar	±σ$_{39}$	^{38}Ar	±σ$_{38}$	^{37}Ar	±σ$_{37}$	^{36}Ar	±σ$_{36}$	%^{40}Ar*	^{40}Ar*/^{39}Ar$_K$	±σ	Age (Ma)	±σ (Ma)	±2σ (Ma)	Ca/K	Δt^{c} (days)	Blank Type	^{40}Ar	±σ$_{40}$	^{39}Ar	±σ$_{39}$	^{38}Ar	±σ$_{38}$	^{37}Ar	±σ$_{37}$	^{36}Ar	±σ$_{36}$
620-01A		4	4.40E-18	21982	64	263.3	7.4	13.8	2.1	562	1500	65.3	3.1	12.44317	10.4	3.5	10.2	3.4	7	4.102713	150 LR	11099	31	122.2	3.8	15.4	1.5	268.4	6.8	52.6	2.0
620-01B		4.5	2.15E-18	10762	49	303.5	6.1	4.0	2.0	915	1400	25.6	2.5	30.39352	10.8	2.5	10.6	2.4	4.9	5.795866	150 LR	11040	28	121.4	3.3	15.8	1.3	267.7	5.9	52.3	1.7
620-01C		5	4.57E-18	22867	57	613.2	8.6	15.5	2.0	802	1400	51.3	2.8	33.93383	12.7	1.4	12.4	1.4	2.7	2.513612	150 LR	10982	27	120.6	3.0	16.1	1.2	267.0	5.5	52.0	1.6
620-01D		5.1	3.67E-18	18340	57	568.7	8.0	9.8	1.9	800	1300	31.5	2.7	49.6602	16.0	1.4	15.7	1.4	2.8	2.705615	150 LR	10913	30	119.7	3.1	16.5	1.2	266.2	5.7	51.6	1.7
620-01E		5.15	6.66E-18	33281	120	613.3	8.5	18.4	2.3	97	1400	84.6	3.1	24.87965	13.5	1.5	13.3	1.5	3.0	0.3044275	150 LR	10854	35	118.9	3.6	16.8	1.4	265.5	6.5	51.3	2.0
620-01F		5.17	1.40E-17	69979	130	2741	29	46.2	2.6	-398	1500	98.5	6.1	58.32694	14.88	0.68	14.60	0.66	1.32	-0.2789075	150 LR	10945	38	119.3	3.8	16.5	1.5	263.0	6.9	52.1	2.1
620-01G		5.5	5.41E-17	270551	300	10785	29	196.2	4.9	2919	1400	348.4	5.1	62.0826	15.55	0.15	15.25	0.14	0.29	0.5202813	150 LR	11130	35	120.7	3.4	15.9	1.3	260.8	6.2	53.5	1.9
620-01H		7	8.05E-17	402222	350	21719	80	293.4	5.1	74	1300	239.3	3.9	82.41353	15.248	0.079	14.961	0.077	0.15	0.0065184	150 LR	11355	32	122.4	3.1	15.0	1.2	258.1	5.5	55.1	1.7
620-01I		8	9.36E-17	467941	370	27187	38	361.8	4.6	4114	1300	1716	7.6	89.23597	15.344	0.086	15.056	0.084	0.17	0.2908729	150 LR	11547	31	123.9	2.9	14.3	1.1	255.8	5.2	56.5	1.6
620-01J		8.5	5.44E-17	272041	260	15660	31	194.3	4.0	1585	1300	101.5	3.2	89.016	15.449	0.071	15.158	0.069	0.14	0.1945899	150 LR	11739	31	125.4	2.8	13.6	1.1	253.5	5.2	57.9	1.6
620-01K		11	6.98E-17	349011	160	20907	37	259.4	5.0	4103	1500	98.8	3.2	91.73144	15.298	0.054	15.011	0.053	0.11	0.377263	150 LR	12228	39	129.3	3.4	11.0	1.3	248.8	6.1	62.2	1.9
620-01L		15	1.48E-16	739879	270	46302	61	568.6	7.2	2568	1300	111.8	3.4	95.56779	15.254	0.030	14.968	0.030	0.06	0.1065983	150 LR	11954	33	127.5	3.2	11.0	1.1	253.7	5.3	61.1	1.7

Plateau Age (steps A - L): 15.00 ± 0.06 Ma

Standard: HD-B1 Age: 24.18 ± 0.09 Ma Swartz and Trieloff (2007)

Explanations
Δt^{c}: Time interval (days) between end of irradiation and beginning of analysis
Blank Type: Ave = average; LR = linear regression versus time
*: Analyzed on the Faraday
Constants used
Atmospheric argon ratios
(^{40}Ar/^{36}Ar)$_A$ 295.5 ± 0.5 Nier (1950)
(^{38}Ar/^{36}Ar)$_A$ 1575 ± 2 Nier (1950)
Interfering isotope production ratios
(^{40}Ar/^{39}Ar)$_K$ 0.0184383 0.0023199
(^{38}Ar/^{39}Ar)$_K$ 0 0
(^{37}Ar/^{39}Ar)$_K$ 0 0
(^{36}Ar/^{37}Ar)$_{Ca}$ 0.0007096 2.5E-06
(^{38}Ar/^{37}Ar)$_{Ca}$ 0 0
(^{40}Ar/^{37}Ar)$_{Ca}$ 0.000281 1.5E-06
(^{38}Cl/^{37}Cl)$_{Cl}$ 316 0
Decay constants
^{40}K λ$_e$ (5.81E-11 ± 0.00)E-11 a^{-1} Steiger and Jäger (1977)
^{40}K λ$_β$ (4.962E-10 ± 0.00)E-10 a^{-1} Steiger and Jäger (1977)
^{37}Ar (2.58 ± 0.03)E-03 a^{-1} Stoenner et al. (1965)
^{39}Ar (0.019725 ± 0.000) a^{-1} Stoenner et al. (1965)
^{36}Cl (2.35 ± 0.02)E-06 a^{-1} Endt (1998)

Sample: R03 Lab: Arizona State University Group 18 Laboratories J: 0.0004456 ± 2.80E-06
White mica IGSN:

N	Power (W)	^{40}Ar (moles)	$\pm\sigma_n$	^{39}Ar	$\pm\sigma_n$	^{38}Ar	$\pm\sigma_n$	^{37}Ar	$\pm\sigma_n$	^{36}Ar	$\pm\sigma_n$	%^{40}Ar*	^{40}Ar*/^{39}Ar$_K$	$\pm\sigma$	Age (Ma)	$\pm\sigma$ (Ma)	$\pm2\sigma$ (Ma)	Ca/K	Δt^1 (days)	Blank Type	^{40}Ar	$\pm\sigma_n$	^{39}Ar	$\pm\sigma_{n1}$	^{38}Ar	$\pm\sigma_n$	^{37}Ar	$\pm\sigma_{n1}$	^{36}Ar	$\pm\sigma_n$
739-01A	4	9.96E-18	49807	89	1014	12	32.3	3.3	-19	20	113.4	4.7	32.70524	16.1	1.4	12.9	1.1	2	-0.0340445	48 LR	22479	54	257.6	6.5	32.5	1.7	308.9	6.0	124.7	2.8
739-01B	4.5	1.63E-17	81484	100	1197	13	57.5	3.4	-30	19	216.3	5.0	21.53018	14.7	1.2	11.74	0.99	2.0	-0.0443692	48 LR	22299	47	249.8	5.4	31.1	1.5	305.6	5.2	122.6	2.5
739-01C	5	2.02E-17	100944	92	2533	15	69.0	3.5	-8	18	395.7	4.7	42.66793	16.99	0.55	13.61	0.44	0.9	-0.0055458	48 LR	22128	44	242.4	4.5	29.7	1.5	302.4	5.0	120.5	2.4
739-01D	5.1	1.82E-17	90802	120	2555	17	60.6	3.4	4	19	154.3	4.5	49.75087	17.66	0.54	14.14	0.43	0.9	0.002704	48 LR	21929	47	233.7	4.1	28.2	1.7	298.8	5.5	118.1	2.6
739-01E	5.15	1.50E-17	74869	100	2201	17	49.7	3.5	-16	20	119.9	4.5	52.63457	17.89	0.62	14.32	0.49	1.0	-0.0132304	48 LR	21759	54	226.3	4.2	26.8	1.9	295.6	6.4	116.1	3.1
739-01F	5.17	3.60E-17	179827	140	5543	20	108.7	4.3	-18	22	255.3	5.6	58.01684	18.81	0.31	15.05	0.24	0.49	-0.0058398	48 LR	21717	57	224.6	4.4	26.2	2.1	294.4	6.8	115.4	3.3
739-01G	5.5	7.26E-17	363219	360	10728	31	227.1	5.1	-14	20	553.8	6.5	54.90618	18.57	0.19	14.87	0.15	0.31	-0.002365	48 LR	21872	51	231.4	4.1	27.1	1.9	296.7	6.1	117.0	2.9
739-01H	7	2.99E-16	1580415*	10000*	58742	71	998	10	18	19	1540.7	8.7	71.16248	19.13	0.17	15.31	0.14	0.27	0.0005589	48 LR	18733*	532*	239.8	3.9	28.1	1.7	299.5	5.5	118.9	2.6
739-01I	8	3.68E-16	1945682*	13000*	93047	95	1271	10	29	19	610.5	6.0	90.7145	18.94	0.13	15.16	0.10	0.21	0.0005509	48 LR	19162*	540*	246.6	4.1	28.9	1.7	301.7	5.1	120.5	2.5
739-01J	8.5	2.56E-16	1356342*	8800*	66122	62	844.6	7.8	-4	19	328.4	5.0	92.83469	19.02	0.13	15.22	0.10	0.20	-0.0001199	48 LR	19392*	560*	253.5	4.4	29.8	1.7	304.0	5.1	122.1	2.4
739-01K	11	2.52E-16	1332469*	8700*	59800	74	855.5	9.4	-27	21	608.6	6.8	86.48532	19.25	0.14	15.41	0.11	0.23	-0.0008109	48 LR	21772*	730*	280.6	5.9	33.6	2.1	313.1	6.0	132.6	2.9
739-01L	15	6.35E-16	3362868*	22000*	166214	130	2100	15	409	26	688.9	7.2	93193801	18.98	0.12	15.193	0.099	0.20	0.004405	48 LR	22438*	640*	282.2	5.2	34.3	1.9	313.6	5.4	138.0	2.6

Plateau Age (steps E - L): 15.25 ± 0.11 Ma

Standard: HD-B1 Age: 24.18 ± 0.09 Ma Swartz and Trieloff (2007)

Explanations
Δt^1: Time interval (days) between end of irradiation and beginning of analysis
Blank Type: Ave = average; LR = linear regression versus time
*: Analyzed on the Faraday
Constants used
Atmospheric argon ratios
(^{40}Ar/^{36}Ar)$_A$ 295.5 ± 0.5 Nier (1950)
(^{40}Ar/^{36}Ar)$_A$ 1575 ± 2 Nier (1950)
Interfering isotope production ratios
(^{40}Ar/^{39}Ar)$_K$ 0.018949 0.0023222
(^{38}Ar/^{39}Ar)$_K$ 0.0128101 0.0000796
(^{37}Ar/^{39}Ar)$_K$ 0.0010055 0.0000794
(^{40}Ar/^{37}Ar)$_{Ca}$ 0.0006783 2.09E-06
(^{39}Ar/^{37}Ar)$_{Ca}$ 0 0
(^{38}Ar/^{37}Ar)$_{Ca}$ 0.000267 1.34E-06
(^{38}Cl/^{39}Cl)$_{Cl}$ 263 2
Decay constants
^{40}K λ_e (5.81E-11 ± 0.00)E-11 a^{-1} Steiger and Jäger (1977)
^{40}K λ_β (4.962E-10 ± 0.00)E-10 a^{-1} Steiger and Jäger (1977)
^{37}Ar (2.58 ± 0.03)E-03 a^{-1} Stoenner et al. (1965)
^{39}Ar (0.019725 ± 0.00) a^{-1} Stoenner et al. (1965)
^{36}Cl (2.35 ± 0.02)E-06 a^{-1} Endt (1998)

Sample: R04 Lab: Arizona State University Group 18 Laboratories J: 0.0005475 ± 2.75E-06
White mica IGSN:

N	Power (W)	^{40}Ar (moles)	$\pm\sigma_n$	^{39}Ar	$\pm\sigma_n$	^{38}Ar	$\pm\sigma_n$	^{37}Ar	$\pm\sigma_n$	^{36}Ar	$\pm\sigma_n$	%^{40}Ar*	^{40}Ar*/^{39}Ar$_K$	$\pm\sigma$	Age (Ma)	$\pm\sigma$ (Ma)	$\pm2\sigma$ (Ma)	Ca/K	Δt^1 (days)	Blank Type	^{40}Ar	$\pm\sigma_n$	^{39}Ar	$\pm\sigma_{n1}$	^{38}Ar	$\pm\sigma_n$	^{37}Ar	$\pm\sigma_{n1}$	^{36}Ar	$\pm\sigma_n$
624-02A	4	1.03E-17	51722	84	886.5	9.9	30.9	2.7	3563	3200	130.0	3.9	2628403	15.4	1.3	15.1	1.3	3	7.725371	150 LR	13790	42	114.7	4.3	22.0	1.5	206.2	6.4	67.3	2.4
624-02B	4.5	9.41E-18	47029	80	1451	12	38.7	2.6	5263	2800	86.5	3.3	4653904	15.11	0.71	14.86	0.69	1.4	6.970837	150 LR	13901	38	116.7	3.8	22.2	1.4	207.5	5.6	68.6	2.1
624-02C	5	1.13E-17	56378	76	2179	15	32.4	2.4	2291	2600	73.7	3.5	61.66893	15.95	0.50	15.69	0.49	1.0	2.02065	150 LR	14005	35	118.6	3.5	22.3	1.2	208.7	5.0	69.8	1.9
624-02D	5.1	1.08E-17	54008	77	2091	14	41.1	2.7	3736	2600	75.9	3.0	5904548	15.26	0.46	15.01	0.45	0.9	3.433841	150 LR	14128	35	120.9	3.4	22.4	1.2	210.2	4.6	71.2	1.8
624-02E	5.15	1.42E-17	70854	92	2618	14	54.7	2.8	8941	2800	104.8	3.7	5730869	15.54	0.44	15.28	0.43	0.9	6.565578	150 LR	14423	44	132.6	4.2	22.5	1.5	215.5	5.2	76.4	2.2
624-02F	5.17	3.37E-17	268378	140	12316	68	183.2	4.6	717	2600	269.4	8.5	70.34838	15.32	0.22	15.07	0.22	0.44	0.1119881	150 LR	14314	38	137.6	3.6	22.2	1.3	216.3	4.6	77.2	1.9
624-02G	5.5	1.09E-16	542620	250	27169	50	399.4	6.0	6395	2500	383.7	5.0	7919609	15.805	0.063	15.544	0.061	0.12	0.4524635	150 LR	14242	35	142.6	3.3	21.9	1.3	217.1	4.3	78.0	1.9
624-02H	7	1.60E-16	798692	1600	46477	63	596.0	7.4	-1476	2700	240.9	4.3	91.0752	15.634	0.049	15.376	0.048	0.10	-0.0610528	150 LR	14151	35	147.7	3.4	21.6	1.5	217.9	4.5	78.8	2.0
624-02I	8	1.31E-16	653510	250	39671	60	488.0	6.2	7853	3000	303.2	3.8	95.44027	15.707	0.038	15.448	0.037	0.07	0.3805249	150 LR	14058	39	152.8	3.8	21.3	1.7	218.7	5.1	79.6	2.3
624-02J	8.5	8.94E-17	446865	200	27690	41	335.3	6.4	8843	3200	52.1	3.5	96.72963	15.596	0.046	15.340	0.045	0.09	0.6139237	150 LR	13990	43	161.3	4.1	21.5	1.9	221.2	5.7	80.7	2.6
624-02K	11	1.19E-16	593280	250	36069	57	419.4	6.5	8019	2900	93.0	3.6	95.48715	15.691	0.040	15.433	0.039	0.08	0.4273539	150 LR	14039	38	164.6	3.8	22.2	1.7	223.0	5.1	81.0	2.3
624-02L	15	3.70E-16	1956092*	2900*	117708	160	1411	10	-30	2600	272	16	95.90475	15.920	0.052	15.657	0.051	0.10	-0.0001611	150 LR	17811*	580*	167.9	3.7	22.9	1.5	224.9	4.7	81.2	2.1

Plateau Age (steps B - L): 15.420 ± 0.030 Ma

Standard: HD-B1 Age: 24.18 ± 0.09 Ma Swartz and Trieloff (2007)

Explanations
Δt^1: Time interval (days) between end of irradiation and beginning of analysis
Blank Type: Ave = average; LR = linear regression versus time
*: Analyzed on the Faraday
Constants used
Atmospheric argon ratios
(^{40}Ar/^{36}Ar)$_A$ 295.5 ± 0.5 Nier (1950)
(^{40}Ar/^{36}Ar)$_A$ 1575 ± 2 Nier (1950)
Interfering isotope production ratios
(^{40}Ar/^{39}Ar)$_K$ 0.0184383 0.0023199
(^{38}Ar/^{39}Ar)$_K$ 0 0
(^{37}Ar/^{39}Ar)$_K$ 0 0
(^{39}Ar/^{37}Ar)$_{Ca}$ 0.0007096 2.55E-06
(^{38}Ar/^{37}Ar)$_{Ca}$ 0 0
(^{38}Ar/^{37}Ar)$_{Ca}$ 0.000281 1.58E-06
(^{38}Cl/^{39}Cl)$_{Cl}$ 316 0
Decay constants
^{40}K λ_e (5.81E-11 ± 0.00)E-11 a^{-1} Steiger and Jäger (1977)
^{40}K λ_β (4.962E-10 ± 0.00)E-10 a^{-1} Steiger and Jäger (1977)
^{37}Ar (2.58 ± 0.03)E-03 a^{-1} Stoenner et al. (1965)
^{39}Ar (0.019725 ± 0.00) a^{-1} Stoenner et al. (1965)
^{36}Cl (2.35 ± 0.02)E-06 a^{-1} Endt (1998)

Sample: R05 Lab: Arizona State University Group 18 Laboratories J: 0.0004421 ± 3.88E-06

White mica IGSN:

N	Power (W)	^{40}Ar (moles)	^{36}Ar	±σ_m	^{37}Ar	±σ_m	^{39}Ar	±σ_{39}	^{37}Ar	±σ_{37}	^{38}Ar	±σ_{38}	%^{40}Ar*	^{40}Ar*/^{39}Ar$_K$	±σ	Age (Ma)	±σ (Ma)	±2σ (Ma)	Ca/K	Δt^{2} (days)	Blank Type	^{36}Ar	±σ_m	^{37}Ar	±σ_m	^{39}Ar	±σ_m	^{37}Ar	±σ_{37}	^{38}Ar	±σ_m
732-01A	4	3.18E-17	158911	120	2859	18	95.3	4.0	62	21	372.0	5.5	30.79228	17.11	0.60	13.59	0.47	1	0.038784	150 LR	25578	53	1329	4.0	25.6	1.8	262.3	6.2	115.8	2.7
732-01B	4.5	3.83E-17	191582	150	4202	20	123.2	4.2	3	18	389.7	5.7	39.85008	18.16	0.43	14.43	0.34	0.7	0.0014168	150 LR	25100	47	134.1	3.5	24.7	1.6	2606	5.4	112.7	2.3
732-01C	5	7.65E-17	382524	360	14483	36	255.2	5.0	27	18	382.7	5.2	70.40691	18.58	0.13	14.76	0.10	0.2	0.0032984	150 LR	24642	46	135.2	3.3	23.8	1.5	2590	5.0	109.8	2.1
732-01D	5.1	4.78E-17	238804	320	10499	31	153.5	4.6	19	18	145.0	4.0	82.0292	18.29	0.13	14.53	0.10	0.2	0.0031025	150 LR	24184	50	136.3	3.4	22.9	1.5	257.5	5.0	106.9	2.2
732-01E	5.15	4.12E-17	205828	320	9250	28	129.0	4.1	25	19	129.3	4.3	81.41455	18.09	0.15	14.37	0.12	0.2	0.0048655	150 LR	23727	57	137.4	3.8	22.0	1.7	253.9	5.6	104.0	2.4
732-01F	5.17	3.70E-17	184948	140	8522	29	139.0	4.3	9	19	99.4	4.1	84.10531	18.23	0.16	14.48	0.13	0.25	0.001823	150 LR	23315	62	143.3	4.1	21.1	1.8	254.6	6.1	102.6	2.6
732-01G	5.5	7.34E-17	368966	370	16022	39	246.6	5.4	35	17	250.7	4.7	79.78461	18.25	0.11	14.500	0.085	0.17	0.003858	150 LR	23466	55	148.8	3.7	21.2	1.6	255.4	5.5	105.1	2.4
732-01H	7	3.29E-16	1740000*	8100*	79301	91	1153	10	120	18	8023.9	7.7	82.58113	18.04	0.11	14.335	0.085	0.17	0.0020849	150 LR	21747*	470*	154.5	3.4	21.2	1.5	256.1	5.1	107.6	2.2
732-01I	8	1.80E-16	951376*	4600*	48397	70	629.3	7.0	74	16	228.9	4.4	92.87933	18.23	0.10	14.484	0.079	0.16	0.002743	150 LR	22001*	460*	160.0	3.4	21.3	1.4	256.8	5.0	110.1	2.1
732-01J	8.5	8.66E-17	433010	380	22753	50	291.6	5.3	56	18	79.6	4.0	94.56048	17.968	0.072	14.276	0.057	0.11	0.004438	150 LR	23949	40	166.5	3.5	21.4	1.4	257.7	5.3	113.0	2.2
732-01K	11	1.01E-16	505612	230	26068	47	343.8	5.5	61	20	102.2	4.2	94.01627	18.208	0.065	14.466	0.051	0.10	0.0042188	150 LR	24216	42	188.8	4.3	22.1	1.6	263.2	6.5	120.8	2.7
732-01L	15	6.08E-16	3220000*	15000*	162188	120	2116	12	1048	33	968.7	7.4	91.09748	18.060	0.093	14.349	0.073	0.15	0.0115707	150 LR	24469*	520*	192.3	3.8	22.4	1.5	266.3	5.7	120.2	2.4

Plateau Age (steps A - L): 14.400 ± 0.060 Ma

Standard: HD-B1 Age: 24.18 ± 0.09 Ma Swartz and Trieloff (2007)

Explanations
Δt^{2}: Time interval (days) between end of irradiation and beginning of analysis
Blank Type: Ave = average; LR = linear regression versus time
*: Analyzed on the Faraday
Constants used
Atmospheric argon ratios

(^{40}Ar/^{36}Ar)$_A$	295.5 ± 0.5	Nier (1950)
(^{40}Ar/^{36}Ar)$_A$	1575 ± 2	Nier (1950)

Interfering isotope production ratios

(^{40}Ar/^{39}Ar)$_K$	0.0184383	0.0023199
(^{36}Ar/^{39}Ar)$_K$	0	0
(^{37}Ar/^{39}Ar)$_K$	0	0
(^{38}Ar/^{39}Ar)$_K$	0.0007096	2.55E-06
(^{36}Ar/^{37}Ar)$_{Ca}$	0	0
(^{38}Ar/^{37}Ar)$_{Ca}$	0.000281	1.58E-06
(^{40}Cl/^{36}Cl)$_{Cl}$	316	0

Decay constants

^{40}K λ_e	(5.81E-11 ± 0.00)E-11 a^{-1}	Steiger and Jäger (1977)
^{40}K λ_β	(4.962E-10 ± 0.00)E-10 a^{-1}	Steiger and Jäger (1977)
^{37}Ar	(2.58 ± 0.03)E-03 a^{-1}	Stoenner et al. (1965)
^{39}Ar	(0.019725 ± 0.00) a^{-1}	Stoenner et al. (1965)
^{36}Cl	(2.35 ± 0.02)E-06 a^{-1}	Endt (1998)

Sample: R06 Lab: Arizona State University Group 18 Laboratories J: 0.0005752 ± 3.21E-06

White mica IGSN:

N	Power (W)	^{40}Ar (moles)	^{36}Ar	±σ_m	^{37}Ar	±σ_m	^{39}Ar	±σ_{39}	^{37}Ar	±σ_{37}	^{38}Ar	±σ_{38}	%^{40}Ar*	^{40}Ar*/^{39}Ar$_K$	±σ	Age (Ma)	±σ (Ma)	±2σ (Ma)	Ca/K	Δt^{2} (days)	Blank Type	^{36}Ar	±σ_m	^{37}Ar	±σ_m	^{39}Ar	±σ_m	^{37}Ar	±σ_{37}	^{38}Ar	±σ_m
626-01A	4	7.57E-18	37844	70	679.3	9.2	23.9	2.1	-3844	1200	92.6	3.2	26.84	14.9	2.2	15.4	1.5	-3	-10.837668	150 LR	10929	30	1600	3.7	17.0	1.2	2822	4.9	65.1	1.7
626-01B	4.5	5.87E-18	29370	64	979	10	20.1	1.9	-2109	1300	46.0	2.8	53.15	15.9	1.4	16.43	0.89	1.8	-4.140912	150 LR	11039	30	1607	3.8	16.7	1.1	2810	5.1	66.4	1.7
626-01C	5	1.01E-17	50305	69	2516	17	41.5	2.6	-99	1500	44.2	3.1	74.01	14.78	0.63	15.28	0.39	0.8	-0.073596	150 LR	11356	37	1637	4.8	15.2	1.3	2756	6.6	69.8	2.0
626-01D	5.1	7.14E-18	35721	67	2045	14	23.7	2.2	90.0	1300	20.9	2.8	82.90	14.47	0.31	14.95	0.41	0.9	0.8551821	150 LR	11225	33	1643	4.2	14.8	1.1	2750	5.6	67.9	1.8
626-01E	5.15	5.97E-18	29838	96	1754	14	20.7	2.0	-1421	1200	19.0	2.7	80.78	13.72	0.32	14.18	0.49	1.0	-1.557586	150 LR	11070	34	1651	4.0	14.4	1.1	274.3	4.9	65.6	1.7
626-01F	5.17	1.68E-17	83828	81	3672	20	65.2	2.6	126	1300	99.2	3.5	65.02	14.83	0.20	15.32	0.31	0.61	0.0661555	150 LR	10939	38	1657	4.3	14.0	1.1	273.7	4.8	63.7	1.8
626-01G	5.5	3.54E-17	177024	200	7987	51	133.7	3.5	3075	1400	218.7	4.1	63.62	14.092	0.091	14.56	0.18	0.37	0.7402129	150 LR	10808	45	1664	4.9	13.6	1.3	273.1	5.3	61.8	2.1
626-01H	7	4.75E-17	237703	140	13576	72	186.9	4.3	930	1500	145.0	7.1	81.99	14.342	0.074	14.82	0.18	0.36	0.1316875	150 LR	10643	48	1686	5.2	13.9	1.4	272.4	5.6	60.9	2.3
626-01I	8	4.38E-17	219093	150	14384	130	176.6	4.0	2702	1300	56.4	3.2	92.50	14.073	0.061	14.55	0.15	0.30	0.3610683	150 LR	10592	41	1709	4.6	14.9	1.2	272.2	4.9	62.4	2.0
626-01J	8.5	5.33E-17	266031	280	17987	38	213.5	4.5	1115	1200	31.4	3.0	96.56	14.320	0.071	14.799	0.063	0.13	0.1194939	150 LR	10549	37	1729	4.1	15.7	1.2	272.0	4.6	63.7	1.8
626-01K	11	7.08E-17	353784	150	21400	38	287.1	4.5	2769	1300	161.5	3.8	86.57	14.298	0.053	14.776	0.060	0.12	0.2487352	150 LR	10505	34	1749	3.9	16.6	1.2	271.9	4.5	65.0	1.8
626-01L	15	1.84E-16	973355*	2900*	63046	70	769.0	6.5	1558	1300	253.5	4.1	92.34	14.268	0.055	14.746	0.054	0.11	0.0473052	150 LR	11172*	590*	1770	4.0	17.5	1.3	271.7	4.7	66.4	1.9

Plateau Age (steps A - L): 14.770 ± 0.070 Ma

Standard: HD-B1 Age: 24.18 ± 0.09 Ma Swartz and Trieloff (2007)

Explanations
Δt^{2}: Time interval (days) between end of irradiation and beginning of analysis
Blank Type: Ave = average; LR = linear regression versus time
*: Analyzed on the Faraday
Constants used
Atmospheric argon ratios

(^{40}Ar/^{36}Ar)$_A$	295.5 ± 0.5	Nier (1950)
(^{40}Ar/^{36}Ar)$_A$	1575 ± 2	Nier (1950)

Interfering isotope production ratios

(^{40}Ar/^{39}Ar)$_K$	0.0184383	0.0023199
(^{36}Ar/^{39}Ar)$_K$	0	0
(^{37}Ar/^{39}Ar)$_K$	0	0
(^{38}Ar/^{39}Ar)$_K$	0.0007096	2.55E-06
(^{36}Ar/^{37}Ar)$_{Ca}$	0	0
(^{38}Ar/^{37}Ar)$_{Ca}$	0.000281	1.58E-06
(^{40}Cl/^{36}Cl)$_{Cl}$	316	0

Decay constants

^{40}K λ_e	(5.81E-11 ± 0.00)E-11 a^{-1}	Steiger and Jäger (1977)
^{40}K λ_β	(4.962E-10 ± 0.00)E-10 a^{-1}	Steiger and Jäger (1977)
^{37}Ar	(2.58 ± 0.03)E-03 a^{-1}	Stoenner et al. (1965)
^{39}Ar	(0.019725 ± 0.00) a^{-1}	Stoenner et al. (1965)
^{36}Cl	(2.35 ± 0.02)E-06 a^{-1}	Endt (1998)

Sample: R07 Lab: Arizona State University Group I8 Laboratories J: 0.0004343 ± 3.16E-06

White mica IGSN:

N	Power (W)	^{40}Ar (moles)	^{40}Ar	±σ_n	^{39}Ar	±σ_n	^{38}Ar	±σ_{38}	^{37}Ar	±σ_{37}	^{36}Ar	±σ_{36}	%^{40}Ar*	^{40}Ar*/^{39}Ar$_K$	±σ	Age (Ma)	±σ (Ma)	±2σ (Ma)	Ca/K	$\Delta t'$ (days)	Blank Type	^{38}Ar	±σ_{38}	^{37}Ar	±σ_n	^{39}Ar	±σ_n	^{37}Ar	±σ_{37}	^{36}Ar	±σ_n
736-01A	4	1.36E-17	68219	100	1161	12	45.1	3.2	-11	21	133.0	5.0	41.49389	24.4	1.3	19.0	1.0	2	-0.0169523	48	LR	22579	53	219.3	4.8	22.3	2.2	3098	6.3	124.0	3.3
736-01B	4.5	2.00E-17	100106	111	2914	17	68.6	3.6	-26	20	150.6	4.5	55.50503	19.05	0.47	14.87	0.37	0.7	-0.0157509	48	LR	22638	48	215.6	4.3	23.5	2.0	305.1	5.7	123.5	2.9
736-01C	5	4.03E-17	201643	147	5496	21	125.2	4.1	-42	20	349.5	5.4	48.74348	17.87	0.31	13.95	0.24	0.5	-0.013706	48	LR	22694	46	212.1	3.9	24.6	1.8	3006	5.3	123.1	2.6
736-01D	5.1	2.68E-17	134181	205	5314	22	87.0	3.6	-6	20	113.1	4.2	75.05758	18.91	0.25	14.77	0.20	0.4	-0.008939	48	LR	22760	46	207.9	3.7	26.0	1.7	295.2	5.1	122.5	2.4
736-01E	5.15	2.06E-17	103097	105	4175	20	58.8	3.5	9	19	75.8	3.9	78.24416	18.42	0.28	14.37	0.22	0.4	0.0035914	48	LR	22816	48	204.5	3.7	27.1	1.7	290.7	5.3	122.1	2.3
736-01F	5.17	1.93E-17	96356	127	3671	18	56.1	3.4	-5	21	88.9	4.0	72.70503	19.06	0.34	14.88	0.26	0.52	-0.0022333	48	LR	22922	63	198.3	4.5	31.3	2.1	274.6	6.6	119.8	2.6
736-01G	5.5	2.41E-15	160632	141	6825	28	98.8	3.5	21	21	113.3	4.4	79.1333	18.60	0.21	14.52	0.16	0.32	0.0054157	48	LR	22798	54	206.7	4.1	31.2	1.8	275.4	5.7	119.0	2.3
736-01H	7	1.88E-16	997313*	4800*	41658	67	635.9	6.7	118	19	718.0	6.7	78.69914	18.82	0.13	14.686	0.099	0.20	0.0030744	48	LR	18968*	570*	215.1	4.2	31.1	1.6	276.2	5.1	118.2	2.2
736-01I	8	2.19E-16	1157783*	5500*	56215	78	744.4	8.5	112	18	367.2	4.9	90.6141	18.64	0.10	14.544	0.080	0.16	0.0035812	48	LR	I9161*	600*	223.4	4.7	31.0	1.6	277.0	5.1	117.4	2.3
736-01J	8.5	1.33E-16	663601.4	562.5641	33653	53	432.6	7.3	87	19	140.8	4.5	93.72185	18.454	0.060	14.403	0.046	0.09	0.0046407	48	LR	22405.92	53.65034	233.2	5.7	30.9	1.8	277.9	5.8	116.4	2.7
736-01K	11	1.62E-16	859886*	4100*	43470	65	557.6	8.0	157	21	167.3	4.9	94.239	18.40	0.10	14.515	0.080	0.16	0.0064455	48	LR	I9793*	750*	241.5	6.2	30.9	1.9	279.5	6.2	115.6	2.9
736-01L	15	6.85E-16	3624891*	17000*	182282	130	2378	12	3003	38	861.9	7.9	92.96346	18.460	0.092	14.407	0.072	0.14	0.0294907	48	LR	20035*	680*	241.1	5.5	31.0	1.7	280.4	5.6	115.7	2.6

Plateau Age (steps B - L): 14.450 ± 0.070 Ma

Standard: HD-B1 Age: 24.18 ± 0.09 Ma Swartz and Trieloff (2007)

Explanations

$\Delta t'$: Time interval (days) between end of irradiation and beginning of analysis

Blank Type: Ave = average; LR = linear regression versus time

*: Analyzed on the Faraday

Constants used

Atmospheric argon ratios

(^{40}Ar/^{39}Ar)$_i$	295.5 ± 0.5	Nier (1950)
(^{40}Ar/^{39}Ar)$_i$	1575 ± 2	Nier (1950)

Interfering isotope production ratios

(^{40}Ar/^{39}Ar)$_K$	0.018949	0.0023222
(^{38}Ar/^{39}Ar)$_K$	0.0128101	0.0000796
(^{37}Ar/^{39}Ar)$_K$	0.0016055	0.0000794
(^{38}Ar/^{39}Ar)$_{Ca}$	0.0006783	2.09E-06
(^{38}Ar/^{39}Ar)$_{Cl}$	0	0
(^{40}Ar/^{39}Ar)$_{Cl}$	0.000267	1.34E-06
(^{36}Cl/^{38}Cl)$_{TI}$	263	2

Decay constants

^{40}K λ_e	(5.81E-11 ± 0.00)E-11 a^{-1}	Steiger and Jäger (1977)
^{40}K λ_β	(4.962E-10 ± 0.00)E-10 a^{-1}	Steiger and Jäger (1977)
^{39}Ar	(2.58 ± 0.03)E-08 a^{-1}	Stoenner et al. (1965)
^{37}Ar	(0.019725 ± 0.00) a^{-1}	Stoenner et al. (1965)
^{36}Cl	(2.35 ± 0.02)E-06 a^{-1}	Endt (1998)

Sample: R08 Lab: Arizona State University Group I8 Laboratories J: 0.0004417 ± 2.02E-06

White mica IGSN:

N	Power (W)	^{40}Ar (moles)	^{40}Ar	±σ_n	^{39}Ar	±σ_n	^{38}Ar	±σ_{38}	^{37}Ar	±σ_{37}	^{36}Ar	±σ_{36}	%^{40}Ar*	^{40}Ar*/^{39}Ar$_K$	±σ	Age (Ma)	±σ (Ma)	±2σ (Ma)	Ca/K	$\Delta t'$ (days)	Blank Type	^{38}Ar	±σ_{38}	^{37}Ar	±σ_n	^{39}Ar	±σ_n	^{37}Ar	±σ_{37}	^{36}Ar	±σ_n
737-01A	4	9.59E-18	47932	92	603	10	32.6	3.1	126	19	154.6	4.3	4.651958	3.7	2.1	2.9	1.7	3	0.3751436	48	LR	22418	42	240.2	4.5	31.1	1.6	2823	5.1	115.8	2.4
737-01B	4.5	1.23E-17	61562	100	1065	13	41.1	2.9	58	21	161.8	4.6	22.30144	12.9	1.3	10.2	1.0	2.1	0.0982141	48	LR	22456	41	239.7	4.4	31.2	1.7	2833	5.3	115.8	2.5
737-01C	5	4.71E-17	235410	160	3665	23	148.5	5.1	26	22	436.7	6.6	45.14872	18.75	0.37	14.88	0.29	0.6	0.0083105	48	LR	22493	47	236.5	5.1	30.9	2.1	2842	6.7	116.8	3.1
737-01D	5.1	2.42E-17	121078	110	4162	19	76.8	3.4	19	19	146.2	4.7	64.27938	18.68	0.35	14.83	0.27	0.5	0.0083063	48	LR	22382	42	234.4	4.4	30.3	1.8	2814	5.7	117.7	2.7
737-01E	5.15	1.11E-17	55647	88	1936	15	34.9	3.1	18	18	66.4	4.2	64.68777	18.58	0.65	14.75	0.52	1.0	0.0168098	48	LR	22273	42	232.3	4.0	29.8	1.6	2786	5.2	118.6	2.5
737-01F	5.17	6.92E-18	34580	89	1254	10	20.1	2.7	61	19	40.4	3.9	65.42028	18.03	0.94	14.31	0.74	1.48	0.0867257	48	LR	22165	46	230.3	4.1	29.2	1.6	2758	5.2	119.5	2.6
737-01G	5.5	2.33E-17	136294	110	2353	16	74.5	3.2	-1	20	239.9	5.0	39.0346	19.27	0.66	15.29	0.52	1.04	-0.000979	48	LR	22037	55	227.8	4.8	28.5	1.8	2725	5.8	120.5	3.1
737-01H	7	1.38E-16	690785	490	21269	47	440.8	6.0	46	22	971.8	7.6	58.39025	18.95	0.13	15.04	0.11	0.21	0.0038971	48	LR	21988	60	229.0	5.2	28.5	1.9	2733	6.2	121.9	3.3
737-01I	8	1.63E-16	864630*	4200*	37662	59	578.8	7.1	72	21	482.2	5.9	83.50099	19.15	0.12	15.193	0.086	0.19	0.0034451	48	LR	I9243*	510*	233.1	4.7	29.1	1.7	2778	5.6	122.4	3.0
737-01J	8.5	8.89E-17	444558.7	220	18474	39	285.2	5.8	88	20	352.4	5.6	76.5309	18.40	0.11	14.603	0.084	0.17	0.0085075	48	LR	22133	49.25681	237.1	4.5	29.6	1.6	2821	5.2	122.9	2.7
737-01K	11	1.79E-16	948369*	4600*	43489	63	620.5	7.6	42	19	425.9	5.8	86.71016	18.88	0.11	14.985	0.090	0.18	0.0017184	48	LR	I9166*	470*	241.8	4.5	30.3	1.5	2874	4.9	123.5	2.5
737-01L	15	4.02E-16	2130000*	9000*	103631	110	1386	10	519	26	594.2	6.0	91.75177	18.847	0.098	14.957	0.077	0.15	0.008962	48	LR	I9128*	481*	245.7	4.8	30.9	1.4	2917	4.8	124.1	2.4

Plateau Age (steps B - L): 14.930 ± 0.080 Ma

Standard: HD-B1 Age: 24.18 ± 0.09 Ma Swartz and Trieloff (2007)

Explanations

$\Delta t'$: Time interval (days) between end of irradiation and beginning of analysis

Blank Type: Ave = average; LR = linear regression versus time

*: Analyzed on the Faraday

Constants used

Atmospheric argon ratios

(^{40}Ar/^{39}Ar)$_i$	295.5 ± 0.5	Nier (1950)
(^{40}Ar/^{39}Ar)$_i$	1575 ± 2	Nier (1950)

Interfering isotope production ratios

(^{40}Ar/^{39}Ar)$_K$	0.018949	0.0023222
(^{38}Ar/^{39}Ar)$_K$	0.0128101	0.0000796
(^{37}Ar/^{39}Ar)$_K$	0.0016055	0.0000794
(^{38}Ar/^{39}Ar)$_{Ca}$	0.0006783	2.09E-06
(^{38}Ar/^{39}Ar)$_{Cl}$	0	0
(^{40}Ar/^{39}Ar)$_{Cl}$	0.000267	1.34E-06
(^{36}Cl/^{38}Cl)$_{TI}$	263	2

Decay constants

^{40}K λ_e	(5.81E-11 ± 0.00)E-11 a^{-1}	Steiger and Jäger (1977)
^{40}K λ_β	(4.962E-10 ± 0.00)E-10 a^{-1}	Steiger and Jäger (1977)
^{39}Ar	(2.58 ± 0.03)E-08 a^{-1}	Stoenner et al. (1965)
^{37}Ar	(0.019725 ± 0.00) a^{-1}	Stoenner et al. (1965)
^{36}Cl	(2.35 ± 0.02)E-06 a^{-1}	Endt (1998)

TABLE A2: RONGBUK VALLEY INDIVIDUAL ZIRCON (U-TH)/HE RESULTS

Sample#	Elevation (m)	Latitude Longitude	Rock Type	[^{238}U]^{a}	Error^{b}	[^{232}Th]^{a}	Error^{b}	[^{4}He]^{a}	Error^{b}	Age$_{RAW}$^{c}	Error^{b}	R1^{d}	R2^{d}	L^{e}	H1^{f}	H2^{f}	β^{g}	a^{h}	F^{i}	Age$_{CORR.}$^{j}	Error^{b}
				pmole	1σ	pmole	1σ	pmole	1σ	Ma	1σ	μm	μm	μm	μm	μm	1/μm	μm	Mean	Ma	2σ
R01	5157	28.14056°N 86.85194°E	Mylonitized leucogranite																		
R01 z001				65.00	0.53	4.36	0.022	0.684	0.008	**8.08**	**0.12**	33.3	31.3	244.4	48.9	37.3	0.070	42.86	0.719	**11.24**	**0.32**
R01 z002				27.49	0.22	1.491	0.009	0.269	0.003	**7.53**	**0.11**	25.5	22.7	203.0	16.4	16.7	0.092	32.61	0.642	**11.72**	**0.34**
R01 z003				17.16	0.14	0.852	0.005	0.188	0.002	**8.43**	**0.12**	25.8	23.7	172.2	37.2	31.6	0.094	31.91	0.636	**13.27**	**0.39**
R01 z004				19.28	0.16	0.671	0.004	0.164	0.002	**6.58**	**0.10**	24.9	26.4	143.5	21.4	19.4	0.091	32.97	0.645	**10.2**	**0.30**
																			Weighted Mean Age:	**11.4**	**2.4**[k]
R02	5114	28.17328°N 86.84003°E	Mylonitized leucogranite																		
R02 z001				31.20	0.24	1.291	0.013	0.353	0.004	**8.74**	**0.13**	31.2	31.1	149.8	14.1	18.3	0.076	39.47	0.697	**12.55**	**0.36**
R02 z002				16.89	0.13	1.426	0.008	0.204	0.003	**9.26**	**0.13**	31.6	30.1	168.3	14.8	14.4	0.076	39.47	0.699	**13.24**	**0.39**
R02 z003				85.20	0.70	3.425	0.018	1.157	0.014	**10.48**	**0.15**	35.9	37.3	222.4	21.6	16.5	0.063	47.62	0.748	**14.02**	**0.41**
R02 z004				11.047	0.086	0.340	0.0050	0.112	0.001	**7.86**	**0.12**	23.8	28	117	12.8	11.5	0.093	32.26	0.636	**12.35**	**0.36**
																			Weighted Mean Age:	**13.0**	**1.5**[k]
R03	5026	28.17300°N 86.84297°E	Mylonitized leucogranite																		
R03 z001				43.33	0.40	1.038	0.01	0.549	0.007	**9.82**	**0.15**	33.3	37	165.1	25.3	16.2	0.068	44.12	0.727	**13.52**	**0.40**
R03 z004				8.66	0.08	0.305	0.003	0.09	0.001	**8.00**	**0.12**	26.6	26.6	127.3	21.5	17.0	0.09	33.33	0.649	**12.34**	**0.38**
																			Weighted Mean Age:	**12.9**	**1.7**[k]
R04	5025	28.18148°N 86.83585°E	Mylonitized leucogranite																		
R04 z001				80.04	0.66	2.408	0.013	0.968	0.012	**10.63**	**0.15**	36.9	41.5	213.8	51.5	51.8	0.062	48.39	0.75	**14.17**	**0.40**
R04 z002				85.93	0.70	2.166	0.011	0.285	0.003	**10.35**	**0.15**	34.7	33.4	187.8	14.5	17.4	0.068	44.12	0.727	**14.25**	**0.42**
R04 z004				89.94	0.76	2.655	0.015	1.018	0.012	**10.89**	**0.16**	39.8	40.1	175.5	18.5	16.9	0.061	49.18	0.755	**14.42**	**0.42**
R04 z005				66.97	0.54	3.766	0.019	0.308	0.004	**10.56**	**0.15**	34.8	34.9	185.8	24.3	24	0.067	44.78	0.73	**14.46**	**0.42**
																			Weighted Mean Age:	**14.32**	**0.21**[l]
R05	5019	28.19000°N 86.83243°E	Leucogranite																		
R05 z001				82.54	0.79	1.537	0.013	0.968	0.012	**9.11**	**0.14**	28.4	27.3	211.1	48.8	33.4	0.082	36.59	0.678	**13.47**	**0.42**
R05 z002				26.48	0.24	1.222	0.009	0.285	0.0000	**8.30**	**0.13**	27.1	27.7	220.8	35.4	31.5	0.082	36.59	0.679	**12.26**	**0.36**
R05 z003				75.55	0.71	0.467	0.004	1.018	0.012	**10.48**	**0.16**	35.4	34.9	203.6	18.9	24.1	0.066	45.45	0.738	**14.23**	**0.44**
R05 z004				28.78	0.27	0.77	0.005	0.308	0.004	**8.29**	**0.13**	28.0	26.9	122.9	24.1	18.0	0.089	33.71	0.655	**12.69**	**0.38**
																			Weighted Mean Age:	**13.1**	**1.7**[k]
R06	5128	28.20502°N 86.82913°E	Mylonitized leucogranite																		
R06 z001				39.96	0.33	1.708	0.010	0.39	0.005	**7.53**	**0.11**	32.3	30.3	173.3	35.3	31.8	0.076	39.47	0.699	**10.76**	**0.32**
R06 z002				40.44	0.33	1.248	0.007	0.414	0.005	**7.92**	**0.11**	37.2	49.0	202.4	56.8	54.8	0.059	50.85	0.76	**10.42**	**0.30**
R06 z003				19.65	0.16	0.651	0.004	0.202	0.002	**7.95**	**0.11**	29.7	28.3	196.6	49.1	36.4	0.081	37.04	0.682	**11.66**	**0.34**
R06 z005				43.68	0.35	1.314	0.007	0.432	0.005	**7.66**	**0.11**	30.9	29.6	137.9	24.2	20	0.08	37.50	0.684	**11.21**	**0.32**
																			Weighted Mean Age:	**11.0**	**1.1**[k]
R07	5017	28.20610°N 86.82580°E	Leucogranite																		
R07 z001				30.44	0.28	0.567	0.005	0.353	0.004	**9.00**	**0.14**	34.8	34.4	222	14.1	16.4	0.066	45.45	0.736	**12.22**	**0.38**
R07 z002				8.358	0.078	0.631	0.005	0.107	0.001	**9.81**	**0.15**	28.2	33.7	202.3	17	22.5	0.074	40.54	0.706	**13.90**	**0.42**
R07 z003				12.06	0.11	0.862	0.007	0.143	0.002	**9.07**	**0.14**	40.6	42.9	283.4	28.7	20.6	0.054	55.56	0.78	**11.63**	**0.36**
R07 z004				8.956	0.087	0.386	0.003	0.105	0.001	**9.09**	**0.14**	36.9	33.7	177.2	27.9	23.9	0.067	44.78	0.73	**12.46**	**0.38**
R07 z005				21.75	0.20	0.931	0.007	0.295	0.004	**10.46**	**0.16**	40.4	41.4	209.9	24.1	26.1	0.058	51.72	0.767	**13.64**	**0.42**
R07 z006				9.172	0.087	0.236	0.002	0.098	0.001	**8.27**	**0.13**	24.8	25.4	174.9	20.7	15.5	0.09	33.33	0.649	**12.74**	**0.40**
R07 z008				25.31	0.23	0.269	0.002	0.332	0.004	**10.21**	**0.16**	32.7	31.4	190.8	27.2	20.7	0.072	41.67	0.714	**14.30**	**0.44**
																			Weighted Mean Age:	**12.9**	**1.9**[k]
R08	4947	28.21285°N 86.82395°E	Leucogranite																		
R08 z001				55.44	0.43	1.028	0.007	0.774	0.009	**10.83**	**0.15**	48.5	49.6	228.3	43.6	32.8	0.049	61.22	0.799	**13.56**	**0.38**
R08 z002				41.51	0.32	0.214	0.002	0.51	0.006	**9.57**	**0.14**	29.8	35.1	179.6	23.5	18.9	0.072	41.67	0.713	**13.43**	**0.38**
R08 z003				23.38	0.18	0.912	0.005	0.308	0.004	**10.19**	**0.14**	38.5	36.2	187.3	25.3	15.9	0.063	47.62	0.745	**13.68**	**0.38**
R08 z004				26.73	0.21	0.258	0.004	0.368	0.004	**10.71**	**0.15**	43.5	43.4	205.2	24.8	21.9	0.055	54.55	0.777	**13.79**	**0.40**
R08 z005				27.51	0.22	1.838	0.009	0.345	0.004	**9.63**	**0.14**	28.7	34.0	142.7	17.1	17.3	0.077	38.96	0.693	**13.88**	**0.40**
																			Weighted Mean Age:	**13.66**	**0.17**[l]

[a]Absolute measured ^{4}He, ^{238}U, and ^{232}Th concentrations are used to calculate the 'Raw Age' that is uncorrected for the effects of ^{4}He loss due to alpha particle recoil.
[b]Based on the propagation of analytical errors
[c]The 'Raw Age' was calculated with an iterative approach to solving the age equation.
[d]R1 and R2 describe the perpendicular half-widths of the zircon.
[e]L describes the total length of the zircon, and
[f]H1 and H2 describe the height of the pyramidal terminations of the zircon crystal.
[g]β represents the surface area to volume ratio for the crystal.
[h]a represents the equivalent spherical radius of the grain (Reiners and Brandon, 2006)
[i]The mean F_T correction was calculated following procedures defined for zircon. A bipyramidal prism geometry was assumed for all calculations (Hourigan et al., 2005).
[j]The F_T corrected age of the crystal. The FT correction was applied to the raw age following procedures defined by Farley et al. (1996).
[k]Uncertainty reported as 2 inverse variance-weighted standard deviations of the dataset for this sample.
[l]Uncertainty reported as 2 inverse variance-weighted standard deviations of the inverse variance-weighted mean. (MSWD indicated no overdispersion.)

TABLE A3: RONGBUK VALLEY INDIVIDUAL APATITE (U-TH)/HE RESULTS

Sample#	Elevation (m)	Latitude Longitude	Rock Type	[^{238}U][a]	Error[b]	[^{232}Th][a]	Error[b]	[^{4}He][a]	Error[b]	Age$_{RAW}$[c]	Error[b]	Rd	L[e]	β[f]	a[g]	F_T[h]	Age$_{CORR.}$[i]	Error[b]
				pmole	1σ	pmole	1σ	pmole	1σ	Ma	1σ	μm	μm	1/μm	μm	Mean	Ma	2σ
R01	5157	28.14056°N 86.85194°E	Mylonitized leucogranite															
R01 a001				0.8942	0.0071	0.5194	0.0099	0.01119	0.00015	**8.53**	**0.13**	61	263.2	0.046	65.93	0.776	**10.99**	**0.34**
R01 a002				0.5284	0.0045	0.0506	0.0080	0.005135	0.000072	**7.34**	**0.12**	62.8	265.2	0.044	67.72	0.784	**9.36**	**0.32**
R01 a004				0.1206	0.0014	0.025	0.0080	0.000799	0.000018	**4.88**	**0.14**	39	155	0.072	41.61	0.662	**7.38**	**0.42**
R01 a006				0.1847	0.0019	0.0094	0.0080	0.001241	0.000043	**5.14**	**0.19**	34	163	0.080	37.41	0.63	**8.16**	**0.62**
R01 a007				0.06950	0.00090	0.0024	0.0080	0.000871	0.000026	**5.93**	**0.26**	31.9	173.7	0.084	35.76	0.615	**8.60**	**0.76**
R01 a009				0.1798	0.0018	0.0026	0.0080	0.001353	0.000045	**2.460**	**0.080**	38.7	156.5	0.073	41.38	0.662	**4.09**[j]	**0.26**
R01 a010				0.1505	0.0019	0.0184	0.0080	0.001188	0.000049	**5.79**	**0.21**	41.6	199.5	0.066	45.73	0.69	**8.74**	**0.62**
																Weighted Mean Age:	**9.3**	**2.8**[k]
R02	5114	28.17328°N 86.84003°E	Mylonitized leucogranite															
R02 a003				0.0669	0.0010	0.0085	0.0011	0.000423	0.000014	**4.78**	**0.18**	32.3	181.6	0.083	36.36	0.62	**7.70**	**0.56**
R02 a004				0.0581	0.0010	0.072	0.0013	0.000592	0.000013	**6.16**	**0.16**	25.5	124.6	0.11	28.12	0.515	**11.96**[j]	**0.62**
R02 a006				0.02740	0.00090	0.1218	0.0018	0.000316	0.000028	**4.43**	**0.40**	28.7	122	0.10	30.99	0.538	**8.20**	**1.5**
																Weighted Mean Age:	**7.76**	**0.52**[l]

[a]Absolute measured ^{4}He, ^{238}U, and ^{232}Th concentrations are used to calculate the 'Raw Age' that is uncorrected for the effects of ^{4}He loss due to alpha particle recoil.
[b]Based on the propagation of analytical errors
[c]The 'Raw Age' was calculated with an iterative approach to solving the age equation.
[d]R describes the width of the apatite.
[e]L describes the total length of the apatite.
[f]β represents the surface area to volume ratio for the crystal.
[g]a represents the equivalent spherical radius of the grain (Reiners and Brandon, 2006)
[h]The mean F_T correction was calculated following procedures defined for apatite.
[i]The F_T corrected age of the crystal. The FT correction was applied to the raw age following procedures defined by Farley et al., 1996
[j]Datum identified as an outlier using the Hempel identifier methods with an outher limit of 4.0
[k]Uncertainty reported as 2 inverse variance-weighted standard deviations of the dataset for this sample.
[l]Uncertainty reported as 2 inverse variance-weighted standard deviations of the inverse variance-weighted mean. (MSWD indicated no overdispersion.)

FIGURE A1.

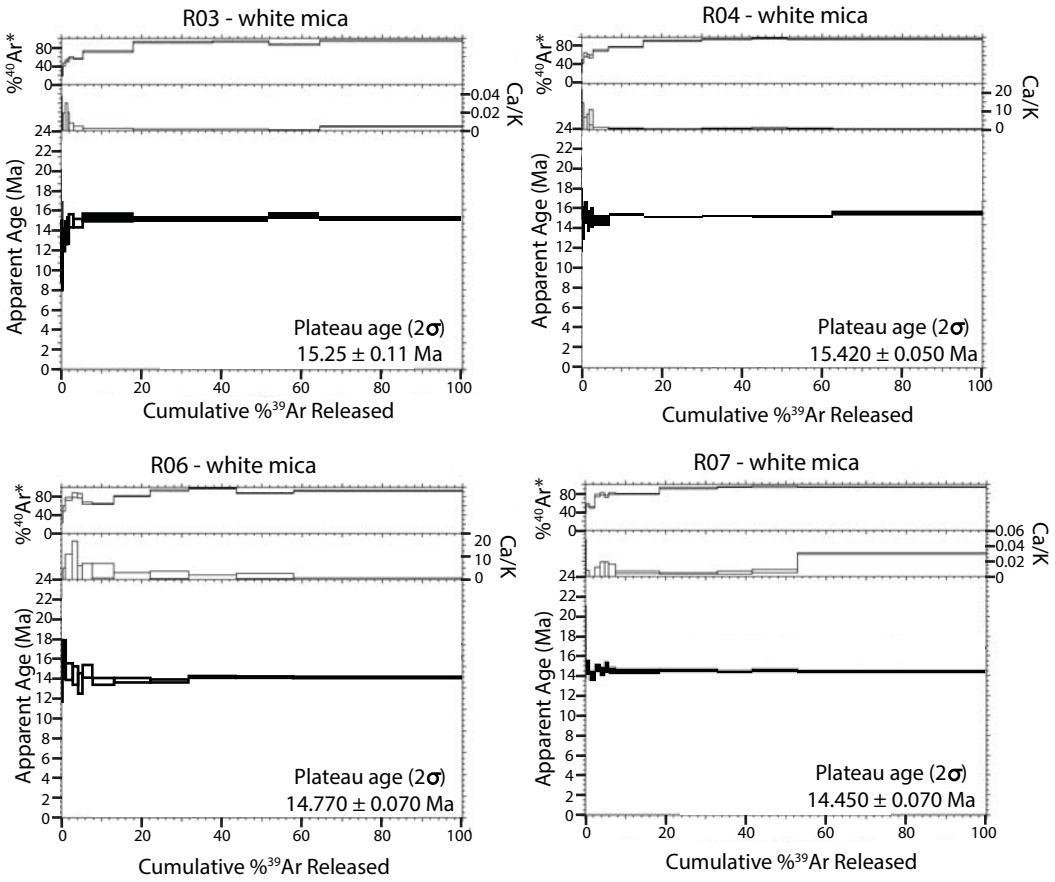
R03 - white mica
%40Ar*
Ca/K
Apparent Age (Ma)
Plateau age (2σ)
15.25 ± 0.11 Ma
Cumulative %39Ar Released
R04 - white mica
%40Ar*
Ca/K
Apparent Age (Ma)
Plateau age (2σ)
15.420 ± 0.050 Ma
Cumulative %39Ar Released
R06 - white mica
%40Ar*
Ca/K
Apparent Age (Ma)
Plateau age (2σ)
14.770 ± 0.070 Ma
Cumulative %39Ar Released
R07 - white mica
%40Ar*
Ca/K
Apparent Age (Ma)
Plateau age (2σ)
14.450 ± 0.070 Ma
Cumulative %39Ar Released

FIGURE A2.

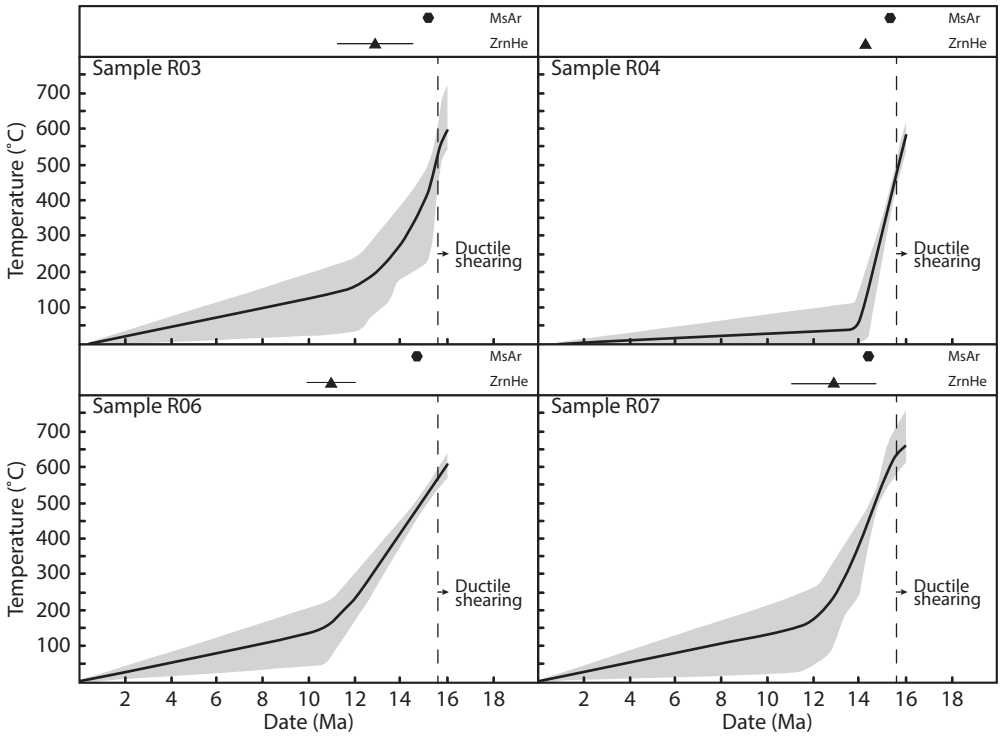
MsAr
ZrnHe
Sample R03
Sample R04
Sample R06
Sample R07
Temperature (°C)
700
600
500
400
300
200
100
Ductile shearing
2
4
6
8
10
12
14
16
18
Date (Ma)

FIGURE A3.

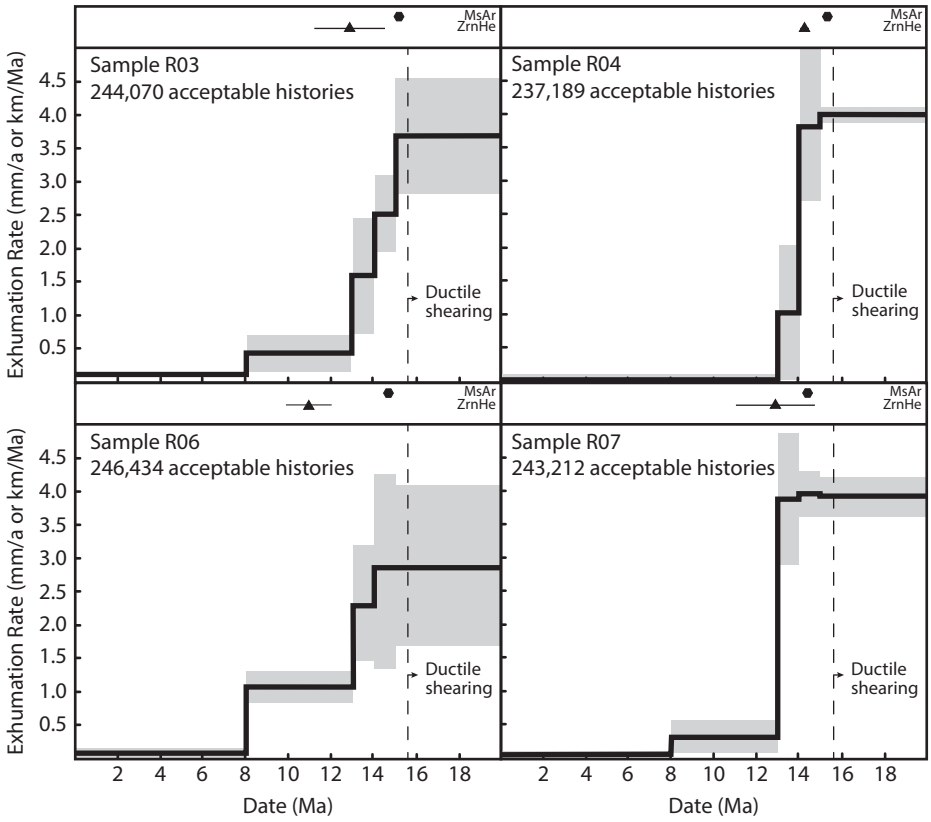
MsAr
ZrnHe
Sample R03
244,070 acceptable histories
Sample R04
237,189 acceptable histories
Sample R06
246,434 acceptable histories
Sample R07
243,212 acceptable histories
Ductile
shearing
Exhumation Rate (mm/a or km/Ma)
0.5
1.0
1.5
2.0
2.5
3.0
3.5
4.0
4.5
2
4
6
8
10
12
14
16
18
Date (Ma)

APPENDIX B

CHAPTER 3 SUPPLEMENTARY MATERIALS

APPENDIX TABLE B1: WHITE MICA AND BIOTITE $^{40}AR/^{39}AR$ STEP-HEATING RESULTS FOR THE RA CHU AND DZAKAR CHU, SOUTH-CENTRAL TIBET

Sample: RC01 Lab: Group 18 Laboratories *J*: 8.88E-05 ±1.36E-06

Material: Biotite

																			Blank Corrections										
N	Power (W)	^{40}Ar (cps)	±σ (cps)	^{39}Ar (cps)	±σ (cps)	^{38}Ar (cps)	±σ (cps)	^{37}Ar (cps)	±σ (cps)	^{36}Ar (cps)	±σ (cps)	*D*[1]:	$\%^{40}Ar^*$	$^{40}Ar^*/^{39}Ar_K$	±σ	Age (Ma)	±2σ (Ma)	±2σ (-J) (Ma)	Ca/K	±σ	Blank Type[2]	^{40}Ar (cps)	±σ (cps)	^{39}Ar (cps)	±σ (cps)	^{38}Ar (cps)	±σ (cps)	^{37}Ar (cps)	±σ (cps)	^{36}Ar (cps)	±σ (cps)
A	*0.8*	*-14*	*-210*	*12.4*	*2.9*	*1.1*	*1.7*	*-5*	*19*	*-5.9*	*2.4*	*0.99799*	*-12847.32*	*140.38046*	*69.5963*	*22*	*22*	*22*	*-0.7172*	*2.68948*	*LR*	*10615*	*156*	*198.3*	*2.0*	*10.1724*	*0.90848*	*230.2*	*2.5*	*55.0*	*1.6*
B	0.8	222808	220	1016.6	5.7	109.6	2.5	61	17	502.6	3.6	0.99799	33.35	73.1	1.2	11.67	0.52	0.38	0.106	0.030	LR	10471	146	192.1	2.0	11.5	1.2	228.5	2.5	52.6	1.5
C	0.9	110697	210	555.0	4.9	48.7	1.9	9	17	219.5	2.9	0.99799	41.40	82.6	1.8	13.18	0.69	0.57	0.029	0.055	LR	10475	131	191.5	1.8	11.7	1.0	228.3	2.2	53.0	1.4
D	1.1	73888	190	603.6	4.9	21.7	1.9	15	18	78.3	2.5	0.99799	68.70	84.1	1.5	13.42	0.62	0.46	0.045	0.053	LR	10480	124	190.8	1.6	11.85	0.95	228.1	2.1	53.4	1.3
E	1.3	*1002759.22	610	9003	14	230.3	3.0	34	20	583.3	3.5	0.99799	82.81	92.24	0.21	14.72	0.45	0.07	0.006	0.004	LR	12062	333	190.2	1.6	12.04	0.91	228.0	2.1	53.9	1.3
F	1.5	472929	300	5359	11	80.6	2.2	48	21	84.1	2.6	0.99799	94.75	83.61	0.24	13.35	0.41	0.08	0.015	0.007	LR	10492	156	189.0	2.0	12.4	1.0	227.6	2.5	54.7	1.6
G	1.7	532273	280	5998	12	98.3	2.4	14	19	96.2	2.6	0.99799	94.66	84.00	0.22	13.41	0.42	0.07	0.004	0.006	LR	10833	152	198.6	1.9	13.0	1.0	230.6	2.5	56.8	1.5
H	1.9	132365	190	1535.0	5.9	20.3	1.9	1	20	15.5	2.2	0.99799	96.55	83.25	0.57	13.29	0.44	0.18	0.000	0.023	LR	11140	135	208.1	1.8	13.42	0.92	233.6	2.2	58.2	1.3
I	2.3	365981	220	4162	10	64.1	2.3	-3	20	58.9	2.4	0.99799	95.24	83.76	0.28	13.37	0.42	0.09	-0.002	0.009	LR	11447	131	217.5	1.7	13.81	0.92	236.5	2.2	59.7	1.3
J	3	610233	290	6830	13	111.6	2.5	24	22	104.9	2.6	0.99799	94.92	84.80	0.21	13.53	0.42	0.07	0.006	0.006	LR	11754	141	226.9	1.9	14.2	1.0	239.4	2.4	61.1	1.4

Plateau Age (Steps F - J): 13.39 ± 0.38 Ma

Total Fusion Age13.84 ± 0.43 Ma

Sample: DC01 Lab: Group 18 Laboratories *J*: 9.01E-05 ± 1.38E-06

Material: White Mica

																			Blank Corrections										
N	Power (W)	^{40}Ar (cps)	±σ (cps)	^{39}Ar (cps)	±σ (cps)	^{38}Ar (cps)	±σ (cps)	^{37}Ar (cps)	±σ (cps)	^{36}Ar (cps)	±σ (cps)	*D*[1]:	$\%^{40}Ar^*$	$^{40}Ar^*/^{39}Ar_K$	±σ	Age (Ma)	±2σ (Ma)	±2σ (-J) (Ma)	Ca/K	±σ	Blank Type[2]	^{40}Ar (cps)	±σ (cps)	^{39}Ar (cps)	±σ (cps)	^{38}Ar (cps)	±σ (cps)	^{37}Ar (cps)	±σ (cps)	^{36}Ar (cps)	±σ (cps)
A	0.6	104739	193	449.4	4.9	47.4	2.0	63	24	223.7	2.9	0.99799	36.87	86.0	2.2	13.92	0.84	0.72	0.226	0.088	LR	11134	140	252.0	2.1	15.0	1.0	318.5	2.4	59.2	1.5
B	0.7	73878	190	807.8	5.4	13.0	1.7	60	24	19.2	2.2	0.99799	92.31	84.4	1.1	13.67	0.54	0.34	0.120	0.048	LR	11347	130	249.2	1.9	15.13	0.91	317.7	2.2	59.8	1.3
C	0.8	74219	180	409.5	5.2	28.1	1.7	28	23	137.5	2.6	0.99799	45.24	82.0	2.2	13.28	0.82	0.72	0.113	0.090	LR	11561	120	246.3	1.8	15.26	0.89	316.8	2.2	60.4	1.3
D	0.9	25041	190	271.5	4.1	2.8	1.6	16	21	7.3	2.4	0.99799	91.37	84.3	3.0	13.6	1.1	0.98	0.10	0.13	LR	11774	130	243.5	1.9	15.39	0.96	315.9	2.5	61.0	1.4
E	1.1	21997	200	252.6	3.9	2.7	1.7	2	20	10.1	2.6	0.99799	86.41	75.3	3.4	12.2	1.2	1.1	0.01	0.13	LR	11988	140	240.7	2.1	15.5	1.1	315.0	3.0	61.6	1.6
F	1.3	472574	270	4367	10	113.0	2.8	-16	23	350.4	3.0	0.99799	78.09	84.51	0.30	13.68	0.43	0.10	-0.0064	0.0086	LR	12432	140	247.4	2.1	16.5	1.1	320.1	2.9	65.2	1.6
G	1.5	256512	210	2919.8	9.0	40.0	2.1	4	22	38.2	2.4	0.99799	95.60	83.98	0.37	13.60	0.43	0.12	0.002	0.012	LR	12642	130	256.0	2.0	17.22	0.95	325.5	2.6	67.9	1.4
H	2	253252	210	2805.2	8.1	42.3	2.2	-65	21	47.9	2.4	0.99799	94.41	85.23	0.37	13.80	0.44	0.12	-0.038	0.012	LR	12852	130	264.6	2.0	17.97	0.88	330.9	2.5	70.6	1.3
I	5	613259	290	6985	14	95.3	2.7	-72	24	69.8	2.4	0.99799	96.64	84.85	0.21	13.74	0.43	0.067	-0.0172	0.0056	LR	13063	150	273.2	2.2	18.71	0.91	336.4	2.7	73.3	1.4
J	8	235889	230	2772.9	8.8	32.6	2.2	-45	22	10.2	2.3	0.99799	98.72	83.98	0.38	13.60	0.43	0.12	-0.026	0.013	LR	13274	170	281.8	2.6	19.5	1.0	341.8	3.1	76.0	1.5
K	8	15370	200	180.7	4.4	0.0	1.9	-17	22	-1.7	2.3	1.99799	103.32	87.9	4.6	14.2	1.5	1.5	0.16	0.10	LR	24855	130	308.7	2.0	24.2	1.1	365.0	2.9	76.0	1.4
L	10	19349	190	181.2	5.2	1.6	1.9	23	27	-0.3	2.5	2.99799	100.41	107.2	5.3	17.3	1.8	1.7	-0.071	0.081	LR	35860	120	302.1	2.2	31.1	1.2	363.5	2.9	76.0	1.7

Plateau Age (Steps F - K): 13.693 ± 0.092 Ma

Total Fusion .13.71 ± 0.43 Ma

Standard: HD Age: 24.18 ± 0.09 Swartz and Trieloff (2007)

Explanations

Blank Type: LR = linear regression versus time

*: Analyzed on the Faraday

Negative values indicate that analysis is indistinguishable from the background

Constants used

Atmospheric argon ratios

$(^{40}Ar/^{36}Ar)_A$	295.5 ± 0.5	Nier (1950)
$(^{40}Ar/^{38}Ar)_A$	1575 ± 2	Nier (1950)

Interfering isotope production ratios

$(^{40}Ar/^{39}Ar)_K$	0.00073	0.00009
$(^{38}Ar/^{39}Ar)_K$	0.01215	0.00003
$(^{37}Ar/^{39}Ar)_K$	0.000224	0.000016
$(^{39}Ar/^{37}Ar)_{Ca}$	0.000695	9.00E-06
$(^{38}Ar/^{37}Ar)_{Ca}$	0.0000196	8.00E-07
$(^{36}Ar/^{37}Ar)_{Ca}$	0.000265	2.20E-06
$(^{36}Cl/^{38}Cl)_{Cl}$	263	2

Decay constants

$^{40}K\ \lambda_e$	(5.81E-11 ± 0.00)|	Steiger and Jäger (1977)
$^{40}K\ \lambda_\beta$	(4.962E-10 ± 0.00	Steiger and Jäger (1977)
^{39}Ar	(2.58 ± 0.03)E-03	Stoenner et al. (1965)
^{37}Ar	(0.019725 ± 0.00)	Stoenner et al. (1965)
^{36}Cl	(2.35 ± 0.02)E-06	Endt (1998)

APPENDIX TABLE B2: RA CHU AND DZAKAR CHU INDIVIDUAL ZIRCON (U-TH)/HE RESULTS

Sample#	Elevation (m)	Latitude Longitude	Rock Type	$[^{238}U]^a$	Error[b]	$[^{232}Th]^a$	Error[b]	$[^4He]^a$	Error[b]	Age_{RAW}[c]	Error[b]	R1[d]	R2[d]	L[e]	H1[f]	H2[f]	β[g]	a[h]	Ft[i]	Age_{CORR}[j]	Error[b]
				pmole	1σ	pmole	1σ	pmole	1σ	Ma	1σ	μm	μm	μm	μm	μm	1/μm	μm	Mean	Ma	2σ
RC01	3942	28.35530 N 86.67233 E	Calc-silicate and Amphibolite																		
RC01 z01				25.18	0.23	0.5786	0.0038	0.2232	0.0027	**6.87**	**0.10**	24.6	27.5	119.9	17.9	17.6	0.093	32.35	0.639	**10.76**	**0.33**
RC01 z02				5.944	0.055	3.283	0.021	0.0589	0.0008	**6.85**	**0.11**	26.3	27.0	127.7	17.5	15.9	0.090	33.51	0.646	**10.62**	**0.33**
RC01 z03				33.28	0.30	0.9328	0.0058	0.3438	0.0041	**8.00**	**0.12**	31.9	25.7	147.2	26.4	25.7	0.084	35.91	0.671	**11.92**	**0.35**
RC01 z04				68.72	0.70	1.435	0.018	0.7772	0.0093	**8.77**	**0.14**	24.9	27.2	152.8	21.1	16.4	0.089	33.81	0.653	**13.44**	**0.42**
RC01 z05				61.59	0.55	1.3510	0.0078	0.7267	0.0086	**9.15**	**0.14**	25.4	28.5	140.6	14.3	17.8	0.087	34.35	0.658	**13.92**	**0.41**
																			Weighted Mean Age:	**11.9**	**1.3**[k]
DC01	3907	28.34593 N 87.22805 E	Mylonitic leucogranite																		
DC01 z01				21.65	0.19	2.192	0.012	0.1988	0.0024	**7.00**	**0.10**	26.7	23.9	149.4	28.8	21.7	0.092	32.53238009	0.640	**10.94**	**0.33**
DC01 z02				4.696	0.040	0.8527	0.0083	0.0397	0.0006	**6.33**	**0.11**	27.0	25.1	139.4	17.8	21.8	0.090	33.31137518	0.647	**9.79**	**0.33**
DC01 z03				16.08	0.13	3.973	0.026	0.1418	0.0020	**6.50**	**0.10**	31.6	29.9	199.7	25.7	21.1	0.074	40.51447781	0.704	**9.24**	**0.30**
DC01 z04				27.60	0.23	3.093	0.020	0.2562	0.0032	**7.05**	**0.10**	27.3	28.7	205.8	31.4	27.9	0.081	37.25156037	0.681	**10.36**	**0.31**
																			Weighted Mean Age:	**10.05**	**0.74**[k]
DC02	3885	28.33858 N 87.25626 E	Biotite Gneiss																		
DC02 z01				6.542	0.054	0.5622	0.0061	0.04600	0.00057	**5.376**	**0.080**	28.8	29.9	167.5	19.7	20.6	0.079	38.03201147	0.687	**7.82**	**0.23**
DC02 z02				2.621	0.022	0.3857	0.0035	0.01938	0.00026	**5.577**	**0.086**	24.4	24.3	146.4	22.0	23.2	0.095	31.59473001	0.630	**8.85**	**0.27**
DC02 z03				3.771	0.031	0.6967	0.0054	0.03040	0.00046	**6.03**	**0.10**	30.9	22.1	137.6	17.8	24.5	0.091	32.78917191	0.642	**9.40**	**0.32**
DC02 z04				2.780	0.023	0.8360	0.0087	0.02310	0.00037	**6.06**	**0.11**	28.4	25.6	143.3	14.5	16.7	0.087	34.5508653	0.657	**9.22**	**0.33**
DC02 z05				5.557	0.046	0.7375	0.0048	0.04730	0.00059	**6.44**	**0.10**	32.3	31.4	154.0	17.4	17.6	0.075	40.17962888	0.702	**9.17**	**0.27**
DC02 z06				3.844	0.036	0.7539	0.0054	0.02798	0.00044	**5.43**	**0.10**	27.4	26.4	149.9	15.2	18.2	0.086	34.75556229	0.660	**8.23**	**0.30**
																			Weighted Mean Age:	**8.67**	**0.54**[k]
DC03	4380	28.33664 N 87.27357 E	Leucogranite and Biotite Gneiss																		
DC03 z01				15.09	0.14	3.422	0.021	0.1727	0.0021	**8.47**	**0.13**	30.6	30.6	198.1	24.0	18.1	0.074	40.39	0.703	**12.05**	**0.36**
DC03 z02				37.66	0.35	8.711	0.049	0.4270	0.0051	**8.39**	**0.12**	36.6	27.9	215.1	28.2	23.0	0.071	41.98	0.713	**11.76**	**0.35**
DC03 z03				42.04	0.38	15.790	0.080	0.5370	0.0064	**9.16**	**0.13**	39.1	37.5	183.3	29.3	25.2	0.062	48.00	0.746	**12.28**	**0.36**
DC03 z04				*4.987*	*0.047*	*2.327*	*0.014*	*0.0442*	*0.0005*	***6.23***	***0.09***	*37.7*	*33.5*	*164.3*	*25.1*	*24.3*	*0.068*	*44.20*	*0.725*	***8.59***	***0.26***
DC03 z05				36.72	0.33	7.206	0.039	0.4480	0.0055	**9.10**	**0.14**	32.1	33.5	210.7	23.4	21.8	0.069	43.25	0.721	**12.61**	**0.38**
DC03 z06				*11.10*	*0.10*	*5.423*	*0.030*	*0.0944*	*0.0012*	***5.96***	***0.09***	*33.9*	*28.9*	*284.8*	*28.3*	*25.8*	*0.070*	*42.79*	*0.717*	***8.31***	***0.25***
																			Weighted Mean Age:	**12.16**	**0.35**[k]

[a]Absolute measured ^4He, ^{238}U, and ^{232}Th concentrations are used to calculate the 'Raw Age' that is uncorrected for the effects of ^4He loss due to alpha particle recoil.
[b]Based on the propagation of analytical errors
[c]The 'Raw Age' was calculated with an iterative approach to solving the age equation.
[d]R1 and R2 describe the perpendicular half-widths of the zircon.
[e]L describes the total length of the zircon, and
[f]H1 and H2 describe the height of the pyramidal terminations of the zircon crystal.
[g]β represents the surface area to volume ratio for the crystal.
[h]a represents the equivalent spherical radius of the grain (Reiners and Brandon, 2006)
[i]The mean F_T correction was calculated following procedures defined for zircon. A bipyramidal prism geometry was assumed for all calculations (Hourigan et al., 2005).
[j]The F_T corrected age of the crystal. The FT correction was applied to the raw age following procedures defined by Farley et al. (1996).
[k]Uncertainty reported as 2 inverse variance-weighted standard deviations of the dataset for this sample.
Single grain analyses in italics were identified as outliers by the Hampel identifier method (Pearson, 2011) and were not used in the calculation of the mean.

APPENDIX TABLE B3: DZAKAR CHU INDIVIDUAL APATITE (U-TH)/HE RESULTS

Sample#	Elevation (m)	Latitude Longitude	Rock Type	[^{238}U][a]	Error[b]	[^{232}Th][a]	Error[b]	[^{4}He][a]	Error[b]	Age$_{RAW}$[c]	Error[b]	Rd	L[e]	β[f]	a[g]	F_T[h]	Age$_{CORR.}$[i]	Error[b]
				pmole	1σ	pmole	1σ	pmole	1σ	Ma	1σ	μm	μm	1/μm	μm	Mean	Ma	2σ
DC03	4380	28.33664 N 87.27357 E	Leucogranite and Biotite Gneiss															
DC03 a01				0.1702	0.0017	0.0645	0.0023	2.197	0.036	9.16	0.17	33.2	150.4	0.0829	40.8	0.616	14.88	0.56
DC03 a02				0.1679	0.0019	0.0351	0.0022	1.824	0.035	7.96	0.18	47.1	221.3	0.0581	58.3	0.722	11.03	0.49
DC03 a03				0.08503	0.00092	0.0963	0.0024	0.686	0.017	4.84	0.13	48.1	153.6	0.0610	54.9	0.703	6.89	0.37
DC03 a04				0.2518	0.0021	0.0841	0.0024	2.642	0.049	7.49	0.15	53.9	184.6	0.0537	62.6	0.740	10.11	0.41
DC03 a05				0.1183	0.0012	0.0258	0.0022	1.453	0.028	8.89	0.20	48.9	186.6	0.0580	58.1	0.722	12.31	0.54
																Weighted Mean Age:	**10.2**	**2.6**[l]

[a]Absolute measured ^{4}He, ^{238}U, and ^{232}Th concentrations are used to calculate the 'Raw Age' that is uncorrected for the effects of ^{4}He loss due to alpha particle recoil.
[b]Based on the propagation of analytical errors
[c]The 'Raw Age' was calculated with an iterative approach to solving the age equation.
[d]R describes the width of the apatite.
[e]L describes the total length of the apatite.
[f]β represents the surface area to volume ratio for the crystal.
[g]a represents the equivalent spherical radius of the grain (Reiners and Brandon, 2006)
[h]The mean F_T correction was calculated following procedures defined for apatite.
[i]The F_T corrected age of the crystal. The FT correction was applied to the raw age following procedures defined by Farley et al., 1996
[j]Datum identified as an outlier using the Hempel identifier methods with an outher limit of 4.0
[k]Uncertainty reported as 2 inverse variance-weighted standard deviations of the dataset for this sample.
[l]Uncertainty reported as 2 inverse variance-weighted standard deviations of the inverse variance-weighted mean. (MSWD indicated no overdispersion.)

APPENDIX C

CHAPTER 4 SUPPLEMENTARY MATERIALS

Analytical methods - $^{40}Ar/^{39}Ar$ thermochronology

Crushing and standard gravimetric and magnetic procedures were used to prepare rough grain concentrates prior to the final purification of mineral separates for thermochronology. In the case of muscovite and biotite for $^{40}Ar/^{39}Ar$ dating, this involved hand-picking of single muscovite and biotite grains and their cleaning in acetone, methanol, and deionized water. Samples were then individually wrapped in aluminum foil packets and loaded into small aluminum disks, which were stacked and secured together to make up the package for neutron irradiation production of ^{39}Ar. Grains of biotite standard HD-B1 (24.18 ± 0.09 Ma, uncertainty at 1σ, *Schwarz et al.,* 2007) were regularly interspersed in the aluminum disks with the samples to monitor the overall neutron flux, and synthetic and natural K and Ca salts were added to determine interfering nuclear production ratios. Khumbu biotites and muscovites were irradiated in a Cd-shielded package at the Oregon State University CLICIT facility for 0.33 hours.

After irradiation, the unknowns, monitors, and standards were loaded into an ultrahigh-vacuum line for argon isotopic analysis. The analytical experiments involved incremental heating of individual crystals using a Photon Machines/Atlex ArF 193 nm excimer laser operated at successively high power levels ranging from 0.8 to 6 W for samples K01, K02, and K08 and 5 to 10 W for the rest of the samples. No attempt was made to monitor sample temperatures during the experiment. Released gasses were purified by passing them over hot and cold SAES NP10 metal alloy 'getters' prior to Ar isotopic analysis with a Nu Instruments *Noblesse* magnetic sector mass spectrometer. For most release steps, signals were measured using an ETP ion counting detector, but a few ^{40}Ar signals were so large that a Faraday detector (fitted with a 10^{11} Ohm resistor) was

used. The fully automated laser heating, automated valves operation, and data acquisition was computer controlled using Alan Deino's *MassSpec* software program.

Total system blanks for our experiments are estimated to have been 2.5E-18, 4.7E-20, 3.1E-21, 5.3E-20, 1.3E-20 moles STP (standard temperature and pressure) for ^{40}Ar, ^{39}Ar, ^{38}Ar, ^{37}Ar and ^{36}Ar, respectively. Unknown analyses were corrected for mass spectrometer discrimination and nuclear interference reactions (see Table A1). Air pipette shots were analyzed regularly to intercalibrate the Faraday and ion counting detector, using the ^{40}Ar peak, and intercalibrations were done using the 'isotopic reference ratio intercalibration' method of Turrin et al*.,* (2010). Apparent ages were calculated using the ^{40}Ar decay constants and branching ratios of Steiger and Jäger (1977). To account for potential gradients in the reactor neutron flux in the irradiation package, J values and errors were calculated for the unknown samples (Table C1) by spatially interpolating J values obtained from age standard minerals (i.e., HD-B1 biotite) evenly distributed within the seven-hole Al irradiation planchettes.

All muscovite laser incremental heating analyses resulted in plateau ages, defined as three or more steps comprising 50% or more of the total ^{39}Ar in a sample, with individual calculated ages that overlap at the 2σ level without propagation of the *J*-value uncertainty Fleck et al., (1977). The reported plateau dates and their 2σ uncertainties (inclusive of the *J*-value uncertainties) represent the ^{39}Ar-weighted means of the ages of all the steps defining each plateau.

All biotite laser incremental heating analyses are reported as inverse-isochron ages as the ^{40}Ar/^{36}Ar ratio for all samples is greater than the atomospheric ratio of 295.5, indicating the presence of excess argon, which is known to occur in Himalayan biotite

grains (Hubbard and Harrison, 1989; Grove and Harrsion, 1996; Adams et al., 2015; Stübner et al., 2017).

Analytical methods - (U-Th)/He thermochronology

Using a binocular microscope, individual crystals of clear, euhedral, and apparently inclusion-free zircon and apatite were picked for (U-Th)/He dating from rough concentrates. We report dates for between one and five individual crystals of apatite and between four and eight zircon grains per sample. Each crystal was measured to establish the necessary parameters for the alpha ejection corrections of the resulting dates using the approach of Farley et al. (1996) for apatite and Hourigan et al. (2005) for zircon. For both minerals, we assumed a homogeneous distribution of U and Th for determining correction factors. The grains were then loaded into small niobium tubes prior to analysis. All helium measurements were made with an Australian Scientific Instruments (ASI) *Alphachron* system, which features a 45 Watt, infrared (980 nm) diode laser for gas extraction and a Balzers *Prisma QMS 200* quadrupole mass spectrometer for isotopic measurements. Gasses including helium were released from apatite by laser heating for five minutes at 9 A, and from zircon by laser heating for ten minutes at 20 A. The released gasses were mixed with a known quantity of ^{3}He spike in preparation for isotope-dilution analysis, after which the mixture was purified of reactive gasses using a combination of hot and cold metal alloy getters. Along with sample unknowns, we also analyzed aliquots of Fish Canyon zircon and Durango fluorapatite to monitor system performance, and empty Nb tubes to allow for blank correction of the resulting data.

After ^{4}He analysis, each sample packet was unloaded from the laser chamber and dissolved for U and Th analysis. Apatites were dissolved using 25 µl of 50% nitric (HNO_3) acid that contains a mixed spike of ~5 ng of ^{230}Th and ~15ng of ^{235}U. In contrast, zircons were digested at elevated temperatures and pressures in Parr vessels using concentrated hydrofluoric (HF), nitric (HNO_3), and hydrochloric (HCl) acids mixed with the U+Th spike. After dissolution, samples, together with specially prepared batches of spiked standard solutions, were analyzed for U and Th using a Thermo Scientific *ICAP-Q* inductively coupled, plasma source mass spectrometer.

The He, U, and Th data were used to calculate raw ages using an iterative approach to the (U-Th)/He age equation. Within this calculation, the concentration of ^{235}U is derived from the measured ^{238}U concentration using the known ratio of these isotopes in nature. The raw ages are then corrected for alpha ejection as described above. All uncertainties for ApHe and ZrnHe dates reflect the full propagation of analytical errors, but no errors were assigned to the alpha ejection correction calculations or propagated into the reported uncertainties.

As is frequently the case for (U-Th)/He data, the dispersion of zircon or apatite dates from a single sample from Khumbu was often greater than would be anticipated from propagated analytical errors alone. The most probable causes of this overdispersion are unquantified, crystal-specific errors in the alpha ejection correction (often due to parent element zoning; Hourigan et al., 2005) or variable amounts of radiation damage that can affect the closure behavior of the zircon or apatite (Flowers et al., 2009; Guenthner et al., 2013). For this study, our approach to handling dispersion was as follows. First, we attempted to identify outliers in the measured zircon or apatite dates for

each sample using the Hampel identifier method (e.g., Pearson, 2011), assuming that any date more than four median average deviations from the median could be reasonably discarded from further analysis. After removing any outliers present, we recalculated the inverse variance-weighted mean of each ensemble of ApHe or ZrnHe dates, as well as: 1) the standard deviation of the weighted mean; 2) the mean squared weighted deviation (MSWD) of the distribution with outliers removed; and 3) the expected ca. 95% confidence range of MSWD for the ensemble based on the number of analyses in the weighted mean (Wendt and Carl, 1991; Mahon, 1996). In cases where the calculated MSWD was within the ca. 95% confidence range of its predicted value of 1.0, we report twice the standard deviation of the inverse-variance weighted mean as a realistic uncertainty for the calculated weighted mean ApHe or ZrnHe date. If the calculated MSWD was higher than this range, then we instead report two standard deviations of the population of dates as a realistic ca. 95% confidence-level estimate of the uncertainty in the inverse-variance weighted mean for that sample.

1-D thermal-kinematic modeling methodology

Our approach to 1D thermal-kinematic modeling and choice of thermal physical properties and boundary conditions follows those used previously in the Everest region and other regions in the Himalaya (e.g., Thiede and Ehlers, 2013; Adams et al., 2015; Schultz et al., 2017). More specifically, we assumed a layer thickness – 30 km; a basal temperature of 650°C; a surface temperature of 5°C; a heat capacity of 800 J $kg^{-1}K^{-1}$; a crustal density of 2750 kg m^3; a thermal conductivity of 2.5 $Wm^{-1}K^{-1}$; and a heat production rate of 2 μWm^{-3}. With these assumptions, we conducted 500,000 forward

models of thermal histories over the past 20 Ma predicted by randomly selected denudation rates between 0.01 and 4.0 mm/a. The ensemble of thermal histories produced by this Monte Carlo scheme were then used to predict MsAr, BtAr, ZrnHe, and ApHe closure ages and these were compared with the actual dates for a sample using the misfit criteria as described in Thiede and Ehlers (2013). A simulation was deemed acceptable if a simulation reproduced all of a sample's closure ages within one standard deviation based on their analytical precisions. The acceptable simulations were then used to calculate ca. 95% confidence ranges for modeled exhumation histories.

The thermo-kinematic modeling began with assuming relatively coarse time intervals of a few million years and we subsequently inserted shorter elements to improve our understanding of how exhumation rates varied with time. Our intention in taking this approach was not to over-interpret the data, for instance small changes in exhumation rate that might actually be aretfacts of the model, but to establish the coarsest set of models that would still illuminate the most important exhumation rate transitions. The modeling results all are based on modeling increments of 3 Ma between 20 and 17 Ma, 1 Ma between 17 and 3 Ma and one increment of 3 Ma from 3 Ma to the present day.

References

Adams, B.A., Hodges, K.V., Whipple, K.X., Ehlers, T.A., van Soest, M.C., and Wartho, J. (2015). Constraints on the tectonic and landscape evolution of the Bhutan Himalaya from thermochronometry, *Tectonics*. *32*(6), 1329-1347.

Farley, K.A., Wolf, R.A., and L.T. Silver, L.T. (1996). The effects of long alpha-stopping distances on (U-Th)/He ages. *Geochimica et Cosmochimica Acta*, *60*, 4223-4229.

Fleck, R. J., Sutter, J.F., and Elliot, D.H. (1977). Interpretation of discordant $^{40}Ar/^{39}Ar$ age spectra of Mesozoic tholeiites from Antarctica. *Geochimica et Cosmochimica Acta*, *41*, 15-32.

Flowers, R.M., Ketcham, R.A., Shuster, D.L., and Farley, K.A. (2009). Apatite (U-Th)/He thermochronometry using a radiation damage accumulation and annealing model. *Geochimica et Cosmochimica Acta*, *73*, 2347-2365.

Grove, M. and Harrison, T.M. (1996). 40Ar* diffusion in Fe-rich biotite. *American Mineralogist, 81,* 940-951.

Guenthner, W.R., Reiners, P.W., Ketcham, R.A., Nasdala, L., and Geister, G. (2013). Helium diffusion in natural zircon: Radiation damage, anisotropy, and the interpretation of zircon (U-Th)/He thermochronology. *American Journal of Science*, *313*, p. 145 – 198.

Hourigan, J.K., Reiners, P.W., and Brandon, M.T. (2005). U-Th zonation dependent alpha-ejection in (U-Th)/He chronometry. *Geochimica et Cosmochimica Acta, 69*, 3349-3365.

Hubbard, M., and Harrison, T.M. (1989). $^{40}Ar/^{39}Ar$ age constraints on deformation and metamorphism in the Main Central Thrust zone and Tibetan Slab, eastern Nepal Himalaya. *Tectonics*, *8*(4), 865 – 880.

Mahon, K. I. (1996). The new "York" regression: Application of an improved statistical method to geochemistry. *International Geology Review*, *38*, 293-303.

Pearson, R.K. (2011). *Exploring data in engineering, the sciences, and medicine*, Oxford University Press.

Schultz, M.H., Hodges, K.V., Ehlers, T.A., van Soest, M.C., and Wartho, J-A. (2017). Thermochronologic constraints on the Miocene slip history of the South Tibetan detachment system, south-central Tibet. *Earth and Planetary Science Letters*, *459*, 105-117.

Schwarz, W.H., and Trielhoff, M. (2007). Intercalibration of ^{40}Ar-^{39}Ar age standards NL-25, HB3gr hornblende, GA1550, SB-3, HD-B1 biotite and BMus/2 muscovite, *Chemical Geology*, *242*, 218 – 231.

Steiger, R. H., and E. Jäger (1977). Subcommission on geochronology: convention on the use of decay constants in geo- and cosmochronology. *Earth and Planetary Science Letters*, *36*, 359-362.

Stübner, K., Warren, C., Ratschbacher, L., Sperner, B., Kleeberg, R., Pfänder, J., and Grujic, D. (2017). Anomalously old biotite 40Ar/39Ar ages in the NW Himalaya. *Lithosphere,* doi: https://doi.org/10.1130/L586.1.

Thiede, R.C., and Ehlers, T.A. (2013). Large Spatial and Temporal Variations in Himalayan Denudation. *Earth and Planetary Science Letters*, 371-372, 278-293.

Turrin, B.D., Swisher III, C.C., and Deino, A. (2010). Mass discrimiation monitoring and intercalibration of dual collectors in noble gas mass spectrometer systems. *Geochemistry, Geophysics, Geosystems*, *11*, doi:10.1029/2009GC003013.

Wendt, I., and Carl, C. (1991). The statistical distribution of the mean squared weighted deviation. *Chemical Geology: Isotope Geoscience setion*, *86*, 275 – 285.

APPENDIX TABLE C1: $^{40}AR/^{39}AR$ THERMOCHRONOLOGY

Sample: K01 | Lab: Group 18 Laboratories | *J*: 8.97E-05±1.22E-06
Material: Biotite

																			Blank Corrections										
N	Power (W)	^{40}Ar (cps)	±σ (cps)	^{39}Ar (cps)	±σ (cps)	^{38}Ar (cps)	±σ (cps)	^{37}Ar (cps)	±σ (cps)	^{36}Ar (cps)	±σ (cps)	D'	$\%^{40}Ar^*$	$^{40}Ar^*/^{39}Ar_K$	±σ	Age (Ma)	±2σ (Ma)	±2σ (-J) (Ma)	Ca/K	±σ	Blank Type[2]	^{41}Ar (cps)	±σ (cps)	^{39}Ar (cps)	±σ (cps)	^{38}Ar (cps)	±σ (cps)	^{37}Ar (cps)	±σ (cps)	^{36}Ar (cps)	±σ (cps)
A	0.5	152203	410	992.8	5.4	51.8	2.4	34.4	22.7	241.2	2.9	0.9980	53.18	81.5	1.1	13.15	0.51	0.37	0.00426	0.005133	LR	13249	390	227.5	1.9	17.1	1.7	259.0	2.6	62.2	1.5
B	0.9	52071	210	167.2	3.8	9.6	2.0	45.0	19.5	18.3	2.3	0.9980	89.61	79.9	1.4	12.88	0.57	0.45	0.137651	0.060021	LR	11873	140	226.8	1.8	16.5	1.4	258.9	2.3	63.5	1.4
C	1.1	38292	200	2127.9	6.6	4.1	1.9	-1.6	20.4	5.7	2.2	0.9980	95.58	79.2	1.7	12.78	0.65	0.55	-0.0066	0.079404	LR	12193	130	226.1	1.8	15.9	1.2	258.8	2.2	64.8	1.3
D	1.3	529547	260	2470.7	6.7	94.2	2.6	13.8	18.6	75.6	2.6	0.9980	95.78	80.83	0.21	13.03	0.36	0.07	0.003526	0.005333	LR	12512	140	225.3	2.0	15.3	1.1	258.6	2.4	66.2	1.5
E	1.5	180488	220	4833	10	28.7	2.2	12.5	21.6	6.3	2.5	0.9980	98.96	79.89	0.43	12.88	0.38	0.14	0.009625	0.017389	LR	12832	160	224.6	2.3	14.7	1.1	258.5	2.7	67.5	1.7
F	1.7	44318	220	4066.3	9.1	7.0	1.8	41.9	19.6	-3.3	2.5	0.9980	102.18	76.7	1.5	12.38	0.58	0.47	0.126835	0.059687	LR	13045	160	227.4	2.3	14.6	1.1	260.9	2.7	68.5	1.7
G	1.9	26493	210	1458.5	6.6	5.0	1.7	3.7	20.7	-3.9	2.3	0.9980	104.38	75.6	2.2	12.19	0.79	0.72	0.017671	0.101733	LR	12948	140	230.7	2.0	15.01	0.95	263.2	2.4	68.2	1.5
H	2.3	118729	200	1152.8	5.8	18.0	1.9	-20.5	21.2	8.9	2.4	0.9980	97.79	79.85	0.66	12.88	0.41	0.21	-0.02563	0.026297	LR	12851	140	234.0	1.9	15.42	0.88	265.6	2.3	67.8	1.4
I	3	200859	220	1657.3	6.6	34.1	1.8	-4.8	19.4	18.5	2.4	0.9980	97.27	79.08	0.40	12.75	0.37	0.13	-0.00389	0.014171	LR	12754	150	237.2	2.1	15.83	0.91	267.9	2.5	67.5	1.4
J	6	604494	340	2528.2	7.3	97.5	2.2	5.7	21.8	37.7	2.7	0.9980	98.16	80.48	0.20	12.98	0.36	0.06	0.000973	0.005327	LR	12658	170	240.5	2.4	16.2	1.0	270.2	2.8	67.2	1.6
K	6	16032	210	1913.1	7.5	-1.2	2.1	-28.5	22.9	0.1	2.4	0.9980	99.80	67.7	3.4	10.92	1.13	1.09	-0.21602	0.174509	LR	13250	130	259.0	1.8	18.08	0.96	286.7	2.2	73.5	1.4

Plateau Age (Steps E - I): 12.80 ± 0.19 Ma

Total Fusion Age 12.99 ± 0.36 Ma

Sample: K02 | Lab: Group 18 Laboratories | *J*: 9.03E-05 ± 1.86E-07
Material: Biotite

																			Blank Corrections										
N	Power (W)	^{40}Ar (cps)	±σ (cps)	^{39}Ar (cps)	±σ (cps)	^{38}Ar (cps)	±σ (cps)	^{37}Ar (cps)	±σ (cps)	^{36}Ar (cps)	±σ (cps)	D'	$\%^{40}Ar^*$	$^{40}Ar^*/^{39}Ar_K$	±σ	Age (Ma)	±2σ (Ma)	±2σ (-J) (Ma)	Ca/K	±σ	Blank Type[2]	^{41}Ar (cps)	±σ (cps)	^{39}Ar (cps)	±σ (cps)	^{38}Ar (cps)	±σ (cps)	^{37}Ar (cps)	±σ (cps)	^{36}Ar (cps)	±σ (cps)
A	0.8	48896	1000	646.5	5.5	60.2	2.4	57	26	288.9	3.3	0.9973	36.42	75.6	1.7	12.28	0.56	0.56	0.158447	0.071	LR	13408	160	357.9	2.5	20.3	1.3	353.0	3.6	88.0	1.6
B	0.9	29915	850	418.0	4.8	18.3	1.9	2	21	78.2	2.7	0.9973	56.42	71.6	2.2	11.62	0.71	0.71	0.010146	0.090	LR	13511	140	355.7	2.3	20.1	1.1	353.2	3.1	88.3	1.4
C	1.1	26882	760	340.8	4.7	13.0	1.8	-24	24	30.1	2.4	0.9973	75.13	78.9	2.5	12.80	0.81	0.81	-0.13	0.13	LR	13613	140	353.5	2.3	19.95	0.99	353.3	2.8	88.7	1.3
D	1.3	849645	1300	9306	14	178.5	3.0	-44	27	344.1	3.1	0.9973	89.31	91.31	0.20	14.813	0.088	0.064	-0.0089	0.0052	LR	15520	360	351.3	2.5	19.8	1.0	353.5	2.9	89.1	1.4
E	1.5	196687	820	2431.2	8.6	32.2	2.3	8	26	13.9	2.5	0.9973	97.95	80.90	0.44	13.13	0.15	0.14	0.005578	0.019	LR	13819	170	349.1	3.0	19.6	1.1	353.7	3.2	89.5	1.6
F	1.7	95999	810	1208.2	7.3	23.8	1.9	18	26	30.7	2.5	0.9973	91.38	79.46	0.82	12.90	0.27	0.27	0.026228	0.039	LR	14155	170	364.8	2.9	20.0	1.1	356.8	3.1	91.8	1.6
G	1.9	56094	760	682.4	5.9	10.3	1.8	33	25	-4.4	2.4	0.9973	102.40	82.2	1.3	13.34	0.43	0.43	0.085425	0.065	LR	14368	150	381.1	2.5	20.41	0.98	359.4	2.7	93.6	1.4
H	2.3	302983	840	3663	10	55.8	2.3	-22	24	45.1	2.6	0.9973	95.78	82.71	0.32	13.42	0.12	0.10	-0.01122	0.012	LR	14581	140	397.4	2.3	20.85	0.96	362.0	2.6	95.4	1.4
I	3	429025	840	5262	11	77.8	2.6	19	25	76.9	2.6	0.9973	94.97	81.53	0.24	13.234	0.094	0.077	0.005995	0.009	LR	14795	150	413.7	2.4	21.3	1.0	364.6	2.8	97.2	1.5
J	6	795539	1200	9753	16	133.6	3.1	-22	25	63.7	2.8	0.9973	97.69	81.57	0.19	13.240	0.081	0.060	-0.0044	0.0047	LR	16585	410	430.0	2.7	21.7	1.2	367.3	3.2	99.0	1.7
K	6	17279	830	208.1	4.5	5.4	2.0	-14	26	0.0	2.6	0.9973	100.04	83.0	4.4	13.5	1.4	1.4	-0.12	0.23	LR	14993	140	445.4	2.3	25.1	1.2	380.8	2.8	102.7	1.4

Total Fusion A: 13.813 ± 0.089 Ma

Sample:K03 Lab: Group 18 Laboratories *J*: 3.28E-04 ↑ 1.54E-06

Material: Biotite

																			Blank Corrections										
N	Power (W)	^{40}Ar (cps)	±σ (cps)	^{39}Ar (cps)	±σ (cps)	^{38}Ar (cps)	±σ (cps)	^{37}Ar (cps)	±σ (cps)	^{36}Ar (cps)	±σ (cps)	D'	%^{40}Ar*	^{40}Ar*/^{39}Ar$_K$	±σ	Age (Ma)	±2σ (Ma)	±2σ (-J) (Ma)	Ca/K	±σ	Blank Type[2]	^{41}Ar (cps)	±σ (cps)	^{39}Ar (cps)	±σ (cps)	^{38}Ar (cps)	±σ (cps)	^{37}Ar (cps)	±σ (cps)	^{36}Ar (cps)	±σ (cps)
A	5	329028	800	14149	17	217.8	1.8	60	170	240.8	2.4	0.9794	82.22	23.254	0.064	13.71	0.15	0.075	0.007223	0.01243	LR	11619	55	27.96	0.78	8.78	0.40	140.4	2.9	41.2	1.1
B	5.4	351383	670	15997	22	222.2	2.0	329	150	123.2	1.9	0.9794	90.61	21.966	0.051	12.96	0.14	0.061	0.036513	0.012195	LR	18235	39	31.76	0.82	12.71	0.36	137.5	2.0	61.40	0.82
C	5.5	344304	540	16055	22	199.0	1.9	362	140	44.4	1.5	0.9794	96.33	21.446	0.045	12.65	0.13	0.053	0.040047	0.016591	LR	17893	42	35.78	0.83	12.67	0.33	134.8	2.1	59.03	0.83
D	5.7	193428	460	9277	15	117.8	1.5	343	150	26.9	1.5	0.9794	96.05	20.849	0.060	12.30	0.14	0.071	0.065877	0.030308	LR	17321	43	39.30	0.85	12.28	0.34	134.2	2.2	56.41	0.86
E	5.9	174902	470	8288	14	108.3	1.5	194	140	23.3	1.5	0.9794	96.21	21.104	0.067	12.45	0.14	0.079	0.041599	0.033022	LR	17063	38	39.26	0.74	11.94	0.32	136.0	2.0	55.91	0.78
F	6.2	176509	460	8270	13	103.5	1.5	129	150	19.8	1.5	0.9794	96.79	21.343	0.065	12.59	0.14	0.076	0.027466	0.035031	LR	16814	42	39.23	0.80	11.61	0.38	137.8	2.3	55.42	0.88
G	7.75	510077	630	23074	22	295.3	2.1	407	160	47.8	1.6	0.9794	97.31	22.106	0.034	13.04	0.13	0.040	0.031207	0.012869	LR	17993	38	52.06	0.75	13.22	0.37	138.0	2.2	59.19	0.83
H	9	498678	640	22329	24	284.2	2.4	590	140	51.5	1.6	0.9794	97.04	22.333	0.037	13.17	0.13	0.044	0.046982	0.012049	LR	17905	38	66.95	0.86	13.19	0.36	139.0	2.2	58.20	0.88
I	9.1	153073	450	6905	12	84.7	1.3	334	150	11.8	1.5	0.9794	97.78	22.168	0.076	13.07	0.15	0.089	0.08616	0.040674	LR	17302	38	69.82	0.87	12.51	0.35	142.3	2.1	56.43	0.87
J	9.3	85973	440	3881.0	8.7	50.2	1.2	16	130	6.9	1.5	0.9794	97.70	22.15	0.12	13.07	0.19	0.15	0.007033	0.06583	LR	16806	40	58.38	0.84	11.89	0.36	144.4	1.9	55.66	0.84
K	15	142434	560	6211	12	115.7	1.6	14	130	212.2	1.8	0.9794	69.43	22.93	0.10	13.52	0.17	0.12	0.003592	0.026855	LR	16503	42	52.27	0.84	11.61	0.36	147.5	1.9	56.84	0.82
L	50	1321	760	126.4	2.7	79.3	1.4	175	150	413.6	2.4	0.9794	1.07	10.5	6.0	6.2	7.1	7.1	2.483327	1.485825	LR	16695	43	57.60	0.88	11.96	0.37	148.5	2.1	58.82	0.82

Total Fusion A: 13.00 ± 0.13 Ma

Sample:K04 Lab: Group 18 Laboratories *J*: 3.37E-04 ↑ 1.06E-06

Material:Biotite

																			Blank Corrections										
N	Power (W)	^{40}Ar (cps)	±σ (cps)	^{39}Ar (cps)	±σ (cps)	^{38}Ar (cps)	±σ (cps)	^{37}Ar (cps)	±σ (cps)	^{36}Ar (cps)	±σ (cps)	D'	%^{40}Ar*	^{40}Ar*/^{39}Ar$_K$	±σ	Age (Ma)	±2σ (Ma)	±2σ (-J) (Ma)	Ca/K	±σ	Blank Type[2]	^{41}Ar (cps)	±σ (cps)	^{39}Ar (cps)	±σ (cps)	^{38}Ar (cps)	±σ (cps)	^{37}Ar (cps)	±σ (cps)	^{36}Ar (cps)	±σ (cps)
A	4	648726	900	23214	23	329.5	2.5	1293	200	270.1	2.2	0.9849	89.05	27.946	0.047	16.92	0.12	0.057	0.099	0.010	LR	17291	35	68.46	0.91	12.95	0.36	116.3	2.0	65.13	0.83
B	4.8	248750	480	8785	14	109.6	1.3	340	180	6.5	1.5	0.9849	99.24	28.316	0.071	17.15	0.14	0.085	0.069	0.024	LR	16942	36	74.5	1.1	12.57	0.35	117.3	1.9	63.90	0.82
C	5.4	688234	820	24663	25	313.5	2.5	288	180	90.9	1.7	0.9849	96.24	27.905	0.044	16.90	0.12	0.053	0.021	0.014	LR	16380	36	82.8	1.2	11.86	0.35	117.0	1.9	61.50	0.82
D	5.5	316722	520	11431	15	149.7	1.5	461	180	48.0	1.5	0.9849	95.71	27.707	0.059	16.78	0.13	0.071	0.072	0.030	LR	16170	38	85.2	1.1	11.55	0.36	115.7	1.9	60.33	0.82
E	5.7	235493	480	8505	14	111.9	1.4	140	180	34.2	1.5	0.9849	95.89	27.688	0.072	16.77	0.14	0.087	0.029	0.040	LR	15815	41	88.8	1.2	11.57	0.39	117.4	2.0	58.73	0.86
F	5.9	205640	480	7480	13	98.4	1.4	82	180	33.2	1.5	0.9849	95.45	27.492	0.080	16.65	0.14	0.096	0.019	0.046	LR	15675	36	90.1	1.1	11.89	0.35	120.3	1.8	58.30	0.74
G	6.2	198304	480	7194	12	89.4	1.5	-242	190	32.3	1.5	0.9849	95.40	27.563	0.081	16.69	0.14	0.098	-0.061	0.049	LR	15534	39	91.3	1.2	12.22	0.40	123.2	2.0	57.88	0.80
H	7.75	514477	670	18550	22	234.1	2.0	227	190	59.9	1.7	0.9849	96.67	27.734	0.049	16.80	0.12	0.059	0.022	0.019	LR	17441	35	98.3	1.1	13.98	0.38	123.5	1.9	66.16	0.88
I	9	349055	540	12603	17	161.9	1.8	343	200	39.9	1.5	0.9849	96.73	27.697	0.057	16.77	0.13	0.069	0.048	0.029	LR	16934	38	101.6	1.1	13.69	0.37	121.2	2.1	64.91	0.84
J	9.1	86931	440	3145	9	39.6	1.1	516	200	11.2	1.5	0.9849	96.35	27.64	0.16	16.74	0.22	0.19	0.29	0.12	LR	16364	38	109.8	1.1	13.22	0.36	120.4	2.1	63.30	0.82
K	9.3	51238	440	1823	6	23.39	0.91	-62	190	3.3	1.5	0.9849	98.12	28.11	0.26	17.02	0.33	0.31	-0.06	0.20	LR	16302	36	114.7	1.1	13.04	0.36	121.8	2.0	62.93	0.82
L	15	487459	630	17535	20	220.8	1.9	350	190	45.4	1.5	0.9849	97.32	27.800	0.048	16.83	0.12	0.058	0.035	0.021	LR	16322	36	116.4	1.1	13.36	0.36	123.1	2.0	62.70	0.84
M	50	14135	1900	912	6	412.1	2.6	957	200	2128.3	5.0	0.9849	2.20	15.5	2.1	9.4	2.6	2.6	1.88	0.41	LR	16403	40	113.4	1.1	13.86	0.36	123.0	2.0	62.83	0.88

Total Fusion A: 16.85 ± 0.12 Ma

Sample:K07 Lab: Group 18 Laboratories *J*: 3.33E-04 ! 1.082E-06

Material: Biotite

																			Blank Corrections										
N	Power (W)	^{40}Ar (cps)	±σ (cps)	^{39}Ar (cps)	±σ (cps)	^{38}Ar (cps)	±σ (cps)	^{37}Ar (cps)	±σ (cps)	^{36}Ar (cps)	±σ (cps)	*D*[1]	%^{40}Ar*	^{40}Ar*/^{39}Ar$_K$	±σ	Age (Ma)	±2σ (Ma)	±2σ (-J) (Ma)	Ca/K	±σ	Blank Type[2]	^{41}Ar (cps)	±σ (cps)	^{39}Ar (cps)	±σ (cps)	^{38}Ar (cps)	±σ (cps)	^{37}Ar (cps)	±σ (cps)	^{36}Ar (cps)	±σ (cps)
A	5	817617	4400	29010	40	443.9	2.9	892	160	475.9	2.9	0.9795	85.32	28.18	0.16	16.83	0.21	0.19	0.055	0.007	LR	18791	1400	55.31	0.87	14.61	0.37	154.2	2.2	71.62	0.78
B	5.2	142302	430	5111	10	59.3	1.2	274	180	-26.2	1.4	0.9795	105.74	27.84	0.10	16.63	0.16	0.12	0.096	0.042	LR	23924	43	68.3	1.0	16.65	0.40	155.7	2.5	81.47	0.87
C	5.4	459083	620	16611	25	209.0	1.9	496	180	36.0	1.7	0.9795	97.73	27.637	0.056	16.50	0.13	0.067	0.053	0.020	LR	23464	44	84.7	1.0	16.79	0.40	157.5	2.5	81.15	0.88
D	5.5	287669	510	10431	16	130.9	1.6	549	160	14.9	1.5	0.9795	98.49	27.578	0.065	16.47	0.13	0.077	0.094	0.030	LR	20193	42	89.1	1.0	15.05	0.37	157.9	2.3	71.80	0.84
E	5.7	259043	500	9349	15	116.6	1.5	590	160	18.2	1.6	0.9795	97.96	27.707	0.070	16.55	0.14	0.083	0.113	0.033	LR	16608	44	93.2	1.1	12.93	0.38	159.1	2.3	61.24	0.87
F	5.9	217846	440	7927	13	101.2	1.3	368	150	18.7	1.3	0.9795	97.52	27.483	0.071	16.41	0.14	0.085	0.083	0.036	LR	16302	41	92.9	1.0	12.55	0.34	159.8	2.0	60.04	0.78
G	6.2	228399	470	8284	13	105.0	1.4	347	160	12.1	1.5	0.9795	98.46	27.570	0.072	16.46	0.14	0.085	0.075	0.036	LR	16010	47	92.7	1.1	12.19	0.37	160.6	2.2	58.89	0.87
H	7.75	545272	660	19852	21	245.0	2.0	71	150	42.2	1.6	0.9795	97.76	27.467	0.044	16.40	0.12	0.053	0.006	0.015	LR	17355	41	86.6	1.0	12.68	0.35	164.5	2.1	62.61	0.83
I	9	423022	540	15324	20	194.5	1.6	45	160	28.1	1.4	0.9795	98.08	27.606	0.051	16.48	0.12	0.060	0.005	0.020	LR	16999	39	90.1	1.1	12.51	0.35	166.8	2.2	61.20	0.88
J	9.1	129118	430	4693	10	58.7	1.2	274	150	5.9	1.4	0.9795	98.66	27.52	0.11	16.43	0.17	0.13	0.104	0.061	LR	16324	38	91.4	1.1	12.43	0.35	165.7	2.2	58.87	0.89
K	9.3	71637	450	2602.0	7.5	33.6	1.1	263	150	4.3	1.5	0.9795	98.27	27.53	0.19	16.44	0.25	0.23	0.18	0.11	LR	16014	38	89.4	1.1	12.52	0.37	162.5	2.1	57.97	0.90
L	15	109211	590	4025.4	8.8	75.1	1.4	183	150	152.0	1.9	0.9795	70.86	27.13	0.16	16.20	0.21	0.19	0.081	0.048	LR	15992	40	96.6	1.1	12.90	0.38	161.9	2.1	59.51	0.90
M	50	*-2134*	*850*	*45.1*	*2.5*	*104.0*	*1.4*	*442*	*160*	*564.3*	*2.7*	*0.9795*	-	-	-	-	-	-	-	-	LR	16286	44	105.9	1.3	13.19	0.37	164.5	2.0	62.00	0.89

Plateau Age (Steps C - J): 16.461 ± 0.059 Ma

Total Fusion A: 16.47 ± 0.13 Ma

Sample: K07 Lab: Group 18 Laboratories *J*: 3.34E-04 ! 1.13E-06

Material: White mica

																			Blank Corrections										
N	Power (W)	^{40}Ar (cps)	±σ (cps)	^{39}Ar (cps)	±σ (cps)	^{38}Ar (cps)	±σ (cps)	^{37}Ar (cps)	±σ (cps)	^{36}Ar (cps)	±σ (cps)	*D*[1]	%^{40}Ar*	^{40}Ar*/^{39}Ar$_K$	±σ	Age (Ma)	±2σ (Ma)	±2σ (-J) (Ma)	Ca/K	±σ	Blank Type[2]	^{41}Ar (cps)	±σ (cps)	^{39}Ar (cps)	±σ (cps)	^{38}Ar (cps)	±σ (cps)	^{37}Ar (cps)	±σ (cps)	^{36}Ar (cps)	±σ (cps)
A	4	10525	610	378.7	3.5	36.7	1.0	565	160	166.8	2.0	0.9805	17.60	27.8	1.6	16.7	2.0	1.9	2.68	0.81	LR	17112	40	95.6	1.0	13.40	0.39	167.8	2.2	63.55	0.93
B	4.8	39592	580	1415.9	5.8	43.04	0.98	154	150	134.6	1.9	0.9805	49.88	27.96	0.42	16.75	0.51	0.50	0.19	0.21	LR	16663	39	93.2	1.1	13.05	0.39	168.0	2.0	61.49	0.85
C	5.4	76144	630	2769.3	7.3	73.3	1.3	65	150	227.8	2.1	0.9805	53.08	27.50	0.24	16.47	0.31	0.29	0.04	0.10	LR	16051	38	90.4	1.1	12.50	0.37	166.4	2.0	59.12	0.82
D	5.5	52399	440	1927.3	6.4	32.1	1.1	78	160	46.2	1.5	0.9805	79.32	27.19	0.24	16.29	0.31	0.29	0.07	0.16	LR	15894	38	90.1	1.1	12.30	0.35	164.6	2.3	58.81	0.82
E	5.7	76183	640	2741.9	7.2	81.2	1.3	245	170	261.5	2.1	0.9805	49.64	27.78	0.24	16.64	0.31	0.29	0.16	0.12	LR	15605	40	90.1	1.1	12.35	0.36	163.1	2.5	58.04	0.86
F	5.9	128140	520	4674.9	9.6	81.9	1.2	439	160	138.1	1.7	0.9805	75.85	27.41	0.12	16.42	0.18	0.15	0.168	0.065	LR	15481	35	90.4	1.0	12.59	0.34	163.3	2.3	57.60	0.74
G	6.2	200650	680	7336	12	135.7	1.6	62	180	250.6	2.2	0.9805	73.04	27.35	0.10	16.39	0.16	0.12	0.015	0.045	LR	15356	37	90.7	1.2	12.83	0.40	163.6	2.5	57.16	0.80
H	7.75	114648	560	4164.2	9.9	71.8	1.4	239	160	128.1	1.8	0.9805	75.18	27.53	0.15	16.49	0.21	0.18	0.103	0.048	LR	16731	39	86.9	1.1	12.85	0.40	164.8	2.1	62.46	0.91
I	9	109714	490	4008.6	9.1	58.8	1.2	-14	170	55.4	1.6	0.9805	87.01	27.37	0.14	16.40	0.20	0.16	-0.007	0.055	LR	16261	37	91.8	1.1	12.62	0.38	163.8	2.2	61.22	0.95
J	9.1	440205	690	16106	21	221.0	2.0	151	160	143.0	1.9	0.9805	91.24	27.331	0.056	16.37	0.13	0.067	0.016	0.019	LR	15589	37	101.9	1.1	12.44	0.37	165.0	2.2	59.22	0.95
K	9.3	224302	560	8209	13	113.9	1.5	438	160	87.8	1.8	0.9805	89.64	27.324	0.080	16.37	0.15	0.10	0.095	0.038	LR	15392	38	107.0	1.2	12.50	0.38	167.3	2.3	58.46	0.91
L	15	391038	660	14227	20	193.8	1.8	314	170	107.3	1.9	0.9805	92.50	27.486	0.060	16.47	0.13	0.072	0.039	0.014	LR	15264	39	128.0	1.2	13.08	0.38	169.0	2.3	59.57	0.90
M	50	206054	550	7580	14	115.2	1.5	446	170	101.1	1.8	0.9805	87.34	27.183	0.088	16.28	0.15	0.11	0.105	0.044	LR	15336	42	144.6	1.3	13.62	0.38	168.5	2.4	61.54	0.90

Plateau Age (Steps A - L): 16.413 ± 0.074 Ma

Total Fusion A: 17.73 ± 0.15 Ma

Sample: K08 Lab: Group 18 Laboratories *J*: 8.82E-05 ! 1.44E-06

Material: Biotite

																		Blank Corrections										
N	Power	^{40}Ar	±σ	^{39}Ar	±σ	^{38}Ar	±σ	^{37}Ar	±σ	^{36}Ar	±σ	*D'*:	%^{40}Ar*	^{40}Ar*/^{39}Ar$_K$	±σ	Age	±2σ	±2σ (-J)	Ca/K	±σ	Blank	^{41}Ar	±σ	^{39}Ar	±σ	^{38}Ar	±σ	^{37}Ar	±σ	^{36}Ar	±σ
	(W)	(cps)	(cps)	(cps)	(cps)	(cps)	(cps)	(cps)	(cps)	(cps)	(cps)					(Ma)	(Ma)	(Ma)			Type[2]	(cps)	(cps)	(cps)	(cps)	(cps)	(cps)	(cps)	(cps)	(cps)	(cps)
A	0.8	95335	1200	989.9	6.1	104.0	2.5	2	19	470.0	3.9	0.9970	40.71	96.3	1.4	15.26	0.66	0.43	0.003	0.034	LR	12175	150	218.7	2.0	13.00	0.85	253.6	2.9	61.8	1.7
B	0.9	91336	860	867.8	5.2	36.7	1.7	16	19	121.0	2.7	0.9970	71.87	105.3	1.2	16.67	0.66	0.37	0.033	0.039	LR	12398	140	221.4	1.8	13.58	0.79	254.2	2.6	63.1	1.5
C	1.1	76576	800	733.3	4.8	22.2	1.7	-3	19	79.7	2.5	0.9970	76.48	104.4	1.3	16.54	0.67	0.40	-0.007	0.047	LR	12621	140	224.1	1.7	14.15	0.82	254.8	2.4	64.3	1.4
D	1.3	1142021*	1400*	10507	17	174.2	3.3	-31	21	239.1	3.0	0.9970	94.17	108.70	0.22	17.21	0.56	0.070	-0.0057	0.0035	LR	13299*	350*	226.8	1.9	14.73	0.93	255.4	2.5	65.5	1.4
E	1.5	336622	880	3172.0	8.2	43.6	2.4	37	23	29.8	2.6	0.9970	97.45	106.12	0.39	16.81	0.56	0.12	0.021	0.013	LR	13069	170	229.6	2.1	15.3	1.1	256.0	2.8	66.7	1.6
F	1.7	152855	800	1450.2	6.5	16.5	1.8	48	21	5.7	2.5	0.9970	98.91	105.40	0.72	16.69	0.59	0.23	0.059	0.026	LR	13614	170	251.3	2.1	17.2	1.1	267.9	2.8	71.4	1.6
G	1.9	103839	790	993.6	5.9	12.7	1.8	6	22	7.6	2.5	0.9970	97.87	104.5	1.0	16.55	0.63	0.32	0.010	0.040	LR	13906	150	268.7	1.9	18.41	0.96	278.2	2.4	74.5	1.4
H	2.3	637119	920	5868	11	80.7	2.7	19	23	57.3	2.5	0.9970	97.41	108.58	0.26	17.20	0.56	0.082	0.0054	0.0072	LR	14199	140	286.0	1.9	19.61	0.92	288.5	2.3	77.6	1.4
I	3	808155	1300	7388	14	97.6	2.3	-10	22	45.2	2.4	0.9970	98.37	109.38	0.27	17.32	0.57	0.085	-0.0029	0.0054	LR	16125	350	303.4	2.1	20.81	0.97	298.8	2.3	80.8	1.5
J	6	668497	930	6215	12	74.6	2.4	30	22	39.4	2.7	0.9970	98.29	107.55	0.26	17.03	0.56	0.082	0.0081	0.0063	LR	14786	180	320.8	2.5	22.0	1.1	309.1	2.6	83.9	1.7
K	6	6370	770	115.2	3.7	0.9	1.7	13	24	1.9	2.4	0.9970	92.01	55.3	6.9	8.8	2.2	2.2	0.20	0.38	LR	14956	140	335.1	2.1	22.13	0.92	328.8	2.6	88.8	1.5

Total Fusion A: 17.18 ± 0.56 Ma

Sample: K08 Lab: Group 18 Laboratories *J*: 8.95E-05 ! 7.70E-07

Material: White mica

																		Blank Corrections										
N	Power	^{40}Ar	±σ	^{39}Ar	±σ	^{38}Ar	±σ	^{37}Ar	±σ	^{36}Ar	±σ	*D'*:	%^{40}Ar*	^{40}Ar*/^{39}Ar$_K$	±σ	Age	±2σ	±2σ (-J)	Ca/K	±σ	Blank	^{41}Ar	±σ	^{39}Ar	±σ	^{38}Ar	±σ	^{37}Ar	±σ	^{36}Ar	±σ
	(W)	(cps)	(cps)	(cps)	(cps)	(cps)	(cps)	(cps)	(cps)	(cps)	(cps)					(Ma)	(Ma)	(Ma)			Type[2]	(cps)	(cps)	(cps)	(cps)	(cps)	(cps)	(cps)	(cps)	(cps)	(cps)
A	0.5	211821	1300	1976.4	7.2	185.0	3.1	3	19	853.3	4.0	0.9978	45.66	107.17	0.78	17.22	0.39	0.25	0.001933	0.018	LR	10019	140	188.0	1.9	10.3	1.1	226.3	2.5	47.8	1.5
B	0.9	153746	870	1500.7	6.3	56.0	2.0	12	18	214.9	2.7	0.9978	70.77	102.45	0.72	16.47	0.36	0.23	0.014353	0.022	LR	10155	130	191.6	1.7	10.19	0.95	225.9	2.2	49.3	1.3
C	1.1	75188	730	725.8	5.5	22.7	1.8	-9	20	56.4	2.3	0.9978	81.86	103.6	1.3	16.65	0.50	0.41	-0.02164	0.049	LR	10291	130	195.2	1.7	10.05	0.88	225.5	2.1	50.8	1.3
D	1.3	52847	840	505.0	4.6	17.0	1.7	-37	17	39.0	2.3	0.9978	82.11	104.6	1.9	16.82	0.68	0.62	-0.0066	0.0038	LR	11831	310	198.9	1.9	9.91	0.91	225.1	2.2	52.3	1.3
E	1.5	1021615*	2200*	9602	15	366.7	3.6	-33	20	1271.6	4.6	0.9978	73.11	106.40	0.28	17.10	0.31	0.091	-0.03322	0.013	LR	12255*	340*	202.5	2.2	9.8	1.0	224.6	2.5	53.9	1.5
F	1.7	252087	900	2436.5	8.1	55.2	2.2	-45	18	123.7	2.8	0.9978	87.34	103.46	0.50	16.63	0.33	0.16	-0.06005	0.049	LR	11016	170	208.4	2.2	10.9	1.0	230.0	2.5	57.7	1.5
G	1.9	69998	700	678.1	5.3	10.5	1.7	-23	18	3.8	2.2	0.9978	98.40	103.2	1.3	16.59	0.51	0.42	0.011904	0.023	LR	11307	150	210.5	1.9	12.12	0.91	235.4	2.2	59.8	1.3
H	2.3	513127	900	4895	10	80.5	2.5	-15	18	103.2	2.5	0.9978	94.39	104.83	0.29	16.85	0.30	0.091	0.19	0.18	LR	12813	290	212.6	1.8	13.30	0.89	240.6	2.2	61.9	1.3
I	3	175661	760	1691.6	7.0	20.2	1.8	12	22	5.0	2.3	0.9978	99.17	103.84	0.62	16.69	0.35	0.20	0.011904	0.023	LR	11885	140	214.7	1.8	14.49	0.96	245.9	2.5	64.0	1.3
J	4.5	21289	780	214.4	3.8	-1.6	1.6	24	21	-3.2	2.4	0.9978	104.63	99.3	4.1	16.0	1.3	1.3	0.04	0.18	LR	12174	160	216.7	2.1	15.7	1.1	251.2	2.9	66.1	1.5

Plateau Age (Steps A - D; F - J): 16.77 ± 0.16 Ma

Total Fusion A: 16.98 ± 0.31 Ma

Standard: HD-1 Age: 24.18 ± 0.09 Ma Swartz and Trieloff (2007)

Explanations

Blank Type: LR = linear regression versus time

*: Analyzed on the Faraday

Negative values indicate that analysis is indistinguishable from the background

Constants used

Atmospheric argon ratios

(^{40}Ar/^{36}Ar)$_A$	295.5 ± 0.5	Nier (1950)
(^{40}Ar/^{38}Ar)$_A$	1575 ± 2	Nier (1950)

Interfering isotope production ratios

(^{40}Ar/^{39}Ar)$_K$	0.00073	0.00009
(^{38}Ar/^{39}Ar)$_K$	0.01215	0.00003
(^{37}Ar/^{39}Ar)$_K$	0.000224	0.000016
(^{39}Ar/^{37}Ar)$_{Ca}$	0.000695	9.00E-06
(^{38}Ar/^{37}Ar)$_{Ca}$	0.0000196	8.00E-07
(^{36}Ar/^{37}Ar)$_{Ca}$	0.000265	2.20E-06
(^{36}Cl/^{38}Cl)$_{Cl}$	263	2

Decay constants

^{40}K λ_e	(5.81E-11 ± 0.00)E-11 a^{-1}	Steiger and Jäger (1977)
^{40}K λ_β	(4.962E-10 ± 0.00)E-10 a^{-1}	Steiger and Jäger (1977)
^{39}Ar	(2.58 ± 0.03)E-03 a^{-1}	Stoenner et al. (1965)
^{37}Ar	(0.019725 ± 0.00) a^{-1}	Stoenner et al. (1965)
^{36}Cl	(2.35 ± 0.02)E-06 a^{-1}	Endt (1998)

APPENDIX TABLE C2: KHUMBU HIMAL INDIVIDUAL ZIRCON (U-TH)/HE RESULTS

Sample#	Elevation (m)	Latitude Longitude	Rock Type	[^{238}U][a]	Error[b]	[^{232}Th][a]	Error[b]	[^{4}He][a]	Error[b]	Age$_{Raw}$[c]	Error[b]	R1[d]	R2[d]	L[e]	H1[f]	H2[f]	β[g]	a[h]	F$_T$[i]	Age$_{Corr}$[j]	Error[k]
				pmole	1σ	pmole	1σ	pmole	1σ	Ma	1σ	μm	μm	μm	μm	μm	1/μm	μm	Mean	Ma	2σ
K02	2901	27.790297°N 86.718155°E	Biotite Gneiss																		
K02 z001				22.80	0.18	2.213	0.014	0.053	0.001	**1.768**	**0.026**	28.2	25.6	245.6	29.9	15.3	0.082	36.76	0.677	**2.611**	**0.078**
K02 z002				13.31	0.11	1.094	0.006	0.025	0.000	**1.432**	**0.023**	22.4	22.5	249.1	32.2	32.2	0.097	31.00	0.624	**2.294**	**0.073**
K02 z003				13.48	0.11	1.011	0.007	0.029	0.000	**1.628**	**0.025**	27.8	28.7	166.7	22.1	33.5	0.082	36.38	0.675	**2.413**	**0.076**
K02 z004				9.188	0.073	0.574	0.005	0.016	0.000	**1.323**	**0.023**	25.2	26.8	184.0	28.8	25.3	0.087	34.43	0.658	**2.011**	**0.070**
K02 z005				11.226	0.097	1.331	0.009	0.029	0.000	**1.971**	**0.033**	31.9	34.3	226.0	39.0	31.8	0.069	43.52	0.724	**2.724**	**0.090**
K02 z006				8.112	0.067	1.567	0.008	0.019	0.000	**1.782**	**0.027**	25.6	24.0	230.6	24.1	29.9	0.088	33.90	0.652	**2.733**	**0.084**
																			Weighted Mean Age:	**2.43**	**0.23[l]**
K03	3663	27.84623°N 86.74149°E	Biotite Gneiss																		
K03 z001				113.40	0.93	2.106	0.013	0.367	0.004	**2.513**	**0.037**	49.2	45.9	288.5	47.6	45.8	0.049	61.58	0.801	**3.319**	**0.091**
K03 z003				9.381	0.075	0.746	0.004	0.020	0.000	**1.657**	**0.024**	29.1	30.7	300.7	19.6	15.6	0.072	41.39	0.711	**2.332**	**0.068**
K03 z004				29.63	0.26	0.948	0.006	0.090	0.001	**2.339**	**0.036**	27.2	32.0	199.2	26.8	16.2	0.077	38.99	0.695	**3.37**	**0.10**
K03 z005				6.208	0.053	0.614	0.004	0.013	0.000	**1.632**	**0.041**	29.4	25.9	154.7	26.6	16.0	0.085	35.47	0.667	**2.45**	**0.12**
K03 z006				11.87	0.11	1.486	0.015	0.026	0.000	**1.673**	**0.028**	36.7	31.0	184.8	30.1	21.2	0.070	43.11	0.721	**2.320**	**0.079**
K03 z007				6.830	0.058	1.793	0.010	0.019	0.000	**2.002**	**0.034**	39.6	35.7	156.4	27.4	19.2	0.065	45.81	0.735	**2.723**	**0.093**
K03 z008				5.821	0.050	0.471	0.004	0.010	0.000	**1.337**	**0.029**	29.0	35.3	126.6	20.1	20.7	0.078	38.42	0.690	**1.937**	**0.083**
																			Weighted Mean Age:	**2.57**	**0.39[l]**
K04	3999	27.87391°N 86.73954°E	Biotite Gneiss																		
K04 z001				1.942	0.017	0.9527	0.0053	0.0058	0.000	**2.096**	**0.042**	28.3	25.3	133.4	17.4	19.1	0.089	33.83	0.649	**3.230**	**0.064**
K04 z002				2.011	0.017	0.2352	0.0019	0.0060	0.000	**2.259**	**0.045**	23.4	29.8	113.5	16.4	15.1	0.093	32.27	0.637	**3.545**	**0.071**
K04 z003				1.828	0.015	0.7044	0.0051	0.0059	0.000	**2.293**	**0.061**	28.0	23.6	171.0	23.6	21.7	0.089	33.80	0.650	**3.529**	**0.094**
K04 z004				6.269	0.049	3.323	0.023	0.019	0.000	**2.110**	**0.039**	28.6	27.6	174.7	22.2	14.1	0.081	36.89	0.675	**3.125**	**0.057**
K04 z005				1.723	0.015	0.6275	0.0042	0.0049	0.000	**2.057**	**0.061**	31.0	30.7	167.0	26.2	25.3	0.076	39.48	0.696	**2.957**	**0.088**
K04 z006				1.823	0.015	0.8560	0.0062	0.0070	0.000	**2.709**	**0.066**	30.6	29.9	153.0	18.8	17.1	0.078	38.43	0.687	**3.941**	**0.096**
																			Weighted Mean Age:	**3.33**	**0.25[l]**
K05	4396	27.89237°N 86.71404°E	Leucogranite																		
K05 z001				18.59	0.15	6.451	0.040	0.058	0.001	**2.234**	**0.033**	41.5	44.1	198.2	39.8	39.1	0.057	52.62	0.767	**2.913**	**0.087**
K05 z002				38.07	0.30	2.482	0.014	0.125	0.002	**2.532**	**0.037**	48.6	54.3	273.8	46.1	29.0	0.046	65.53	0.812	**3.118**	**0.092**
K05 z003				36.50	0.29	2.649	0.015	0.138	0.002	**2.910**	**0.043**	32.2	39.7	220.3	40.3	38.1	0.065	45.99	0.738	**3.94**	**0.12**
K05 z004				37.77	0.31	1.758	0.010	0.142	0.002	**2.895**	**0.043**	51.6	33.7	241.9	42.4	46.6	0.057	52.27	0.767	**3.77**	**0.11**
K05 z005				33.78	0.30	3.824	0.028	0.138	0.002	**3.106**	**0.046**	44.1	53.9	244.3	79.3	46.6	0.051	58.73	0.791	**3.93**	**0.12**
K05 z006				29.67	0.26	3.077	0.022	0.105	0.001	**2.686**	**0.044**	40.1	44.2	213.8	63.3	35.9	0.058	51.68	0.764	**3.51**	**0.11**
K05 z007				36.11	0.32	2.363	0.019	0.109	0.001	**2.323**	**0.035**	40.3	41.2	242.6	63.9	43.0	0.058	51.56	0.764	**3.040**	**0.092**
K05 z008				27.79	0.24	1.331	0.010	0.099	0.001	**2.745**	**0.041**	40.7	36.1	214.7	57.2	33.9	0.062	48.13	0.749	**3.67**	**0.11**
																			Weighted Mean Age:	**3.39**	**0.29[l]**
K06	4596	27.92701°N 86.70844°E	Gneiss																		
K06 z001				3.756	0.031	1.763	0.009	0.016	0.000	**3.041**	**0.073**	26.4	26.0	124.8	17.2	13.4	0.091	32.97	0.641	**4.75**	**0.11**
K06 z002				9.117	0.074	4.952	0.046	0.046	0.001	**3.497**	**0.059**	29.5	27.2	196.6	21.7	15.1	0.079	37.74	0.682	**5.130**	**0.087**
K06 z003				2.705	0.022	1.696	0.011	0.009	0.000	**2.364**	**0.054**	26.5	24.9	115.0	15.6	11.1	0.094	31.88	0.629	**3.759**	**0.085**
K06 z004				2.383	0.020	0.645	0.004	0.007	0.000	**2.263**	**0.043**	24.8	28.1	111.1	18.9	13.6	0.093	32.27	0.636	**3.560**	**0.068**
																			Weighted Mean Age:	**4.14**	**0.77[l]**
K07	4766	27.94913°N 86.69547°E	Leucogranite																		
K07 z001				14.80	0.12	0.638	0.005	0.164	0.002	**8.55**	**0.12**	25.7	27.2	192.9	23.6	24.6	0.085	35.31	0.666	**12.84**	**0.37**
K07 z002				19.48	0.15	1.061	0.006	0.217	0.003	**8.57**	**0.12**	49.8	51.2	257.3	46.8	45.3	0.047	63.53	0.806	**10.63**	**0.31**
K07 z003				21.23	0.17	0.887	0.006	0.200	0.002	**7.27**	**0.11**	28.1	27.3	215.0	29.6	40.5	0.081	36.85	0.679	**10.71**	**0.31**
K07 z006				52.91	0.45	5.124	0.032	0.627	0.008	**9.03**	**0.13**	42.3	40.3	254.3	50.8	54.0	0.057	52.81	0.769	**11.74**	**0.34**
K07 z007				34.30	0.30	2.433	0.016	0.435	0.005	**9.73**	**0.14**	28.9	30.2	184.1	28.2	25.7	0.078	38.57	0.691	**14.08**	**0.42**
K07 z008				43.87	0.371	15.50	0.10	0.684	0.008	**11.22**	**0.16**	40.0	43.8	165.6	29.3	24.7	0.060	50.36	0.757	**14.83**	**0.42**
																			Weighted Mean Age:	**12.1**	**1.4[l]**
K08	5295	27.99920°N 86.84812°E	Leucogranite																		
K08 z001				18.15	0.15	0.435	0.002	0.222	0.003	9.47	0.14	26.4	27.0	145.9	21.6	19.2	0.088	34.27	0.657	**14.41**	**0.42**
K08 z002				57.31	0.45	2.125	0.012	0.716	0.009	9.65	0.14	38.6	35.0	274.8	29.8	29.2	0.061	49.32	0.754	**12.79**	**0.36**
K08 z004				37.13	0.30	2.547	0.014	0.415	0.005	8.57	0.12	24.1	23.0	183.7	16.9	17.2	0.094	31.81	0.633	**13.54**	**0.39**
K08 z005																			***Weighted Mean Age:***	**13.50**	**0.93[l]**

[a]Absolute measured ^{4}He, ^{238}U, and ^{232}Th concentrations are used to calculate the 'Raw Age' that is uncorrected for the effects of ^{4}He loss due to alpha particle recoil.
[b]Based on the propagation of analytical errors
[c]The 'Raw Age' was calculated with an iterative approach to solving the age equation.
[d]R1 and R2 describe the perpendicular half-widths of the zircon.
[e]L describes the total length of the zircon, and
[f]H1 and H2 describe the height of the pyramidal terminations of the zircon crystal.
[g]β represents the surface area to volume ratio for the crystal.
[h]a represents the equivalent spherical radius of the grain (Reiners and Brandon, 2006)
[i]The mean F_T correction was calculated following procedures defined for zircon. A bipyramidal prism geometry was assumed for all calculations (Hourigan et al., 2005).
[j]The F_T corrected age of the crystal. The FT correction was applied to the raw age following procedures defined by Farley et al. (1996).
[k]Uncertainty reported as 2 inverse variance-weighted standard deviations of the dataset for this sample.

APPENDIX TABLE C3: KHUMBU HIMAL INDIVIDUAL APATITE (U-TH)/HE RESULTS

Sample#	Elevation (m)	Latitude Longitude	Rock Type	[^{238}U]^{a}	Error^{b}	[^{232}Th]^{a}	Error^{b}	[^{4}He]^{a}	Error^{b}	Age$_{RAW}$^{c}	Error^{b}	Rd	L^{e}	β^{f}	a^{g}	F$_{T}$^{h}	Age$_{CORR}$^{i}	Error^{b}
				pmole	1σ	pmole	1σ	pmole	1σ	Ma	1σ	µm	µm	1/µm	µm	Mean	Ma	2σ
K01	2766	27.69531°N 86.72565°E	Biotite Gneiss															
K01 a001				0.04990	0.00080	0.0051	0.0020	0.000068	0.000027	**1.05**	**0.42**	24.0	144.4	0.11	30.87	0.515	**2.04**	**1.62**
K01 a004				0.2169	0.0021	0.0035	0.0032	0.000391	0.000026	**1.378**	**0.093**	40.4	190.1	0.068	49.98	0.682	**2.02**	**0.27**
K01 a006				0.0455	0.0070	0.0053	0.0020	0.000068	0.000025	**1.15**	**0.23**	26.9	147.8	0.099	34.14	0.555	**2.07**	**0.81**
																Weighted Mean Age:	**2.03**	**0.25**[l]
K02	2901	27.790297°N 86.718155°E	Biotite Gneiss															
K02 a001				0.3387	0.0031	0.0084	0.0032	0.000740	0.000029	**1.69**	**0.070**	34.4	126.3	0.083	40.55	0.619	**2.73**	**0.22**
K02 a003				0.05644	0.00084	0.0024	0.0032	0.000173	0.000026	**2.33**	**0.35**	31.8	136.5	0.087	38.69	0.601	**3.9**	**1.2**
K02 a004				0.1595	0.0014	0.0026	0.0032	0.000759	0.000027	**3.64**	**0.14**	40.8	188.6	0.067	50.32	0.684	**5.32**	**0.40**
K02 a005				0.3161	0.0026	0.02203	0.00053	0.000546	0.000029	**1.31**	**0.070**	37.1	191.4	0.073	46.61	0.660	**1.99**	**0.21**
K02 a006				0.4731	0.0038	0.00252	0.00044	0.002064	0.000039	**3.36**	**0.070**	44.7	244.4	0.060	56.68	0.716	**4.70**	**0.19**
																Weighted Mean Age:	**3.4**	**1.3**[k]
K03	3663	27.84623°N 86.74149°E	Biotite Gneiss															
K03 a001				0.4825	0.0039	0.0080	0.00046	0.000533	0.000027	**0.853**	**0.043**	34.5	183.7	0.078	43.6	0.640	**1.33**	**0.13**
K04	3999	27.87391°N 86.73954°E	Biotite Gneiss															
K04 a001				0.5385	0.0044	0.0196	0.0019	0.000114	0.000025	**1.627**	**0.039**	42.4	199.5	0.065	52.4	0.695	**2.34**	**0.11**
K04 a002				0.1079	0.0011	0.0046	0.0019	0.000017	0.000014	**1.18**	**0.10**	26.7	125.5	0.10	33.0	0.543	**2.17**	**0.37**
																Weighted Mean Age:	**2.32**	**0.11**
K08	5295	27.99920°N 86.84812°E	Leucogranite															
K08 a001				0.3862	0.0035	0.0238	0.0030	0.004390	0.000063	**8.67**	**0.15**	46.0	155.8	0.063	53.3	0.701	**12.36**	**0.42**
K08 a003				0.6408	0.0057	0.0828	0.0031	0.004841	0.000064	**5.670**	**0.090**	54.5	149.3	0.056	59.9	0.733	**7.75**	**0.25**
K08 a004				0.0974	0.0010	0.0187	0.0030	0.000442	0.000017	**3.32**	**0.14**	38.2	178.9	0.072	47.2	0.664	**5.00**	**0.41**
																Weighted Mean Age:	**8.1**	**3.4**[k]

[a]Absolute measured ^{4}He, ^{238}U, and ^{232}Th concentrations are used to calculate the 'Raw Age' that is uncorrected for the effects of ^{4}He loss due to alpha particle recoil.
[b]Based on the propagation of analytical errors
[c]The 'Raw Age' was calculated with an iterative approach to solving the age equation.
[d]R describes the width of the apatite.
[e]L describes the total length of the apatite.
[f]β represents the surface area to volume ratio for the crystal.
[g]a represents the equivalent spherical radius of the grain (Reiners and Brandon, 2006)
[h]The mean F_T correction was calculated following procedures defined for apatite.
[i]The F_T corrected age of the crystal. The FT correction was applied to the raw age following procedures defined by Farley et al., 1996
[j]Datum identified as an outlier using the Hempel identifier methods with an outher limit of 4.0
[k]Uncertainty reported as 2 inverse variance-weighted standard deviations of the dataset for this sample.
[l]Uncertainty reported as 2 inverse variance-weighted standard deviations of the inverse variance-weighted mean. (MSWD indicated no overdispersion.)

FIGURE C1

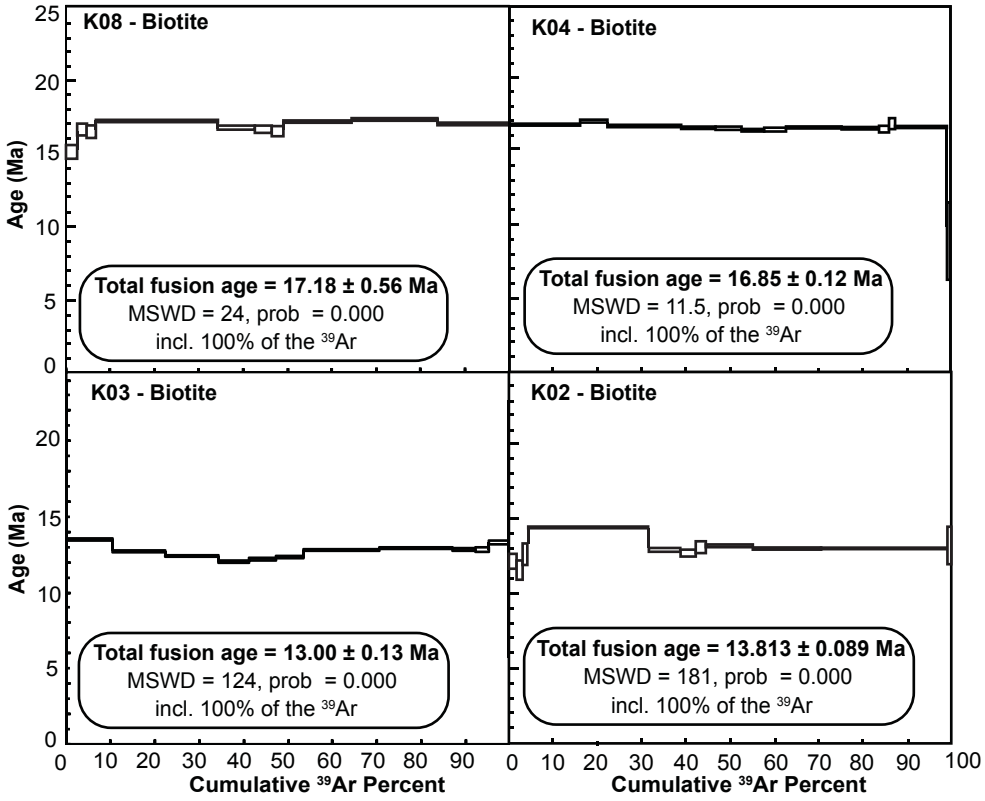
K08 - Biotite
Total fusion age = 17.18 ± 0.56 Ma
MSWD = 24, prob = 0.000
incl. 100% of the 39Ar
K04 - Biotite
Total fusion age = 16.85 ± 0.12 Ma
MSWD = 11.5, prob = 0.000
incl. 100% of the 39Ar
K03 - Biotite
Total fusion age = 13.00 ± 0.13 Ma
MSWD = 124, prob = 0.000
incl. 100% of the 39Ar
K02 - Biotite
Total fusion age = 13.813 ± 0.089 Ma
MSWD = 181, prob = 0.000
incl. 100% of the 39Ar
Age (Ma)
Cumulative 39Ar Percent

APPENDIX D

STATEMENT OF PERMISSION FROM CO-AUTHORS

Chapters 2-5 were prepared independently for publication with help from Kip Hodges (Chapters 2-5), Matthijs van Soest (Chapters 2-5), Chris McDonald (Chapters 3,4), Todd Ehlers (Chapters 2,4), and Jo-Anne Wartho (Chapter 2). These co-authors have acknowledged and granted permission for the use of this work in the context of this dissertation.